The StratoCruiser

Design Synthesis Exercise:
Stratospheric Airship for Thermal Infrared Earth Observation

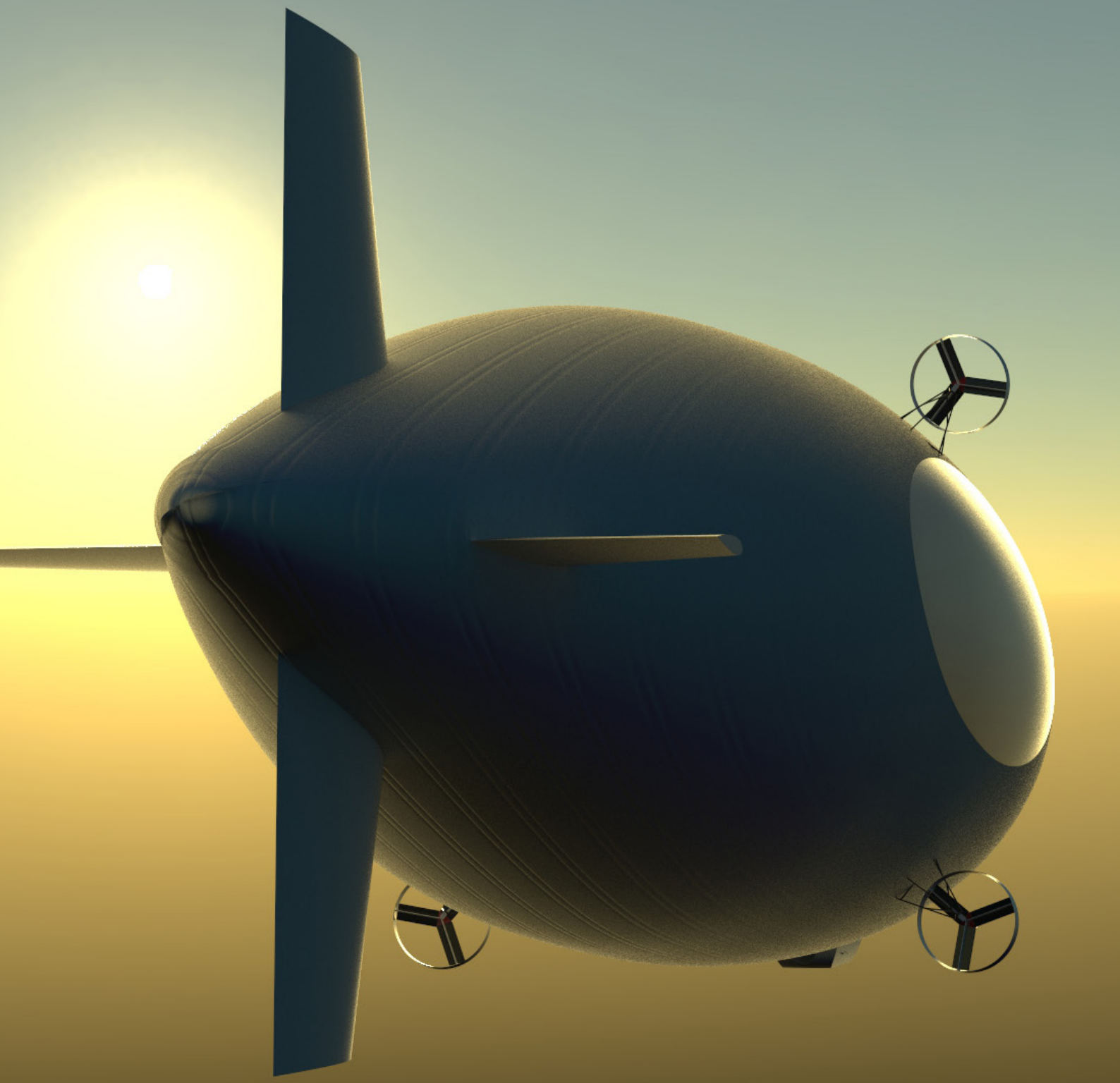

TU Delft

Group S10

June 2019

Delft University of Technology

Aerospace Design Synthesis Exercise:
Stratospheric Airship for Thermal Infrared Earth Observation

Group S10

Final Report : StratoCruiser

In partial fulfillment of the bachelor curriculum of Aerospace Engineering

Authors:
Bart Debeuckelaere (4537467)
Seok Joon Kim (4463005)
Marko Maricic (4526406)
Guido Monechi (4559827)
Petre Calin Nae (4535650)
Young Hyun Ryu (4542150)
Sorin Șeremet (4535707)
Rushil Vohra (4534506)
Stein Willems (4577248)

Tutors:
Dr.ir. Hans Kuiper
Ir. Jasper Bouwmeester
Coaches:
Dr.ir. Jeannette Heiligers
Yuqian Tu

July 2, 2019

Table of Contents

1 Executive Overview **1**

2 Introduction **5**

3 Market Analysis **6**

4 Conceptual Design **8**
4.1 Environmental Analysis . . . 8
4.2 Basic Airship sizing . . . 9
4.3 Airship Type . . . 10
4.4 Coverage Area . . . 13
4.5 Power . . . 14
4.6 Control . . . 15
4.7 Lifting Gas . . . 15
4.8 Structure . . . 16
4.9 Chosen Concept . . . 16

5 Detailed Design **17**
5.1 Aerodynamics . . . 17
5.2 Buoyancy . . . 23
5.3 Instrumentation . . . 29
5.4 Instrument Integration . . . 37
5.5 Propulsion . . . 44
5.6 Attitude Determination & Control . . . 52
5.7 Power . . . 60
5.8 Thermal Control . . . 67
5.9 Telemetry, Tracking & Command . . . 75
5.10 Command & Data Handling . . . 79
5.11 Structures . . . 80

6 System Integration **88**
6.1 Resource Allocation . . . 88
6.2 Data, Communication, Software and Power Flows . . . 91
6.3 Sensitivity Analysis . . . 93

7 Final Design **99**
7.1 Configuration . . . 99
7.2 Performance Analysis . . . 101
7.3 Manufacturing, Assembly and Integration . . . 102

8 Verification and Validation **104**
8.1 Verification . . . 104
8.2 Validation . . . 109
8.3 Compliance . . . 111

9 Operations **116**
9.1 Functional Analysis . . . 116
9.2 Logistics . . . 116
9.3 Constellation Analysis . . . 117

10 Non-Technical considerations **121**
10.1 Costs . . . 121
10.2 Return on Investment . . . 121
10.3 Risks . . . 122
10.4 Reliability, Availability, Maintainability and Safety (RAMS) . . . 126
10.5 Sustainability . . . 127

11 Conclusion **129**

12 Recommendations **130**

Bibliography **134**

Acronyms

a-Si Amorphous Silicon.

AR Aspect Ratio.

ATC Air Traffic Control.

C&DH Command & Data Handling.

c.g. Center of Gravity.

CCD Charged-Coupled Device.

CDR Critical Design Review.

CFD Computational Fluid Dynamics.

CTE Coefficient of Thermal Expansion.

EO Earth Observation.

FOV Field of View.

FR Fineness Ratio.

GaAs Gallium Arsenide.

GDP Gross Domestic Product.

Ge Germanium.

GSD Ground Sampling Distance.

HAPS High Altitude Platform Stations.

ISA International Standard Atmosphere.

LWIR long-wave infrared.

MTR Midterm Review.

NA Not Applicable.

OBC On-Board Computer.

PCB Printed Circuit Board.

PEM Proton-exchange membrane.

RAMS Reliability, Availability, Maintainability and Safety.

Re Reynolds Number.

RoI Return on Investment.

SiC Silicon Carbide.

SNR signal-to-noise ratio.

TBC To Be Confirmed.

TBD To Be Determined.

TIR thermal infrared.

TT&C Telemetry, Tracking, & Command.

Vol Buoyant Gas Volume.

VTOL Vertical Take-Off and Landing.

1 Executive Overview

Earth Observation (EO) is a field of scientific data gathering that relies heavily on high quality instruments and technologies. Within this field, thermal infrared (TIR) imagery is a commonly sought after form of data as it has applications for the military, natural disaster management, and environmental research, amongst other industries. Currently, EO missions are predominantly carried out on satellites which are expensive, unsustainable, and difficult to maintain. This is due to their reliance on launch vehicles and lack of accessibility. This project is an effort to find a solution. The **mission need** is thus: **Design a thermal imaging Earth observation system which is cheaper and more maintainable than current Earth observation satellite systems.** There is a range of ways to address this, the chosen one is using a stratospheric balloon. The **project objective** of this design synthesis is **to design a stratospheric balloon as a platform for TIR EO with a spatial resolution of 50 *cm* or better, a pointing accuracy of 5 *arcsec* or better at an altitude range of 20-30 *km*.** The use of a stratospheric airship instead of a satellite is potentially cheaper and more sustainable, while providing the same quality of imagery as through the use of spacecraft-grade instrumentation.

Requirement Analysis

The design process begun with an in-depth analysis of the requirements that must be imposed on the airship. This took place using a requirements discovery tree rooted in the mission need statement and stakeholder requirements. This led to the identification of driving requirements that guided the subsequent phases of the design. For example, **SB-Subs-ADCS-04** states that the attitude control stability shall be 1 arcsec or better. The design of the instrument mounting is heavily influenced by such a requirement.

Conceptual Design

Starting from the driving requirements, the team undertook an ideation phase to conceive and compare different design concepts. These concepts differed on aspects such as their reliance on buoyancy and/or aerodynamics, the use of fixed or moving instruments, and their operational altitude. The concepts were participants in trade-offs where they were evaluated on the basis of their capability to satisfy important requirements such as pointing stability and sustainability. These trade-offs led to the choice of a conventional airship with a single moving instrument that is reliant on hydrogen as its lifting gas. This design was then further investigated in the detailed design phase.

Detailed Design

With the chosen concept in mind, the team began the design of different subsystems. A name for the airship - 'StratoCruiser' - was also chosen at this stage.

Aerodynamics

Obtaining a reliable estimation of the aerodynamic forces on the airship is important as the aerodynamic drag significantly affects the design of the other subsystems. A refined drag estimation was obtained using Computational Fluid Dynamics (CFD) simulations. Limitations of this method are described. For example, the atmosphere was modelled as an ideal gas, and steady state conditions have been assumed. Accurate drag estimation allowed the analysis of different envelope shapes to minimize drag and facilitating the choice of an optimal airfoil shape. After that, a full simulation of the balloon was performed and the total drag was calculated, about 1720 N during daytime. The results were verified using CFD simulations and validated using wind tunnel test data.

Buoyancy Control

The airship controls its altitude by controlling the aerostatic lift. The lifting gas, hydrogen, is lighter than air and produces lift. With an analysis of the physical phenomena governing buoyant lift, the

hardware required for buoyancy control was designed. This consists of six ballonets, two ducts, a compressor, sensors, and gate & butterfly valves. The ballonets and ducts would be constructed using Dyneema, a lightweight composite fabric. The duct runs from the gondola all the way to the front- and rearmost ballonets and is called the "spine". The valves and compressor were sized based on performance requirements during climb and descent. Besides altitude control, the ballonets may also be used for trimming the pitch angle and attitude control. For this, the system must be able to inflate the front ballonets while deflating the rear ones and vice versa, thereby shifting the Center of Gravity (c.g.).

Instrumentation

The payload of the StratoCruiser is a TIR imaging system that is comprised of a set of mirrors and a detector. The primary mirror is the main focus of the design as it greatly influences the performance of the subsystem and ultimately that of the whole system. The detailed design focused on providing the required signal-to-noise ratio (SNR) of the images while accommodating the instrument in the airship, physically as well as in terms of its budgets. The resultant mirror that is used to reflect the rays from the Earth onto the detector is concave and parabolic. The substrate of the mirror is made of Silicon Carbide (SiC) and a protective silver coating is applied to ensure the durability and reflectivity of the mirror surface. To limit the noise measured by the detector, a cooled baffle and a Germanium (Ge) filter are used. The instrument is capable of capturing images in the infrared spectrum (8 to 12 μm) with a resolution of 1 m, up until an off-nadir angle of 25°. Recognizing that a resolution of 1 m does not meet the requirement of 0.5 m, a recommendation is made to investigate the feasibility of super-resolution algorithms. These machine-learning algorithms can artificially increase the resolution without changing the instrument design and are therefore a promising option to still meet the required resolution of 0.5 m. This makes the StratoCruiser suitable for monitoring traffic flows in and around cities, ports and borders by observing cars, trucks and ships.

Instrument Integration

A key aspect of the scientific mission is the quality and volume of the images captured, which translates to requirements on temporal resolution, pointing accuracy, and stability. In order to satisfy these, a choice was made between fixed and moving instruments. A single moving instrument was chosen, entailing that its mount had to be capable of reorienting the mirror while satisfying the temporal resolution and stability. It was found that a coordinated system of linear actuators, also known as a parallel manipulator, is the most suitable option as a result of its accuracy and payload capacity. Therefore, the parallel manipulator was further designed with regards to the positioning of the actuators and their control; it was concluded that the actuators may be placed at a radius of 0.6m from the mirror center to satisfy the driving requirements.

Propulsion

To design the propulsion subsystem, the type of propulsion was first chosen as electric. Parts such as the propeller blades and gearbox housing were designed in detail, while other parts were chosen off-the-shelf. The propulsion subsystem includes propeller blades, motor, motor controllers, linear actuators & engines for the variable pitch, gearboxes, ducts, and pylons. The final design of the system includes four large propellers, each of which have a blade diameter of 4.88m and consumes 13.9kW. The propellers were placed in order to maximize the potential control provided when using thrust differential and also to reduce drag by cleverly utilizing the airflow around the airship.

Attitude Determination and Control

The design of the attitude determination and control subsystem began with the justified choice of the conventional tail configuration over the X tail. The next step involved choosing an airfoil for the tail surfaces. This was done by comparing the aerodynamic performances of several common NACA series airfoils. After choosing the NACA 0012 due to its superior performance, a preliminary sizing

of both the vertical and horizontal tail surfaces was made, based on their position and the airship size. Following this, the tail size was iterated with a parametric method, incorporating the lateral and longitudinal stability and controllability of the airship with different tails. Finally, a choice of attitude determination sensors was made.

Power

The power requirements of the airship are met with the help of a renewable energy generation and storage system comprised of a solar array connected to the airship's various subsystems via a distribution network and to the energy storage unit. An optimal placement in terms of mass and cost of the solar panels on the airship surface was identified by studying the effect of solar incidence angles on the balloon exterior throughout the year. This was done for the most critical condition of the year, the winter solstice, resulting in a solar array design capable of satisfying the power requirements all year-round. The final generation system includes a $4198m^2$, $504kg$ solar array of amorphous Silicon cells with a Kapton substrate. The energy is stored and distributed using hydrogen fuel cells and an electrolyzer. During the day, solar energy is used to electrolyze water and store the resulting hydrogen and oxygen in carbon fiber tanks. These are then used as reactants in fuel cells overnight to supply power. The only exhaust of the fuel cells, water, is stored to be electrolyzed the following day, closing the loop in a sustainable way.

Thermal Control

The thermal control subsystem deals with maintaining instrument temperature and was designed by modelling the thermal behaviour of the airship itself. Primarily, liquid nitrogen has been chosen as a coolant for the instrument where a closed loop cryosystem continuously maintains the temperature of the baffle and the mirror at 90K. The thermal behaviour of the balloon was modelled for the longest and shortest days. Using white tedlar as a surface finish minimizes temperature differences throughout the day, as a result, minimizing the pressure difference of the buoyancy gas. This allows for the selection of a suitable envelope that can withstand the loads and temperatures that can be experienced throughout the course of a day. Temperature control for other electronic components within the gondola is maintained using the dissipated heat from the fuel cell; any excess heat is radiated out to the stratosphere.

Telemetry, Tracking & Command

The Telemetry, Tracking, & Command (TT&C) subsystem design consisted of constructing a link budget tool for calculating the SNR of both uplink and downlink communications. This was initially done via comparison to other missions and then refined as choices of antennas and estimates of data rates were made. It was concluded that both the uplink and downlink budgets easily close with the chosen antennas - a high gain horn antenna for downlink and a low gain helical one for uplink.

Command & Data Handling

The Command & Data Handling (C&DH) design began with a definition of the data handling architecture. This was updated towards the end of the detailed design phase as more was known about the functioning and interconnections of subsystems. Additionally, data rates were estimated for both the scientific payload and each of the subsystems. Based on this, a choice of computing components was made - a Lenovo workstation is used as the main computer, while Printed Circuit Boards are used within each subsystem.

Structures

The structure of the airship primarily pertains to the structure of the envelope. There are three possible solutions for envelope structures: rigid, semi-rigid and non-rigid. The non-rigid structure was selected as it has the lowest mass and allows for the best ballonet integration. Such a structure

consists of a pressurized envelope and a curtain/wire suspension system that distributes the loads of the payload evenly through the skin. The chosen configuration is therefore a non-rigid envelope with two rows of curtains. The ballonets are attached to the curtains to allow for a more efficient deflation and avoid folding. At the longitudinal position of the gondola the wires extend through the ballonets all the way to the bottom part of the envelope to transfer part of the load introduced by the gondola into the top part of the envelope. Regarding the material choice for the structure, it is a composite fabric that uses Dyneema as its structural fiber and white Tedlar for thermal protection. For the wires Dyneema is again the material of choice as it allows for better integration with the ballonets.

System Integration

During the course of the design, the various mass, power, and cost budgets of subsystem were tracked to avoid an unfeasible design. In addition, diagrams showing the data flow, electrical flow, communications, and software between subsystems are drawn. Finally, there are a number of sensitivity analyses demonstrating the influence of changes in specific parameters on the performance of the airship. The mass of the entire airship is about 8 tons, while the material cost is approximately €3.6 million. Manufacturing costs were not estimated at this stage.

Operations

The logistics of operating a large airship are important. These were analyzed with regards to topics such as maintenance, storage, and hydrogen handling. In order to monitor the whole country of the Netherlands, an in-depth analysis of balloons response time and coverage was done. It was found that each balloon can instantaneously cover an area with $7.22km$ of diameter only, meaning that it is almost impossible to entirely cover the Netherlands real-time. An optimization algorithm was developed to determine the required number of airships to cover the Netherlands with a certain response time, along with their optimal locations. With 3 operating airships, for example, the entire country can be covered in about half an hour.

Non-technical Considerations

The market viability of the StratoCruiser is evaluated through an analysis of the market for EO data. This, along with an estimation of the costs of the airship, led to an approximate Return on Investment (RoI). At this stage, the annual operational costs are approximated to be about €5 million, while the annual revenues are between €9 million and €13 million, assuming 3 airships are used to cover the Netherlands. This yields a positive return on investment. Additionally, the risks involved with the operation of the airship are described, along with mitigation strategies for the most serious ones. Finally, aspects related to the reliability, maintainability, availability, safety, and sustainability of the airship are described.

Verification, Validation & Recommendations

The various numerical models used in the design of the StratoCruiser were verified and validated in multiple ways, a summary of these methods is provided. In addition, suggestions are made for further procedures to improve the models. Recommendations for further research and testing are included with regards to the design of each subsystem.

2 Introduction

High Altitude Platform Stations (HAPS), vehicles flying between 20 to 30 km, provide an attractive option for different fields such as EO, telecommunications and many others. Various feasibility studies for such systems have been performed [1, 2], but no design has been fully developed and built yet. Lighter-than-air vehicles have the potential to be cheap, versatile and flexible EO platforms, also assuring maintainability and upgradability possibilities that other observation systems such as satellites do not possess. The StratoCruiser, a stratospheric airship specialized in TIR EO, is designed to fill this niche gap. It provides a long-term, stable and sustainable platform for precise EO which can be used for purposes such as monitoring traffic flows in and around cities, border, ports, etc. Additionally, its modular design allows for easy maintenance and upgrades to suit the mission needs and conditions.

Firstly, a market analysis is performed in Chapter 3 to understand the potential of the system and the main advantages compared to other observation platforms. Secondly, a summary of the conceptual phase of the design as performed in the midterm report [3] is presented in Chapter 4, with the objective of selecting the main characteristics of the airship. Different airship types are analyzed, together with a brief analysis of the operational environment and the choice for the instrumentation concept.

A final concept is then chosen and that is developed in Chapter 5, where the detailed design of all different airship components and subsystems is presented. In Chapter 6 the system engineering approach to combine all different subsystem is presented, by illustrating the budgets, software and communication interfacing and several sensitivity analyses. The final design is then presented in Chapter 7, the performance and characteristics of the system are analyzed, together with a brief manufacturing plan.

The design approach and model used are verified and validated in Chapter 8, where the requirement compliance of the system is also presented. The airship logistics concepts, cruise functional flow analysis and analysis of possible a airships constellation is present in Chapter 9, followed by other non technical consideration such as risks, RAMS and an explanation of the sustainable design approach in Chapter 10. The in-depth recommendations and potential planning are given for a potential next-phase of the design in Chapter 12, after the report conclusion.

3 Market Analysis

There are broadly four markets that the StratoCruiser is intended to be involved in - EO Data, Monitoring, Telecommunications, and Stratospheric Experiments. The analysis of these markets in the Netherlands is presented in this section. The EO Data and Monitoring markets are analyzed using data from the Euroconsult Group and the European Commission market report about the Copernicus mission [4, 5].

EO Data Market

The StratoCruiser would be involved in the EO market through the sale of TIR images captured and stored over time. Worldwide, this market is dominated by demand for data relating to defense, infrastructure, energy, and environmental monitoring. In 2017, this market in Europe was valued at $ 252 mil [5]. To evaluate the size of the Dutch market for EO data, these four industries in the Netherlands are compared to that of the entirety of Europe. The comparison is conducted using the value of representative parameters in the Netherlands compared to their value in Europe overall; this is presented in Table 1. Defense is measured using defense spending, environmental monitoring is measured by environmental protection spending, energy is measured by energy consumption, and several miscellaneous industries, such as disaster management and infrastructure are compiled in 'Others', which are compared using Gross Domestic Product (GDP) due to lack of a more suitable parameter.

Table 1: Summary of EO Data Demand in the Netherlands (NL) compared to Europe [5] [4]

Industry	**% of Data Market**	**NL as % of Europe**	**NL Market (mil$)**
Defense	61	4.1	6.34
Env. Monitoring	2	9.1	0.46
Energy	6	3.9	0.59
Others	31	5.2	4.04
Total	-	-	11.44

This approximates that the spending on EO data in the Netherlands in 2017 was approximately $ 11.44 mil. Clearly, defense is the largest industry buying EO data, so it should certainly be catered to by the StratoCruiser.

Monitoring

The market for monitoring as a service is currently more than twice as large as the EO data market worldwide. In Europe, it is valued at $ 632 mil and its demand is primarily comprised of defense, environmental monitoring, energy, and finance [4]. The first three of these industries can be compared using the parameters described previously, and finance is evaluated using the total value of consolidated assets in the Netherlands and Europe. In addition, industries like infrastructure, natural resources, and location-based services are evaluated using GDP, and grouped in 'Others' in Table 2:

Table 2: Summary of Demand for Monitoring in the Netherlands compared to Europe [5] [4]

Industry	**% of Monitoring Market**	**NL as % of Europe**	**NL Market (mil$)**
Defense	18	4.1	4.69
Env. Monitoring	22	9.1	12.59
Energy	8	3.9	1.99
Finance	1	7.5	0.47
Others	51	5.2	16.68
Total	-	-	36.42

Evidently, the monitoring service market has far more value in the Netherlands than the EO data market. This gap is projected to increase in the future as the use of monitoring for finance and location-based services grows. In total, the worldwide data and monitoring markets are projected to increase from $4.6 billion currently to $5.7 billion by 2027 [4]. The design of an airship, which has as a unique selling point its capability to hover above a specific place without having to have an airspeed, could therefore be very promising given the opportunity in the market for monitoring services. Even more so because alternative platforms for monitoring services, like satellites or long endurance airplanes require an airspeed at all times in order to maintain altitude.

Telecommunications

The telecommunications market is a huge opportunity for High Altitude Platform Stations. From 20 km altitude, which is the target cruise altitude of the mission, an area with 500 km radius of coverage is visible [1], meaning that installing a communications payload on the airship could provide service to a large area. One single high altitude airship can replace numerous ground-based communication infrastructures [2]. Furthermore, the cost of a single balloon would most likely be cheaper than a satellite and it would have the big advantage of having negligible path loss compared to space-based systems [2]. Furthermore, because of lower distance compared to geostationary satellites, latency would be lower.

Stratospheric Experiments

Stratospheric airships can also offer payload opportunities for scientific experiments that needs to be executed in stratospheric conditions. Satellite hardware can be tested in near-space conditions, as well as experiments that require low atmospheric density or pressure.

Opportunity

EO is currently dominated by satellite remote sensing. Although a satellite based solution is predictable and not energy intensive in the long term, it has a number of disadvantages in comparison to an airship such as the StratoCruiser:

- Flexibility: satellites are bound to being in orbit around the Earth. In a particular orbit, it is limited to observing locations on the ground only when it passes close enough to them. Changing orbit in order to change observation regime is difficult as it requires energy, approval, and coordination with other missions. The StratoCruiser, on the other hand, can be transferred between locations with ease. With 3 airships stationed around the Netherlands, any point can be reached within about half an hour (further described in Chapter 9).

- Monitoring: the maximum frequency at which a ground location can be monitored is 2-3 times per day for low-Earth orbiting satellites in general. Airships, by comparison, can theoretically offer any frequency of monitoring as they can be stationed indefinitely above a given location. This is advantageous for monitoring points of interest with frequent activity.

- Accessibility: once they are in orbit, satellites are very difficult to access. This also means they are difficult to maintain and upgrade. The StratoCruiser, on the other hand, can be descended within hours. This allows easy maintenance as well as the option of changing the payload or other subsystems.

- Sustainability: satellites dependent on rockets for launch perform badly in terms of sustainability due to the massive emissions

4 Conceptual Design

This chapter presents the concepts on mission level, airship level and some concepts on subsystem level that affect the entire mission. Note that, though presented in this report as a linear process, all trade-offs in conceptual design and subsystem analysis were done in parallel. The knowledge from the analysis and considerations in trade-offs were applied to the other trade-offs to reach a refined and well supported final concept to continue development with. The options discussed in this chapter are listed below:

- **Operational altitude**
- **Balloon type:** weather balloon, conventional blimp, hybrid airship.
- **Coverage area:** single airship, constellation of airships, single nadir pointing instrument, moving instrument, turning the entire airship, multiple fixed instruments.
- **Instrument placement:** within the balloon, within a gondola.
- **Solar cell placement:** fixed, pointing through airship attitude, pointing cells on rails, inside the airship.
- **Control:** remote control, autonomous
- **Lifting gas:** hydrogen, helium

4.1 Environmental Analysis

Before any choices were made on how to fulfill the mission, an analysis was done on the environment in which the StratoCruiser will operate. Both the altitude and the cruise velocity will be addressed.

Operational Altitude Analysis

The StratoCruiser should operate in the stratosphere in an altitude range between 20 to 30 km [6]. The horizontal winds and the density of the atmosphere heavily affect other subsystems such as the power generation, propulsion, the instrumentation and buoyancy control. Firstly, the regulations regarding the operational altitude were analyzed and it was found that the airspace above FL650 (20km) is uncontrolled, which means that coordination with the Air Traffic Control (ATC) is not needed [2]. An altitude of 20 km is therefore identified as the lower limit for the altitude range. The horizontal winds were analyzed using the empirical Horizontal Wind Model (HWM14) [7, 8] in order to find the lowest required drag as a function of altitude. Based on these winds, as presented in the Midterm Review (MTR) [3], it was found that the most optimal operational altitude in the allowable range was at 20 km. In order to find the upper altitude value of the operating range of the StratoCruiser, the density variations occurring at 20 km were analyzed and it was found that the density changes periodically during the year, reaching a maximum in summer and a minimum in winter. The lowest density is achieved in February, corresponding to a value of 0.083 kg/m^3 [3], which results in the buoyant force being lowest in the winter. Finally, the maximum operating altitude in standard conditions, using the International Standard Atmosphere (ISA), was calculated by finding the altitude value corresponding to a value of 0.083 kg/m^3. This results in a cruise altitude range between 20 and 20.5 km. This operating altitude range is found to be similar to the one presented by other reports which also minimize for the drag [2]. Based upon this analysis, requirement **SB-Sys-14**, which previously stated that the airship shall operate in altitude ranging from 20 to 30 km, is changed. **SB-Sys-14-mod** now states that the airship shall have a service ceiling of 20.5 km (ISA).

Cruise Velocity Selection

The horizontal wind speed is very important as the airship should be able stay stationary over a point of interest during high winds, which heavily influences the design of the propulsion subsystem, which

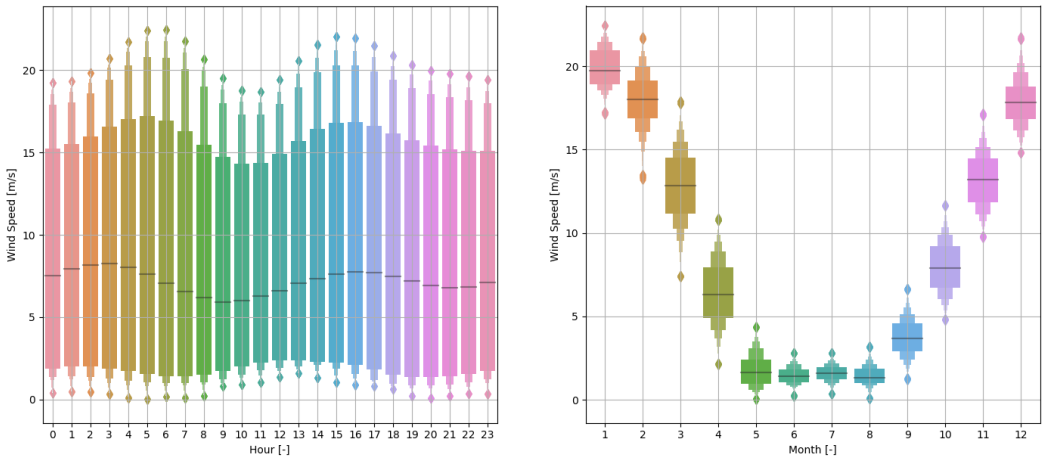

(a) Daily Variations (b) Monthly Variations

Figure 1: Horizontal Wind Variations

in turn influences the design of the power subsystem. It was chosen to select the cruise speed, relative to the wind, equal to the 95th percentile of the yearly wind. As no input solar power is available during the night, it was decided to design the airship to vary its altitude within the operational range to find the lowest winds and consume less power at nighttime. The airship will also be able to deal with higher exceptional winds, as the maximum thrust and peak power produced will be higher and the balloon can also change altitude to find a calmer atmospheric layer [3]. HMW14 was used to obtain the horizontal winds in the operational altitude range to analyze the typical wind distribution. The daily and monthly variations are shown in Figures 1a and 1b.

It can be seen that winds remain reasonably constant during the day, while they greatly vary during the year, with high wind speeds during the winter and low speeds during the summer. In the end, the cruise velocity during the day was set to 21 and 20 m/s during the daytime and nighttime respectively [3].

4.2 Basic Airship sizing

After the operating environment has been analyzed, a basic sizing for airships is done to obtain the preliminary size of the balloon. This sizing is based on statistical data.

To speed up the iteration process and aid with the sensitivity analysis, a python script was developed. The sizing algorithm is almost identical to the sample problems found at the end of Chapters 11 and 12 of Fundamentals of Airship Design [9], with small changes made to the propulsion and power systems. The geometry of the envelope is assumed to be an ellipsoid and, where available, the best and most efficient solution for each subsystem was considered. A loop that changes the volume by a small increment was added to obtain the smallest volume and mass for a given altitude and velocity.

During the conceptual design and preliminary sizing processes of the project the program was altered to quantify the performance of the different options of each subsystem. The values of the starting point of the project can be seen in Table 3. For the analysis of the aerodynamic performance of the platform the volume of 200000 m^3 and its equivalent lift were used. The high number of significant digits is not required as the relative performance is analyzed.

Table 3: Initial size of the high altitude platform

Parameter	Value	Units
Volume	229366	m^3
Mass	17098	kg

4.3 Airship Type

Now that the basic size of the airship has been established, three balloon types were identified to possibly perform EO with the specified requirements. The first one is the weather balloon. This is a balloon with the equipment suspended below the lifting gas. It goes up until the envelope bursts because of over-pressure and descends on a parachute. This is the cheapest option but it is not controllable. If one wants to monitor an area, which was identified in the market analysis as a promising opportunity for a stratospheric platform, balloons would need to be launched and recovered continuously. This is unacceptable from a logistics and sustainability point-of-view, ATC would not approve the continuous launching of uncontrolled balloons and in bad weather conditions, it might not even be possible to launch or the balloon might miss its target. Therefore this concept was discarded very early on in the project.

Two other types are the conventional blimp and hybrid airship. A conventional blimp provides all of its lift through aerostatics. It has a fixed envelope volume. The volume changes of the lifting gas are compensated for by internal air bags or ballonets. These can be used to control its altitude. A propulsion system allows the airship to have a horizontal cruise speed. A hybrid airship has the same characteristics but also provides part of its lift aerodynamically. A conventional blimp and 4 concepts for hybrid airships are sketched in Figure 2.

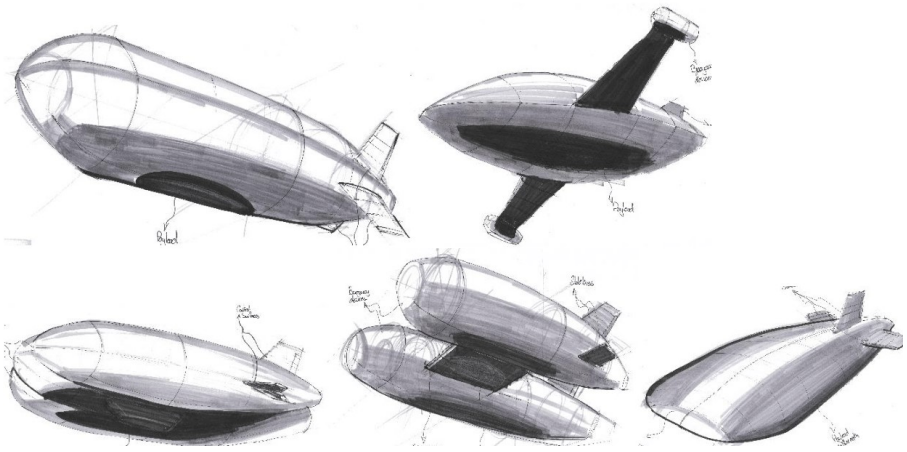

Figure 2: One conventional and four hybrid airship concepts.

As a hybrid airship partially relies on aerodynamic lift to maintain altitude, the airship needs a horizontal cruise speed at all times, which introduces stringent requirements on the power subsystem as it requires continuous power. Moreover, hybrid airships neither have the convenience of Vertical Take-Off and Landing (VTOL) nor the capability to hover overhead a point of interest. On the other hand, hybrid airships can provide significant aerodynamic lift, which means means that the balloon can be made smaller as aerostatic lift is linearly dependent on the mass of lifting gas as can be seen from Equation 4.1 [3]. In this aerostatic lift equation, m refers to mass, T to temperature, p to pressure, M to molar mass and g to the gravitational constant. The subscript g stands for gas and atm for the atmosphere.

$$L = m_g g \left(\frac{T_g}{T_{atm}} \frac{p_{atm}}{p_g} \frac{M_{atm}}{M_g} - 1 \right) \tag{4.1}$$

The extent to which the volume of a hybrid airship can be reduced compared to a conventional blimp requires a more in-depth aerodynamic analysis.

Aerodynamic Forces Estimation

Estimation methods for the aerodynamics are presented in this section to analyze the feasibility of the conventional and hybrid options. Aerodynamic lift and drag are usually defined as:

$$L = C_L q S_{Ref} \tag{4.2}$$

$$D = C_D q S_{Ref} \tag{4.3}$$

where L and D are the Lift and Drag forces respectively, C_L and C_D are the lift and drag coefficients, q is the dynamic pressure and S_{Ref} is a reference surface area.

The choice of the reference surface is important as it affects the coefficients. For airplanes, the reference surface is usually taken as the planar surface, however, this is not the case for balloons. By convention, the Buoyant Gas Volume (Vol) is taken as a reference for aerodynamic forces. More specifically, the volume parameter used is $Vol^{2/3}$ [9]. The conversion between planar surface and $Vol^{2/3}$ can be estimated as follows for typical airship shapes:

$$S_{plan} = N_L Vol^{2/3} \tag{4.4}$$

N_L is dependent on the number of lobes of the envelope, as explained in [9], while $Vol^{2/3}$ is the gas volume of the airship to the power of two thirds and S_{plan} is the planar surface of the balloon.

The aerodynamic lift can be found with Equation 4.2, if the lift coefficient is determined. For incompressible flow and low-sweep shapes, the lift coefficient derivative with respect to the angle of attack (C_{L_α}) can be calculated with the Helmbold equation [9] and can be simplified as follows for a low Aspect Ratio (AR):

$$C_{L_\alpha} = \frac{2\pi AR}{2 + \sqrt{4 + AR^2}} \approx \frac{\pi AR}{2} \tag{4.5}$$

It should be noted that the previous equations are for a lift coefficient referenced to the planar area, therefore they should be converted using a combination of Equation 4.4 and Equation 4.2.

Similarly to the lift coefficient, the drag coefficient needs to be determined and can be estimated using the following equation [10]:

$$C_D = C_{D_0} + KC_L^2 \tag{4.6}$$

Where C_{D_0} represents the zero lift coefficient, and K is a non-dimensional coefficient dependent on the airship geometry.

The total drag-due-to-lift factor K can be approximated using the empirical relation [9]:

$$K = -0.145AR^{-4} + 0.182AR^{-3} - 0.514AR^{-2} + 0.838AR^{-1} - 0.053 \tag{4.7}$$

About 60% of the airship zero-lift drag is usually produced by the envelope drag [11], while the rest is a combination of tails, propulsion system mounting, gondola and other external components. The envelope drag is mostly composed by skin friction and pressure drag. The skin friction is dependent on the wetted area, while the pressure one is mostly dependent on the Fineness Ratio (FR), which is defined as the ratio of length and diameter [9, 11]. With low FR pressure drag dominates, while skin friction drag increases with higher FR . The envelope zero lift drag is also dependent on the Reynolds Number (Re) and can be estimated using the Hoerner relation [11]:

$$C_{DV_0} = \frac{0.172(FR)^{1/3} + 0.252(FR)^{-1.2} + 1.032(FR)^{-2.7}}{Re^{1/6}} \tag{4.8}$$

Where C_{DV_0} is the zero lift drag referenced to the volume reference surface parameter. The Re is calculated using the $Vol^{1/3}$ (cubic root of the gas volume) as a reference length. The minimum drag occurs at an FR in the range from 4.5 to 5.5.

The increase in C_{D_0} due to the gondola, tails and other external components can be found from empirical relations in [9].

Concept Aerodynamics Comparison

Starting from an initial volume estimate of 200000 m^3, from the preliminary mass estimation, two simple airship designs were studied to analyze the feasibility of a stratospheric hybrid airship. A conventional airship was compared to a 3-lobed hybrid airship, with a constant total lift. The 3-lobed

airship was chosen as it effectively represent most of the hybrid design concepts for an initial feasibility study. The angle of attack was determined by minimizing the power consumption [9]:

$$\alpha = \frac{\sqrt{\frac{3C_{D_0}}{K}}}{C_{L_\alpha}} \tag{4.9}$$

Where α is the optimal angle of attack, found to be about 12 degrees. The results of this feasibility study are summarized in Table 4.

Table 4: Comparison Between Hybrid and Conventional Design

Design	Volume $[m^3]$	Aerodynamic lift [kN]	Buoyant lift [kN]	Lift [kN]	Drag [kN]
Conventional	203800	0	150.00	150.00	2.71
Hybrid	173500	22.26	127.74	150.00	4.96

It can be seen that in order to achieve the same total lift, the hybrid design requires less gas volume as some lift is provided by the aerodynamic shape of the envelope. On the other hand, the drag is much higher compared to the conventional design, which will correspond to an increase in the propulsion subsystem mass, which in turn will increase the mass of the power subsystem. This adds to the previous observation that those two subsystems had to be bigger for hybrid airships in the first place, due to the constant need of a horizontal airspeed. Furthermore, the more complex envelope shapes of a hybrid airship require a heavier structure. This adds mass because of a heavier structure, which implies an additional lift required to maintain altitude and thus, more buoyant gas volume. This compensates for the advantage of having a smaller airship and even makes the airship heavier and larger. Moreover, the hybrid airship is more complex to design and manufacture because of the integration between the aerodynamic surfaces and the envelope and because of the aerodynamic shapes. The only possible advantage of hybrid airships over conventional blimps is that they can use the aerodynamic surfaces for control. It is however, questionable to what extent this is an advantage as the market analysis showed great opportunity in monitoring services, for which the ability to hover is more valuable. Furthermore, it was found that controllability is primarily important during landing and that the conventional blimp has sufficient control for this. Because the hybrid airship is heavier, more complex and less practical, the conventional blimp concepts was chosen for further development. This is summarized in Table 5, in which the relative importance of the criteria is proportional to the width of its column.

Table 5: Concept trade-off.

	Mass	**Controllability**	**Complexity**	**Practicality**
Conventional	No structure for aerodynamic lift	Control through propulsion and tail surfaces	Simple	VTOL
Winged	Wing structure, more powerful power and propulsion	Aerodynamic control, tail and ailerons	More complex	Requires runway and wide hangar
Multi-cell	More powerful power and propulsion	Aerodynamic control, tail	Relatively simple	Requires runway
Flying wing	Structure to keep shape, more powerful power and propulsion	Aerodynamic control, tail	More complex structure	Requires runway
Double balloon	Wing structure, two balloons, more powerful power and propulsion	Aerodynamic control, tail	Complex structure and integration	Requires runway

The most important criterion is mass as this determines how large the airship must be. Controllability is especially important during landing. Complexity is included because a more complex system is more

difficult and expensive to design and manufacture and it has more potential points of failure. Lastly, practicality is included because the operations of a large airship are already complex.

4.4 Coverage Area

A single airship has a limited coverage area. If a client wants to monitor a larger area with the same response time (time to reach any point in the area), a constellation of balloons is needed. To be able to reach any point in a certain area, the airship must be able to cruise from one point to another and must therefore be controllable. **SB-Sys-10** confirms that the weather balloon is not suitable for this mission, as it states that the airship shall have a range of 500 km. The coverage area with a certain response time depends on the cruise speed. A higher cruise speed increases the coverage area for a certain response time and reduces the number of airships required. If the airship wants to hold station, its cruise speed must compensate for the wind, as stated in Section 4.1. Increasing the cruise speed primarily impacts propulsion subsystem which influences the power generation as a higher solar cell area and mass would be required to supply power to the propulsion subsystem. Section 9.3 explains how many airships are needed in a given situation.

4.4.1 Instrument Type and Integration Concepts

How much of the visible area of the airship can actually be monitored depends on the instrument performing the observations. The airship can be equipped with: one nadir pointing instrument, multiple instruments at fixed angles, or a moving mirror (which can be pointed in a given direction).

For the airship to take a picture of a new location with a single nadir pointing mirror, the entire airship could change attitude. As an airship is inherently stable and very large, large control actuators would be required to actually point the instrument at a desired attitude. These control actuators could be control surfaces or vectored thrust. The airship could also fly a pattern to sweep an area. In both cases, pointing the instrument would be very slow, meaning that the area that can be observed in an amount of time is low. This makes this option economically inefficient. Having multiple instruments pointing in a fixed direction would improve the coverage.

Another option is a moving mount. This system can point the mirror in a different direction, again allowing larger coverage than a nadir pointing mirror. This adds a little mass but can quickly change the pointing of the instrument. These three options are compared with regards to the following criteria and the corresponding weight:

- Flexibility (weight = 4): this is very important in order to satisfy the temporal resolution requirement of 1 minute, implying that the instrument must capture an image and return to the same point within a minute.
- Coverage area (weight = 4): an option with a larger coverage area is preferable as it reduces the frequency at which the airship must be displaced.
- Mass (weight = 3): the mass of the instrument closely influences the mass of the structure and the airship in general, but it does not directly affect the performance regarding the scientific mission, so it has a smaller weight.
- Cost (weight = 2): finally, cost is an important parameter but it also does not affect the scientific mission or the overall design, so it is given the lowest weight.

Using a single mirror offers the least coverage area and minimal flexibility as the entire airship must be relocated or reoriented in order to view a different area. In terms of mass and cost, however, this system is the best performing. Specifications of similar instruments are used to estimate the cost of \$130,000 and mass of 200kg[1].

Multiple fixed mirrors would perform the same in terms of flexibility as a single mirror. On the other hand, the coverage area would be larger. If the orientation of each mirror is properly tuned,

[1]URL: https://www.edmundoptics.com/f/precision-parabolic-mirrors/11895/

the coverage area can be assumed to increase proportionally to the number of mirrors used (n). This trend cannot continue indefinitely, but is feasible for a small number of mirrors. Similarly, the mass and cost would increase linearly compared to a single mirror.

Finally, the moving instrument would provide the highest coverage as well as flexibility, as it could change orientation independently of the airship. This would be faster and more precise. The mass is estimated to be about 600kg by looking into possible mounts for such a moving instrument, which weigh up to 400kg[2] [3]. This is added to the original instrument mass of 200kg. Similarly, the cost of potential mounts is up to $40,000, leading to a total cost of the instrument and mount of $170,000.

Due to its performance in the most important criteria of flexibility and coverage, the moving mirror is chosen for further design. This tradeoff is summarized in Table 6.

Table 6: Summary of instrument configuration tradeoff

Configuration	Flexibility	Coverage	Mass	Cost
Single fixed	Bad	Smallest	About 200 kg	About $130,000
Multiple fixed	Bad	Larger	$200kg \cdot n$	$\$130,000 \cdot n$
Moving	Best	Best	About 600 kg	About $170,000

There are two options for the placement of the instrument - inside the airship or in a gondola attached below the airship. Placing it inside the airship has the main advantage of having less aerodynamic drag. The bottom surface would need a transparent window for the observations. This could be made from Germanium or a plastic that transmits infrared wavelengths. Because the instrument is taking up volume inside the airship, the instrument can be placed inside a ballonet. Placing it outside a ballonet means it is submersed in the lifting gas, making it unreachable for maintenance. Inside a ballonet, it means that this volume cannot be taken up by the lifting gas during climb. This effect is negligible for a single instrument because the volume it takes is very low relative to the entire airship. The instrument has a diameter of 1 m and is 3 m tall. In case of multiple instruments, this becomes more significant. As a result, the airship would have to be a bit larger.

The main advantage of the gondola placement is accessibility. The drag penalty is small. This gondola could be placed directly behind the air intake of the buoyancy subsystem (Section 5.2), thereby minimizing the drag the gondola adds to this. The gondola can also be used to store other subsystems. Accessibility is a very useful feature for all subsystems as this can significantly speed up testing and maintenance, thereby save time and money. Mainly because of this and partially for not needing the transparent window and considerations in ballonet design, the gondola placement is the chosen placement concept.

4.5 Power

The power subsystem is responsible for generation, distribution and storage of electrical energy onboard the airship. This section contains the basic working principles of the power subsystem to help elucidate the differences between various concepts considered. A more detailed analysis of the design challenges is included in the Midterm Report [3]. The mission requirement dictates that the operational lifetime is virtually unlimited from the point of view of power generation, hence only renewable energy sources have been considered. As such, for the two applicable energy sources, solar energy is preferred over wind energy. As most of the generated energy is expected to be redirected into countering the drag of the airship [9], extracting energy from the incoming wind and subsequently increasing the drag by doing so is not efficient. The low wind speeds expected at such an altitude and the complex design tied to the wind energy concept further supports the choice of solar energy.

[2]URL: urlhttp://motionforsimulators.com/2dofs3dof-motion-systems/

[3]URL: urlhttps://www.aerotech.com/product-catalog/gimbals-and-optical-mounts/aom360d.aspx

Solar cell configuration

Solar cells will be used to generate power. The simplest implementation is having them fixed on the airship surface. In that case, to make more optimal use of the solar cells, they can be pointed toward the sun by changing the attitude of the airship. This works in combination with the selected instrument type, which involves a moving mount. Otherwise, a change in attitude would presume a shift in the observed area.

Another way to point the cells is by having them on rails going around the airship, which may increase the total mass substantially. With rails, the solar cells are not flush with the surface and create additional drag. Lastly, rolling the solar cells to the side of the balloon causes the airship to roll. This should be compensated for by for example also having the gondola on rails.

A last option considered was a transparent envelope and having the cells inside the balloon. In that case the ballonets should be made from a transparent and flexible material. With no clear benefits, such a material would not perform well structurally and would limit solar array performance. Given clear drawbacks with no real advantages, this concept was discarded early on.

The added complexities of more complex solutions seem to outweigh their advantages, hence the fixed solar array is selected. The solar cells shall be designed for surface attachment in further analysis.

Concept Power Comparison

For a fixed solar cell placement pattern, the incidence angle at each point on the array varies based on the local envelope slope and time of the day and year. As explained later on in Section 5.7, the photovoltaic cells performance shall be assessed by investigating their placement on a discretized surface model.

The array shall be positioned such that the most productive areas on the envelope are used for power generation on a specific day. Hence, there is a diminishing efficiency when attempting to increase the energy output of the array, seeing as that would presume using less efficient patches of area to extract the extra energy needed. Applying this logic to the hybrid airship type, this would imply that due to the higher power requirement of it over the conventional type, its power subsystem mass may escalate greatly, since mass would not scale linearly with power capacity. Since mass is an influential design parameter, these considerations further confirm the choice of a conventional balloon.

4.6 Control

The airship can be controlled by a pilot on board, remotely by a pilot, or autonomously. A pilot on board requires a pressurized cabin with life support. As the airship can stay airborne for months at a time, a pilot on board is not possible. A remotely controlled airship needs to be operated continuously by trained personnel. This would drastically increase operational costs. Autonomous control needs dedicated software and additional computing capacity. Besides that, it does not influence the design. This is safer than a pilot controlling the airship as it does not make human errors. The biggest issue of autonomous control is what happens if the airship encounters a situation which it is not programmed for. Because autonomous control is the cheapest and safest option, the airship shall operate autonomously. The autonomous control can still be overwritten by remote control, just in case.

4.7 Lifting Gas

The two options for lifting gas are hydrogen and helium, and are compared in Table 7. The sources for the cost estimations can be found in the footnotes [4] [5].

[4] URL: `http://www.h2-fuel.nl/en/h2fuel_pdf/independent-report-dutch-government/` [Accessed on 22/05/2019]

[5] URL: `http://www.chemicool.com/elements/helium.html` [Accessed on 22/05/2019]

Table 7: Lifting gas trade-off.

	Volume	Cost	Sustainability	Risk
Hydrogen	Lightest gas	Cheap: 5.5-10 EUR/kg.	Extracted from water with electricity	Highly combustible
Helium	8% more volume + snowball effect	Expensive: 52 EUR/kg.	Very scarce resource, mined	Inert gas

Volume was considered because a smaller volume is more convenient. Because the volume of airships is very large, the cost is also big so this is a criterion as well. Sustainability is a consideration throughout the entire project. Given the large amount of gas, this is an criterion as well. Lastly, chemical properties of gasses can impose risks.

Hydrogen is a more performant lifting gas. To produce the same lift with helium, 8% more volume is required. This makes the balloon heavier and thus the mass will grow even more due to this snowball effect.

For the same weight, helium is 10 times more expensive. But twice as much helium mass is required compared to hydrogen to fill the same volume due to hydrogen. To fill the same volume, twice as much helium mass required compared to hydrogen as it has twice the molecular weight. Next to that, the volume is 8% larger plus the snowball effect. This makes helium over 22 times more expensive.

Hydrogen is produced from water using electrolysis. This can happen in the factory and potentially on renewable energy only. Helium is a scarce resource obtained through mining.

Hydrogen is highly combustible if it is contact with oxygen; it can spontaneously combust due to a discharge of static electricity, friction when operating valves, etc. Helium, on the other hand, is an inert gas, it does not react to anything.

Technically, hydrogen outperforms helium significantly. The only issue is risk. The risks are not acceptable for human transport or low altitude operations. For this airship, the risks are largest during take-off and landing, ground manoeuvres, and storage in the hangar. The use of hydrogen is accepted because the risks can be mitigated as explained in Section 9.

4.8 Structure

There are three possible solutions for the structure of an airship. A rigid structure that defines the envelope and carries the lifting gas in dedicated bladders, a semi-rigid structure that has a inflatable envelope and transfers the load of the gondola and other equipment using a rigid keel and a non-rigid structure. Due to the very high altitude requirement of this application the rigid structure is not feasible due to wasted space and the semi-rigid solutions keel would interfere with the buoyancy control system. A non-rigid solution is prefered.

4.9 Chosen Concept

The chosen concept from this chapter will continue to the detailed design in the following chapter, this chosen concept is also summarized below. can be summarized as follows:

- It is a conventional airship, relying solely on buyancy for lift.
- A single instrument on a moving mount will be placed in a gondola.
- The solar cells will be fixed to the top half of the surface.
- The airship will operate autonomously.
- Hydrogen will be used as a lifting gas.

5 Detailed Design

This chapter presents the detailed design of the StratoCruiser. For clarity, the documentation of the detailed design is split up in sections corresponding to the different subsystems that together make up the airship. Contrary to what this way of splitting up the chapter suggests, the design for every subsystem is related.

5.1 Aerodynamics

In this section, the detailed design phase related to aerodynamics is presented. The process to estimate aerodynamic characteristics of the airship will be described together with the choice of envelope shape and the final results of the StratoCruiser drag. Throughout this whole section a consistent coordinate system, presented in Figure 3 is used, with the wind moving in negative x direction.

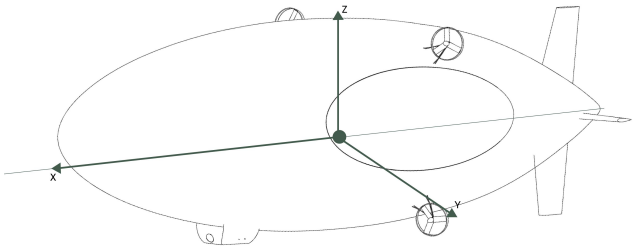

Figure 3: Aerodynamics Reference System.

5.1.1 Airship Aerodynamics

Reliable aerodynamics force estimations for the whole airship are critical as they affect the requirements on thrust and power for the propulsion and power subsystems. For conventional balloons, no lift is usually generated during cruise flight as they mostly fly at 0° angle of attack. The most important parameter for airship aerodynamics is therefore the zero-lift drag, which consists of about 60 % of the envelope drag, while the rest is produced by other external components such as tails, cables and the gondola [11]. The envelope drag is mostly composed by skin friction and pressure drag. The skin friction is dependent on the wetted area, while the pressure one is mostly dependent on the FR. For optimal FR, most of the drag would be caused by skin friction [9, 11].

The skin friction drag is caused by the friction between the flow and the airship skin, and is highly dependent on the type of flow in the boundary layer. Laminar flows consist of smooth and regular flow path lines, while turbulent flow consists of irregular fluid element paths. This difference causes frictional effects in turbulent flows to be much more severe, therefore increasing the friction drag of the shape. On the other hand, laminar flow is much more prone to flow separation, which can significantly increase the pressure drag. For slender bodies it is generally preferable to have laminar flow throughout the whole shape in order to minimize the skin friction drag [10].

This also applies to airships, as it is very important to delay the transition from laminar to turbulent flow as far away as possible from the tip, to maximize the laminar flow region [9]. The transition is mostly dependent on Re and can be facilitated by adverse pressure gradient on the surface [10], caused for example by unfavorable surface curvature.

5.1.2 Aerodynamic Estimation Methodology

Analytical and semi-empirical models, such as Equation 4.8, were found to be too inaccurate to get correct aerodynamic estimations for the airship [3]. In order to obtain a more accurate model for the aerodynamic forces, different methods such as Vortex Lattice Methods and CFD simulations were considered. Vortex Lattice Methods are able to accurately estimate lift and pressure drag of low AR

bodies for inviscid incompressible flow [10], and would therefore not be able to estimate skin friction drag, a big part of the total airship drag. CFD simulations are therefore the only option to obtain better aerodynamic estimations.

CFD simulations have been successfully used for stratospheric balloons [12, 13]. Many different types of software are available, with the most popular ones being Star-CCM+, Ansys and OpenFoam. The first two are commercial software, while the latter is Open-Source and free to use. Ansys was chosen as it was used for similar applications, it contains integrated 3D modelling and meshing software and, most importantly, the academic license was available to use for TU Delft students.

The major assumptions used for the presented CFD simulations are as follows:

- **Incompressible Flow:** The flow is considered incompressible. This is a valid assumption as the Mach number of the flow is well below 0.3.
- **Ideal gas:** The ideal gas equation is used to model the gas. This is a valid assumption as the temperature and pressure are not extreme, therefore the gas will behave like an ideal one.
- **Steady State:** Only the steady state behaviour of the flow is analyzed. This is the case as winds are quite constant and therefore a steady flow should be reached because of the balloon slenderness.
- **No Heat Exchange:** It is assumed that no heat is transmitted from the balloon skin to the airflow. The airship skin temperature is usually close to the atmospheric one, but during the day the airship heats up quite a lot because of solar radiation. Heat transmission from the balloon skin to the flow could anticipate flow transition from laminar to turbulent and therefore increase the total drag [10]. This effect is considered minor compared to the whole drag of the airship, and therefore it is ignored.

The 3D model of the airship was exported from CATIA in a .stp file and then imported into Ansys. The computational domain size was chosen based on literature. It is important to have at big domain size in order to decrease as much as possible the influence of the airship on the flow and the boundary conditions (which are applied at the edges of the computational domain). A cylindrical domain was chosen, with the long side being the airship longitudinal axis. The computational domain size is based on the results for the CFD simulation of a cylinder [14], as it was found that the upstream length, downstream length and diameter of the domain should be 15, 20 and 15 times the diameter of the shape respectively in order to avoid errors. This was adapted for the airship, by substituting the diameter with the length of the airship (about 200 meters). Furthermore, the domain was halved by taking advantage of the symmetry plane of the airship (cutting the airship in half longitudinally through the gondola and applying a symmetry boundary condition there) in order to reduce the computation time. This domain, together with the appropriate boundary conditions is shown schematically in Figure 4.

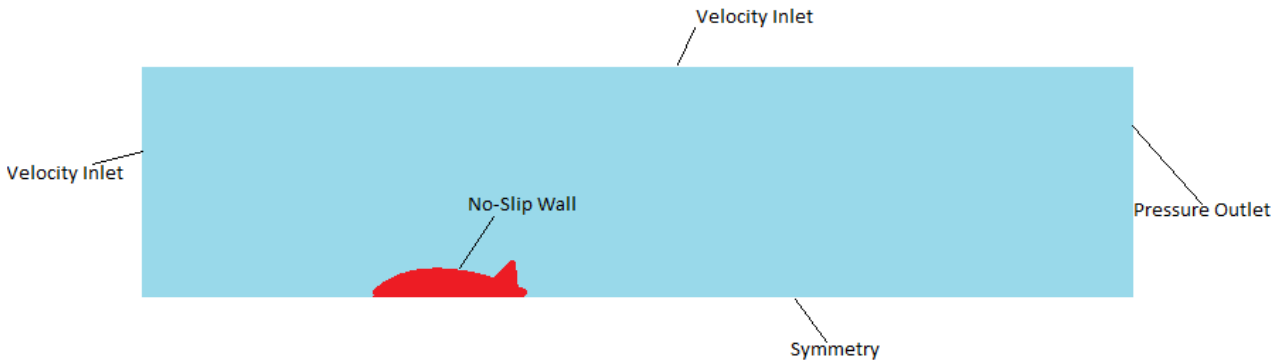

Figure 4: XZ-Projection of the Computational Domain and boundary conditions, not to scale.

The boundary conditions were chosen to simulate the flight of the balloon in a free stream at the atmospheric condition experienced during cruise (21 m/s) at 20 km altitude.The boundary conditions were also checked and compared with similar incompressible flow simulations [14, 15].

Velocity inlet boundary conditions are applied to simulate the free flow far from the balloon, by setting the velocities normal to the inlet and tangent to the outer boundary at 21 m/s. The pressure boundary condition at the outlet is needed to set the outlet static pressure to the atmospheric pressure. Finally, the no-slip wall boundary condition states that the flow velocity at the boundary is equal to zero when in contact with the wall.

Lastly, as the flow is viscous, a turbulence model had to be chosen. Extensive literature is available on turbulence modelling, also specifically for airships. The Standard $\kappa-\epsilon$ Turbulence model was chosen as it is robust, and currently the most widely-used model for industrial applications [16]. Furthermore, it was found to be one of the most accurate models for airships at zero angle of attack [17].

The 3D model was meshed using the built-in mesh software in Ansys. Special care was put to make sure that the elements near the balloon skin were smaller compared to the one far from it, to obtain more accurate simulation results while minimizing the computational power needed. An inflation layer was used to properly model the boundary layer near the balloon skin. This consists of a number of prisms, stacked on top of each other to correctly model the velocity gradient in the boundary layer, to help the convergence of the whole simulation.

Finally, convergence criteria are critical for correct simulations results. CFD simulations solve the Navier-Stokes partial differential equation iteratively. Residuals represent the difference of relevant values such as velocity magnitude and pressure of all elements between two consecutive iterations. It is standard practice to use residuals to quantify convergence of a simulation, and the standard convergence criterion for Ansys is to stop the simulation when all scaled residuals drop 3 orders of magnitude from the initial iteration[6]. This condition can be not appropriate for certain cases and therefore it was chosen to set the convergence scaled residuals convergence requirement to a drop of 4 orders of magnitude. Furthermore, the change in drag force each iteration was also monitored to make sure that the value drag coefficient was properly converged at the end of the simulations.

The final results of the simulation are analyzed in during the post-processing phase, which mostly consists of aerodynamic forces quantification, automatically calculated by Ansys, and the analysis of the flow behaviour. Different sets of simulations were performed, such as the simulations to select an optimal envelope shape, the one to calculate the overall drag of the airship and the mesh convergence analysis, as presented in the next few sections. The only simulations with an angle of attack different than zero were the ones to estimate the aerodynamic moment of the envelope, which are later used in Section 5.6.

5.1.3 Envelope Design

As already presented, the envelope produces about 60% of the drag of the whole airships. Many different shapes for the airship have been proposed to minimize drag, such as GNVR, NPL and NACA Series 66 profiles [3]. Another important design parameter for the envelope is the FR, which is optimum between 4.5 and 5.5 [9]. The ellipsoid shape with FR of 6 was taken as a baseline design and CFD simulations were performed on the bare envelope to find the most optimum FR and shape with respect to drag given a volume. The simulations were all performed at the same Re, first by varying the FR for an ellipsoidal shape, and then by fixing the FR at 6 and varying the shape. The results are summarized in Table 8 and Table 9 respectively.

[6]URL:`http://www.afs.enea.it/project/neptunius/docs/fluent/html/ug/node833.htm#sec-judging-convergence` [Accessed on 20/06/2019]

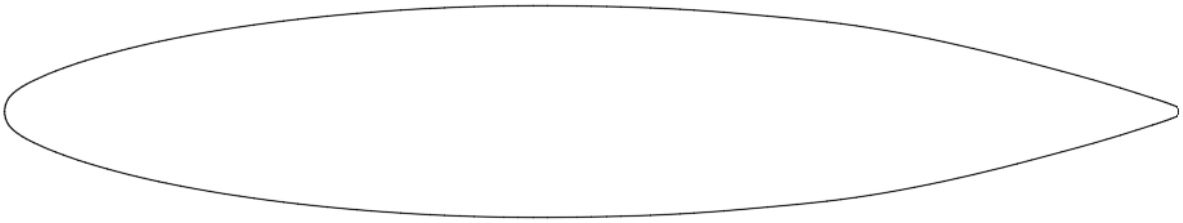

Figure 5: Bare Envelope improved NACA shape.

Table 8: Drag variation with respect to the baseline for different FR.

FR	Drag Variation [%]
6 (baseline)	0.00
5.5	-2.48
5.2	0.50
5	-0.33
4.57	1.66
4	11.05

Table 9: Drag variation with respect to the baseline for different envelope shapes.

Shape	Drag Variation [%]
Ellipse (baseline)	0.00
NPL	-1.94
GNVR	-0.31
NACA66	2.71
NACA66-improved	-3.48

It should be noted that the simulations were performed with a constant volume (123000 m^3, from an intermediate design iteration), with a constant domain size and number of mesh elements. This was done in order to obtain a fair comparison between all the different options and to remove any differences caused by mesh convergence and effect of domain size. It can be seen that 5.5 is the most optimal FR for the envelope, in accordance to the semi-empirical methods presented in Section 4.3. Different shapes were also compared, and it was found that a NACA-Series 66 improved shape was the most optimal to minimize drag. NACA-Series 66 airfoils are usually used as a baseline for envelope optimization, but it was found that the unmodified airfoil performed worse than the baseline ellipse. The flow behaviour around the envelope was analyzed and it was seen that the drag increase was caused by an early transition from laminar to turbulent flow, accentuated by the curvature of the airfoil which caused an adverse pressure gradient in the final half of the envelope.

In order to improve the drag characteristics of the NACA shape, the geometry was modified to slightly change the curvature and delay the turbulent flow transition as much as possible. This was successful as it was found that the improved NACA airfoil performed better, in terms of drag minimization, compared to other shapes. For the other shapes, the increase in drag with respect to the improved NACA airfoil can be explained with the blunt tail, which induces a small separation at the trailing edge, causing an increase in pressure drag. Sharp tails, such as the NACA ones, were found to perform better, in accordance with literature [9]. The final chosen envelope shape was therefore the improved NACA airfoil with a FR of 5.5, and the general shape is shown in Figure 5.

5.1.4 Envelope Lift Estimation

In order to properly size the tails it is important to know the lift that the envelope creates. It was found that the estimations provided in Section 4.3 were not accurate, as lift coefficient values for airship envelopes change with a factor of 2 with respect to the analytical estimations [9]. In order to properly estimate the lift, CFD simulations were set up by simulating the full domain (no symmetry plane) and varying the angle of the airship form 0 to 25 degrees with respect to the flow. As expected, the lift increases linearly while the drag increases parabolically. No significant flow separation was observed. The results of these are discussed in Section 5.6.

5.1.5 Complete Airship Drag Estimation

After selecting the envelope and finalizing the design of the tails and the gondola of the airship, a complete CFD simulation of the airship was performed to obtain the final drag. The propellers were not included in the simulation as it was not possible to properly analyze the flow acceleration due to their rotation given the computational and timing constraints. It was therefore chosen to neglect them altogether from the simulation as they would not produce a correct value for the drag. The drag for propellers, engine mount and cabling was therefore calculated form empirical data [9].

In order to perform the simulation, the full 3D model including tails and gondola was imported from CATIA and it was post-processed to prepare it for the simulation. This consists of simplifying the geometry, removing small and sharp edges and creating the computational domain, following the same methodology presented earlier. The sizes of the tails, envelope and gondola were the final iteration ones, as presented in Chapter 7. The model was then meshed and imported in the Fluent Ansys software for simulations. The same boundary and operating conditions explained earlier were applied, and the simulation was run. It should be noted that, because of short time and low computational power available, the simulations were constrained to a limited number of mesh elements. The results are therefore based on the best possible simulation performed with the available hardware. A more in-depth analysis of this is presented in Chapter 8.

It was found that the aerodynamic drag of the full model is 14% higher compared to the bare envelope. This is due to the gondola and the tails, which increase the drag coefficient. The flow behaviour around the gondola can be observed in Figure 6, where the underside of the gondola is seen at top. The streamlines around the gondola are visualized using a color-map, which describes the velocity magnitude of the air.

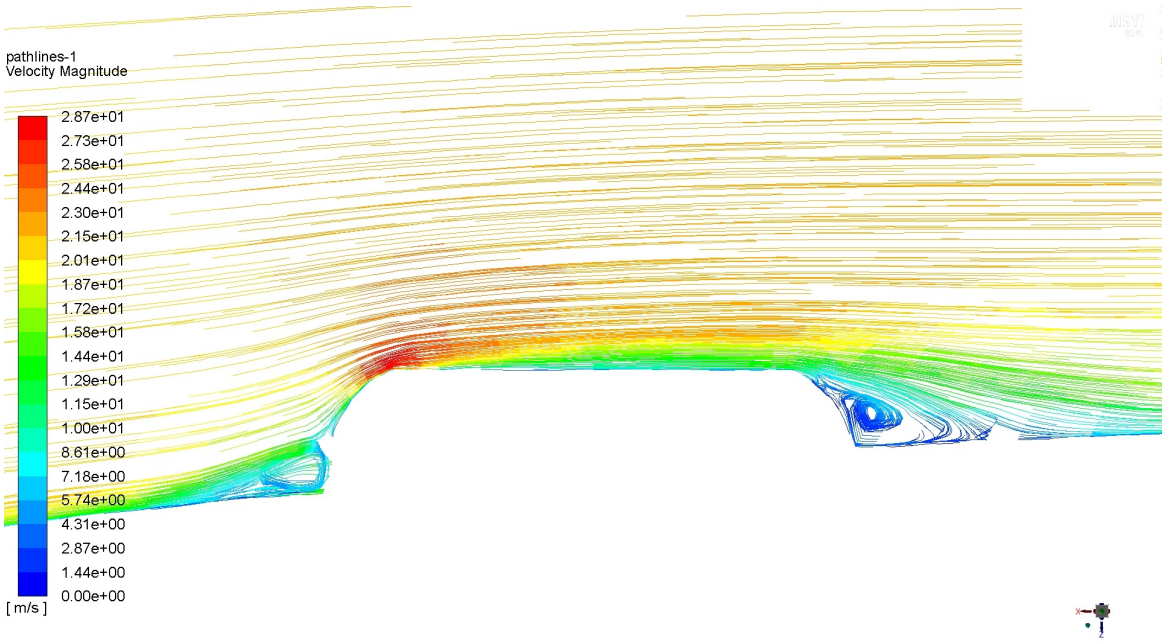

Figure 6: Flow behaviour around the gondola.

It can be observed that 2 significant areas of separations are present, one before and one after the gondola. This is caused by the sudden change in shape, which cause the flow to separate because of the adverse pressure gradient. By following the flow lines it can be seen that the flow recirculates on the back of the gondola due to the low pressure area. This phenomenon can significantly increase the drag, and therefore the shape of the gondola could be further optimized. An increase of velocity can also be observed at the forward upper edge (the red area on the top), caused by the sudden change in frontal area of the balloon because of the gondola, which forces the flow to accelerate.

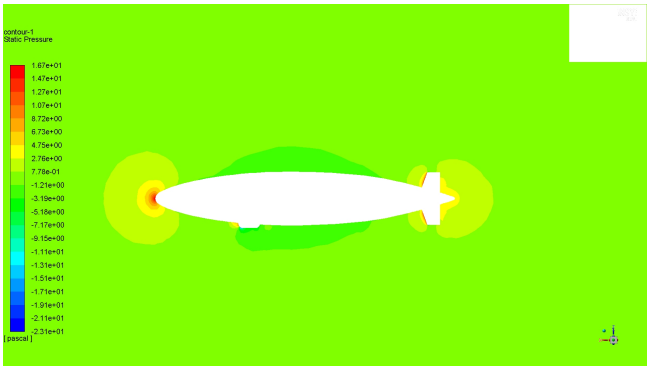

Figure 7: XZ-projection of the pressure distribution around the airship.

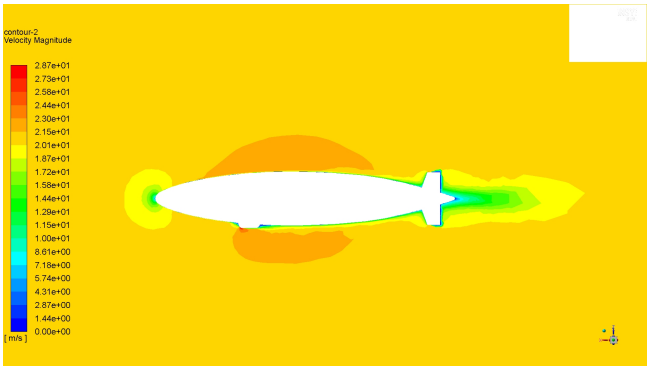

Figure 8: XZ-projection of Velocity distribution around the airship.

The static pressure distribution is shown in Figure 7. Some high pressure areas (in red) can be seen in front of the nose, gondola and tails, which significantly increase the pressure drag of the whole airship. As already mentioned previously, the shape of the gondola can be further optimized to decrease overall drag. The velocity flow magnitude is shown in Figure 8. The air flows from left to right, in local negative x direction at 21 m/s for the free-stream. The stagnation point, where the flow local velocity is zero, is visible at the tip of the airship. Along the body an increase of velocity can be observed, due to the presence of the airship, which accelerates the flow around the envelope. The wake of the airship can be observed on the rear of the balloon, as the reduction in airflow speed, due to the StratoCruiser body, is clearly visible.

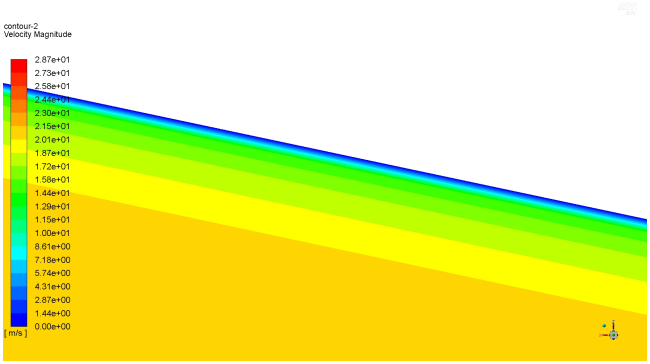

Figure 9: Boundary layer detail.

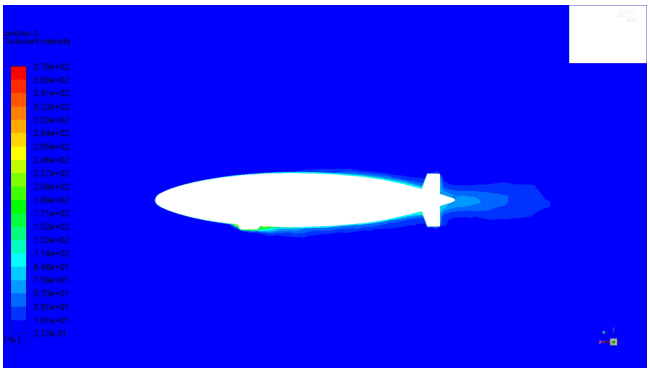

Figure 10: XZ-projection of the turbulent intensity of the flow.

Figure 9 shows an in-detail velocity profile in the boundary layer near the skin of the envelope. The envelope is in the top (white area), while the velocity is shown using a gradient colormap. The purpose of the inflation layers in the mesh is clear, as a high velocity gradient is present and a fine mesh is required to capture this.

Figure 10 illustrates the turbulence intensity of the flow around the airship, where the turbulence intensity is defined as the ratio between the root-mean-square of the turbulent velocity fluctuations and the mean flow velocity[7]. The turbulence intensity is 0 in the free flow as it is laminar, but increases around the airship because of turbulent transition. It can be seen that the flow increases its turbulence after travelling about half of the upper airship, while on the lower side turbulence is created due to the gondola placement. The turbulence induced by the gondola is even higher than the one in the wake of the balloon, likely because of the separation regions.

[7]URL: `https://www.simscale.com/docs/content/simulation/model/turbulenceModel/kEpsilon.html` [Accessed on 22/06/2019]

5.1.6 Final StratoCruiser Drag Estimation

The final drag coefficient can now be calculated using the CFD simulations results. The other most influential components of the drag that have not been taken into account yet are the bracing cables and the engine mounts and nacelles. These contributions can be calculated from empirical data [9]. The drag coefficient breakdown is presented in Table 10. The drag coefficient of the bare envelope is represented by $C_{DV_{0_{env}}}$, as calculated previously in Section 5.1.5. It should be noted that all drag coefficients presented are referenced to $Vol^{2/3}$, and all volumes appearing in the equations are to be calculated in feet cubed (the empirical equations use imperial units). Many other smaller influences that increase drag should also be taken into account, therefore it is decided to use a safety factor of 1.3 to take care of these drag uncertainties.

Table 10: Airship total drag coefficient breakdown.

Component	Estimation	Drag Coefficient
Full body + tails + gondola	CFD simulation	0.02821
Bracing cables	$(9.7e^{-6}Vol + 10.22)/Vol^{2/3}$	0.00193
Engine Mount	$(0.044 \cdot C_{DV_{0_{env}}} Vol^{2/3} + 0.92)/Vol^{2/3}$	0.00128
Engine Nacelles	$(4.25 \cdot (\#engines))/Vol^{2/3}$	0.00069
Total C_{DV_0}	Sum of all components	0.03252
Total with safety margin	Total $C_{DV_0} \cdot 1.3$	0.04227

The final drag force at cruise speed can be finally calculated with Equation 4.3 by using the total drag coefficient presented in Table 10. The final drag forces for the StratoCruiser cruise speeds are calculated to be about 1720 N during daytime (at 21 m/s) and 1560 N at nighttime (20 m/s). These drag forces, which already include the previously mentioned safety factor, will be used for the sizing of the propulsion and power subsystems. The corresponding design C_{DV_0} for the whole airship is then 0.4227.

5.2 Buoyancy

The subsystem that controls the net lift of the airship is the buoyancy control. The full theoretical analysis is explained in the Midterm Report [3]. The first section summarizes the key observations to get a proper understanding of the working principles of aerostatic lift. Consequently, the hardware is designed in Section 5.2.2.

5.2.1 Buoyancy Theory

There are two forces involved in aerostatic lift: the upwards Archimedes force equal to the mass of the air the gas replaces and the mass of the gas. Lift is the Archimedes force minus the mass. Lift depends on the volume, state of the atmosphere and state of the gas. The lift equation (Equation 4.1) can conveniently be rewritten for a constant mass of gas.

Below the service ceiling, lift is constant with altitude, as shown in Figure 11. This assumes that pressure and temperature inside the airship are close to atmospheric conditions or that there is a small constant over-pressure. This can only be true if the gas is allowed to expand. The airship has a constant total volume. To allow the gas to expand, ballonets are used. Ballonets are internal bags filled with air. When the lifting gas expands, air can escape from the ballonets, giving more volume to the lifting gas. When the lifting gas contracts, air is pumped back into the ballonets. When the gas occupies the total volume of the airship, it cannot expand anymore and lift decreases with increasing altitude. In Figure 11 this happens at 20.5 km. The variation of air mass in the ballonets as a function of altitude is visualized in Figure 12.

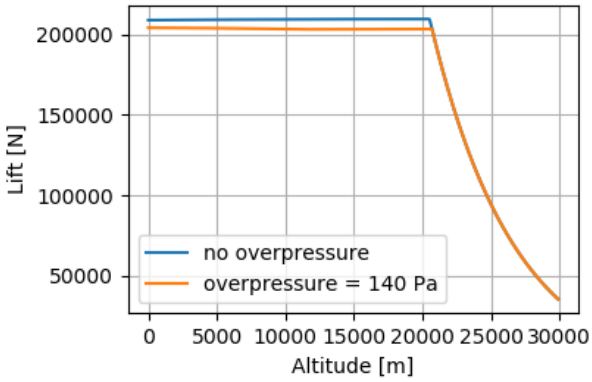

Figure 11: Lift stays constant with altitude and over-pressure decreases lift.

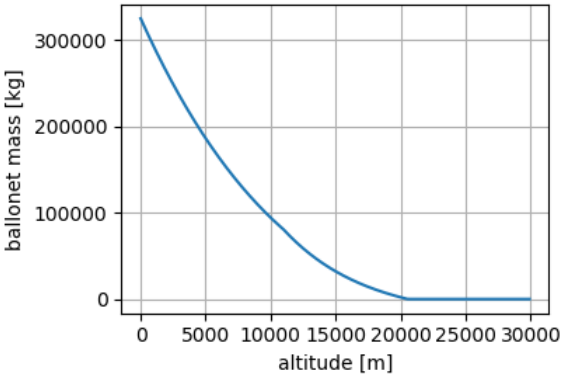

Figure 12: The air mass in the ballonets decreases with altitude.

The envelope is sized to have enough space for 612 kg of hydrogen. This can produce a total lift of 77 000 N. This is about 8 kN more than the total mass of the airship as shown in Section 6.1. In order to climb, the airship must provide more lift than its mass to compensate for the drag.

With a constant over-pressure, lift is lower and still constant with altitude up until when the lifting gas occupies the complete airship volume. A small pressure difference has a large effect on the lift. This is because to increase pressure, air must be added to the ballonets. The mass of this extra air reduces the net lift. For the StratoCruiser, lift decreases linearly with over-pressure at 17 N/Pa as shown in Figure 13. This effect is used to control the lift of the airship.

The minimum pressure comes from the over-pressure to keep the balloon in shape. This was set at 140 Pa in the Midterm Report [3]. Increasing the over-pressure to 240 Pa reduces the lift by 1700 N. A CFD analysis should confirm whether this is enough to reach the climb and descend velocity requirement, **SB-Sys-13** [18], of 1.5 m/s.

Both the total volume of the airship and the percentage which the ballonets must be able to occupy depend on the service ceiling. With a ceiling of 20.5 km, the ballonets must be able to occupy 93.4% of the total volume as can be seen in Figure 14. This means that at sea level, 93.4% of the total volume is taken up by the ballonets which are filled with air. As the airship climbs, air is vented from the ballonets to allow the gas to expand and lift to stay constant. At the ceiling, the ballonets are empty and the gas takes up the total volume. To reduce lift, air can be pumped into the ballonets. This adds mass to the airship such that the net lift decreases. Consequently, internal pressure increases. Increasing the ceiling increases the ballonet percentage with a few points. The total volume increases rapidly. Increasing the ceiling by 4km doubles the volume. That does not even take into account the snowball effect.

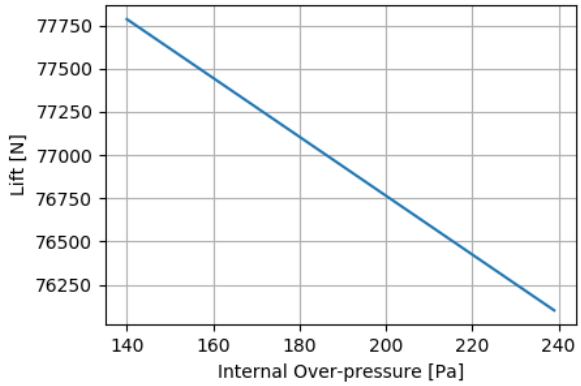

Figure 13: Lift decreases linearly with internal over-pressure

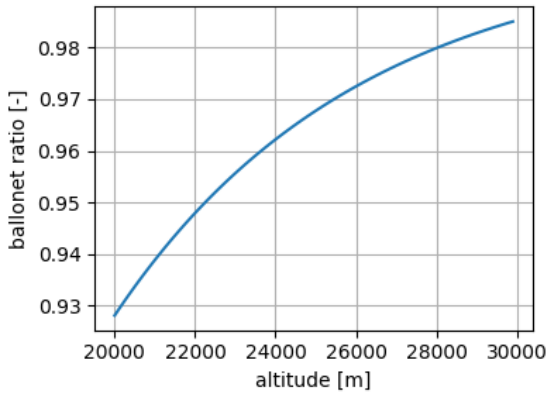

Figure 14: Maximum ballonet ratio determines service ceiling.

This analysis assumes a standard atmosphere. In reality, there are variations. These are mostly season dependent. Section 4.1 concluded that the density changes throughout the year. The lowest density at 20 km altitude can be found in February and is 0.083 $\frac{kg}{m^3}$. This corresponds to 20.5km in the standard atmosphere. It can be concluded that as the airship is designed for 20.5 km ISA, the StratoCruiser can only reach 20 km in February and this is the minimum ceiling throughout the year.

5.2.2 Buoyancy Control Hardware

The hardware consists of the ballonets and an air distribution system. The air distribution system includes a compressor pumping air in the ballonets through a duct. The ballonets are connected to this duct through gate valves. The opening of a gate valve is regulated by a linear actuator and a sliding door. Lastly, internal and external temperature and pressure sensors measure gas and atmospheric state. This information is used to autonomously operate the compressor and valves to control altitude.

The mass flow to and from the ballonets depends on the climb and descend rate. The duct is sized such that the mass flow from the ballonets, corresponding to the required climb rate of 1.5 m/s, can be passively reached. This means that the over-pressure in the ballonets is the only driving force. The equation of total pressure, Equation 5.1 [10], is used to calculate the velocity of the vented gas where q is the total pressure, p the static pressure, v and ρ the velocity and density respectively. In the ballonets, the air has no velocity and static pressure equals total pressure. When the air is vented, the static pressure will drop to atmospheric pressure. Because there is a slight over-pressure in the airship, part of this pressure is converted to velocity.

$$q = p + \frac{1}{2}\rho v^2 \tag{5.1}$$

Equation 5.2 [10] is subsequently used to calculate the required area to reach the mass flow corresponding to a 1.5 m/s climb where $\dot{m}$ is the mass flow, A is the vent area, v and ρ are velocity and air density.

$$\dot{m} = \rho A v \tag{5.2}$$

With an over-pressure of 140 Pa, the required valve area becomes 1.92 m^2. The outlet is placed at the rear of the gondola such that the low pressure zone behind the gondola helps with the venting. This low pressure is not considered in the computation of the required area because the mass flow must still be reached when the airship is not going forwards and there is no low pressure zone behind the gondola.

To descend, air must be actively pushed back into the ballonets using an electric fan. The fan gives velocity to the air entering the duct such that the total pressure of the air after the fan equals the static pressure inside the balloon, where the air has no velocity anymore. The inlet of the compressor has an area is sized with a similar method as the valve are. The difference is that the over-pressure

to descend is larger because the lift must be reduced. $240Pa$ was used to size the compressor. This means that the compressor must provide enough velocity to reach that over-pressure. The required area is 1.2 m^2 and the inlet faces forward. This way the incoming air already has some velocity and the fan only has to give an extra push instead of giving all the velocity.

Ballonets

The ballonets are the internal air bags. They vary from 0 to 93.4% of the total volume. They must be divided in separate sections for several reasons. Firstly, sectioning the ballonets limits the effect of sloshing. This is a shift in c.g. when the air in the ballonets moves longitudinally. Secondly, multiple sections can be inflated and deflated separately. This can be used to control the c.g. and trim the airships pitch angle. Lastly, it is more practical for production and assembly to make multiple smaller ballonets. Smaller ballonets can be more easily replaced if needed. On the other hand, more ballonets means that more material is needed for the ballonets and more valves are needed. This increases both cost and mass. Eventually, the choice was to have 6 section longitudinally. As the airship has a length of 192 m (see Section 7.2, this means each section is 32 m long. Laterally, there are 2 sections. This is to fit around the internal structural wires and curtains. The ballonets are suspended from the top of the airship such that they do not collapse to the bottom when deflated. This makes sure that all air can escape because the ballonets cannot collapse onto themselves, resulting in bubbles.

The ballonets are made out of a Dyneema CT1E.08 composite fabric. This is one of the most lightweight fabrics available on the market with an areal density of 18 g/m^2 [8]. Multiplying this by the total area results in 330.9 kg. With a cost of €31 $/m^2$ [9], the material costs for the ballonets equals 891 k€. The ballonets are not structural components. The only load that they experience is a slight pressure during the inflation procedure and sloshing of the air inside. This fabric has a tensile strength of 552 $N/5$ cm which means that a strip of fabric with a width of 5 cm can handle a tensile force of 552 N. It was argued that this will be strong enough and no further analysis is needed.

Duct

The duct transports air from the in- and outlet to the ballonets. There are two possibilities for the configuration; having 1 duct for both inflation and deflation or having 2 separate ducts. The advantage of designing 2 ducts is that the ballonets can be inflated and deflated at the same time. Air can be constantly replaced. In doing this, the compressor uses a lot of energy. In practice, this will not be used. An advantage of separate ducts is that the front ballonets can be inflated while deflating the rear ones, keeping overall lift constant in the process. This shifts the c.g. to trim the pitch of the airship. A single duct can also do this with 4 additional valves. Figures 15 and 16 show the working of this. Open valves are indicated by a green dotted line. A closed valve is a solid red line. The additional valves include one to close the outlet, one to divide the duct between the front and rear part in between the in- and outlet, one in front of the inlet and a small outlet in front of the main inlet to let air escape from the front ballonet while inflating the others. Note that this additional outlet does not need to have a large area. This is only used to trim the pitch of the airship, not to achieve a certain climb rate. The single duct option is lighter as there is no need for a second duct with additional valves to the ballonets. This is also a more elegant solution and was chosen for the StratoCruiser.

[8] URL: `https://www.extremtextil.de/en/dyneema-composite-fabric-ct1e08-18g-sqm.html` [Accessed on 28/06/2019]

[9] URL: `https://www.extremtextil.de/en/dyneema-composite-fabric-ct1e08-18g-sqm.html` [Accessed on 28/06/2019]

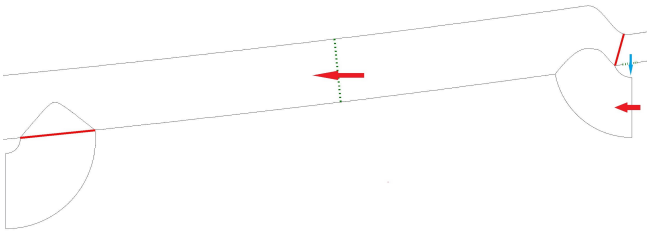

Figure 15: Valve schematic for inflating the rear ballonet while deflation the front one.

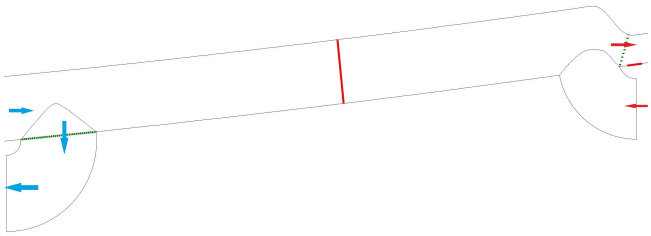

Figure 16: Valve schematic for inflating the front ballonet while deflation the rear one.

The radius required for deflation is larger than that required for inflation. The largest of the two is used. The outlet area is 1.92 m^2 as explained in the Midterm Review (MTR) [3]. Since mass flow scales linearly with area and the ballonets were designed to roughly have the same volume, the area of a section of a duct must be $\frac{1}{6}$ times the number of ballonets it is feeding. This gives the ducts a variable area, which changes in discrete steps at each ballonet. The duct is shown in Figure 17.

Figure 17: Duct feeding air to the ballonets.

The ducts are made from the same Dyneema fabric just as the ballonets are. Multiplying the area of the duct times the mass per area of the fabric results in 7 kg. The pressure in the duct can drop to atmospheric pressure while the internal over-pressure is pressing on the duct. An aluminum coiled wire keeps the duct in shape. The wire is assumed to have a radius of 1 mm and the coils have a pitch of 10 cm. Over the total length of the duct, this adds a mass of 47 kg. Additional analysis and tests must determine whether this is sufficient to prevent to duct from collapsing under the over-pressure. This was not done due to time constraints. The Dyneema and coiled wire duct was found to be almost 200 kg lighter than an expanded pvc duct as recommended by "Curbell Plastics", an aluminium duct (like a soda can) or a carbon fibre sandwich. The Dyneema duct is more expensive. With a cost of €31 $/m^2$ [10], the cost for the entire duct is €8000. A pvc duct would be the cheapest option at €200 based on the mass and price per kilo [11]. However, by adding mass, the envelope has to be larger, adding additional costs there. As discussed in Section 5.11, the Dyneema is also used in the envelope. A specific number was not calculated but it was reasoned that the additional costs of a larger envelope compensate for the cost saving in the duct by using pvc. The lighter option, Dyneema, will be used for the duct.

Valves

Two types of valves are used; gate valves and butterfly valves. Gate valves have a sliding door on the side of the duct that is operated by a linear actuator as in Figure 18.[12] They connect the ballonets to the duct. A butterfly valve has a rotating disk in the duct operated by a linear actuator as in Figure 19.[13] This type is used where a complete section of duct has to be closed of. This is the case at two locations as shown in Figures 15 and 16.

[10] URL: https://www.extremtextil.de/en/dyneema-composite-fabric-ct1e08-18g-sqm.html [Accessed on 28/06/2019]

[11] URL: https://plasticker.de/preise/pms_en.php?show=ok&make=ok&aog=A&kat=Mahlgut [Accessed on 28/06/2019]

[12] URL: https://en.wikipedia.org/wiki/Gate_valve [Accessed on 20/06/2019]

[13] URL: https://www.vortexglobal.com/4-reasons-not-to-use-butterfly-valve-when-handling-dry-material/ [Accessed on 20/06/2019]

Since mass flow scales linearly with area and the ballonets were designed to roughly have the same volume, the area of a valve connecting a ballonet to the duct must be $\frac{1}{6}$ of the total area of 1.92 m^2. This corresponds to an area 0.32 m^2. The gate valve is suited best for this application because its area is directly controllable. A butterfly valve can also be partially opened to limit the airflow but the mass flow is less predictable. The gate valve also takes very little out of plane space such that it will be flush with the duct surface. The valve is operated by a linear actuator. Note that the valve must be placed on the lowest point of the ballonets to allow all air to escape.

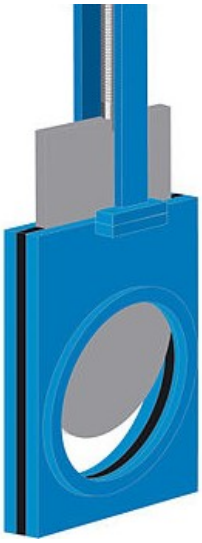

Figure 18: Gate Valve

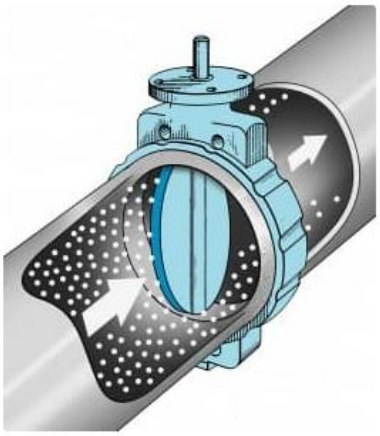

Figure 19: Butterfly Valve

The linear actuator that was chosen is the SKF CAHB-10. This actuator has a mass of 1.5 kg [14]. Another 0.5 kg is added to account for the valve itself. The forces on the valve are small. In total, the 14 valves (1 per ballonet + 2 gate valves at the outlets as seen in Figures 15 and 16) thus add up to 24 kg. Then, the 2 butterfly valves also add mass. These are assumed to have a mass of 3 kg, bringing the total to 30 kg for the valves. It is possible to make detailed models and drawings of the valves to get a more accurate mass estimation. As the mass of the valves is small, it was decided not to put too much effort in this and rather focus on other parts of the project.

Compressor

An electric fan is used to push air into the ballonets. The fan must provide enough velocity to the air to reach the internal over-pressure of 240 Pa at the mass flow corresponding with a descend of 1.5 m/s. For this, the compressor needs an intake area of 1.2 m^2.

$$P = \dot{m}(\frac{v_2^2}{2} - \frac{v_1^2}{2}) \tag{5.3}$$

The fan needs a 37 kW motor. This was calculated from Equation 5.3 where $\dot{m}$ is the mass flow, v_1 is the speed of the flow in front of the fan and v_2 is the speed of the air after the fan. The mass flow is determined by the size of their airship and the climb and descend rates. The lower v_2, the lower the required power. The minimum velocity v_2 can be calculated using the equation of dynamic pressure, Equation 5.4, where Δp is the dynamic pressure, ρ is the air density and v the velocity. The dynamic pressure that the fan adds to the flow translates into static over-pressure once it comes to a standstill in the ballonets.

$$\Delta p = \frac{1}{2}\rho v^2 \tag{5.4}$$

[14] URL: https://nl.rs-online.com/web/p/products/7643474/?grossPrice=Y&cm_mmc=NL-PPC-DS3A-_-google-_-DSA_NL_NL_Automation+%26+Control+Gear_LV4-_-Linear+Actuators-_-DYNAMIC+SEARCH+ADS&matchtype=b&dsa-652763901244&gclid=EAIaIQobChMI75TFsL3S4gIVbbftCh3ulAarEAAYAiAAEgK4k_D_BwE&gclsrc=aw.ds [Accessed on 20/06/2019]

The power that the fan needs to provide to the air during climb was computed in function of altitude. An efficiency of 0.8 was assumed to account for mechanical losses and losses from the fan. The result is that the motor must provide 37 kW. A more extensive study of the efficiency is not required. If a slightly more powerful motor would be required, the original can be easily swapped out with a more powerful one. This new motor will only be slightly heavier and will not effect the overall airship design.

Note that this power is not included in the power budget because this power is only required during descend. All stored energy can be used. It does not matter if the airship is out of energy after landing. A single duct is used for both inflation and deflation of the ballonets. A set of valves allows to inflate the front ballonets while simultaneously deflating the rear ballonets and vice versa.

The compressor is a critical system. Failure of the compressor means that the airship can only be brought down by venting hydrogen. As agreed with the risk manager, redundancy must be incorporated in the compressor by having a backup motor. Due to time constraints, the propeller design for propulsion is scaled and used here.

AMK provides motors in this power range to the Formula Student Team Delft. These have a mass of 3.5 kg and a price tag of €5000[15]. The mass of the 2 motors is 7 kg. Another 13 kg was added for the mounting of the motors and the fan blades. As for the valves, more detailed models would give a more accurate view on this but it was decided to focus on other parts of the project.

Pressure and Temperature Sensors

The airship must operate autonomously. Software is needed to calculate the how much each valve should open and how much power the compressor should get. Pressure and temperature sensors monitor the state of the gas, air in the ballonets and atmosphere. These are input for the control software. Figure 78 in Section 6.2 visualizes the flow of information through functions of the control code that operates the systems. More information on the software can be found in that section.

Mass and Power

Table 11 provides an overview of the mass and costs of the components. Due to their sheer size, the ballonets give the largest contribution.

Table 11: Buoyancy control subsystem mass budget

Component	**Mass [kg]**	Cost [EUR]
Compressors	20	15000
Valves	30	6000
Ducts	47	14433
Ballonets	330.9	890872
Total	428.6	926306

5.3 Instrumentation

This section documents the design of the instrumentation subsystem. The instrumentation subsystem is responsible for producing images for the purpose of EO. The subsystem consists of a primary mirror, a set of several smaller mirrors and a detector. The primary mirror reflects the thermal infrared rays, coming from the observed spot on the Earth's surface, onto the secondary and possibly tertiary mirror, which in turn reflect the rays onto the detector, which translates the rays into an image. The primary mirror will be the main focus of the instrument design, as it has a major influence on the performance of the subsystem, and ultimately on that of the whole system. The design of the secondary and tertiary mirror will be neglected as this is beyond the scope of this design process and because the

[15]Public data is not available. This information comes from private conversations with the Formula Student Team Delft as they use similar motors

subsystem can be adequately analyzed without having to design the secondary and tertiary mirrors. In the analysis of the instrumentation subsystem they are treated as a black box. The detector will not be neglected in the design process as this has a large effect on the subsystem's performance through, for example, the detector pixel size and the pixel array size.

5.3.1 Preliminary Analysis

The first step in the design of the instrumentation subsystem is to do a first order optical analysis. The full derivations of this analysis are documented in the MTR [3]. In this section, the fundamental optical parameters including the focal length and the aperture diameter as well as the shape and the material of the primary mirror are briefly touched upon.

Focal length

The back focal length of the primary mirror that has to be designed for can be calculated using Equation 5.5 as derived in the MTR [3].

$$f = \frac{H}{1 + (d_{ground}/d_{detector})} \approx H \cdot \frac{d_{detector}}{d_{ground}} \tag{5.5}$$

In this equation, f refers to the back focal length, H refers to the altitude of the airship, assuming that the observed spot on the Earth is at sea-level and exactly at nadir, d_{ground} refers to the size of a pixel on the ground and $d_{detector}$ refers to the size of a pixel on the detector. From Equation 5.5 it becomes clear why the detector is not neglected in the analysis of the instrumentation subsystem as it is the only possibility to change the focal length for a given altitude and a given resolution. Generally speaking, the larger the focal length, the more voluminous the optical instrument will be.

Aperture Diameter

The aperture of the primary mirror has to be sized properly for two reasons. First of all, it has to be able to reach the required spatial resolution and secondly, the mirror must collect enough light to focus on the detector to meet the SNR.

The minimum required aperture diameter in order to reach a certain resolution is stated by Equation 5.6 [3].

$$D = 1.22 \frac{H\lambda}{d_{ground}} \tag{5.6}$$

In this equation, D is equal to the aperture diameter, λ is the wavelength of the observed rays and f and d_{ground} are still the focal length and the ground pixel size, respectively. It should be noted that Equation 5.6 finds the minimum diameter required to meet the spatial resolution. It is wise to design for a slightly higher diameter to take into account imperfections in the image forming that are the result of manufacturing errors, thermal deformations and optical aberrations. The latter will be discussed in more detail later on in this section.

To ensure that the detector is able to form a clear image, meaning that it is not blinded by stray light, a requirement is set on the SNR to be at least 100 [6]. To cover the detector from stray light, a baffle will be used to minimize the majority of the background noise. A preliminary sketch of this baffle and position with respect to the mirror and the detector is given in Figure 20.

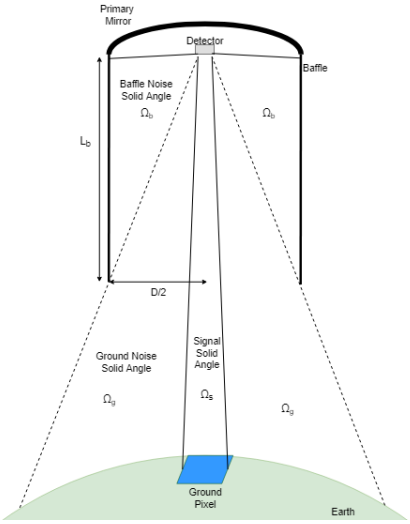

Figure 20: Baffle sketch

The SNR is calculated with Equation 5.7 where, S is the signal that is received by the detector, B_{baffle} is the background noise due to the baffle and B_{ground} is the background noise from the ground [3].

$$SNR = \frac{S}{\sqrt{N_{shot} + B}} = \frac{S}{\sqrt{S + B_{baffle} + B_{ground}}} \tag{5.7}$$

The parameters S, B_{baffle} and B_{ground} are calculated with Equation 5.8, as explained more thoroughly in [3], by using the corresponding spectral radiance L and solid angle Ω for each of the three sources of radiation.

$$S = L_s \cdot A \cdot \Omega_s \cdot t_i \cdot \Delta\lambda \cdot \eta \cdot QE \tag{5.8}$$

In this equation, the aperture area A which relates to the aperture diameter, the integration time t_i which imposes requirements on the stability of the mirror, the bandwidth $\Delta\lambda$ which is specified by requirement **SB-Subs-Meas-03** and is regulated by a Ge filter which will be elaborated on in Section 5.3, the throughput η and the quantum efficiency QE are independent of whether S, B_{baffle} or B_{ground} is computed.

Primary Mirror Shape

As documented in the MTR, a concave parabolic mirror will be used to focus the TIR rays coming from the Earth onto the detector. The mirror will have no spherical aberration because it is an aspherical surface, but it will have both coma aberration and astigmatism. These aberrations are analyzed by using Equation 5.9 and 5.10, respectively [19].

$$\beta_{coma} = \frac{U}{16(f\#)^2} \tag{5.9}$$

$$\beta_{astigmatism} = \frac{(L-f)^2U^2}{2f^2f\#} \tag{5.10}$$

where, U is the half field angle, f is the focal length, L is the distance between the optical surface and the aperture stop and $f^{\#}$ is the focal ratio which is equal to the focal length over the aperture diameter. These equations show why, besides structural considerations, the aperture cannot be made infinitely large because that would make the aberrations very large. To decrease aberrations, the focal length can be increased by merging pixels together to form a super pixel which increases $d_{detector}$. The effect of merging multiple pixels together into one 'superpixel' is that there are less superpixels on the pixel array. This directly relates to the size of a single picture on the ground as the size of each superpixel on the ground is equal to the Ground Sampling Distance (GSD). Therefore, the area of a single picture is equal to the GSD times the amount of superpixels.

Primary Mirror Substrate Material

The material that has been selected for the mirror substrate is SiC. This material has a high strength, a low Coefficient of Thermal Expansion (CTE) and a high conductivity, all of which are desirable properties for a mirror substrate. The density of SiC is slightly high but due to the high strength, the aerial density can be as low as 7.8 kg/m^2 according to manufacturers [20]. Studies are being done to find ways to lower the aerial density even more by using silicon based foams [21]. The brittleness of the material is rarely an issue due to the high strength [20]. This makes SiC a very suitable material for the mirror substrate.

5.3.2 Detailed Analysis

This section will discuss the detailed design of the instrumentation subsystem. The starting point of the detailed design of the instrumentation subsystem is the preliminary instrumentation design as proposed in the MTR [3]. This proposed design made a compromise on the GSD, by having a resolution of 1.5 m instead of 0.5 m, to have an SNR of over 100. The parabolic primary mirror in this design had an aperture of 1 m and utilized a baffle of 2.6 m to minimize the noise effects of straylight entering the optical system. In order to limit the coma aberration, the 10 μm detector pixels were merged in a 4x4 configuration to make the size of a superpixel 40 μm. The SNR was over 100 for this design if the temperature of the observed ground pixel was 300 K, the temperature of the ground was 279 K and the temperature of the baffle was 110 K. This combination of these parameters would, at an altitude of 20500 m and for an integration time of 0.02 s, have an SNR of 102.

Detailed Optical Analysis

For this proposed design, the focal length would be 0.533 which results in a focal ratio of 0.533 as well, as the aperture of the mirror is set to 1 m. With this design, Dr.ir. J.M. Kuiper and his PhD-candidate D. Dolkens made an effort to get a detailed design of the assumed black-box to finalize the design of the entire instrument. This brought to light that for this focal ratio of 0.5, the focal point is too close to the mirror which means that the angle that the rays make with the optical axis as they reach the focal point is too large. These large angles amount to large aberrations when the rays pass through the secondary lens, which was used as an optical surface to focus the light onto the detector in the design of the black-box as proposed by Dr.ir. J.M. Kuiper and D. Dolkens. To make the design of the entire instrument work, a focal ratio in the order of 1 is required. This can be achieved by increasing the focal length, which can be done by lowering the GSD or by increasing the detector pixel size.

As the GSD for the proposed design was violating the spatial resolution requirement, it is intuitive to lower it to increase the focal ratio. This would, however, heavily decrease the SNR because this increases the solid angle of the noise while it decreases the solid angle of the signal. To compensate this decrease in the SNR, both the integration time and the bandwidth will have to be increased to ensure that the detector receives enough radiation. Given that the size of the airship, as estimated in Section 4.2, will result in a high moment of inertia and that the environment in the stratosphere is relatively calm, as established in Section 4.1, an increase in integration time from 0.02 s to 0.06 s can be justified. Moreover, the bandwidth has to be increased to allow the detector to receive more signal. A bandwidth other than one ranging from $10 - 12$ μm, will violate **SB-Subs-Meas-03**. Upon consultation with the stakeholder, this requirement was changed such that a bandwidth ranging from 8 to 12 μm can be measured. The bandwidth was stretched towards the lower end of the spectrum rather than the higher end of the spectrum, because longer wavelengths are more prone to diffraction based on Equation 5.11. The effect of this stretched bandwidth is that the spectral radiance, which is integrated over the bandwidth for the detailed design, increases which is beneficial for the SNR. For these changes in the integration time and the bandwidth, the GSD can be decreased from 1.5 m to 1 m. Ideally, the GSD is decreased even further to 0.5 m as specified by requirements. This would, however, require the integration time to be as high as 1 full second, which is unreasonably high, in order to maintain a SNR of 100.

Decreasing just the GSD is not enough to increase the focal ratio to 1. To achieve this, the detector pixel size has to be increased as well. The detector pixel size in the proposed preliminary design of 10 μm is increased to 12 μm by selecting a detector such as the ATTO640™ as supplied by SOFRADIR.[16] If for this pixel size, the pixels are merged in a 4x4 configuration such that the size of a super pixel is 48 μm, the focal length of the system increases 0.96 m. Given that the aperture of 1 m is unchanged with respect to the proposed design, the focal ratio is increased to 0.96 as well. This focal ratio is close enough to 1 in order to design a properly function set of secondary and tertiary mirrors, according to Dr.ir. J.M. Kuiper. The effect of having to merge pixels in a 4x4 configuration is that there are less superpixels that cover an area of 1 by 1 meter. For a detector array size of 2048x2048, the coverage area of a single image is now 512 m x 512 m.

Now that the spatial resolution is changed, the required aperture diameter can be updated. To find the minimum required aperture diameter to meet the spatial resolution, Equation 5.6 is used. With the maximum altitude set at 20500 m and a maximum measured wavelength of 12 μm, the aperture should be at least 0.3 m in order to have a GSD of 1 m.

For the changes in the design of the instrument that were necessary to get the focal ratio up to 0.96, it should be verified whether the required SNR of 100 is maintained. For a more in-depth SNR calculation, the estimations for the quantum efficiency and the throughput have to be revisited. The amount of photons that are converted to electrons is considered through the quantum efficiency. For a Charged-Coupled Device (CCD), which is used for infrared applications, the quantum efficiency can be as high as 0.9 according to [19]. Therefore, the first estimate of 0.9 based on advice from Dr.ir. J.M. Kuiper was a good one and will not be changed. The throughput of the system relates to the transmittance of infrared rays by the atmosphere. It should be noted that this throughput only holds for the signal and the background noise from the ground, as the background noise from the baffle does not have to pass through any atmosphere and is therefore set to 1. The throughput for the rays coming from the Earth is found from the transmission spectrum as visualized in Figure 21.[17]

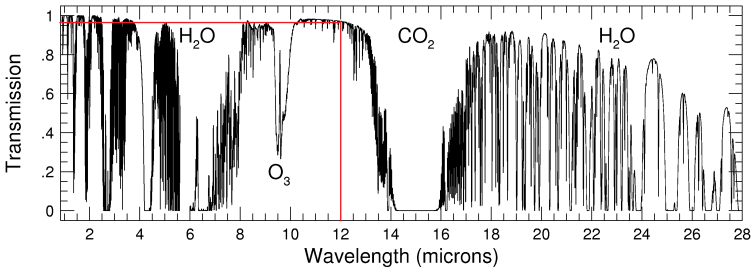

Figure 21: Transmission spectrum

From Figure 21 it becomes clear that the initial estimate of 0.9 was too conservative as the actual transmission for the specified bandwidth from 8 to 12 μm is as high as 0.95. This throughput, however, only holds for a clear sky. Infrared radiation is attenuated by clouds to such an extent that the instrument is useless for imaging the Earth on cloudy days [22]. This issue will be addressed further in Chapter 9. The stretched bandwidth ensures that the detector will receive more radiance. The length of the baffle was slightly decreased from 2.60 m to 2.50 m, as the increase in the transmission gave some design room. Furthermore, the aperture diameter was kept the same as in the MTR at 1 m. The temperature to which the baffle will be cooled is 90 K with the thermal design as explained in Section 5.8. This leaves the temperatures of the pixel and the ground to influence the SNR. How these temperatures influence the SNR will be analyzed and documented in the sensitivity analysis in Section 6.3.1. In the remainder of this section, details of the instrumentation subsystem will be explained, starting with a filter to enforce the specified bandwidth.

[16]URL: `https://www.lynred-usa.com/products/vga-resolution/atto640-infrared-sensors.html` [Accessed on 27/06/2019]

[17]URL: `http://www.astronomy.ohio-state.edu/~pogge/Ast161/Unit5/atmos.html` [Accessed on 20/05/2019]

Germanium filter

As established previously, the bandwidth is increased from 10-12 μm to 8-12 μm. An optical filter will be used to enforce this bandwidth by reflecting most of the wavelengths other than the long-wave infrared (LWIR) so that they do not reach the detector. The detector itself will measure only the specified bandwidth from 8 and 12 μm. Therefore, the filter should transmit infrared radiation with a bandwidth that resembles the specified bandwidth as much as possible and it should reflect all the other wavelengths. The material that has "excellent" transmission in the LWIR and that is widely used for thermal imaging is germanium according to Edmund Optics.[18] Ge filters with an anti-reflective coating for thermal imaging have 0.96% transmission for wavelengths from 8 to 12 μm, as can be seen in Figure 22, which is taken from the same source.

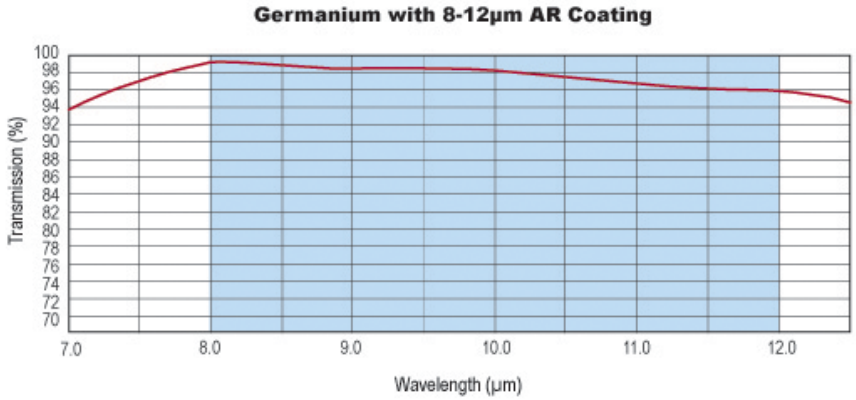

Figure 22: Transmission of the Ge filter

Although it can be seen that the transmission for wavelengths outside the 8 to 12 μm is not zero, it will be assumed that only wavelengths in this bandwidth are transmitted by the filter. For the SNR calculation, the throughput of the signal and the ground noise will have to be multiplied with the factor 0.96 to account for presence of the filter. The filter will be placed at the end of the baffle so that as little radiation as possible enters and consequently heats up the baffle. This is beneficial for the thermal subsystem as it needs less power to keep the baffle at cryogenic temperatures in this way. To cover the whole end of the baffle, the filter has to have a diameter of 1 meter. The price of a filter with that diameter was estimated to be € 100,000 by extrapolation based on the Ge filter prices of Edmund Optics.[19]

Deformation

The deformations of the instrument are yet to be determined. This step needs to be done after coming up with a plausible structure that integrates all of the components of the instrument. Currently, the sensor sub-assembly and baffle integration are unknown. Without a clear idea of how those components interact with each other and the mirror it is impossible to determine the deformations and their effect on the performance of the instrument. A very thorough finite element analysis is required to obtain those displacements. To obtain the required accuracy of the analysis, the geometry of all of the components that are part of the instrument must be very well defined.

Image quality

The quality of the image that is formed by the detector depends on the optical aberrations as given by Equation 5.9 and 5.10. A ratio between optical aberration and diffraction of 0.5 is optimal according to Dr.ir. J.M. Kuiper, as this ensures the optical system is diffraction-limited, which is the best possible

[18] URL: `https://www.edmundoptics.com/resources/application-notes/optics/the-correct-material-for-infrared-applica` [Accessed on 14/06/2019]

[19] URL: `https://www.edmundoptics.eu/f/germanium-ge-windows/13137/` [Accessed on 10/06/2019]

resolution one can achieve [3]. The spatial diffraction can be calculated by multiplying the angular diffraction with the focal length. The angular diffraction is found by Equation 5.11 [19].

$$\alpha = 1.22\frac{\lambda}{D} \tag{5.11}$$

where, α is the angular diffraction, λ is the wavelength and D is the aperture diameter. For an aperture of 1 m and a wavelength of 12 μm, this yields an anglular diffraction of $1.46 \cdot 10^{-5}$ rad. Multiplying this with the focal length gives the linear blur diameter due to diffraction, which is $1.44 \cdot 10^{-5}$ m. This is less than half of the size of a superpixel which means that the system is limited by diffraction rather than by the detector pixel size. Given that the primary mirror will be parabolic, no spherical aberration is present. The coma aberration of a parabolic mirror can be approximated with Equation 5.9 as given in Section 5.3.1. With the current design this results in $1.57 \cdot 10^{-6}$ rad. Because this is smaller than half of the diffraction, it will ensure the system is diffraction limited. The coma aberration could be lowered even more by merging pixels in a 3x3 configuration, but this would decrease the Field of View (FOV) and make the size of the image on the ground smaller. Astigmatism, as approximated by Equation 5.10, is mitigated by locating the aperture stop at the same distance from the vertex as the focal length. With an aperture of 0.5 m and a focal length of 0.96 m, the parabolic equation giving the final shape of the mirror is $y = 3.94x^2$.

Off-nadir Angle

In the conceptual design, a moving instrument was chosen over both multiple instruments and over a fixed instrument. Section 5.4 will elaborate on the mount that will be used to move the mirror around. This section, on the other hand, will discuss the maximum angle that the optical axis of the instrument can make with nadir, also called the off-nadir angle. For the operations of the StratoCruiser, this angle is important to know as it influences how far the instrument can look around without having to move the airship. This will dictate the ground that the instrument can cover which will influence the amount of airships that are required to provide full coverage of the Netherlands.

To find the maximum off-nadir angle that the instrument can make, some assumptions have to made. The first assumption that is made is that the atmospheric attenuation of the signal is the same for off-nadir viewing and nadir viewing. In reality, the rays have to pass through more atmosphere in the case of off-nadir viewing, which will decrease the throughput. This will, however, be neglected in order to simplify the problem. Secondly, it is assumed that the blur due to the change in focal length is allowed to be 10% of the spatial diffraction. If the blur due to the change in focal length is an order of magnitude smaller than the spatial diffraction, the image distortion is still smaller than half the pixel size as the spatial diffraction is 14.4 μm and the superpixel size is 48 μm.

In the case of off-nadir viewing, the subject distance increases, which increases H in Equation 5.5, which increases the focal length. The amount by which the focal length is allowed to increase can be calculated with the allowable linear blur diameter, by using Equation 5.12 [19].

$$B = \beta \cdot f \tag{5.12}$$

In this equation, B is equal to the linear blur diameter, β is equal to the angular diffraction and f is equal to the focal length. When the focal length is known, the subject distance can be calculated with Equation 5.5 and the maximum allowable off-nadir angle can be computed with the trigonometric relation that the cosine of the off-nadir angle is equal to the ratio of the subject distance in nadir viewing to the subject distance in off-nadir viewing. This eventually leads to a maximum off-nadir viewing angle of 25°. Upon comparison with the maximum off-nadir angle for satellites, which is typically 30°, the angle is slightly lower but this makes sense as the altitude of the airship is lower than the altitude for satellites.[20] With this maximum off-nadir viewing angle, the instrument can cover a circle with a radius of 9.32 km on the ground, centered at nadir.

[20]URL: `http://www.landinfo.com/buying-optical-satellite-imagery-2.html` [Accessed on 16/06/2019]

Mirror coating

For a SiC mirror, a coating has to be applied to make the mirror more durable by protecting it from scratches and to increase the reflectivity of the surface to maximize the performance of the mirror. The coating can either be made of protected gold or protected silver for the LWIR application.[21] Protected silver coatings have a 98% specular reflectance in the infrared and are cheaper than protected gold coatings [23]. Therefore, a silver coating with a protective layer of silicon monoxide will be used for the primary mirror. The protective layer allows for the mirror to be cleaned during integration and assembly of the instrument and it prevents the soft metal from getting damaged easily [19].

5.3.3 Final design

The final design parameters of the instrumentation subsystem are presented in Table 12. The pixel temperature and the ground temperature are not included in this table because these are not parameters that can be designed but are rather environmental parameters that result in a certain SNR for the given design, which will be explained in Section 6.3.1.

Table 12: Optical parameters

Parameter	Value	Unit	Parameter	Value	Unit
Aperture diameter	1	m	Throughput	0.95	-
Pixel size detector	12	μm	Quantum efficiency	0.9	$e^-/photons$
Super pixel size	48	μm	Integration time	0.06	s
Pixels on detector	2048x2048	-	Maximum off-nadir angle	25	$^\circ$
Altitude	20500	m	Ge filter throughput	0.96	-
Observed wavelength	8 - 12	μm	Baffle temperature	90	K
Bandwidth	4	μm	Baffle length	2.5	m
GSD	1	m	Ground coverage picture	512x512	m^2

5.3.4 Resource allocation

The mass and power breakdown for the instrumentation subsystem is given in Table 13. The mirror mass was found by neglecting the mass of the coating and therefore assuming that the mirror is fully made out of the substrate material. The resulting mass of 20 kg is a bit on the high side when comparing it to for example the 1.5 m aperture of the telescope presented in [20], which is 6.5 kg. However, that design is optimized for lightweight, which is something that still has to be done in future work for the primary mirror of the StratoCruiser. The mass of the filter is estimated with the density of Ge as given by Edmund Optics, the supplier of the filter.[22] The influence of the surface finish and the insulating material was neglected for computing the mass of the baffle, as the aluminum will account for most of the mass and because the insulation material is not specified yet. The mass and the power consumption of the sensor are provided by the supplier.[23] Likewise, the mass and the power consumption of the mount are provided by the supplier as explained in Section 5.4. The mirror and the filter do not consume energy. The energy that is used to cool the baffle is included in the thermal subsystem.

[21] URL: `https://www.edmundoptics.com/resources/application-notes/optics/metallic-mirror-coatings/` [Accessed on 20/06/2019]

[22] URL: `https://www.edmundoptics.eu/f/germanium-ge-windows/13137/` [Accessed on 13/06/2019]

[23] URL: `https://www.lynred-usa.com/products/xga-resolution/pico1024gen2-infrared-sensor.html` [Accessed on 14/06/2019]

Table 13: Mass budget for the instrumentation subsystem

Component	Mass [kg]	Power [W]
Mirror	20	0
Filter	20	0
Baffle	35	0
Sensor	0.03	0.22
Mount	300	1500
Total	375	1500.22

The cost budget of the instrumentation subsystem is given in Table 14. The cost of the mirror was estimated based on extrapolation of the price for parabolic mirror with diameters up until 400 mm as supplied by Edmund Optics.[24] The price of the filter was estimated, as specified in Section 5.3.2, to be 100,000 EUR. The price of the baffle was based on the price of a 9x3x3 *inch* baffle as sold by Vixen Optics.[25] This prices was multiplied by a factor of 5, as the baffle that is required for the instrument will have to be about five times the size of the baffle that was priced at $70. The typical prices of TIR sensor range from 8,000 to 20,000 EUR [24]. Therefore, a cost of 20,000 is used to obtain a conservative cost estimate. The price of the mounting system was estimated based on off-the-shelf examples as explained in Section 5.4.5. As this way of estimating prices for all the components is not accurate, all values are rounded up to the nearest 100.

Table 14: Cost budget for the instrumentation subsystem

Component	Price [k€]
Mirror	62.0
Filter	100.0
Baffle	0.4
Sensor	20.0
Mount	40.0
Total	222.4

5.4 Instrument Integration

The integration of the instrumentation into the gondola must be designed in order to satisfy the requirements on temporal resolution, pointing accuracy and pointing stability of the instrument. These are three requirements which drive the design of the mechanism in the mounting of the instrumentation:

- **SB-Subs-Meas-01** The instrument shall have a temporal resolution of 1 minute.
- **SB-Subs-ADCS-03** the attitude control accuracy shall be 5 arcsec.
- **SB-Subs-ADCS-04** The attitude control stability shall be 1 arcsec.

This chapter describes the design of the instrument integration system with regards to each of these three requirements

5.4.1 Temporal Resolution

The imaging regime is defined using **SB-Subs-Meas-01**, the image size (A_{image}), the integration time (t_{int}) and the maximum off-nadir angle (δ). With $\delta = 25°$ (equating to 9.32 km on the ground), fitting square images into the field of view is done as shown in Figure 23:

[24]URL: `https://www.edmundoptics.com/f/precision-parabolic-mirrors/11895/` [Accessed on 14/06/2019]
[25]URL: `https://www.vixenoptics.com/Vixen-Light-Baffle-Hood-p/3732.html` [Accessed on 15/06/2019]

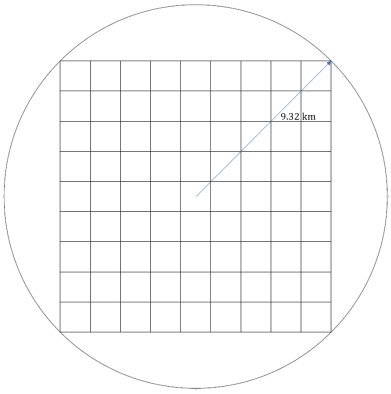

Figure 23: Schematic drawing of observation regime.

With each small square representing one picture of side length ($l_{pic} = 512m$), this amounts to 697 pictures captured in such an arrangement. This is considered unfeasible; to loosen this requirement the off-nadir angle is decreased to 10°. With this new angle, the number of pictures required in a minute is 100. The maximum off-nadir angle should be optimized in further design depending on the capabilities of the mounting system. The imaging regime can be visualized as shown in Figure 24. The red arrow shows the direction in which consecutive images are captured.

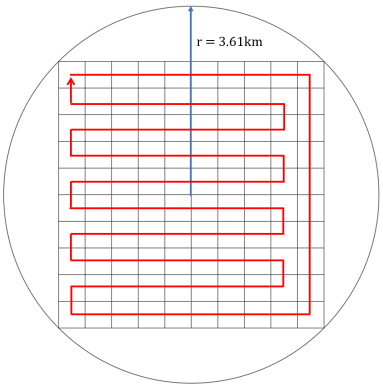

Figure 24: Schematic drawing of observation regime with new off-nadir angle

The integration time of 0.06s for 100 pictures in the minute means that there is 0.54s remaining for each reorientation. Every reorientation is simply a shift of $arctan(512/20500) = 1.431°$ in either 'roll' or 'pitch' of the instrument. This leads to a kinematic profile illustrated in Figure 25.

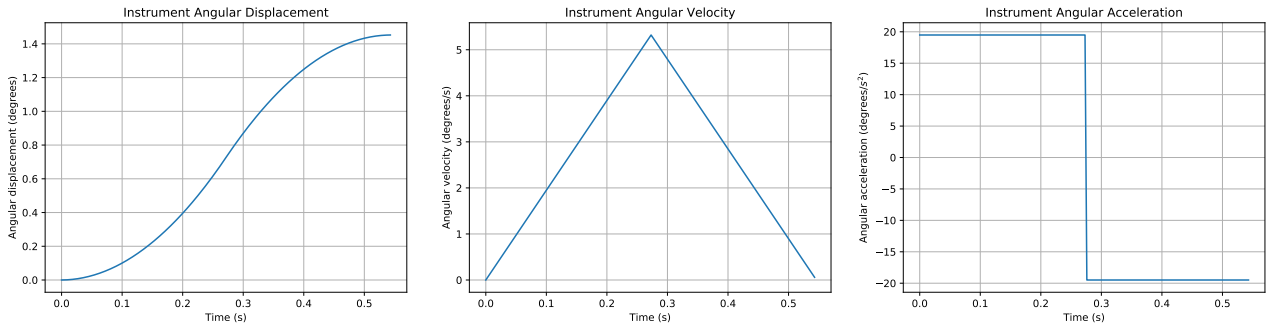

Figure 25: Ideal kinematic profile of a single reorientation of the instrument.

To calculate the required torque to reorient the instrument, it may be modelled as an impulse, described by Equation 5.13:

$$\tau \cdot \Delta t = I \cdot \Delta\omega \tag{5.13}$$

τ is the required torque, Δt is the time interval over which it is applied, I is the mass moment of inertia, and $\Delta\omega$ is the change in angular velocity. The maximum $\Delta\omega = 5.3\ ^\circ/s = 0.092\ rad/s$; this change occurs over half the time interval, so $\Delta t = 0.5 \cdot 0.564 = 0.271\ s$. The mass moment of inertia of the instrument and baffle about the vertex of the instrument is required, since the rotation must also take place about this point to avoid translation of the center of the mirror. This is calculated be about 285 kgm^2 using a computer-aided design software (CATIA). Therefore, the $\tau = 97\ Nm$. This can be achieved using two general mechanisms: a gimbal mount that rotates the instrumentation as required, or a parallel manipulator, which is a set of linear actuators arranged to exert forces on the edges of the mirror to rotate it about its center. Both of these options are further analyzed after considering the other two driving requirements.

5.4.2 Pointing Accuracy

Since controlling the airship with an accuracy of 5 arcsec stipulated by **SB-Subs-ADCS-03** was deemed unfeasible in the conceptual design phase, Chapter 4, this requirement must be satisfied by the mounting system. The team concluded that this may be achieved by employing high accuracy star trackers and gyroscopes to measure the attitude of the airship relative to the ground and using the controller of the instrument mount to provide the processor with the attitude of the instrument relative to the airship. The processor can then calculate the attitude of the instrument relative to the ground, and compare it to its required attitude as given by ground commands. If there is a discrepancy, the central processor can command the mount controller to change the instrument orientation to the corrected value.

5.4.3 Pointing Stability

Designing for pointing stability led the team to a similar solution, however with increased stringency. Instability can occur at any moment due to a gust, for example, and must be minimized to 1 arcsec during the integration time of the instrument (0.06 s). This meant that the control loop described in Section 5.4.2 must occur several times within 0.06 s. Star trackers lack the necessary sampling frequency (generally no more than 10 Hz), therefore gyroscopes must be included for intervals between the star tracker's measurements. The chosen gyroscope achieves up to 262 Hz measurement frequency, with a mass of 0.052 kg, and a power consumption 1.5 W.[26] Therefore, the control loop can be defined as shown in Figure 26.

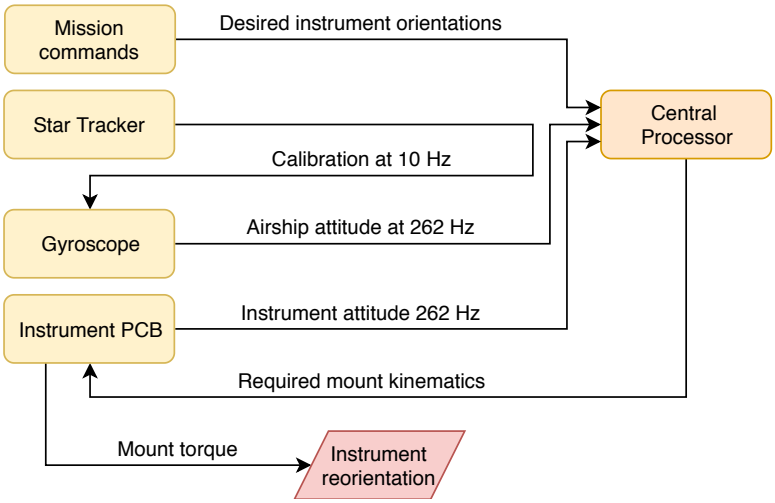

Figure 26: Instrument attitude control loop.

To ensure that **SB-Subs-ADCS-04** is satisfied, the accuracy of the attitude determination and control mechanisms must be accounted for. The sensors chosen have the following relevant characteristics:

[26] URL: `https://www.sensonor.com/products/gyro-modules/stim202/` [Accessed on 22/06/2019]

- Day star tracker: accuracy of ±0.145 arcsec, sampling frequency of 10 Hz. This sensor is also described in Section 5.6 [25].
- Gyroscopes: bias instability of $0.3°/hour$, measurement range $\pm 400°/s$, measurement frequency of 262 Hz[27].

The bias instability of the gyroscope is its drift rate, which directly affects the accuracy of the attitude measurements between star tracker measurements i.e., during 0.1 s. For this time interval the gyroscope accuracy can be calculated:

$$\frac{0.3°/hr}{10Hz \cdot 3600s} = 0.03 \; arcsec \; in \; 0.1s$$

In the context of pointing stability, the accuracy of the star tracker actually does not need to be taken into account. It serves simply to calibrate the gyroscope at 10 Hz; during the image integration time (when pointing stability is important) only the gyroscope and mount are involved. Therefore, it is found that the budget remaining for the instrument control mechanism, without safety factors, is $1 - 0.03 = 0.97$ *arcsec*. With this in mind, the instrument mounting mechanism is designed.

5.4.4 Gimbal Mount

The most capable off the shelf gimbal system found has the following characteristics[28]:

- Maximum payload diameter: 0.508m
- Maximum payload mass: 50 kg
- Pointing accuracy characteristics
  - Resolution: ± 0.0275 *arcsec*
  - Repeatability: ± 0.25 *arcsec*
  - Precision: ± 0.5 *arcsec*
- Maximum angular velocity: 300°/s
- Mass: 234kg
- Power consumption: 24W

Although it has a high angular speed and accuracy, the gimbal system is not ideal due to its small maximum diameter, considering the mirror is 1m large. This would mean potentially mounting the mirror onto a smaller platform which is then held in the gimbal, but this solution would introduce more mass and inertia into the gimbal payload, which is already low at 50kg. Another issue is the large moment of inertia of the entire instrumentation assembly (about 285 kgm^2) due to the long baffle.

5.4.5 Parallel Manipulator

The other option involves using a parallel manipulator, which is a commonly controlled group of linear actuators symmetrically arranged along the periphery of the mirror, allowing it to change orientation (illustrated in Figure 27). The distance of each actuator from the center of the mirror (r_{act}) and the inclination of the actuator (β) may be varied. Most commonly 6 actuators are used for such platforms, however this could be varied to increase or decrease the loads on each actuator.

[27] URL: `https://www.sensonor.com/products/gyro-modules/stim210/`[Accessed on 24/06/2019]

[28] URL: `https://www.aerotech.com/product-catalog/gimbals-and-optical-mounts/aom360d.aspx` [Accessed on 14/06/2019]

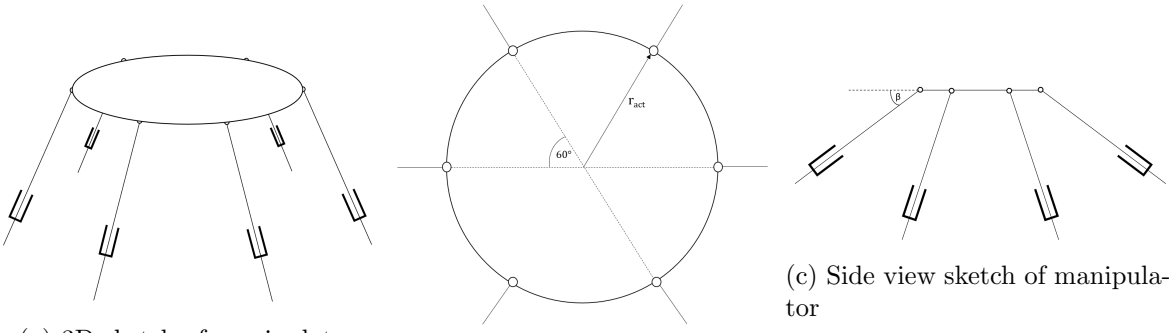

(a) 3D sketch of manipulator

(b) Top view sketch of manipulator

(c) Side view sketch of manipulator

Figure 27: Schematic representation of parallel manipulator

In the worst case scenario, the instrument would need to be rotated around an axis that intersects with the attachment points of two of the actuators, therefore only 4 actuators would be able to provide the necessary torque. Additionally, since the entire assembly is nadir-facing, the weight of the instrumentation must also be carried by the mounting. The loads on one of the 4 actuators providing a force can be illustrated as shown in Figure 28.

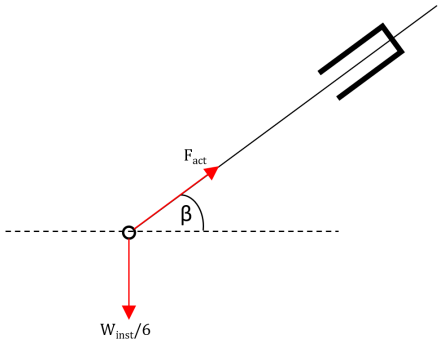

Figure 28: Forces (shown in red) acting on actuator

W_{inst} represents the weight of the instrumentation (it is divided by 6 as there are 6 actuators equally carrying the load), and F_{act} is the force required for the reorientation which can be calculated from the torque as follows:

$$F_{act} = \frac{\tau}{r_{act} \sin 60° \sin \beta}$$

Therefore, the force that 1 actuator must be capable of providing is:

$$F = \frac{W_{inst}}{6 \cdot \sin \beta} + F_{act} \tag{5.14}$$

The sensitivity of required force to changes in r_{act} and β is plotted in Figure 29.

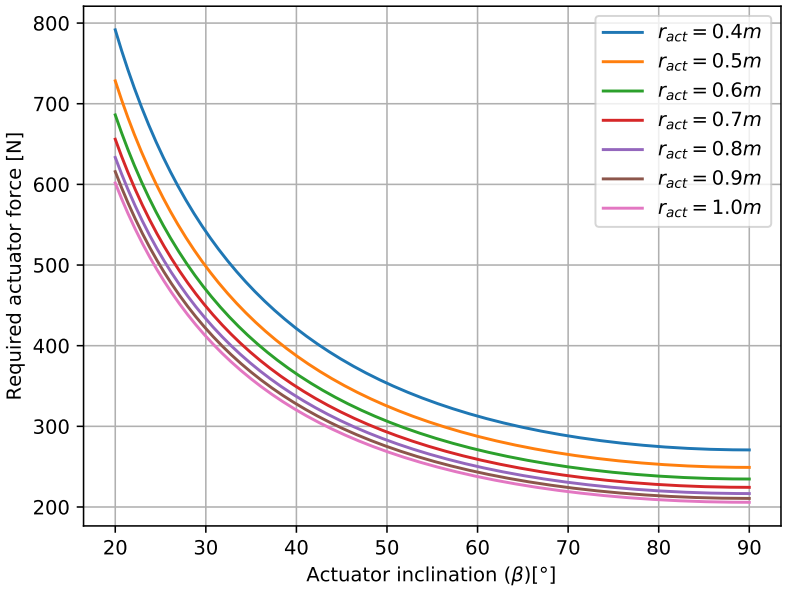

Figure 29: Sensitivity of required actuator force to r_{act} and β

There are various commercially available actuators which can provide up to 800N, so the requirement on the accuracy is what drives the choice of actuators and their arrangement. The accuracy (δ_{act}) can be calculated for small angles using the actuator precision:

$$\delta_{act} = \frac{precision \cdot \sin\beta}{r_{act}} \tag{5.15}$$

The most accurate actuator found[29] has the following characteristics:

- Maximum continuous force = 800N
- Accuracy characteristics
  - Precision = $\pm$ 5 μm
  - Resolution = $\pm$ 0.05 μm
  - Repeatability = $\pm$ 0.5 μm
  - Maximum stroke = 5220 mm

With this precision, a sensitivity diagram of the pointing accuracy of the mount with respect to r_{act} and β can be made. Figure 30 shows this, along with the budgeted accuracy = 0.97 $arcsec$:

[29] URL: `http://www.intellidrives.com/linear-actuators-c-15.html/Linear-Actuators-Linear-Servo-Motors/Linear-Actuators-LinearServoSlide/Linear-Actuator-LSS200` [Accessed on 20/06/2019]

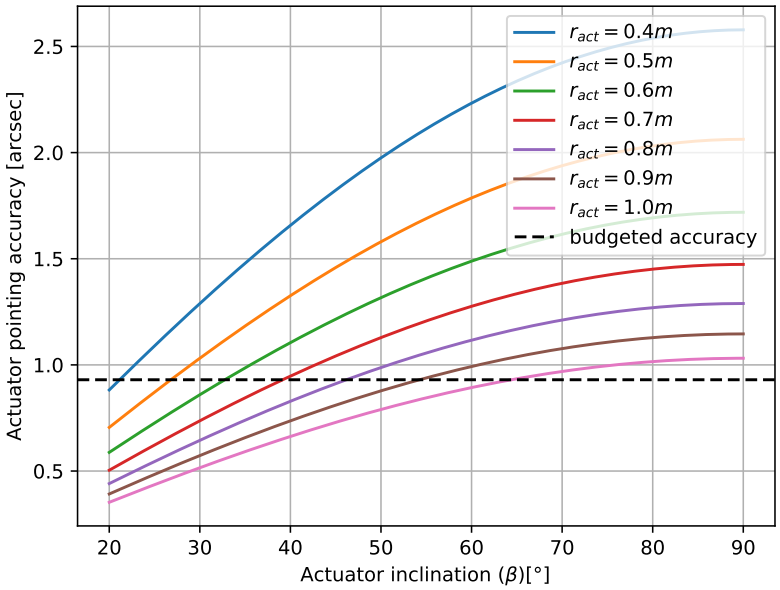

Figure 30: Sensitivity of actuator accuracy to r_{act} and β

To minimize the actuator arm r_{act} and therefore avoid a heavy bracket around the mirror, r_{act} is chosen to be 0.6m. With $\beta = 30°$, this leads to the stability budget shown in Table 15.

Table 15: Pointing stability budget for the instrument attitude control and determination system

Component	Pointing accuracy [arcsec]
Gyroscope	0.0300
Parallel manipulator	0.8594
Total	0.8894
Requirement	1
Margin	0.1106

Choosing $\beta = 30°$ has the benefit of allowing a margin of 0.1106; in practice this will likely be consumed by deformations of components and of the mirror itself. These were not analyzed due to a lack of time, however, they should be analyzed in the subsequent phase of the project. For example, having $r_{act} = 0.6m$ implies some supports around the mirror onto must be included onto which the actuators are attached. This will introduce further inaccuracies in the system. Although the mounting system was not designed in any further detail, the team consulted a company manufacturing parallel manipulators of such size and capabilities to obtain estimates of the mass, volume, cost and power[30]. This yielded this following budget estimates:

- Mass (including actuators, attachment, and ceiling mount): about 300 kg
- Power consumption: 1500 W
- Volume: 0.864 m^3
- Cost: about $40,000

5.4.6 Vibration Isolation

A potential risk of such a mechanism is that the frequency of accelerations on the instrument could cause high-amplitude vibrations in the assembly. Since the torque introduced by the mount acts

[30]Motion For Simulators, personal communication, May-June, 2019

directly at the mirror, the baffle is the most susceptible to vibrations as it extends 3 m from the point where the load is applied. The mirror and sensor are much closer to the location of the torque application, so for this analysis they are considered to be clamped. The baffle is modelled as a beam with all of its mass concentrated at the end, with loads as shown in Figure 31. W_{baffle} represents the weight of the baffle, τ is the applied torque, and m is the concentrated mass of the baffle. The stiffness can be modelled according to Equation 5.16 which is dependent on the baffle radius r, thickness t, length l and E-modulus E, leading to the equation of motion in Equation 5.17:

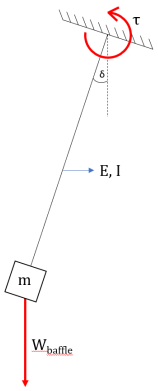

Figure 31: Baffle model used for vibrational analysis

$$k = \frac{EI}{L^3} = \frac{E\pi r^3 t}{L^3} \tag{5.16}$$

$$L \cdot m \cdot \ddot{x} + L \cdot k \cdot x = -L \cdot W_{baffle} \cdot sin\delta - \tau \tag{5.17}$$

The input for τ is modelled by Equation 5.18, a signum function, which has the value of $+1$ when the sign of its argument is $(+)$ and -1 when the sign of the argument is $(-)$.

$$\tau = 97 sign(sin(2\pi f t)) \tag{5.18}$$

f is the frequency of the torque inputs by the mount, 100/60 $pictures/second$. The signum function is suitable as it accurately models the acceleration profile shown in Figure 25. Using the baffle dimensions and material specified in Section 5.3, the response of the system to this input for 20 seconds is modelled in MATLAB. The amplitude of the vibrations never exceeds 20 μm, which is insignificant considering it is at the end of the baffle.

5.5 Propulsion

The propulsion subsystem is responsible for the airship's ability to move to an observation point, perform station keeping, and finally to provide attitude control when landing. First, the airship has to be able to provide enough thrust to move against the flow of the wind in the stratosphere to move to an observation spot when needed. Secondly, station keeping needs to be performed to a high degree of accuracy. This essentially means that the airship's propulsion subsystem needs to be able to provide the thrust necessary to be able to 'hover' over a ground segment. Lastly, when landing, the propulsion system must be able to provide relatively quick turning and braking capabilities so that the airship is able safely approach for landing.

The propulsion of the airship is provided by an electric propeller propulsion system. The design options for the various propulsion systems are presented in the MTR and the rationale behind the group's decision is explained in more depth there. However, some of the main reasons are presented briefly below. The reasoning behind the choice on electric propeller as the propulsion type is multi-faceted. First, it is chosen because the duration of the mission is relatively long. The mission duration is projected to be in the magnitude of months. Therefore, it would not make sense to utilize fossil-fuel based propulsion type as all of the fuel will have to be carried onboard. This will incur penalties in the mass and the volume of the airship. Instead, it would make sense to use fuel that the airship can generate onboard such as electricity. Secondly, the propellers are chosen as they are efficient at low speeds. And lastly, the electric propulsion system does not produce secondary byproducts

that are harmful to the environment and are therefore a sustainable option. To sum up, the electric propeller propulsion system is chosen for its high efficiency, no required fuel to take on board, and high sustainability.

5.5.1 Propeller blade section and blade number choices

The propeller blade section, i.e., airfoil, is chosen between the CLARK Y and RAF-6 airfoils. These are airfoils that were introduced in the 1940s. However, although they were made in the 1940s, these airfoil sections are attractive choices. This is because the airfoils have a plethora of public records including its design and performance graphs. These are largely unavailable for other airfoil sections used in propellers. The CLARK Y and RAF-6 airfoils have public data from the test done by the National Advisory Committee for Aeronautics. Most importantly, these two airfoils in the 1940s are not significantly different from the modern day propeller blade sections, in terms of their efficiency. Modern day, state-of-the-art propeller blade sections are only about 5 % more efficient than the blade sections from the 1940s [9].

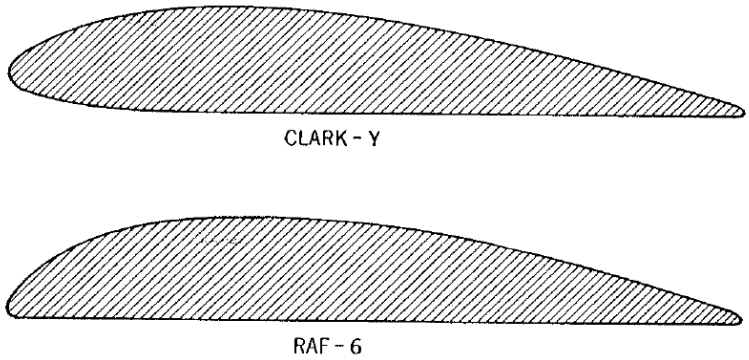

Figure 32: Blade section of the CLARK Y and RAF-6

Between these two airfoils, the CLARK Y airfoil is chosen. This is because, under the same conditions, the CLARK Y airfoil has less overall drag compared to the RAF-6 airfoil section [26]. Although it is a small difference, over a long period of time as in magnitudes of months, this becomes a significant difference in power wasted. Therefore, the CLARK Y airfoil section is chosen over the RAF-6 airfoil.

Normally, under the momentum theory, which is one of the main theoretical approaches to propeller analysis, as the number of blades increases, the efficiency is predicted to decrease. This is mainly due to the tip disturbances caused by each blade to one another. Therefore, when comparing 2, 3, and 4 number of blades, it would be expected for the 4 blade number choice to be the most inefficient and 2 blade number choice to be the most efficient choice. However, in a study done by the National Advisory Committee for Aeronautics in 1938 using the CLARK Y airfoil section on 2, 3, and 4 blade numbers, the 3 blade design is shown to be the most efficient in most of the speed-power coefficient range [27]. the difference in efficiency between the two and four blade configuration is a mere 2%, but this difference becomes significant over a long period of time such as the one that the mission requirement mandates.

5.5.2 Propeller Diameter, Pitch, and Efficiency Determination

The design of the propeller also involves the determination of the propeller diameter, pitch angle, and the evaluation of the efficiency of the propeller as a whole. To do this, the following four-step method is followed. Each step is explained in more detail below in the list. It should be noted that unless otherwise noted, the sources for this method and the equations given in this section are given in [9]. This was presented in the MTR, but it is the crucial step in determining the propeller design and therefore is included in this report as well.

1. Determine power requirement with assumed propeller efficiency

2. Determine speed-power coefficient, i.e., design condition

3. Obtain pitch, diameter and efficiency using the design performance graph.

4. Iterate until convergence.

Determine power requirement with assumed propeller efficiency: The initial assumption of the propeller efficiency is 0.8. It has been verified that the initial condition, i.e., the initial assumption of efficiency, does not affect the end-value. The assumed propeller efficiency, η is used in conjunction with the drag estimate of the airship, D $[N]$ and the airspeed of the airship in cruise, V $[m/s]$ to obtain the power required in cruise, P_r $[W]$ as shown in Equation 5.19.

$$P_r = \frac{D \cdot V}{\eta} \tag{5.19}$$

2. Determine speed-power coefficient: The speed-power coefficient, C_s is a design condition that is determined from the power-required, P_r, air density, ρ, rotational speed of the propellers, n, and the airspeed of the airspeed, V. In essence, it describes the design condition of the propeller at a certain airspeed, altitude, and the power required. All of the variables other than the rotational speed of the propellers are already known. Consequently, the rotational speed of the propellers is assumed to be held constant at 10 *rps* for high efficiency. Rotational speed of 10 *rps* to 20 *rps* are typical values of rotational speed of propellers in airships [9]. The speed-power coefficient is obtained using the Equation 5.20.

$$C_s = (\frac{\rho}{P_r \cdot n})^{0.2} \cdot V \tag{5.20}$$

3. Obtain pitch, diameter and efficiency using the design performance graph: Using the speed-power coefficient, which is the design condition, the pitch angle, diameter, and the efficiency of the propeller can be obtained from the readings of the Figure 33. Using the value of the speed-power

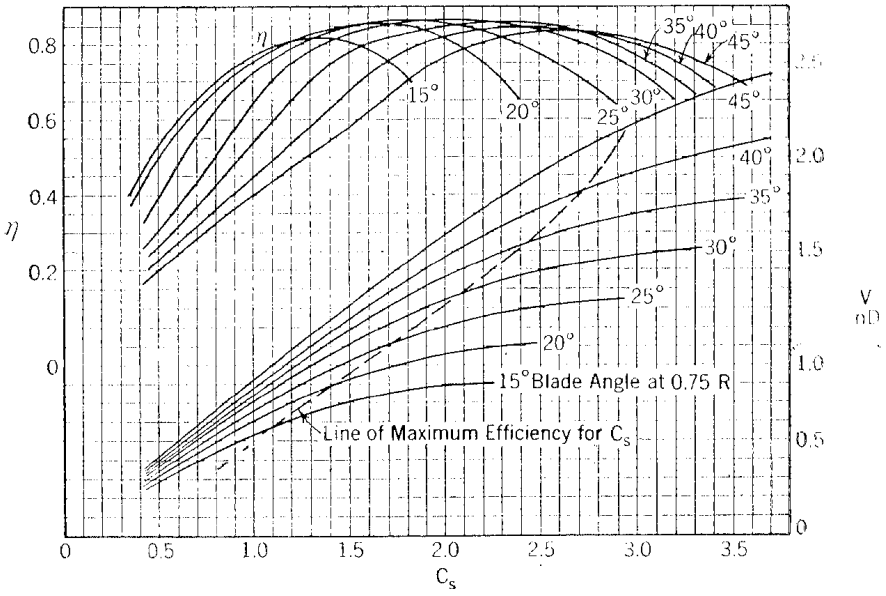

Figure 33: Design chart for propeller, CLARK Y section, three blades

coefficient and looking at the lower half of the design chart, the pitch angle should be determined by looking at the line of maximum efficiency for C_s, which is the pitch angle. Once the pitch angle is determined, the right hand axis should be read next, in which the diameter can be obtained from the value. Finally, the upper half of the design chart can be read with the corresponding pitch angle, to read the efficiency of the propeller on the left hand axis.

4. Iterate: Finally, step 3 is iterated over and over again, until the efficiency of the propeller converges. Then the final value of the pitch angle, diameter of the propeller, and the efficiency of the

propeller can be determined. The final power required can also be determined by updating the value of efficiency in Equation 5.19.

To sum up, the propeller diameter obtained from this is **16.0227 *ft***, which is equal to **4.88 *m***. The pitch angle of the propeller is **15 °**. And finally, the propeller efficiency is **0.68**. Using this propeller efficiency, the final power required can be calculated and is equal to **13.9 *kW***.

5.5.3 Determination of Thrust Levels

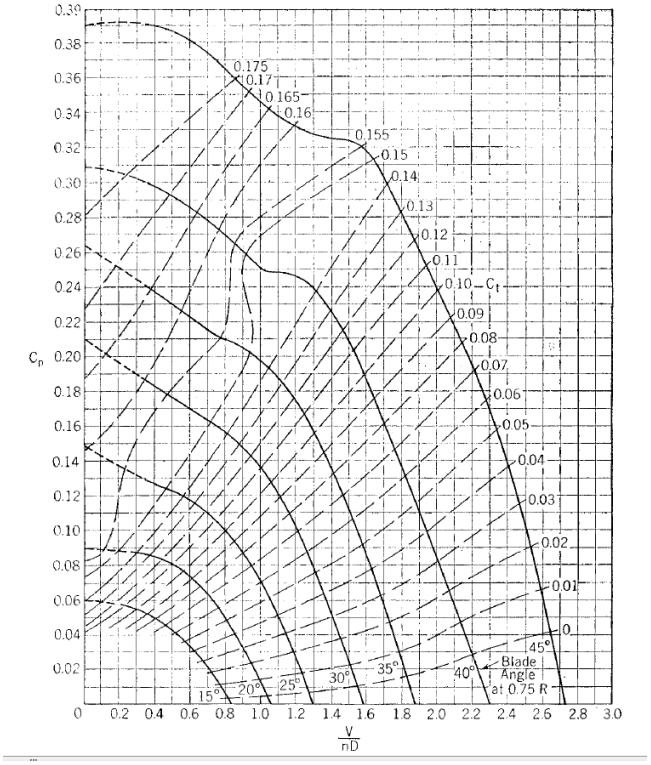

Figure 34: Performance chart of CLARK Y blade section with three blades [26]

The thrust is determined by looking at Figure 34. Then, the thrust coefficient is obtained from Figure 34. Here, the V/nD value that was obtained in designing the blade diameter in Section 5.5.2 is read with the corresponding pitch angle. Then the thrust can be obtained from Equation 5.21 [9]. In the equation, C_T is the thrust coefficient, which is 0.08 in this case as the pitch angle is 15 ° and the V/nD value was around 0.4. ρ is the air density, which is 0.088 kg/m^3 = 0.000171 $slug/ft^3$ at the target altitude. n is the rotational speed of the blade, which was assumed to be at 600 rpm = 10 rps for maximal efficiency. And finally, D is the propeller diameter, which was obtained as 4.88 m = 16.023 ft. It should be noted that the critical drag that was supposed to be overcome was 1720 N = 387 lbf from Section 5.1.6.

$$T = C_T \rho n^2 D^4 \tag{5.21}$$

The resulting value of thrust per propeller is 90.163 lbf. Multiplying this value of thrust, 90.163 lbf, by 4 for having four propellers, the resulting thrust is $\approx$ 360 lbf = 1601.4 N. This is a 6.5 % difference from the prescribed thrust. Although this is not exact perhaps for the aforementioned reason, it is not a substantial difference, which can easily be offset by the increase of rotational speed. For context, increase of rotational speed of 10 rps to 11 rps shows that the thrust increases up to 435.8 lbf = 1938.5 N. The maximum thrust is limited bx'y the maximum rotational speed of the propeller blades, which is in turn limited by the tip velocity. The tip velocity is calculated using Equation 5.22 and should be under 700 m/s [9]. In the equation, V_{tip} is the tip velocity in $[m/s]$, n is the rotational speed of the blades in $[rps]$, and D is the diameter of the propeller blades in $[m]$.

$$V_{tip} = \pi n D \tag{5.22}$$

Using this, the maximum thrust is provided when the rotational speed is 13 *rps* and the maximum thrust is given as 152.15 $lbf = 676.8$ N per propeller, which amounts to a total of 2707.2 N.

5.5.4 Propeller Thickness and Chord Determination

Building from the previous section that was previously presented in the MTR, the propeller thickness and chord can also be determined. The propeller thickness and chord lengths are determined using the common value of the aspect ratio of propellers. It is given that the aspect ratio of advanced turbofan propellers is usually 2.5 [28]. Since the aspect ratio is the ratio between the span of the propeller over the chord, and the diameter has been determined in Section 5.5.2, the chord can be determined by dividing the span by the aspect ratio of 2.5. The resulting chord length is 91 *cm*. Then, using the thickness to chord ratio of the airfoil, 11.7 %, the thickness of the airfoil can also be determined and it is 10.7 *cm* [31].

5.5.5 Propeller Number and Placements

The propeller number and placements are presented in the MTR [3]. To sum up, the propellers are placed at 50 % of the entire length of the airship and around the airship in an 'X' configuration as discussed in the MTR. The propellers are placed at 50 % of the airship, because this is where the airflow starts to become turbulent. If the propellers are placed after the airflow becomes turbulent and is about to separate from the body, it can reinvigorate the flow and reduce drag [29]. In a cross-sectional view, the propellers are placed at ±45 ° and ±135 °. This was to have high efficiency and controllability and the advantages from these two aspects outweigh the disadvantage coming from the increase in mass due to the increase in number of supporting strucutres, motors, etc.

5.5.6 Motor, Motor Controller, Gearbox, Gearbox Housing

So far, the design choices have been in regards to the propeller. Now, more attention can be directed towards the motor, motor controller, and the transmission selection. The preliminary design of these elements of the propulsion subsystem has been given earlier in the MTR. However, the detailed design of these are done by mostly selecting off the shelf components. It should be noted that the components that are chosen off the shelf are an example of the design and may be subject to change should a better component be developed or found. The advantage of selecting off the shelf components here comes from the fact that a concrete number can be placed on mass, power, and cost budgets.

First, for the motor selection, it is important to note that the power required obtained in the propeller design needs to be updated with the final efficiency value. This value is 13.9 kW for the required power per propeller. The motor has to be able to provide a continuous power output at this level. For this, the EMRAX 188 was selected as it has one of the best power density in its class of electric motors, ranging at 10 kW/kg [32]. This power density is significantly higher than its competitors, which are rated at around 2 kW/kg [33]. Even Siemens, one of EMRAX's main competitors in the electrical motor market produces engines that are rated at 5 kW/kg [34]. It also has a high efficiency of 98%. The motor can be seen in Figure 35. The motor cooling method chosen as combined cooled since a detailed performance chart is given for the combined cooled EMRAX 188. Combined coooled means that it is partially air-cooled and partially liquid-cooled. Since the performance chart for the combined cooled EMRAX 188 is given, an accurate power output reading can easily be obtained. Additionally, the motor includes a set of hall sensors that measures the magnitude of the magnetic field and helps the motor keep track of its rotational speed and position. The motor provides continuous power of up to 60 kW, which is far more than the needed power requirement of 13.9 kW per propeller obtained from the propeller design. From the technical data provided by EMRAX, EMRAX 188 can provide this continuous power at around 3000 *rpm*. However, it should be noted that when the propeller was

[31] URL: `://http://airfoiltools.com/airfoil/details?airfoil=clarky-il` [Last accessed: 24/06/2019]
[32] URL: `://https://emrax.com/products/emrax-188/` [Last accessed: 24/06/2019]
[33] URL:`://https://www.nextbigfuture.com/2015/04/siemens-and-emrax-claim-best-power-to.html`
[34] URL:`://https://www.nextbigfuture.com/2015/04/siemens-and-emrax-claim-best-power-to.html`

designed, the rotational speed of the propeller was assumed to be 11 rps, which is equal to 660 rpm. Therefore, to reconcile the two different rotational speed, a step-down gearbox system is needed.

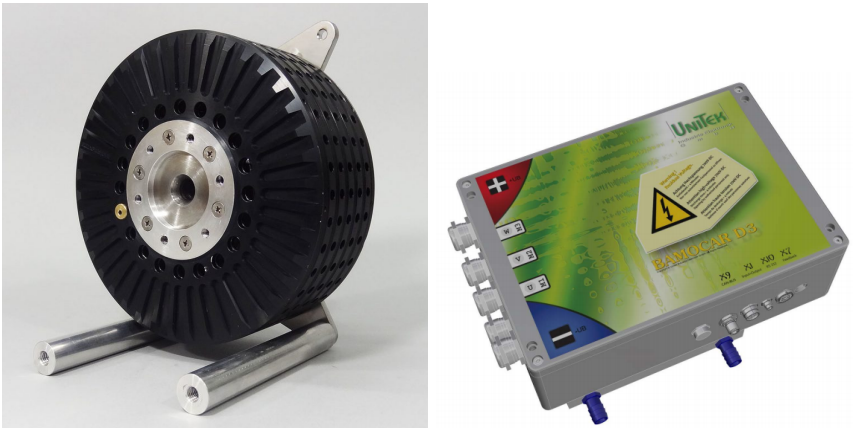

Figure 35: EMRAX 188 electric motor (left) and BAMOCAR-PG-D3 motor controller (right)

The gearbox needs to have a step-down ratio of approximately 5 : 1, which approximately corresponds to the ratio of the rotational speed, 3000 : 600. The gearbox mass was estimated by multiplying the empirical factor of 0.2 kg/hp to the horsepower of the propeller, which is 18.65 $hp = 13.9\ kW$ [11]. Multiplying the aforementioned values yields the estimated mass of the gearbox as 3.73 kg. The dimensions of the gearbox is estimated by selecting an off the shelf component that is comparable in mass and has the required step-down ratio. From this, the dimension $150 \times 90 \times 90\ mm$ as shown in the Table 16 is obtained [35].

The components discussed so far: electric motor, motor controller, and the gearbox are the components that will be placed together in a gearbox housing. The electric motor and motor controller could have been placed within the airship, but the electric motor's manual highly recommends shortest cabling if possible and therefore, the motor and motor controller are placed next to the gearbox. The gearbox housing must encompass all these components from the outside environment to not only protect the individual components from debris or contamination, but also to aerodynamically design them. However, since the components are relatively small compared to the propeller, for simplicity, the gearbox housing is chosen to be a rectangular shape to simply house the components. To do this, the dimensions of each components must be known and are given in Table 16.

Table 16: Dimension of each component that need to be housed in the gearbox housing

Component	Length [mm]	Width [mm]	Height [mm]
Electric Motor	77	188	188
Motor Controller	250	403	145
Gearbox	150	90	90
Gearbox Housing	477	403	188

It should be noted that whilst length is the sum of all the components' lengths, the width and height are simply maximum values. This is because the components are stacked along the length, therefore the gearbox housing needs to have the length as the sum of all those values. However, since the components are not stacked along the width and the height, the dimension of the gearbox housing need not be the sum of its components, but simply the maximum values. Taking this into account, the thickness of the gearbox housing can be determined by multiplying it by a factor of 0.007 and adding 4 mm [30]. This yields the thickness of the gearbox housing as 7.48 mm. However, as previously noted, there is room for improvements in the design of the gearbox housing.

[35] URL:://https://www.alibaba.com/product-detail/2019-low-backlash-arcmin-5-RA_62056778701.html?spm=a2700.7724857.normalList.2.3d5348f652TEds&s=p

5.5.7 Variable Pitch

From a preliminary analysis of the operation of the airship, one of the major problem in the operation was how the airship will reduce its speed when landing. Initially, it was thought that the drag of the airship would be enough to slow down the airship enough, which at that point, the airship can be tethered down. However, the preliminary analysis showed that the time it would take for the airship to brake merely using its drag would be in the order of hours. Therefore, a need for reverse thrust was realized. To achieve reverse thrust capabilities, there are two main options: vector thrust and variable pitch. Vector thrust could in fact give more degree of freedom when taking off and landing, because the thrust can be vectored at odd angles, other than 0 ° and 180 °. However, it was deemed that implementing a vector thrust mechanism would require a major re-design of the engine pylon and it would be relatively heavier compared to the variable pitch mechanism. The vector thrust mechanism is deemed relatively heavier, because although both systems require a system of actuator and a motor, for the vector thrust, the entire pylon needs to be more heavily reinforced to allow such movements. Therefore, the variable pitch mechanism was selected. As part of the variable pitch mechanism, a set of linear actuators and a small electric motor has been selected. To select the linear actuator, the load that it can handle should be larger than the total load from the thrust and the weight of the propellers, which resulted in 1080 lbf. MOOG's flight control surfaces linear actuator has a stall load of 3000 lbf, which is far greater than this, and merely weighs 8 lb, which is equal to 3.63 kg [36]. The power required for this linear actuator is given at 0.94 hp, which is 700.9 W. Therefore, an electric motor that is able to provide this much output is needed. Motion Dynamic's Dayton 800W Planetary Gear Motor is selected for this, for it's relatively light weight and its capability of running in both forward and reverse directions. However, it should be noted that the power of this electric motor is not included in the power budget presented in Table 17, as this power is required for an insignificant amount of time compared to the entire mission duration. The time required to move the actuators to change the pitch of the propellers is insignificant compared to the mission duration.

5.5.8 Fan Duct

As introduced in the MTR, the design choice has been made to include a duct around the propeller. The reasoning behind this is because the advantage coming from the increase in efficiency far outweighs the disadvantages coming from increased mass [11]. It is crucial in the design of the duct to have a clearance of 2 mm from the propellers [11].

5.5.9 Engine Mounting

Now that all of the components of the propulsion systems are designed and selected for, it is crucial to find a suitable mount for the engine on the airship as a whole. This is taken care in Section 5.11.3.

5.5.10 Propulsion Subsystem Mass, Power, and Cost Budget

In this section, the mass budget for all the components in the propulsion subsystem will be obtained. Some are simply obtained from the product descriptions as they are picked off the shelf, whilst others are obtained from material density and statistically obtained estimates.

Propeller blades: The propeller blade mass estimation comes from the diameter of the propeller given in Section 5.5.2 as 4.88 m. Given a blade area ratio of 0.35, as given in [31], the expanded blade area needs to be first determined by Equation 5.23. In Equation 5.23, EBA refers to the expanded blade area and BAR refers to the blade area ratio.

$$EBA = BAR \cdot \frac{\pi D^2}{4} \tag{5.23}$$

[36] URL: https://www.moog.com/content/dam/moog/literature/Space_Defense/spaceliterature/actuationmechanisms/Moog-ElectromechanicalActuators-Datasheet.pdf [Accessed on 12/06/2019]

The expanded blade area obtained from Equation 5.23 is 6.546 m^2. A value of the blade density, 5 kg/m^2 is multiplied to this value of expanded blade area to obtain the final mass estimation of the propeller blade of 32.73 kg [32].

The cost of the propeller blades was estimated by multiplying the material cost given in per kg. It was assumed that the blades would be made out of carbon fibers and therefore, the material cost of €100/kg was multiplied [37]. This results in the cost estimate of the propeller blades as € 3273 per propeller. It should be noted that as mentioned in the Section 6.1.2, the labor costs and manufacturing costs are not included in the cost estimate.

Electric Motor for Propulsion, Motor Controller, Gearbox, Linear Actuator, Electric Motor for Actuator, and Gearbox Housing: Most of these components are selected off the shelf and their mass is given in Table 17. It should be noted that Table 17 is only pertaining one set of propeller and therefore must be multiplied by 4 to obtain the full propulsion subsystem mass of these components. The mass of the gearbox housing is obtained from multiplying the volume of the material, which could be obtained from the dimensions given in the table, Table 16 and the thickness obtained in that section. The volume could be multiplied by the material density, which is assumed to be 2810 kg/m^3 since Aluminium 7075-T6 is used [38]. The power required from the electric motor is the same as the power required calculated in Section 5.5.2 and is 13.9 kW. The cost is obtained in a similar fashion as the mass, by multiplying the cost per kg, which is taken as € 1.94 /kg [39].

Table 17: Mass, power, and cost budget per propeller of off the shelf components in the propulsion subsystem.

Component	**Mass [kg]**	**Power [W]**	**Cost [EUR]**
Electric Motor for Propulsion	7	13908	3330
Motor Controller	5.8		2726
Gearbox	5	-	142
Linear Actuator	3.6	-	517
Electric Motor for Actuator	6.1	-	
Gearbox Housing	14.5	-	28
Total	27.5	13908	6743

Duct: The weight of the duct is obtained from a statistically determined factor that is multiplied by the power of the propeller. This factor is given as 0.45 [11]. The power required value per propeller of 13.9 kW which corresponds to 18.65 hp is multiplied with 0.45 and the final duct weight is obtained as 8.39 kg per propeller.

Taking carbon fiber as the material of the duct, again, the material cost of € 100 /kg is multiplied by the mass of the duct and a cost of € 839 per propeller is obtained[40].

Engine Pylon: the weight of the engine pylon is obtained from multiplying the material density to the volume of the engine pylon. This was designed in Section 5.11.3 and is given as 44 kg per propeller.

Taking Aluminium 7075-T6 as the material for the pylon, the material cost of € 1.94 /kg is multiplied to the total mass. Therefore, the total cost of € 85.36 per propeller is obtained for the engine pylon.

The total mass and cost budget of the entire propulsion subsystem, therefore including all four

[37] URL: https://www.reuters.com/article/sgl-fibres/cheaper-carbon-fibre-will-slash-auto-making-costs-manufacture
[Last accessed: 24/06/2019]

[38] URL: http://www.matweb.com/search/DataSheet.aspx?MatGUID=4f19a42be94546b686bbf43f79c51b7d [Last accessed: 24/06/2019]

[39] URL: https://markets.businessinsider.com/commodities/aluminum-price [Accested on 24/07/2019]

[40] URL: https://www.reuters.com/article/sgl-fibres/cheaper-carbon-fibre-will-slash-auto-making-costs-manufacture
[Last accessed: 24/06/2019]

propellers are presented in Table 18. Note that for this, all four propellers are included in the mass and cost budget.

Table 18: Total mass, power and cost budget of the propulsion system

Component	**Mass [kg]**	**Power [W]**	**Cost [k€]**
Blades	130.93	-	13.1
Electric Motor	28	55636	13.3
Motor Controller	23.2		10.9
Gearbox	20	-	0.6
Variable Pitch (actuator + motor)	58	-	2068
Gearbox Housing	58	-	0.1
Duct	33.56	-	3.4
Pylon	176	-	0.3
Total	528	55636	43.7

5.6 Attitude Determination & Control

In this section, the detailed design processes for Attitude Determination and Control are discussed. Firstly, a decision on tail configuration is presented. Next, several airfoils for tails are analyzed and compared using the software **XFLR5**, where the best performing airfoil is chosen. Finally, the tail sizing process is conducted.

5.6.1 Tail Configuration

In the MTR, the X tail was chosen over other tail configurations. This was due to its high performance in providing yawing and pitching moments that are needed to counteract the innate aerodynamic moment of the airship hull for stability and control of the airship. However, this configuration does not allow independent design of the horizontal and vertical tails as each of the inclined surfaces are supposed to provide both yawing and pitching moments.

In this mission, the airship increases its altitude using buoyancy. This implies that the airship does not need to pitch-up to climb, unlike conventional heavier-than-air aircraft. Also, as the mission altitude ranges only from 20km to 20.5km, agility in vertical movement is less of an importance. The relatively low nominal airspeeds of 21m/s and the high operating altitude also imply that the forces that can be created by the horizontal tails are not sufficient to overcome the innate pendulum stability of the airship. This is another reason why the airship cannot achieve the climb/descent by pitching up/down. Therefore, the size of the horizontal tail can be significantly reduced. For yawing stability (weathervane stability), the vertical tail is crucial and it has to be as big as possible, as long as the total tail weight stays below 1500 kg. However, the bigger the vertical tail, the more stable the airship becomes and the less maneuverable it becomes. With the horizontal tail being less imposing and vertical tail being more imposing, the conventional tail configuration allows the independent analysis of the vertical and horizontal tail. Therefore a huge reduction in weight from the horizontal tail can be achieved. Thus, the conventional tail configuration has been chosen for further design process as Figure 36 shows.

Figure 36: Tail Configuration

5.6.2 Airfoil Choice

For both the vertical and the horizontal tail, a symmetrical airfoil is used as cambered airfoils lead to unequal performance of tail for positive and negative angles of attack/sideslip angles. 22 symmetric NACA airfoils are compared using the software **XFLR5**. 9 NACA 4-Series airfoils are compared and the 3 best performing airfoils are selected as in Figure 37. 8 NACA 6-Series airfoils are analyzed and the 4 best performing airfoils are further investigated as in Figure 38. 5 NACA 16-Series airfoils are compared and the 3 best 16-Series airfoils are depicted in Figure 39.

Figure 39 shows that 3 NACA 16 airfoils are under performing when it comes to $\frac{C_l}{C_d}$ and C_l compared to NACA 4-Series and 6-Series in Figure 37 and Figure 38. Looking at the NACA 4-Series and NACA 6-Series airfoils, both of them have a maximum $\frac{C_l}{C_d}$ of around 120. Looking at the 2nd figure of Figure 37 and the 2nd figure of Figure 38, NACA 0012 and NACA 0015 show steeper slopes than every NACA 6-Series airfoil and this leads to higher C_l values from 0 degrees to 20 degrees (linear parts). Lastly, comparing NACA 0012 and NACA 0015, NACA 0012 shows better $\frac{C_l}{C_d}$ performance than NACA 0015 in the lower range of angle of attack (up to 13°). Therefore, NACA 0012 has been chosen for both the horizontal tail and vertical tail.

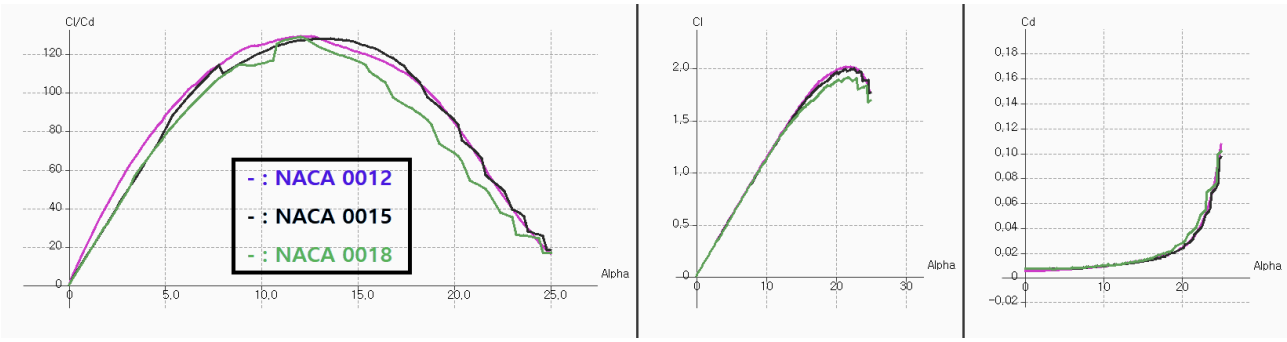

Figure 37: NACA 4-Series airfoil performance comparison

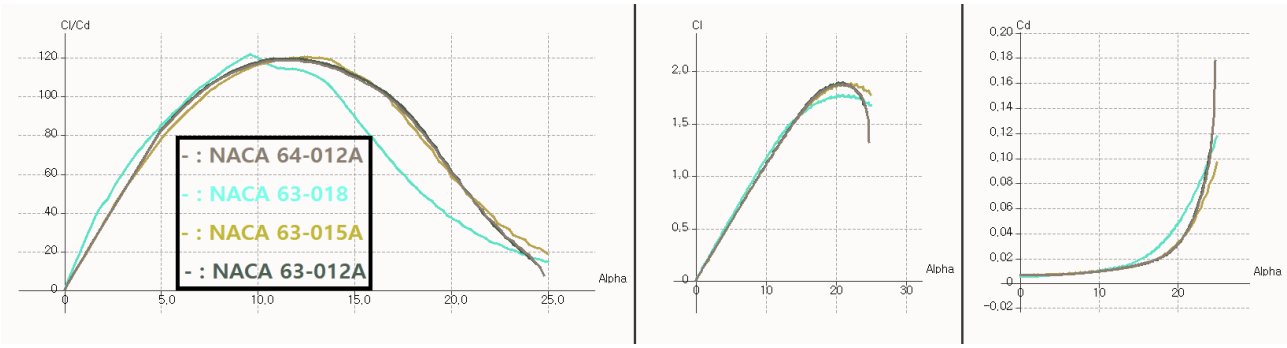

Figure 38: NACA 6-Series airfoil performance comparison

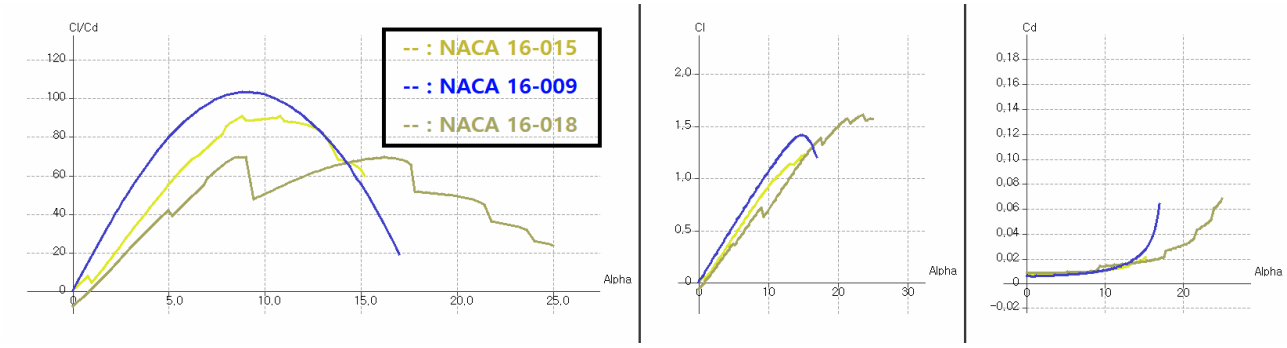

Figure 39: NACA 16-Series airfoil performance comparison

5.6.3 Tail Location

Tail sizing starts with the preliminary sizing using historical data. Figure 40 shows the historical data correlating C_{HT} and C_{VT} with the envelope volume[41]. By using the envelope volume in Table 19, two tail volume coefficients (C_{HT} and C_{VT}) can be obtained to be 0.07 and 0.063, respectively.

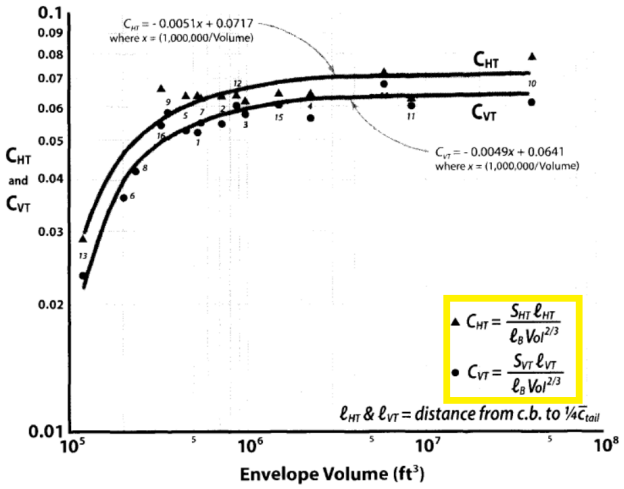

Figure 40: Preliminary Tail Sizing [9]

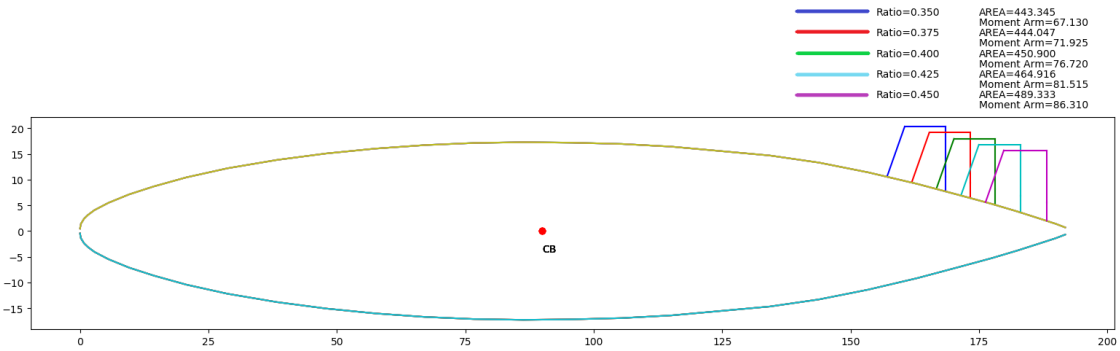

Figure 41: Tail Location

$$S_{HT} = \frac{C_{HT} \times l_B \times Vol^{\frac{2}{3}}}{l_{HT}} \qquad (5.24) \qquad\qquad S_{VT} = \frac{C_{VT} \times l_B \times Vol^{\frac{2}{3}}}{l_{VT}} \qquad (5.25)$$

Most of airships have moment arms (l_{VT} and l_{HT}) ranging between 35-45 percent of body length [9]. Using this information, tail location can be further optimized. Ratio on the top right corner of Figure 41 represents how far the tail is from the center of buoyancy compared to the airship body length. As this ratio changes from 0.35 to 0.45, the location of the tail changes and thereby the moment arms (l_{VT} and l_{HT}) change. For each value of the moment arms, S_{HT} and S_{VT} can be obtained using Equation 5.24 and Equation 5.25. By taking into account the hull shape at each tail location and deducting unexposed (hidden) tail area from the obtained S_{HT} and S_{VT}, the exposed tail area (**AREA**) on the top right corner of Figure 41 can be calculated. This includes both vertical and horizontal tail areas. It can be seen that the tail exposed area and the moment arm increase as the tail is positioned farther away from the center of buoyancy. Having bigger moment arms is

[41]Envelope volume must be in ft^3 to use the relation in Table 19. This is why Envelope Volume is given in ft^3 in Table 19

beneficial as the tails can create bigger moments but the area of the tails also increases which increases the weight of the tails and thereby the airship weight. For the tails to create enough moment but to keep the weight below 1500 kg, the ratio is chosen to be 0.42. For this ratio, the corresponding value of the moment arms (l_{VT} and l_{HT}) are 80.56 m, respectively. Using Equations 5.24 and 5.25, with the obtained coefficients, the moment arms (l_{HT} and l_{VT}), body length (l_B), and Volume (Vol)[42], the horizontal and vertical tail areas can be obtained. These result are obtained to be 380.35 and 339.55 m^3, respectively. S_{Final} is obtained to be 359.95 m^2, by averaging S_{HT} and S_{VT}. This averaging process is performed to decrease the horizontal tail size and to increase the vertical tail size as having the big horizontal tail is not necessary, as it was explained previously in Section: Tail Configuration. It is important to note that S_{VT}, S_{HT} and S_{Final} include not only the exposed tail area but also the unexposed tail area inside the hull.

Figure 42 shows the tail design for this tail location assuming an AR of 2 and a taper ratio of 0.7. The root chord (C_R) is 11.6 m, the tip chord (C_T) is 8.1 m and the wing span is 19.7 m.

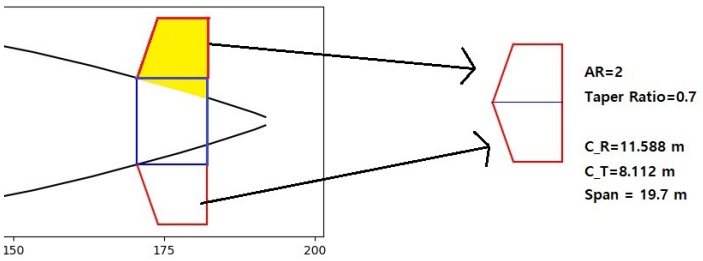

Figure 42: Tail Sizing

Table 19: Values for preliminary tail sizing

	Value	Unit
Envelope Volume	3819987.5	ft^3
$\boldsymbol{l_B}$	191.8	m
$\boldsymbol{l_{HT}}$	80.56	m
$\boldsymbol{l_{VT}}$	80.56	m
$\boldsymbol{C_{HT}}$	0.070	-
$\boldsymbol{C_{VT}}$	0.063	-
$\boldsymbol{S_{HT}}$	380.4	m^2
$\boldsymbol{S_{HT}}$	339.6	m^2
$\boldsymbol{S_{Final}}$	360	m^2

Table 20: Aerodynamics of Hull

α,$-\beta$	$(C_m)_H$,$(C_n)_H$	$(C_L)_H$,$(C_Y)_H$
0 deg	0	0
2 deg	0.002	0.009
5 deg	0.005	0.022
10 deg	0.011	0.045
15 deg	0.020	0.080
20 deg	0.024	0.097
25 deg	0.031	0.122
$(C_{m_{\hat{q}}})_H$,$(C_{m_{\hat{r}}})_H$	-0.073	
$(C_{m_{\hat{q}}})_H$,$(C_{m_{\hat{r}}})_H$	0.024	

5.6.4 Parametric Tail Sizing

The tail sizing can be further refined by estimating the aerodynamic influences of the geometry of the tail surface. The parameters used are listed in Table 21a. They are for a pair of opposite-sided tail surfaces, including the hidden area inside the hull, so that it acts as a full wing span. It is important to note that the tail span and the tail aspect ratio are for full span tails including the hidden area. For horizontal tails, the dihedral angle is 0° while for vertical tails, it is 90°.

Table 21b shows the factors that take into account tail-body interference (η) and control surface effectiveness (τ). These parameters (Table 21a) and factors (Table 21b) can be used to obtain coefficients for tail stability and controllability using Equation 12.1. Equation 12.1 can be seen in Appendix.
The first row of Equation 12.1 is for calculating tail lift curve slope and aspect ratio of the tail. The second, third and fourth rows of Equation 12.1 are for lateral stability and control coefficients while the fifth, sixth and seventh rows of Equation 12.1 are for longitudinal stability and control coefficients. The results are shown in Table 21c.

[42]This time, the volume must be in m^3 as other values are given in SI units.

The tail surface contribution (represented by the obtained coefficients Table 21c) should be combined with the aerodynamic contribution of the hull, which is given in Table 20.

The linearized equations for calculating yawing and pitching moment coefficients (C_n, C_m) and Y, Z force coefficients (C_Y, C_L) are shown in Equation 5.26. The coefficients vary for different sideslip angle (β), angle of attack (α), rudder deflection (δ_r) and elevator deflection (δ_e).

(a) Tail Parameters

	Symbol	Value
Number of tail pairs	N	1
Exposed tail area	S_T	230.68
Total tail area	$S_{T_{total}}$	359.95
Tail moment arm c.b. to tail c/4	l_T	84.68
Tail moment arm c.b. to hinge line	l_{T_δ}	89.66
Tail span	b_T	34.016
Tail aspect ratio	AR_T	3.21
Tail sweep angle at maximum thickness (radian)	Δ	0.34
Tail lift curve slope (per radian)	$(C_{L_\alpha})_{tail}$	3.39
Tail dihedral angle (degree)	Γ	0/90
Reference volume	Vol	108170
Length of body	l_B	191.8
Vertical offset c.g. to c.b.	Γz_{cg}	6.668
Air density at 20 km	ρ	0.089

(b) List of Factors

	Symbol	Value
Tail Moment Interference Factor	η_M	0.4
Tail Force Interference Factor	η_F	0.5
Control Surface Moment Interference Factor	η_{M_δ}	0.9
Control Surface Force Interference Factor	η_{F_δ}	1.0
Control Surface Effectiveness Factor	τ	0.5

(c) Results

$(C_{n_\beta})_T$	0.095	$(C_{m_\alpha})_T$	-0.095
$(C_{Y_\beta})_T$	-0.269	$(C_{L_\alpha})_T$	0.269
$(C_{n_{\hat{r}}})_T$	-0.422	$(C_{m_{\hat{q}}})_T$	-0.422
$(C_{Y_{\hat{r}}})_T$	0.956	$(C_{L_{\hat{q}}})_T$	0.956
$(C_{n_{\delta_r}})_T$	0.102	$(C_{m_{\delta_e}})_T$	0.102
$(C_{Y_{\delta_r}})_T$	-0.241	$(C_{L_{\delta_e}})_T$	-0.241

$$\begin{aligned} C_n &= (C_n)_H + \left(C_{n_\beta}\right)_T \beta + \left(C_{n_{\delta_r}}\right)_T \delta r & C_m &= (C_m)_H + (C_{m_\alpha})_T \alpha + \left(C_{m_{\delta_e}}\right)_T \delta e \\ C_{n_{\hat{r}}} &= (C_{n_{\hat{r}}})_H + (C_{n_{\hat{r}}})_T & C_{m_{\hat{q}}} &= \left(C_{m_{\hat{q}}}\right)_H + \left(C_{m_{\hat{q}}}\right)_T \\ C_Y &= (C_Y)_H + \left(C_{Y_\beta}\right)_T \beta + \left(C_{Y_{\delta_r}}\right)_T \delta r & C_L &= (C_L)_H + (C_{L_\alpha})_T \alpha + \left(C_{L_{\delta_e}}\right)_T \delta e \\ C_{Y_{\hat{r}}} &= (C_{Y_{\hat{r}}})_H + (C_{n_{\hat{r}}})_T & C_{L_{\hat{q}}} &= \left(C_{L_{\hat{q}}}\right)_H + \left(C_{L_{\hat{q}}}\right)_T \end{aligned} \tag{5.26}$$

For the parametric tail sizing, the coordinate system used is as follows: X-axis goes through the nose, Z-axis points to the nadir direction and Y points to the right when the airship is seen from the back.

5.6.5 Lateral-Directional Stability and Control

The lateral-directional stability of the airship is governed by the combination of lateral and directional motion. Lateral motion is a translation in Y and directional motion is a rotation around Z. When the airship translates sideways, the resulting sideslip causes the vertical stabilizer to create a lateral force in the opposite direction of the original translation which decreases the disturbance over time. Also, the force created by the vertical stabilizer creates a counteracting moment that cancels out the moment created by the hull experiencing the sideslip. This phenomenon is called 'weathervane" stability. The lateral and directional motions are both affected by the sideslip and the yaw rate.

$$\dot{r} \approx \frac{N}{I_z} = \frac{\left(C_n + C_{n_{\hat{r}}}\hat{r}\right) q_{dyn} Vol^{2/3} l_B}{I_z} = 0 \tag{5.27}$$

$$\dot{\beta} \approx \frac{\dot{v}}{V_\infty} = \frac{\frac{Y}{m} - V_\infty r}{V_\infty} = \frac{\left(C_Y + C_{Y_{\hat{r}}}\hat{r}\right) q_{dyn} Vol^{2/3}}{m V_\infty} - r = 0 \tag{5.28}$$

Equations 5.27 and 5.28 show that the conditions for a steady state occur when yaw rate and $\dot{\beta}$ are constant. The yaw moment (N) can be described with the static N coefficient, which is a function of β and δ_r (Equation 5.26), and the dynamic yaw moment yaw rate derivative ($C_{n_{\hat{r}}}$). The sideslip angle rate can be simplified as the ratio of sideslip acceleration ($\dot{v}$) and the true windspeed (V_∞). The $\dot{v}$ is a combination of the side force divided by the mass and the Coriolis term (V_∞r) caused due to the rotation of the body axis relative to the inertial axis.

$$\begin{aligned} C_n &= -C_{n_{\hat{r}}}\hat{r} \\ C_Y &= \frac{m V_\infty r}{q_{dyn} Vol^{\frac{2}{3}}} - C_{Y_{\hat{r}}}\hat{r} \\ \frac{C_n}{C_Y} &= \frac{-C_{n_{\hat{r}}}}{\frac{2m}{\rho Vol} - C_{Y_{\hat{r}}}} \\ \frac{C_n}{C_Y} &= \frac{-C_{n_{\hat{r}}}}{2 - C_{Y_{\hat{r}}}} \end{aligned} \tag{5.29}$$

Equation 5.29 derives the steady state turn condition from Equations 5.27 and 5.28. With a ratio $\frac{C_N}{C_Y}$, the critical line for steady-state turn condition can be obtained. $\frac{C_N}{C_Y}$ is further simplified for a neutrally buoyant airship, with the mass equal to the mass of the displaced air ($m = \rho \times Vol$).

5.6.6 Longitudinal Stability and Control

The longitudinal stability of the airship is governed by the combination of vertical translation and pitching motion. The vertical motion is a translation in Z and pitching motion is a rotation around Y.

The longitudinal analysis is similar to the lateral-directional analysis. When the airship translates vertically, the resulting angle of attack causes the horizontal stabilizer to create the vertical force in the opposite direction of the original translation. Also, the force created by the horizontal stabilizer creates counteracting moment that cancel out the moment created by the hull that increases the pitch up moment or pitch down moment. However, for the longitudinal analysis, pendulum effect must be taken into account. The pendulum effect occurs due to the offset between the center of gravity and the center of buoyancy. When the airship pitches up, the buoyant force acts vertically on the center of buoyancy which creates the counteracting moment that makes the airship pitch down. For the situation of the airship pitching down, the buoyant force again creates the pitching up moment which stabilizes the airship.

$$\dot{q} \approx \frac{M}{I_y} = \frac{\left(C_m + C_{m_{\hat{q}}}\hat{q}\right) q_{dyn} Vol^{2/3} l_B - \Delta z_{cg} \rho g \,\mathrm{Vol} \sin\theta}{I_y} = 0 \tag{5.30}$$

$$\dot{\alpha} \approx \frac{\dot{w}}{V_\infty} = \frac{\frac{-L_{aero} + F_g - L_{buoy}}{m} + V_\infty q}{V_\infty} = \frac{-\left(C_L + C_{L_{\hat{q}}}\hat{q}\right) q_{dyn} Vol^{2/3} + (m - \rho Vol) g}{m V_\infty} + q = 0 \tag{5.31}$$

Equations 5.30 and 5.31 show that the conditions for a steady state pitch of the airship are, pitch rate and angle of attack being constant. The pitch moment (M) can be described with the static yaw moment coefficient which is a function of the α and δ_e (Equation 5.26), and the dynamic pitch moment pitch rate derivative ($C_{m_{\hat{q}}}$). On top of that, the aforementioned pendulum effect must be taken into account. The $\dot{\alpha}$ can be simplified as the ratio of vertical acceleration ($\dot{w}$) and the true windspeed (V_∞). The vertical acceleration is a combination of the sum of vertical forces (L_{aero},F_g,L_{buoy}) divided by the mass and the Coriolis term ($V_\infty q$) caused due to the rotation of the body axis relative to the inertial axis.

$$C_m = \frac{\Delta z_{cg} \rho g \,\mathrm{Vol}^{1/3} \sin\theta}{q_{dyn} l_B} - C_{m_{\hat{q}}}\hat{q} \tag{5.32}$$

$$C_L = \frac{qmV_\infty + (m - \rho\,\mathrm{Vol})g}{q_{dyn} Vol^{2/3}} - C_{L_{\hat{q}}}\hat{q} \tag{5.33}$$

Equations 5.32 and 5.33 lead to the steady state pitch condition from Equation 5.30 and Equation 5.31. With $\frac{C_m}{C_L}$, the critical line for steady-state pitch condition can be obtained.

5.6.7 Results of Parametric Tail Sizing

Figure 43 and Figure 44 show the results of the parametric tail sizing. Figure 43 shows the performance of the vertical tails and Figure 44 shows the performance of the horizontal tails. For Figure 43, blue lines represent C_N and C_Y for different values of β and δ_r that were obtained using Equation 5.26. The middle blue line represents the case with $\delta_r = 0$. The top two blue lines represent the case where the airship is yawing in the positive direction for turning right with the rudder deflected in such a way that it is aiding the turning process by creating the positive yawing moment. This can be witnessed with the increased yawing moment coefficient, C_N. The bottom two lines are for the case where the airship tries to recover its attitude towards the wind direction (weathervane stability) by deflecting its rudder, creating negative yawing moment. This can be witnessed by the decreased C_N and the increased C_Y. The red line represents the critical line, on which the airship can achieve steady state turning. This maximum achievable turn rate is indicated with the green dot on Figure 43 with the value $2.18°/s$ for $\delta_r = 30$. For this maximum turning rate, the β would settle around -23°. To clarify,

if the airship is in the unstable region with $\delta_r = 30$ (the top blue graph) from -0 to -22 of β, then the β angle will decrease to -23 degree. On the other hand, if the β is smaller than -23 degree (-24, -25 degree), the airship will increase its β angle to -23 degree. As the middle and the top bottom blue graphs are below the critical line (in the stable region), the airship has enough control power to return to $\beta = 0$ in all cases.

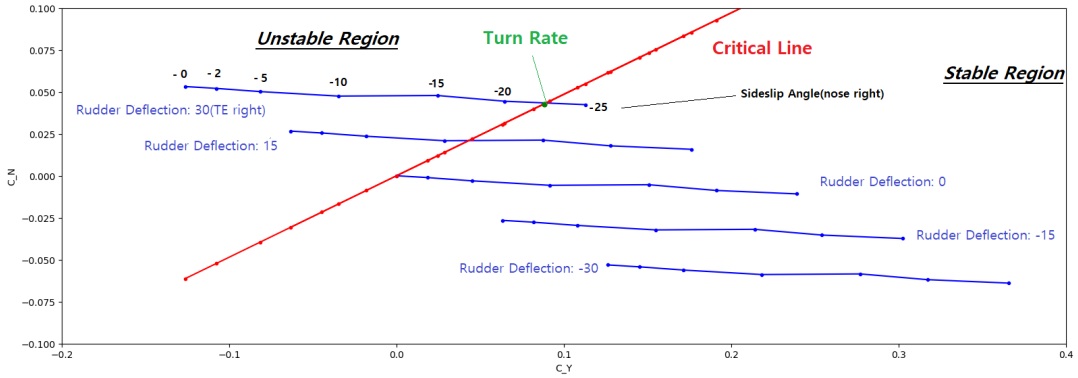

Figure 43: Results of parametric tail sizing for Vertical Tail

The middle graph shows that the airship can return to $\beta = 0$ in any situation, even with $\delta_r = 0$. This fact can be used to decrease the size of the vertical tail and make use of the natural directional instability of the airship to achieve a higher turning rate[43]. However, as the airship must be as stable as possible for accurate pointing of the TIR imaging camera and can be less agile, the vertical tail size can be left as it is.

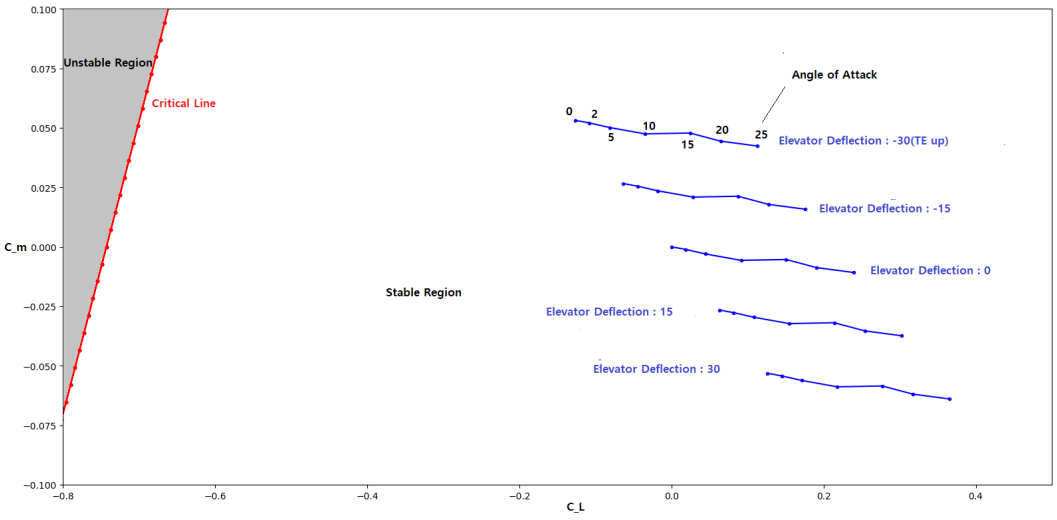

Figure 44: Results of parametric tail sizing for Horizontal tail

Figure 44 works exactly same as Figure 43. The critical line is shown in red with the top region being unstable region and the bottom region being stable region. The top two blue lines belong to the cases where the elevator is deflected upwards (seen from the back of the airship). The bottom two blue lines belong to the cases where the elevator is deflected downwards. In all cases, the blue lines are below the critical line with a very big margin and this shows that the airship is very stable in longitudinal direction due to the pendulum stability. The horizontal tail is solely for stability. As mentioned previously, this is why the horizontal size can be decreased from its original size. To meet the weight requirement, the new horizontal tail is shown in Figure 45.

[43] the bigger the vertical stabilizer (tail), the less maneuverable the airship becomes and the more stable it becomes.

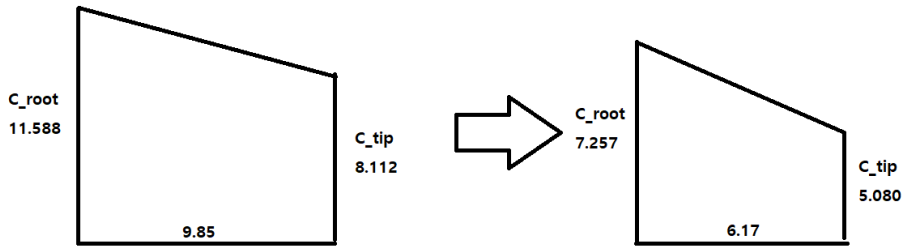

Figure 45: New Horizontal Tail Sizing

5.6.8 Attitude Determination

Determining altitude accurately is crucial for the airship to navigate but also for the successful operation of the TIR imaging payload. For the TIR camera and the airship, the required pointing accuracy is 5 arcsec (SB-Subs-ADCS-03), while the pointing stability needs to be within 1 arcsec (SB-Subs-ADCS-04).

To meet the requirement, several different sensors were investigated, such as: sun sensors, horizon sensors and star sensors. Due to the strict accuracy requirement, among many different sensor types, star sensor is the only possible option [33]. However, at 20km altitude, the star sensor cannot be used during the day time as sun light can interfere with star detection and therefore make measurements inaccurate and noisy. In order to tackle this technological challenge, new star sensors have been proposed, specifically for high altitude airships and for all day operation [25, 34]. Currently, other companies are also developing (or have already made available) daytime star sensors[44] [45]. Two star sensors are needed for correct 3D attitude determination.

In addition to the two daytime star trackers, other types of sensors are needed as star trackers cannot operate at all times due to the sun exclusion angle. Also, measurement frequencies of the star sensors are limited, so other sensors have to provide accurate measurements in between two star tracker measurements [33]. Gyroscopes (IMU) or GNSS (Global Navigation Satellite System) can be used for this. GNSS receivers are a good option as it is already going to be used for general navigation of the airship and placing them with sufficient separation provides sufficient accuracy, especially for large vehicles [33]. By using the high precision Galileo service it is possible to obtain the position with a precision of less than 20 cm[46]. Gyroscopes[47] are also needed to provide an inertial measurement in absence of star tracker data, as described in Section 5.4.

5.6.9 Mass, Cost and Power budget for ADCS subsystem

Table 22: Mass Budget for ADCS subsystem

	Value	Number	Total	Unit
Vertical Tail	340.25	2	680.5	kg
Horizontal Tail	146	2	292	kg
GPS	0.108	2	0.2155	kg
Gyro	0.7	2	1.4	kg
Star Sensor	31.8	3	95.4	kg
		Total	1069.5	kg

Table 23: Power Budget for ADCS

	Value	Number	Total	Unit
Vertical Tail	-	2	-	W
Horizontal Tail	-	2	-	W
GPS	1.4	2	2.8	W
Gyro	8	2	16	W
Star Sensor	89.1	3	267.3	W
		Total	286.1	W

[44]URL: `https://www.ball.com/aerospace/markets-capabilities/capabilities/technologies-components/star-trackers` [Accessed on 22/05/2019]

[45]URL: `http://www.trexenterprises.com/Pages/Products%20and%20Services/Sensors/opticalgps.html` [Accessed on 22/05/2019]

[46]URL: `https://gisuser.com/2019/05/galileo-gnss-starts-high-accuracy-service-in-2019/` [Accessed on 24/06/2019]

[47]URL: `https://www.althensensors.com/sensors/gyroscope-sensors/high-precision-gyroscopes/4685/crh02-gyroscope/?` [Accessed on 23/06/2019]

Table 24: Cost Budget for ADCS

	Value	Number	Total	Unit
Vertical Tail	37427.5	2	74855	€
Horizontal Tail	16060	2	32120	€
GPS	365	2	730	€
Gyro	7160	2	14320	€
Star Sensor	20000	3	60000	€
		Total	182025	€

Table 22, Table 23 and Table 24 show the budgets for the mass, power and cost of the ADCS subsystem, respectively. The mass of the tails have been estimated in Table 34. Material property sheet from MIT[48] provides cost estimate for CFRP laminate (graphite) of 110 $\frac{\$}{m^2}$. By multiplying the areas of the tails obtained, the cost of the vertical tail and horizontal tail can be estimated. For GPS and Gyroscopes, products of similar applications have been used for estimations as data regarding the chosen sensors were not available. For the gyroscopes' power and mass estimation, KVH's IMU 1750 has been used. For their cost estimation, a quote for the chosen product has been obtained from the company Althen directly. For the GPS receivers' mass, power and cost, TN72 GPS Receiver has been used as a reference product. Most importantly, for the star sensors' mass, power and cost, DayStar Critical Design Review presentation [25] have been used.

5.7 Power

The main requirements imposed on the electrical power subsystem driving the design are the generation, distribution and storage of electrical energy. The main components of the subsystem are the electrical generation unit, storage and power management unit. Deriving from the mission profile, the airship's power subsystem shall provide enough energy for nominal continuous operation according to the power budget.

This chapter starts with a description of the energy generation environment and conditions, followed by the methodology for the selection of appropriate optimal technologies and eventual designing.

5.7.1 Solar environment

Conducive to designing the solar power generation unit, the apparent movement of the Sun as seen from Earth has been studied by means of using a solar model developed by the National Oceanic & Atmospheric Administration[49]. The model contains solar elevation (θ) measured up from the local horizon and azimuth angle (γ) measured from North as functions of latitude, longitude, time of the year and of the day. These are shown in Figure 46 and Figure 47[50]. It has been established that the solar conditions vary significantly, having their extremes on the 22^{nd} day of December and June.

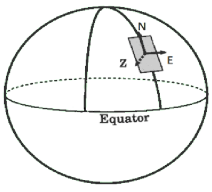

Figure 46: Local horizon coordinate frame

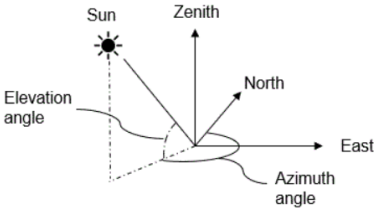

Figure 47: Local horizon solar angles

The model indicates the relevant angles as observed from Earth's surface. To include the effect of altitude onto these, the dip angle shown in Figure 48 is computed according to Equation 5.34:

[48] http://web.mit.edu/course/3/3.11/www/modules/props.pdf
[49] URL:`https://www.esrl.noaa.gov/gmd/grad/solcalc/calcdetails.html` [Accessed on 14/06/2019]
[50] URL:`https://keisan.casio.com/exec/system/1224682331` [Accessed on 20/06/2019]

$$\Omega = cos^{-1}(\frac{R}{R+h}), \tag{5.34}$$

where R is the Earth's radius and h is the design altitude. For the mission concerned, the dip angle equals 4.65 degrees. Implementing this angle into further calculations, airship daylight time is declared as the time interval in which the solar elevation is bigger than -4.65 degrees, as opposed to 0 for Earth's surface daylight. This is applicable under the assumption that the Sun can be modelled as a point source of energy and that it is sufficiently far away.

Figure 49 quantifies the effect of atmospheric attenuation on the perceived solar irradiance as a function of geometric altitude and solar elevation angle. For the two extreme cases, their respective solar flux densities are corrected for atmospheric attenuation based on the elevation angle temporal average during daylight. On the winter solstice, the temporal average of the solar elevation angle is about 9°. For an altitude of 21 km (denoted with the red line in the figure), this would point to a solar flux density of approximately 100 W/ft^2 out of a total of 126 W/ft^2. Using the ratio of the two, the solar flux density is expected to be as low as $\frac{100}{126} * 1312 = 1041 W/m^2$, $1312 W/m^2$ being the winter solstice value for a 90° solar elevation angle. Analogously, on the summer solstice, when the average elevation angle is 34° and the solar irradiance is $1404 W/m^2$, the value becomes $\approx \frac{115}{126} * 1404 = 1281 W/m^2$ [3].

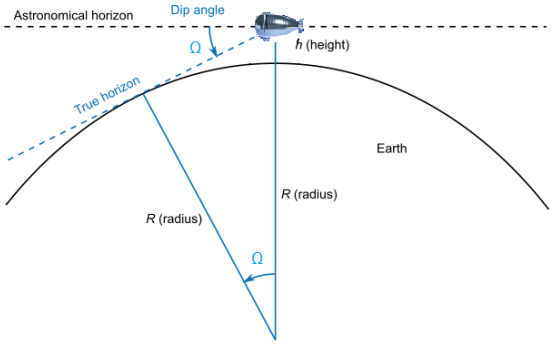

Figure 48: Dip angle of the horizon

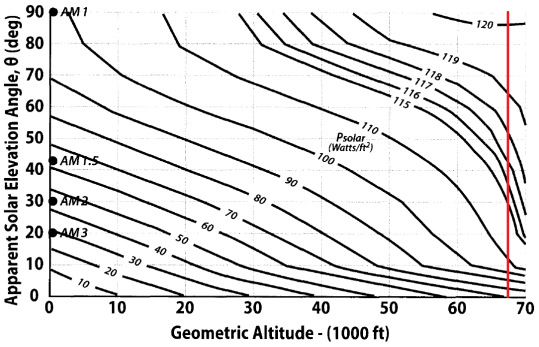

Figure 49: Solar constant as function of altitude and solar elevation angle [9]

5.7.2 Surface incidence model

Given the complex case of accurately designing for a solar array attached to a double-curved surface immersed in a three-dimensional Sun vector environment, a surface incidence model was needed to predict power generation behaviour for such an application and provide support for an optimization algorithm.

As a starting point for a MATLAB script, the surface of the airship has been simplified to an ellipsoid reflecting the same dimensions. As a means of verifying the resemblance of the mesh to the actual shape, the length, diameter and surface area of the two have been compared. The surface has been discretized into 16384 patches of area, 128 elements both in radial and longitudinal direction.

In order to determine the incidence angle on each patch element, the two relevant sets of vectors, surface normals and the Sun position vectors at each point in time are computed. The Sun vector $\vec{S}$ can be expressed in airship coordinate frame unit vectors as per Equation 5.35, assuming nominal operational conditions with no pitch or roll angle:

$$\vec{S} = \begin{bmatrix} cos(\theta) * cos(\pi/2 + \beta - \gamma) \\ sin(\theta) \\ cos(\theta) * sin(\pi/2 + \beta - \gamma) \end{bmatrix} \cdot \begin{bmatrix} \vec{i} \\ \vec{j} \\ \vec{k} \end{bmatrix}, \tag{5.35}$$

where $\vec{i}$,$\vec{j}$ and $\vec{k}$ are the unit vectors of the body-fixed airship reference frame and β is the yaw angle of the airship in a vehicle-carried normal Earth reference frame, set to 0 for Northern orientation and

ranging from $-\pi$ to π, positive Eastward, as shown on Figure 50. For subsequent analysis, given the predominant zonal winds in the stratosphere whilst aiming for drag minimization, β is set to $\pi/2$ or $-\pi/2$. Similarly, the yaw angle can be adjusted to assess the incidence of the Sun rays on the airship whenever the mission profile dictates an off-nominal orientation, for instance, when relocating in a North-South direction.

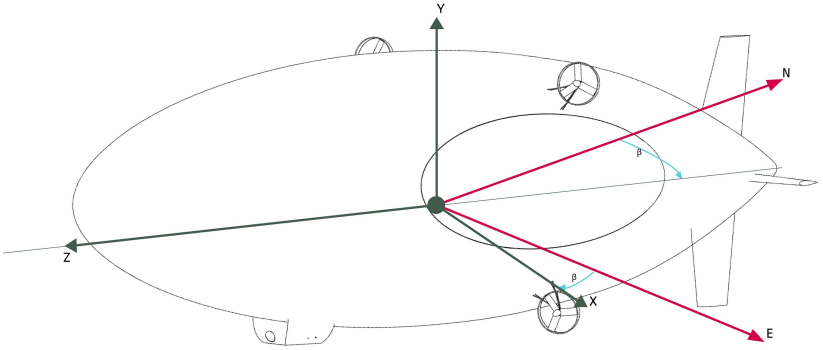

Figure 50: Ellipsoidal coordinate frame

The following steps are undertaken for the computation of the surface patch normals. For a quadrilateral with vertices ABCD expressed in Cartesian coordinates, the surface normal vector $\vec{n}$ is computed via the cross product expressed in Equation 5.36:

$$\vec{n} = \vec{AB} \times \vec{AD}, \tag{5.36}$$

$$\vec{AB} = \begin{bmatrix} x_B \\ y_B \\ z_B \end{bmatrix} - \begin{bmatrix} x_A \\ y_A \\ z_A \end{bmatrix} \tag{5.37}$$

$\vec{AD}$ is obtained analogously to $\vec{AB}$ in Equation 5.37. Computing these vectors for all the relevant points in time and for the entire discretized surface allows for the computation of the incidence angle α via Equation 5.38, with the necessary numerical conditions implemented for a 4 quadrant arctangent (atan2d):

$$\alpha = arctan \frac{norm(\vec{n} \times \vec{S})}{\vec{n} \cdot \vec{S}} \tag{5.38}$$

For the numerical simulation, at a certain instant, only polygons satisfying $\alpha < \frac{\pi}{2}$ are receiving solar flux. Further on, the polygon area has been computed according to Equation 5.39:

$$A_{patch} = \|\vec{n}\| \tag{5.39}$$

The instantaneous patch power generation can be expressed as per Equation 5.39. The condition is set such that only polygons that are expected to have incident sunlight are producing power. This is applicable for a convex body (adjacent surface does not block sunlight).

$$P_{patch} = \begin{cases} Q_{Sun} * A_{patch} * \eta_{solararray} * cos\alpha, & \text{if } \alpha < \frac{\pi}{2} \\ 0, & \text{otherwise} \end{cases} \tag{5.40}$$

5.7.3 Solar array design

In this section, the solar array placement optimization steps are presented, as well as the considerations for fulfiling the requirements set for the power generation capacity and a listing of possible configurations.

In order to optimize the solar cell placement for a specific time of the year, the array shall be positioned such that the most productive areas on the envelope on a specific day are used for power generation. In practice, this implies selecting the surface patches that collect the most energy per day and placing as many solar cells in those locations as it takes, up until the daily energy requirement generation is met. In this context, since the array's power output is not constant as the instantaneous energy requirement dictates, the energy storage unit shall balance out the fluctuations by storing or accessing reserve energy when needed. The daily energy required for uninterrupted airship operation is calculated in Equation 5.41:

$$Q_{day} = \frac{P_{day}}{\eta_{day}} * t_{daylight} + \frac{P_{night}}{\eta_{night} * \eta_{electrolyzer}} * t_{night}, \tag{5.41}$$

where P_{day} and P_{night} are the power consumptions during the day and at night respectively, η for day and night stand for transmission efficiency, t stands for the time duration the airship is immersed in sunlight or eclipse during an Earth day and $\eta_{electrolyzer}$ is the efficiency of the electrolyzer used for energy storage, set to 75%[51].

Since there is a tendency of decreasing efficiency as the number of occupied cells increase, the most performant surface patches are limited in number. This raises the question whether having a more efficient but heavier solar cell technology is better in terms of mass and cost while still meeting the same requirements (installing Gallium Arsenide (GaAs) instead of Amorphous Silicon (a-Si) as selected in the MTR). This argument can be settled numerically in the simulation.

The polygon element daily energy production in Joules is plotted on the colorbar in Figure 51, depicting the winter and summer solstice in the Northern hemisphere case. It assumes the entire envelope surface is covered with a-Si solar cells and uses a coarse meshing for better visual representation.

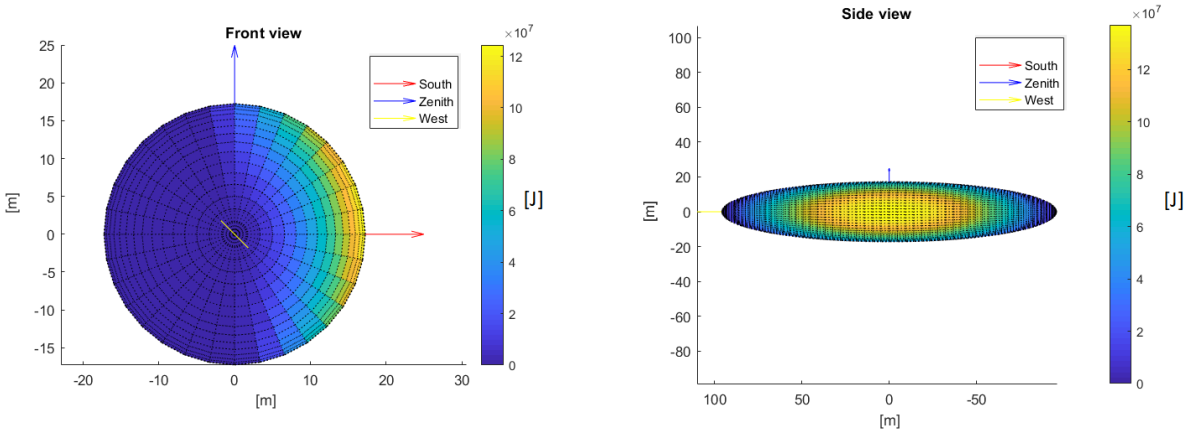

Figure 51: Patch energy production on 22 Dec

[51] URL:https://www.sintef.no/globalassets/project/novel/pdf/2-4_nrckurchatov_fateev_public.pdf [Accessed on 8/06/2019]

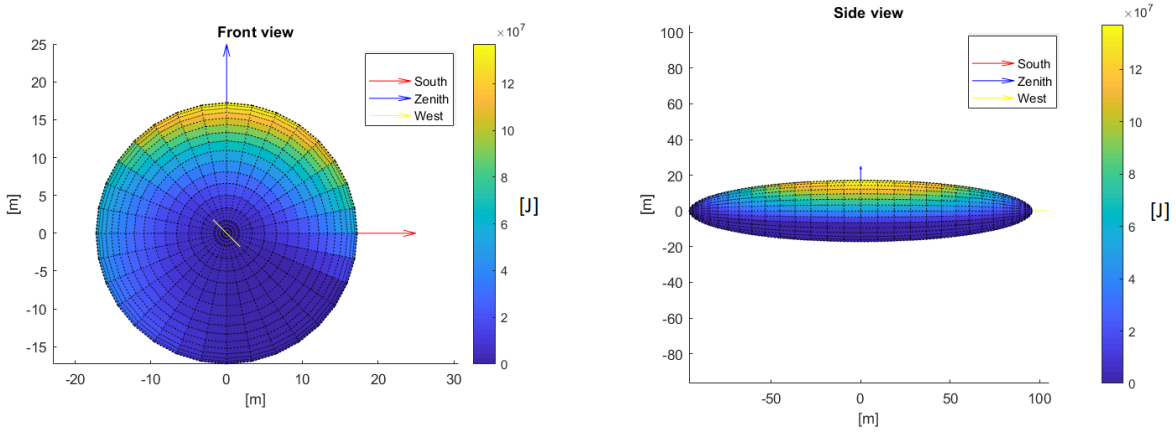

Figure 52: Patch energy production on 22 Jun

As expected, since the azimuth angle range of the exerted Sun vector throughout the duration of a day is symmetrical about the xy plane, the most daily energy can be harvested from solar panels attached to the surface in the middle of the airship longitudinally ($z = 0$). In winter, only the Southern side of the airship receives sunlight. This is opposed to the summer case where both sides receive solar radiation, although still preponderantly on the Southern side. To locate and express the location of the concerned surface patches, their centerpoints are translated into ellipsoidal coordinates (λ for longitude and ϕ for latitude) as shown in Figure 53[52]. Equation 5.42 and Equation 5.43 are used in that sense, in which a and b stand for the semi- major and minor axes of the ellipsoid. Although such an optimization algorithm would imply placing more solar panels on one side of the balloon, this is avoided to prevent a sideways c.g. shift. For that reason, solar cells are mirrored over the yz plane. This also allows for turning the balloon 180° and producing the same amount of power, which is useful given the expected wind profile.

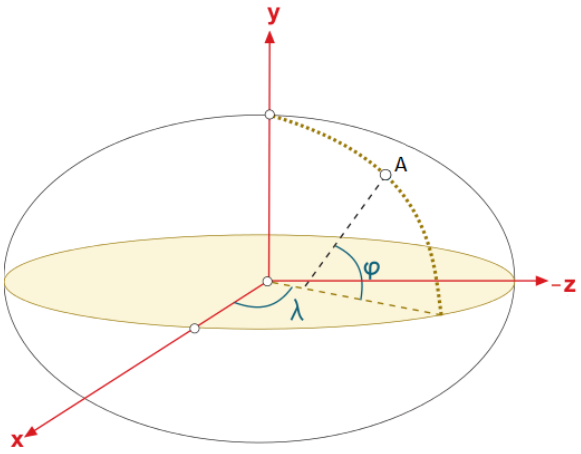

Figure 53: Ellipsoidal coordinate frame

$$\lambda = arctan\frac{y}{x} \tag{5.42}$$

$$\phi = arctan\frac{z}{(1-e^2) * \sqrt{x^2+y^2}} \tag{5.43}$$

$$e = \frac{a^2-b^2}{a^2} \tag{5.44}$$

[52]URL:https://gssc.esa.int/navipedia/index.php/Ellipsoidal_and_Cartesian_Coordinates_Conversion [Accessed on 12/06/2019]

As part of the final iteration, for a design power of 68 kW and 65 kW for night- and daytime as per Table 46, the following solar cell placement yields the lightest and cheapest solar array design for the winter solstice, shown in Figure 54 in blue, the most critical day expected during the year. At this level of accuracy, a-Si outperforms GaAs cell type. The solar array shape may be approximated as an ellipsoid centered at $\lambda = 9°$ and $\phi = 0°$, and having a semi-major and semi-minor axis lengths of $50m$ and $10m$ respectively. Having a $120g/m^2$ energy density for a 12% efficient thin film a-Si solar cell + Kapton substrate [1] and a yearly ageing degradation of 4% [33] in combination with a design life of 2 years, the array mass is approximately 504 kg and the surface area is $4198m^2$. Considering a price of 0.44 €/W[53], which is approximated to about 310 €/m^2, the estimated solar array price is 130 k€.

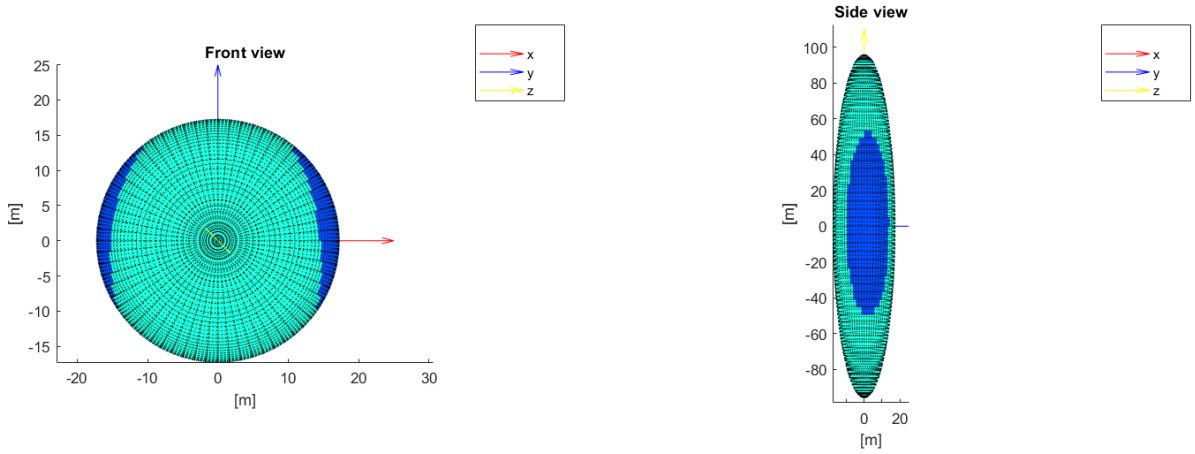

Figure 54: Solar cell placement

The aforementioned points raise the question whether designing for a specific day is sufficient. Considering the fact that sunlight duration is always longer or equal to the winter solstice one, it may be the case that the solar array produces enough energy for normal operation even in suboptimal array placement. This option would entail having a responsive energy storage unit to accommodate the larger energy difference expected. Power production for a solar array placement optimized for the winter solstice throughout the year is summarized in Figure 55a. The power output in the first half of the year is the same as in the second half, hence the months July through November are omitted.

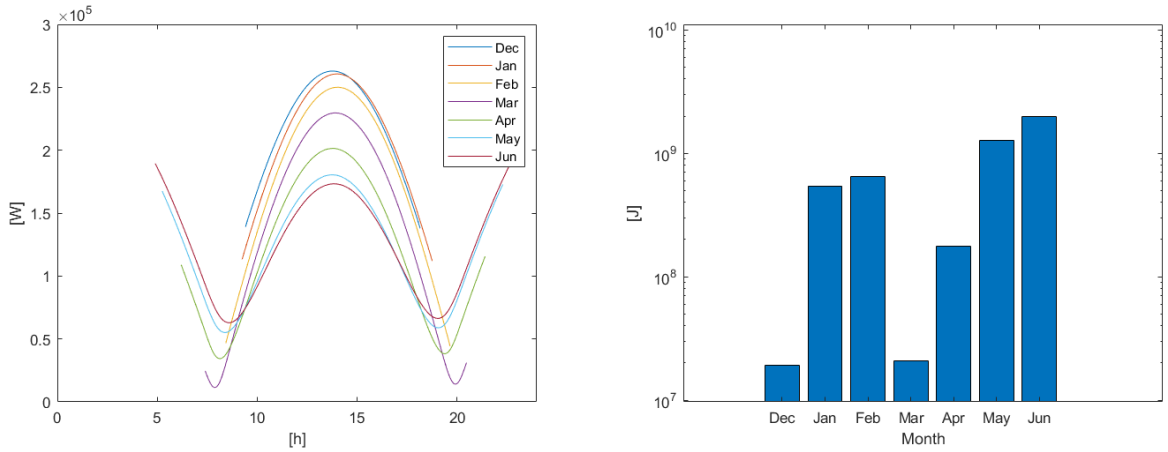

(a) Energy production throughout day

(b) Daily excess energy

As long as the area under the graphs is larger or equal to the total energy required on the day of the winter solstice, this solar cell placement may be used all year round. This can be checked via inspection of Figure 55b, which represents the daily excess of energy produced on the 21^{st} day of

[53] URL:https://www.solarenergyforus.com/amorphous-silicon-thin-film/ [Accessed on 12/06/2019]

the respective month. This is indeed the lightest cell pattern that may be used to power the airship throughout the year.

5.7.4 Fuel cell sizing

As discussed in the MTR, a hydrogen fuel cell and electrolyzer assembly shall be used to generate electrical power by means of extracting the electro-chemical bond energy contained in water. A schematic representation of a hydrogen fuel cell using the Proton-exchange membrane (PEM) technology is presented in Figure 56. The energy storage unit is composed of an electrolyzer, a fuel cell system, reactant tanks, tubes and the relevant regulators.

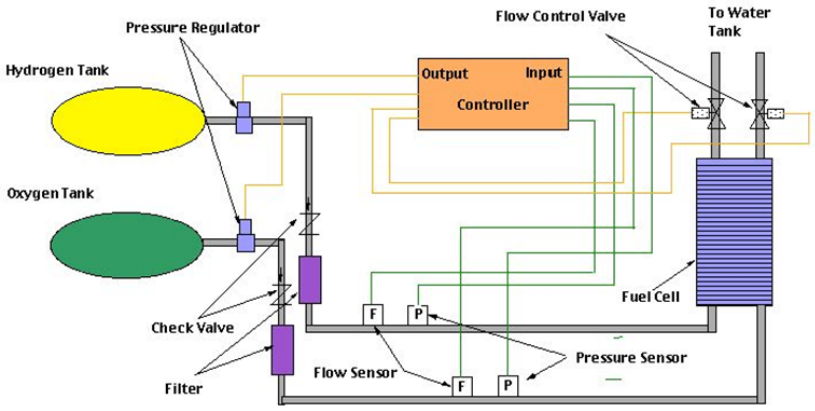

Figure 56: Schematic view of the fuel cell [1].

A fuel cell system, such as the POWERCELL MS-100[54] comprises a series of smaller fuel cells and is capable of regulating the energy input and maintain a normal operational temperature of the fuel cells, having a mass of 100 kg and estimated price of 45 k€. During day, the energy input is used to power the electrolyzer, which in turn triggers the reaction of water to produce hydrogen and oxygen molecules in gaseous form at a high output pressure. These are subsequently fed into their respective storage tanks. In common practice, hydrogen storage tanks are designed for 350 and 700 atm pressure differences[55]. Whenever needed, the stored energy can be retrieved and fed into the power distribution unit by activating the fuel cell system, which fuses together the reactants, yielding energy and creating water as a residual, which is stored into the water tank. The mass of the electrolyzer and water tank is estimated as per [1], yielding a value of 140 kg. Market price of these is estimated at 69 k€[56].

A noteworthy assumption is that all the energy lost via the electrolyzer and fuel cell efficiency is dissipated in the form of heat. The POWERCELL MS-100 fuel cell has an $\eta_{fuelcell}$ of 65%. For a fuel cell producing a power output of 68 kW at 65% efficiency, the heat load is 37 kW. Similarly, for the electrolyzer storing on average 150 kW at 75% efficiency, the heat load is as high as $\approx 50kW$.

The energy capacity requirement may be derived from the energy balance performed during the winter solstice day, shown in Figure 57. The design energy capacity can be calculated according to Equation 5.45.

[54]URL:https://www.powercell.se/en/products/powercell-ms-100-50-100kw/[Accessed on 22/06/2019]
[55]URL:https://en.wikipedia.org/wiki/Hydrogen_tank [Accessed on 22/06/2019]
[56]URL:https://www.hydrogen.energy.gov/pdfs/review18/mn017_mann_2018_p.pdf[Accessed on 22/06/2019]

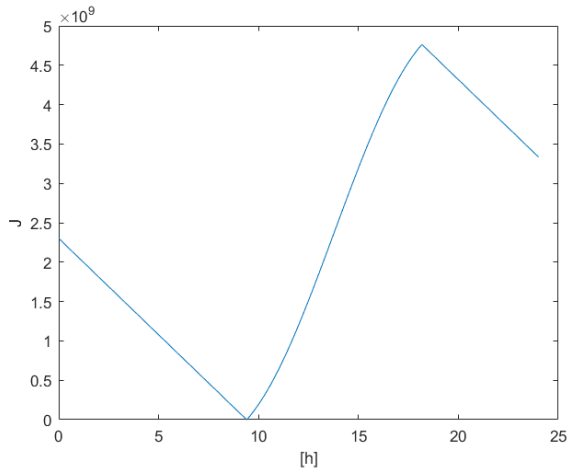

Figure 57: Energy balance 22 Dec

$$Q_{stored} = Q_{max} - Q_{min} - Q_{excess}, \tag{5.45}$$

$$m_{H_2O} = \frac{Q_{stored}}{E_{H_2O} * SF \times \eta_{fuelcell}}, \tag{5.46}$$

$$m_{tank} = 6\pi \times r_{tank}^3 \times \Delta p \times \frac{\rho_{tank}}{\sigma} \times SF_{tank} \tag{5.47}$$

Q_{max} and Q_{min} stand for the maximum and minimum energy portrayed in Figure 57 and Q_{excess} is the excess energy produced that day.

As expected, the highest energy storage requirement arises on the winter solstice day, equal to 4.5 GJ. The computation of reactant mass required is done via Equation 5.46, where E_{H_2O} stands for the energy content of the electro-chemical bond of water, equal to $3.7kWh/kg$[57] and SF is a 1.2 safety factor as recommended by [1].

The reactant tanks shall be made out of a carbon fibre composite with a yield stress $\sigma = 3500MPa$ and a density of $1608kg/m^3$ with a thin metal liner to prevent leakage [1]. The tanks are cylindrical, with a width to radius ratio of 2, having semi-elliptical ends. The tank radius r_{tank} is calculated based on the volume and pressure required, and the tank masses for pressurized vessels can be calculated using Equation 5.47. The results are indicated in Table 25.

Table 25: Reactant tank design

	Volume $[m^3]$	**r_{tank} $[m]$**	**Mass $[kg]$**	**Material cost [€/kg]**	**Cost [€]**
Oxygen tank	0.92	0.45	27	61.7	1671
Hydrogen tank	2.75	0.64	145	61.7	8956

5.8 Thermal Control

Since the MTR, further thermal analyzes have been conducted on various sections of the StratoCruiser. This section will present the thermal behaviour of the instrumentation, electronics within the gondola, and the airship itself. Likewise, temperature sensing devices will be presented at the end of the section.

In a nutshell, the temperature of the instrumentation will be controlled with the use of cryogenics. The on-board electronics will control its temperature with the heat dissipated from the fuel cell. White Tedlar will be applied as a surface finish to the airship skin as a means of minimizing the temperature differential throughout a day.

The mass, power, and cost budgets of the thermal control components are found in this section. These values can also be seen in Section 6.

5.8.1 Instrumentation Cryogenics

As presented in Section 5.3, a cylindrical baffle will enclose the parabolic mirror which minimizes background noise that the TIR detector will receive. This baffle must be kept at cryogenic temperatures

[57] URL`https://hypertextbook.com/facts/2005/MichelleFung.shtml` [Accessed on 12/06/2019]

for minimizing noise, 90 K to be exact. In order to support a cooling system for the instrument, its heat load must first be quantified.
Assumptions must first be considered in order to conduct a first level thermal analysis of the instrumentation; they are listed below:

- It is assumed that the instrument only receives Earth infrared and albedo radiation, since the instrument is pointed in nadir direction.
- It is assumed that heat transfer between the gondola environment and the baffle is negligible, as the baffle and mirror are insulated from the environment they are in.
- It is assumed that all the input heat will be removed by the coolant in the baffle.
- Only infrared radiation is able to enter the baffle environment since a germanium filter is used. Around 49% of solar radiation received is in infrared[58].
- Due to the cryogenic temperature requirement, liquid nitrogen was deemed as the only viable coolant for maintaining the baffle temperature.
- The interior of the walls of the baffle will be composed of aluminium due to its conductive properties.
- The aluminium will be coated with black polyurethane paint, which absorbs more radiation than other surface finishes. The absorptance (α) and emisivity (ϵ) are 0.95 and 0.90 respectively [35].

In this analysis, the baffle is designed for maximum heat load, which is when maximum albedo radiation is received. Albedo infrared radiation ($q_{albedo_{IR}}$) is obtained from Equation 5.48. Here, $I_{sun} = 1361\ W/m^2$ and $Albedo = 0.33$.

The planetary radiation at balloon altitude ($q_{IRgroundZ}$) is obtained from Equation 5.49 and is equal to 250.6 W/m^2. On the surface, infrared radiation ($q_{IRground}$) is obtained from multiplying the ground emisivity (ϵ_{ground}), which is 0.95, with the Stefan-Boltzman constant (σ) and the ground temperature (T_{ground}) being 290 K (as stated in Section 5.3).

Since the planetary radiation must travel through around 20 km of altitude, a transmission factor must be calculated. Here, the maximum attenuation factor (A_{IR}) is 0.45. P_{air} refers to the atmospheric pressure at airship altitude, which is obtained from the ISA and is 5475 Pa. The sea level pressure, $P_{sealevel}$ is 101325 Pa [9].

The aforementioned $q_{IRgroundZ}$ is obtained from the product of the transmission factor and $q_{IRground}$.

$$q_{albedo} = 0.49 \cdot Albedo \cdot I_{sun} \tag{5.48}$$

$$q_{IRground} = \epsilon_{ground} \cdot \sigma \cdot T_{ground}^4$$

$$Transmisson_{IR} = A_{IR}\left(\frac{P_{air}}{P_{sealevel}} - 1\right) + 1 \tag{5.49}$$

$$q_{IR} = q_{IRgroundZ} \cdot Transmisson_{IR}$$

From the aforementioned assumptions, a basic $Q_{out} = Q_{in}$ model can be created to quantify the heat load on the baffle.

$$Q_{cool} + T_{Ni}^4 A_e \epsilon\sigma = Q_{al} + Q_{IR}$$

$$Thus, \tag{5.50}$$

$$Q_{cool} = Q_{albedo} + Q_{IR} - T_{N2}^4 A_e \epsilon\sigma$$

In Equation 5.50, Q_{cool} refers to the heat required to remove from the system. Q_{albedo} and Q_{IR} refer to the heat received from albedo and planetary radiation respectively. The boiling temperature of nitrogen is indicated as T_{N2}, which is 77.52 K [59]. A_e is the area emitting radiation in the baffle, which

[58] URLhttps://www.fondriest.com/environmental-measurements/parameters/weather/photosynthetically-active-radiation/ [Accessed on 22/06/2019]

[59] URL: https://www.engineeringtoolbox.com/nitrogen-d_1421.html[Accessed on 21/06/2019]

is $2\pi r^2 + 2\pi rl$ where the radius is 0.5 m and the length is 2.5 m (as indicated in Section 5.3). The emissivity of the material is indicated by ϵ.

The heat received by albedo radiation is shown in Equation 5.51. Here α is the absorbtance of the baffle. The projected area (A_p) is πr^2 in this case, which corresponds to the filter area.

$$Q_{albedo} = \alpha A_p q_{albedo} \tag{5.51}$$

Similarly, heat received through planetary radiation is shown in Equation 5.52.

$$Q_{IR} = \epsilon A_p q_{IRgroundZ} \tag{5.52}$$

Regarding all these quantities, the maximum heat (Q_{cool}), which occurs during daytime, that must be removed by the coolant is around 304.6 W. During the night, that is $Q_{albedo} = 0$, $Q_{cool} = 145.9$ W. From this thermal model, a cooling system can be devised.

Two possible methods can be used to control the nitrogen flow into the baffle. One is a system consisting of a set volume of liquid nitrogen flowing from a cryogenic cylinder into the baffle which then boils and vents out to the atmosphere. The other is a closed loop system which consists of a cold head and a compressor which re-condenses the nitrogen once it has been evaporated. Both have their own benefits and drawbacks, which are investigated in the following paragraphs.

Open Loop Cooler

With the known heat load of the baffle, the mass of nitrogen required for a mission length of 6 months can be computed. With this configuration, any nitrogen that boils from cooling the baffle will be released to the atmosphere. The required nitrogen for the entire mission duration will be stored in a cryogenic cylinder. A pump for liquid nitrogen would be used to control the flow of the coolant to the baffle. This pump would receive temperature readings from a sensor within the baffle that would give command the liquid nitrogen pump. A liquid hydrogen pump is usually in the price range between 15 $k€$ to 19 $k€$[60].

Using the relation for specific latent heat, $Q = mL$, the mass of nitrogen required to bring aluminium from an atmospheric temperature (T_0) of 216 K to a required temperature (T_{req}) of 90 K can be computed. In Equation 5.53, m_{Al} and m_{Ni_1} are the masses of the aluminium baffle and the nitrogen respectively, c_{Al} is the specific heat of aluminium (900 J/kgK), and L_{Ni} the latent heat of vaporization of nitrogen (199 KJ/kg)[61].

$$m_{Al}c_{Al}(T_0 - T_{req}) = m_{Ni_1}L_{Ni} \tag{5.53}$$

In Equation 5.53, $m_{al} = 2\pi r t_{Al}\rho_{Al}$. T_{Al} is the thickness of the aluminium baffle (2 mm) and ρ_{Al} is the density of aluminium (2710 kg/m^3). With these quantities known, m_{Ni_1} was found to to be 24.14 kg.

If the length of a day were split into 12 hours for night and the same for day, the mass of nitrogen needed to keep aluminium at the required temperature can be done using Equation 5.54. The variable $t_{mission}$ is the mission duration in seconds (7.76×10^6 s). Finally, m_{Ni} is 17537 kg.

$$m_{Ni} = m_{Ni_1} + \frac{t_{mission}(Q_{cool_{day}} + Q_{cool_{night}})}{L_{Ni}} \tag{5.54}$$

Containing this amount of liquid nitrogen would require a cryogenic tank or a large number of cryogenic cylinders. This will also greatly contribute to the mass but it is unnecessary to compute as the mass of nitrogen computed for using an open loop system is, in any case, unfeasible for this mission. This would force considerable changes within all other subsystems of the StratoCruiser. It is unrealistic for the thermal control of the instrumentation to be this large. Therefore, a closed loop configuration has been also looked at in the following paragraphs, which gives much more feasible results.

[60] URL: `https://www.ilkdresden.de/en/project/pump-for-liquid-nitrogen-hydrogen-helium-lng/` [Accessed on 21/06/2019]

[61] URL: `https://www.engineeringtoolbox.com/fluids-evaporation-latent-heat-d_147.html` [Accessed on 20/06/2019]

Closed loop cryocooler

A closed loop cryocooler works similarly to the aforementioned open loop case, however, in this configuration, the liquid nitrogen is re-condensed by a coldhead. This is best depicted in Figure 58.

Here, a cooled load immersed in liquid nitrogen, which then causes the nitrogen to boil. Once the nitrogen comes into contact with the condensation plate, the coldhead forces the nitrogen to re-condense. This liquid nitrogen is then re-looped to the cooled load.

In the setup of the instrumentation, the cooled load is the instrument and the baffle, where liquid nitrogen will fill into a dewar surrounding the two. This immerses the instrument and liquid nitrogen; with a cold head attached to the system, the mirror and baffle can be actively cooled for the optimum reduction of background noise.

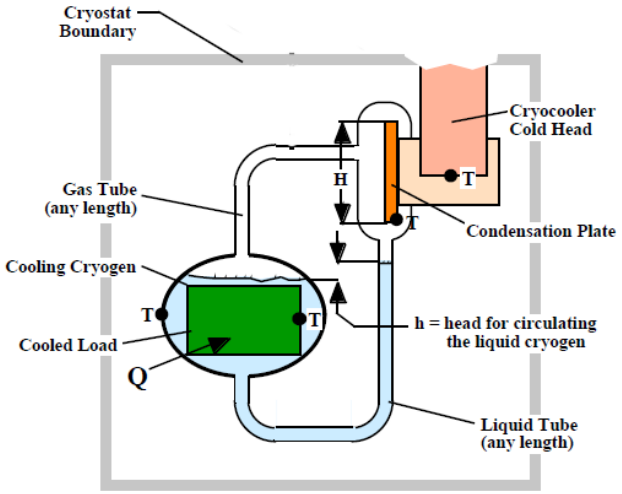

Figure 58: A schematic representation of a closed loop heat transfer system with liquid nitrogen [36].

A suitable cryocooler is the 'AL300 Cryocooler' from 'CRYOMECH'[62]. This coldhead must work with the 'CPA2870' water cooled compressor[63]. This cryosystem has a cooling capacity of 320 W at 80 K, which meets the required heat load of the system. However, the input power of this system is 7.0 kW.

Unfortunately, a quote was not received from the supplier, thus the actual price of the system is not known. From [37], Equation 5.55 was obtained. Here cost (C, in $k\$$) is related to cooling power (Q_c) using an empirical relation. With the 'AL300' cooling power of 320 W, a price of 48.49 $k\$$ is obtained. A water cooled cryo-compressor would be used to power the coldhead, where water from the fuel cell could be used to cool the cryo-compressor.

$$C = 1.81 * Q_c^{0.57} \tag{5.55}$$

Table 26 showcases the specification of the open loop cooler for the instrument. The total price was converted from dollars to euros.

The table also indicates that 320 W of cooling is provided at 80 K. Thus it is possible that the temperature of the baffle could indeed go below 90 K. Looking at Figure 83, it is evident that the SNR does not change noticeably with this temperature difference.

The mass of nitrogen needed for this system can be assumed to equal m_{Ni_1} from Equation 5.53. Furthermore, For redundancy, two compressors systems will be brought on board (discussed further in Section 10.3), therefore the total mass of the system (and therefore the cost) is multiplied by two. The mass of the nitrogen is not double, because it assumed that the nitrogen will be contained in the dewar within the baffle, and not in cryosystem. The estimated price consists is double of the value obtained in Equation 5.55.

[62]URL: `https://www.cryomech.com/products/al300/` [Accessed on 21/06/2019]
[63]URL: `https://www.cryomech.com/articles/cp2800-and-cp1000-series-compressor/` [Accessed on 24/06/2019]

In the end, mostly because of the significantly lower mass, the closed loop system is chosen.

Table 26: Table showing specifications of the selected cryocooler

AL300 with CP2870	
Cold head	*AL300*
Cooling capacity	320W@80K
Mass	18.6kg
Compressor package	*CP2870 water cooled*
Mass	112 kg
Input power	7.0 kW
Dimensions	48 x 46 x62 cm
Flexible lines	
Length	3 m
Mass per pair	4.2 kg
Coolant	*Liquid nitrogen*
Mass	24.1 kg
Total mass	159 kg
Total mass w/ redundancy	294 kg
Estimated price	85.3k

5.8.2 Thermal Behaviour of Balloon Skin

In the MTR, the thermal environment of an airship in the stratosphere was extensively described. Relations such as Equation 5.49 were first introduced in the previous report. In any case, the MTR investigated the steady state temperature of the balloon skin, with a constant solar flux. However, this did not show how the temperature changes throughout the course of a day.

Modelling the thermal behaviour of the balloon is necessary for quantifying the pressure change of the lifting gas within the airship. The airship envelope must be able to maintain its shape so that lifting performance is minimally affected. The change of volume of the envelope must be minimized to achieve this. The envelope material selected in Section 5.11 takes this thermal behaviour into account for material selection. Moreover, white Tedlar has been selected as a surface finish. In the MTR, silvered Teflon was also considered, however further material properties were not retrieved.

The thermal model was constructed with a 'MATLAB' script where solar incidence angle determines the amount of radiation the airship received throughout the course of a day. Nevertheless, numerous assumptions were taken into account for this analysis which would cause results to differ significantly with reality. They are as follows:

- The StratoCruiser is assumed to be orientated in East-West direction throughout the analysis. In reality the orientation would not remain unchanged, and a different orientation will provide different solar incidence angles which affects the heat received from the sun. However, because of the wind direction, the airship will mostly be oriented in this direction
- As stated in the MTR, convective heat transfer is assumed to be negligible in the stratosphere as its density is 5% of that at sea level. This assumption allows for the airship in the thermal model to achieve a minimum temperature lower than that of the stratosphere.
- The heat transfer due to wind is neglected. In reality, the temperature of the airship skin would decrease with windspeed [38].
- It is assumed that the airship is a perfect ellipsoid with a semi-major axis (a) of 96 m and a semi-minor axis (b) of 17.1 m. The surface area would only slightly differ with the actual shape, but this assumption greatly facilitates the calculations of the wetted area (A_w), planar area (A_{plan}), and the projected area (A_{proj}).

- It is assumed that the airship receives albedo and planetary radiation normal to its planar area. In reality, the receiving area for these two kinds of radiation is not equal.
- The airship is modeled as one thermal node. Conductive heat transfer between the surface finish, the envelope, and the lifting gas is neglected; a weighted average is taken for the specific heat coefficient for the single thermal node.
- The absorptance and emisivity of the surface finish are assumed to be constant throughout the surface area. Only the α and ϵ of the surface finish are taken into account for this model. For more detailed analysis, properties such as transmissivity and reflectance of the material should be taken into account.
- Solar irradiance is assumed to be a constant value 1361 W/m^2 [35]. In reality this value fluctuates by ± 45 $\frac{W}{m^2}$, which was deemed insignificant for this analysis.

Within the script, a day was set discretized into 86400 seconds where two arrays containing elevation and azimuth angles were created. These angles were respective to the geographic location of the Netherlands and the date. These arrays were used to calculate the solar incidence angle on the balloon throughout the course of a day. Equation 5.56 shows how the incidence angle has been computed with θ and γ relating to elevation and azimuth angle respectively.

$$B = \cos^{-1}(\cos(\theta)\cos(\gamma - \frac{\pi}{2})) \tag{5.56}$$

The solar incidence angle is used to calculate the projected area (A_{proj}) of the StratoCruiser, with Equation 5.57. This is essentially the surface area of the airship that receives solar radiation, which is always changing throughout the course of a day [11].

$$\begin{gathered} A_{proj} = \pi b^2 \sqrt{\cos(B)^2 + (\tfrac{a}{b})^2 \sin(B)^2} \\ A_w = 2\pi b(b + \tfrac{\sqrt{a^2-b^2}}{a} \sin^{-1}\left(\tfrac{a^2}{\sqrt{a^2-b^2}}\right)) \\ A_{plan} = \pi ab \end{gathered} \tag{5.57}$$

The areas obtained in Equation 5.57 are used for quantifying the heat received by the airship, shown in Equation 5.58. The radiation due to albedo is similar to Equation 5.48 except that in this analysis, solar elevation is taken into account for albedo intensity, resulting in: $q_{albedo} = Albedo \cdot I_{sun} \cdot \sin(\theta)$. The radiation due to earth, q_{IR}, is identical to the relation in Equation 5.49. The values for α and ϵ are shown in Table 27[64]. The total mass of the white tedlar was computed from using the total surface area of the airship, which was obtained from the CATIA model.

$$\begin{aligned} Q_{sun} &= \alpha A_{proj} q_{sun} \\ Q_{albedo} &= \alpha A_{plan} q_{albedo} \\ Q_{IR} &= \epsilon A_{plan} q_{IR} \end{aligned} \tag{5.58}$$

The heat balance equation, shown in Equation 5.59, is used to characterize the change in temperature of the balloon over the course of a day. As the balloon is treated as single node, the mass, m, is the summed mass of the surface finish, the envelope and the lifting gas. The specific heat coefficient is a weighted average of the aforementioned components [35]. The values of each are shown in Table 28. Here, the dyneema mass is including both airship skin and the ballonets.

$$mc\frac{dT}{dt} = Q_{sun} + Q_{albedo} + Q_{IR} - \sigma\epsilon A_w T^4 \tag{5.59}$$

Computing Equation 5.59 cannot be done analytically and must be done numerically. This was done with a forward Euler integration method as shown in Equation 5.60. With T_i being the temperature at a particular index, and δt being a time step of 1 s. Starting at an index one, the starting temperature T_0 would be tested until the model converges after a day.

[64] URL:`https://www.dupont.com/content/dam/dupont/products-and-services/membranes-and-films/pvf-films/documents/DEC_Tedlar_GeneralProperties.pdf` [Accessed on 24/06/2019]

The temperature model is shown in Figure 59. Both temperature models for the summer and winter solstice are shown.

$$T_i = T_{i-1} + \delta T \; where \; \delta T = \frac{dT}{dt}\delta t \tag{5.60}$$

Table 27: Material properties of white Tedlar [39].

Property	Value	Unit
α	0.3	-
ϵ	0.85	-
thickness	3.81×10^{-5}	m
density	1370	kg/m^3
mass	796	kg
cost	0.05	€/m^2
total cost	840	€

Table 28: Mass properties of notable airship components.

Component	Mass, m [kg]	Specifc Heat, c $[J/kgK]$
White Tedlar	796	1050
Dyneema	1870	14000
Hydrogen	612	1850
Total	2948	3924

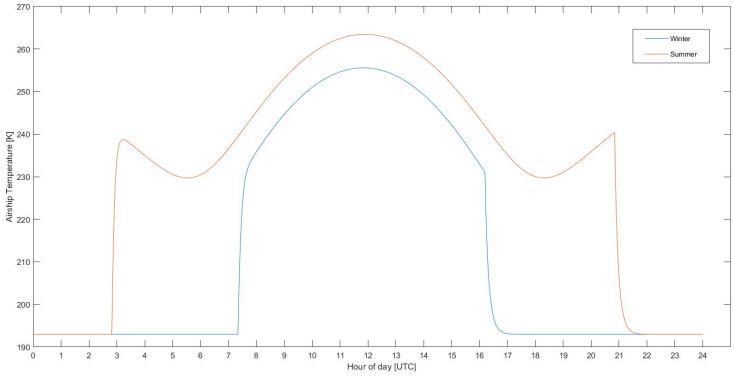

Figure 59: Graph showing the thermal behavior of the airship skin over the course during the summer and winter solstice. The time shown is in UTC.

Figure 59 shows how the temperature progresses throughout the day for both winter and summer cases. Undoubtedly, the summer case will contain the peak temperature since the airship receives the highest amount of solar radiation through this period. The peak temperature that the balloon experiences is 263 K for summer and 255 K for winter. It is also evident that during summer, the temperature at the start and end of the day are higher than at around 05:30UTC and 18:30UTC. This due to the East-West orientation of the StratoCruiser.

The minimum temperature for both cases is 193 K. This is physically not possible since the outside air temperature does not go much lower than 216 K. However, this value is obtained since only radiative heat transfer is considered within this model. According to the graph, the maximum differential that the airship can experience is during the summer solstice and it is 70 K. However, a more realistic value is would be 47 K, if it is assumed that the lowest temperature the airship experience is the outside air temperature.

Furthermore, it is seen that the temperature has a large spike when the sun comes into or out of the view. Even though the mass is large, this occurs due to this mass being spread over a large area. The mass of the white Tedlar shown in Table 27 is subject to change due to possibility of integrating the thermal coating in the envelope, as explained in Section 5.11.2.

In any case, an idea of the temperature differential is obtained from this graph. The structure of the airship is developed further within Section 5.11 with the pressure change of the lifting gas now known. The verification and validation methods of this section and Section 5.8.1 are found in Section 8.1.

5.8.3 Gondola Components

A handful of components within the gondola must be kept within a specific temperature range. For instance the cryogenic compressor must operate at a temperature range of 7 to 38°C. The on board computer also. Undoubtedly, the water tank within the fuel cell must be kept above freezing point, which is around 0°C.

This was not deemed problematic as the fuel cell dissipates heat on a range of 37 to 50 kW, as explained in Section 5.7. The use of heat-pipes and heat exchangers would facilitate the energy transfer between the fuel cell and the electro-mechanical components within the gondola. The water tank temperature could be maintained with the use of a heat exchanger within the water tank.

In all, the fuel cell would still dissipate an excess amount of heat that would have to be radiated to the environment. This could be done with the use of louvers or radiators that are exposed to the outside environment.

Further investigation is definitely needed for this section. If heat is not dissipated correctly, components in the gondola could overheat which could lead to issues in the mission.

5.8.4 Temperature Sensors

The various components of the StratoCruiser require different temperature sensing ranges. The sensors presented in this section would not be the final selection as the thermal control is subject to further development, if this project were to continue. This section is used to get an idea of the costs involved with utilizing such sensors, which would aid in requirement generation for detailed design. Costs for each of the sensors are located in Table 29.

The cryogenic system would use three silicon diode cryogenic temperature sensors[65]. These sensors have an operating temperature range of 30 to 100 K with an accuracy of ± 0.5 K. Three sensors would be needed for redundancy.

The outside air temperature can be measured with a 'Series 0129'[66]. These sensors could be used for measuring the temperature of the lifting gas and the stratospheric environment. At least five of these sensors would be needed for redundancy.

Finally, 'GSFC space qualified thermistors' [67] could be used to monitor the temperature of various components within the gondola. A fairly large temperature range can be monitored ($-55°C$ to $70°C$) with an accuracy of $\pm 0.1°C$. At least 10 of these sensors would be required within the gondola.

Table 29: Table showing cost breakdown of aforementioned sensors.

Sensor	**Price per Unit [€]**	**Units**	**Total Price [€]**
Cryogenic Temperature Sensor	295.68	3	887.04
OAT Sensor	158.4	5	792.00
GSFC Space Qualified Thermistor	35.2	10	352.00
Total			2031.04

[65]URL: `https://www.omega.nl/pptst/CY670.html` [Accessed on 24/06/2019]

[66]URL:`https://utcaerospacesystems.com/wp-content/uploads/2018/04/Total-Air-Temperature-TAT-Sensors.pdf` [Accessed on 24/06/2019]

[67]URL: `https://www.mouser.com/ds/2/418/44906-709889.pdf` [Accessed on 24/06/2019]

5.9 Telemetry, Tracking & Command

The design of the TT&C is conducted by constructing a link budget tool to investigate the signal-to-noise performance of the system. It must satisfy **SB-Subs-TTC-02**, stipulating a minimum SNR of 10. This is done for signals being sent from the ground station to the airship (uplink) and from the airship to the ground station (downlink). In this report, only the uplink budget is presented, as the downlink budget follows in a similar manner. A choice of antennas is made to ensure the link design works in practice.

5.9.1 Antenna Choice

The required uplink data rate is not exactly calculated but estimated from similar Earth observation missions[68]. It is found that the required data rate (R) does not exceed 64 kilobits/second (*kbps*). For this purpose, an off-the-shelf helical antenna with the following characteristics is used for receiving uplink commands [69]:

- Gain: 16 dB
- Length: 11 cm
- Mass: 46 g
- Power: Up to 5W. This is not known exactly but estimated using literature [33]
- Price: $25, including shipping

For the downlink, a data rate requirement of 2370 megabits/second (Mbps) was obtained, as described in Section 5.10. To transmit this, a high gain horn antenna with a built-in pointing mechanism was chosen[70]. The pointing mechanism is necessary as to allow the StratoCruiser to send data to the ground station in Delft from anywhere in the Netherlands. It has the following properties:

- Operating frequency: X-band, 8.5 GHz. This implies an operating wavelength (λ) of 0.0353 m.
- Diameter (D): 0.274 m.
- Gain: 18 dB.
- Mass: 3.3 kg, including pointing mechanism.
- Power: 4W
- The price of the antenna is not known, but should not exceed $500 by comparison to the antennas found in literature [33].

Although the entire budget is not presented, the main difference this causes compared to the uplink budget calculation is the half-power angle (α_{HP}):

$$\alpha_{HP} = \frac{225}{\frac{\pi \cdot D}{\lambda}} = 9.46^{\circ} \tag{5.61}$$

[68] URL: `https://earth.esa.int/web/eoportal/satellite-missions` [Accessed on 24/06/2019]
[69] URL: `https://bit.ly/2REIe65` [Accessed on 24/06/2019]
[70] URL: `https://satsearch.co/products/sst-us-15-dbi-x-band-apm` [Accessed on 25/06/2019]

5.9.2 Uplink Budget

The uplink budget is shown in Figure 60, followed by an explanation of the elements.

INPUTS				OUTPUTS		
Parameter	**Value**	**Unit**		**Parameter**	**Value**	**Unit**
Uplink power	0.5	W		Wavelength	0.12	m
Receiving antenna loss factor	0.8			Transmitter gain (G_t)	1425.61	
Transmitting antenna loss factor	0.7			Transmitter half power angle ($\alpha_{HP,t}$)	4.2	°
Boltzmann constant (k)	1.38E-23	J/K		Receiver half power angle ($\alpha_{HP,r}$)	56.96	°
Uplink frequency (f)	2.5E+09	Hz		Transmitter pointing offset angle (PO_t)	2.1	°
Receiver antenna length (L)	0.11	m		Receiver pointing offset angle (PO_r)	28.48	°
Transmitting antenna diameter (d_g)	2	m		Transmitter pointing loss	-3	dB
Transmitting Antenna efficiency (η_t)	0.52			Receiver pointing loss	-3	dB
Receiving antenna efficiency (η_r)	0.7			Uplink system noise (T)	614	K
Altitude (h)	20500	m		Space loss (L_s)	1.34E-15	
Maximum ground distance from ground station (G_D)	260000	m				
Maximum distance from ground station (D_{max})	260807	m		**Uplink Budget**		
Elevation angle (β)	0.078683	rad		Uplink Power	-3.010	dB
sin(β)	0.078602			Transmitter loss factor (L_l)	-1.549	dB
Required UL data rate	64	kbps		Transmitter gain (G_t)	31.540	dB
Speed of light (c)	3E+08	m/s		Transmission path loss (L_a)	-0.013	dB
				Receiver gain (G_r)	9.922	dB
				Space loss (L_s)	-148.726	dB
				Total pointing loss (L_{pr})	-6	dB
				Receiver loss factor (L_r)	-0.969	dB
				Required data rate	-48.061	dB
				Boltzmann constant	228.599	dB
				System noise temperature	-27.882	dB
				SNR required	10	dB
				SNR	33.850	dB
				SNR margin	23.850	dB

Figure 60: Uplink budget tool for the StratoCruiser

Inputs:

- The variable in the budget tool is the uplink signal power (P), which may be varied to meet the SNR requirement.
- Antenna loss factors: these are estimated based on the antenna choice [33]
- Uplink frequency (f): 2.5 GHz; the S-band is chosen for the uplink frequency based on comparable missions[71]
- Antenna characteristics: the length of the helical antenna is known (0.11 m), as well as the diameter of the parabolic antenna at EWI, Delft (2 m)
- Altitude and distance: the maximum cruise altitude (h) for the airship is 20500m. The maximum distance between the airship and the ground station (D_{max}), is about 260.8 km (when the airship is near Groningen). This is the hypotenuse of the ground distance (G_D) and h; it is used when calculating the space loss.
- Elevation: the elevation angle (β) is also dependent on h and D_{max}; and it is calculated using Figure 61 and Equation 5.62. β is important when calculating the atmospheric attenuation.

The outputs are calculated as follows

- Antenna gains: the transmitting antenna gain (G_t) follows Equation 5.63 for a parabolic antenna, while the receiving antenna gain (G_r), given by Equation 5.64 is for a helical one.

[71] URL: `https://earth.esa.int/web/eoportal/satellite-missions` [Accessed on 24/06/2019]

- Half-power angles ($\alpha_{HP,t}$, $\alpha_{HP,r}$): assuming the antenna circumference $C \approx \lambda$ [33], this can be calculated for the receiver (r) and ground station transmitter (t) using the antenna characteristics, signal frequency, and signal wavelength ($\lambda = 0.12$ m) [33]. The relation between the signal wavelength and frequency is also provided, where c is the speed of light, see Equation 5.65 to Equation 5.67.
- Pointing loss: If the pointing offset angle is 50% of the half-power angle for both the transmitting and receiving instrument, pointing losses are each -3 dB, resulting in a total pointing loss (L_{pr}) of -6 dB. [40].
- Space loss (L_s) is calculated using the distance between the airship and the ground station and the signal wavelength, given by Equation 5.68.
- An estimate of the system noise temperature (T) is made using Table 30 [40].
- Finally, the transmission path loss due to atmospheric attenuation for nadir pointing is found from Figure 62 [33]. At 2.5GHz, the loss due to atmospheric attenuation is approximately $10^{-3}dB$ at 0km. To account for the elevation angle, Equation 5.69 is used, where is the elevation angle calculated previously.

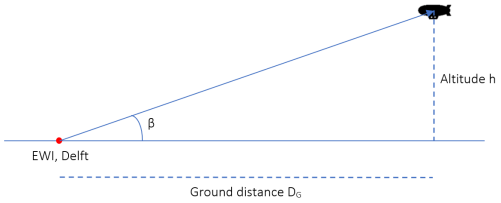

$$\beta = arcsin\left(\frac{h}{D_{max}}\right) = arcsin\left(\frac{20500}{260800}\right) \quad (5.62)$$

Figure 61: Airship elevation angle

$$G_t = \eta\left(\pi\frac{d_s}{\lambda_d}\right)^2 \quad (5.63) \qquad G_r[dB] = 10.3 + 10 \cdot log(\frac{L}{\lambda}) \quad (5.64)$$

$$\alpha_{HP,r} = \frac{52}{\sqrt{\frac{L}{\lambda^3}}} = 56.9^\circ \quad (5.65) \qquad \lambda_d = \frac{c}{f_d} \quad (5.66) \qquad \alpha_{HP,t} = \frac{21 \cdot 10^9}{f \cdot d_g} = 4.2^\circ \quad (5.67)$$

$$Ls = \left(\frac{\lambda_d}{4\pi \cdot D_{max}}\right)^2 \quad (5.68)$$

Table 30: System noise temperature for various signal frequencies

Noise Temperature	**Frequency [GHz]**					
	Downlink			**Crosslink**	**Uplink**	
	0.2	**2-12**	**20**	**60**	**0.2-20**	**40**
Antenna Noise [K]	150	25	100	20	290	290
$(CableLossFactor)^{-1}$ [dB]	0.5	0.5	0.5	0.5	0.5	0.5
Cable Loss Noise [K]	35	35	35	35	35	35
Receiver Noise Figure [dB]	0.5	1.0	3.0	5.0	3.0	4.0
Receiver Noise [K]	36	75	289	627	289	438
System Noise [K]	**221**	**135**	**424**	**682**	**614**	**763**

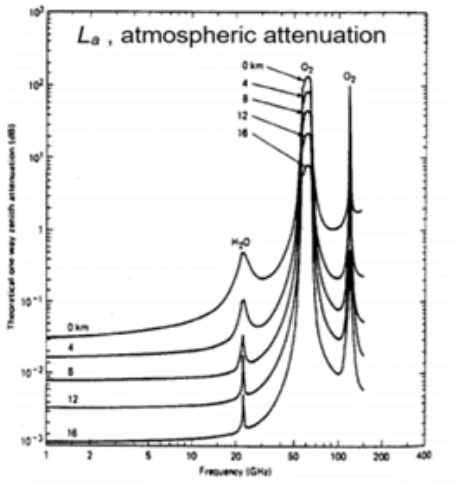

Figure 62: Signal atmospheric and rain attenuation

$$L_a = \frac{L_a, nadir}{sin(\beta)} \tag{5.69}$$

All of these terms are converted to dB using Equation 5.70, leading to the SNR calculated using Equation 5.71.

$$X[dB] = 10 \cdot log(X) \tag{5.70}$$

$$\frac{E_b}{N_0}[dB] = P + G_t + G_r + L_a + L_s + L_{pr} - R - k - T \tag{5.71}$$

This results in a link budget that closes with a margin of 23.85 dB using a signal power of 0.5 W. The downlink budget also closes, with a signal power of 5.5 W and a margin of 5.48 dB.

5.9.3 Antenna Layout

Two additional aspects of the design considered during the detailed design phase were the need for redundancy, as is expressed in Section 10.3, and the logistics of being able to continuously communicate with the grounds station. The first issue is accounted for by simply accommodating two of each type (helical and horn) of antenna. This has a negligible effect on the mass and power budgets. Regarding the second aspect, it was decided to mount the antennas on either side of the gondola, such that no matter where the airship is, the ground station will be in view of at least one of them.

5.10 Command & Data Handling

The C&DH subsystem consists of a definition of its architecture, followed by the sizing and choice of the main computer and subsystem computers.

5.10.1 Architecture

The data handling architecture is depicted visually in Figure 63 and described below.

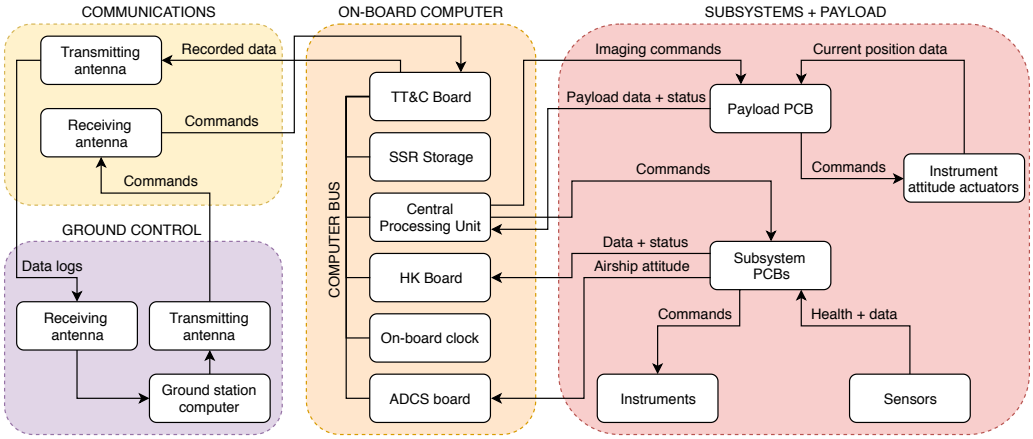

Figure 63: C&DH system architecture

Commands are sent by ground station and received by the receiving antenna on the airship. These are transmitted to the On-Board Computer (OBC), allowing them to be processed by the central processor. The different boards are connected in a bus, however, in practice this will simple be different software running in parallel because a commercial computer is chosen. Next, specific commands are transmitted to Printed Circuit Board (PCB)s of individual subsystems, e.g., adjusting the thrust or the pointing of the antennas. The subsystems proceed to execute the commands through their specific instruments. The PCBs are also responsible for transmitting data recorded by subsystem sensors and conveying them to the OBC, where housekeeping (HK) data are logged in the solid state recorder (SSR) and instrument measurements may be used to calculate new commands. For example, when the airship attitude is measured by star trackers, this data is compared with the current position of the instrument mount actuators and ground commands to specify new actuator positions. Recorded data, including payload measurements and data logs, are sent from the SSR to the ground station once an hour via the transmitting antenna.

5.10.2 OBC Selection

The OBC was sized with regards to required storage by making an estimate of the amount of data recorded in an hour ($D_{hr,PL}$). This is calculated using Equation 5.72, where S_{image} is the size of a single picture taken by the instrument in pixels (1024 x 1024) and n is the number of images captured in a minute, which is 100 images, n_{bits} is the number of bits in each pixel, here assumed to be 24 [40]:

$$D_{hr,PL} = S_{image} \cdot n_{bits} \cdot n \cdot 60 \tag{5.72}$$

The resulting amount of data recorded in an hour is equal to 150995 $Mbit$. In addition to this, there is housekeeping data pertaining to each subsystem and data measured by sensors of each. It is difficult to get an accurate value for this, however, by comparison to spacecraft, the subsystem data per hour ($D_{hr,SS}$) is calculated using the number of parameters to be sampled (n_{par}, assumed to be 1000), the sampling frequency (f, assumed to be 500 Hz), and the bits per sample ($n_{b/s}$, assumed to be 12) [33]:

$$D_{hr,SS} = n_{par} \cdot f \cdot n_{b/s} \cdot 60 \tag{5.73}$$

The resulting subsystem data per hour is equal to 21600 $Mbit$. Summing the two figures, this amounts to 172595 $Mbit$, or about 173 $Gbit$ recorded per hour. Evidently, the estimates must be treated with

a healthy margin; taking a safety margin of 2 results in a storage capacity of at least 345 $Gbit$, or about 43 $GBytes$ (GB).

The throughput of the processor can also be estimated in a similar manner, and is found to be about 40 $Mbit/s$. Various commercial workstations satisfy this requirement[72], the Lenovo ThinkCentre M715q is chosen as it is meant to run a range of scientific software, and it is relatively small, light, and cheap compared to other workstations. It has the following characteristics[73]:

- 128 GB SSR
- Power consumption = 65 W
- Mass = 1.3 kg
- Price = \$400

For the subsystem controllers, the estimated throughput is about 6 $Mbit/s$. For these applications, PCBs such as Raspberry Pi 3's are chosen because they can achieve throughputs of up to 300 $Mbit/s$, several thousand MIPS (million instructions per second), and up to 1.4 GHz clock speeds, which make them adequate for subsystems of this size [33]. In total, considering 10 PCBs, the mass would be 2.4 kg, the power consumption would be 150 W, and cost would be \$500 [74].

5.11 Structures

In section 4 it was concluded that the structure of the envelope is a non-rigid one. Out of the three possible solutions that were presented, this one has the lowest mass and the best integration with the buoyancy control system. The general layout of such a structure is a pressurized envelope with a suspension system on the inside that transfers part of the envelope load more evenly into the skin.

This section presents the development process of the envelope membrane material, the suspension system for the gondola and ballonets and a proposed design of the propulsion system mount and how to integrate it into the envelope. The most challenging part of designing the structure was coming up with achievable requirements for the envelope. This proved to be difficult due to the lack of public information on similar missions.
A significant amount of time was spent working on optimizing the aerodynamic performance of the envelope, as the geometric properties greatly affect the structural design. The envelope behaves like a pressure vessel and, as such, the radius and curvature are required to have a load distribution. Without a well defined geometry of the envelope it would have been impossible to determine the loads and investigate weather a material that can meet and sustain the induced stresses exists.

Due to the time constraint, not all of the components presented have been fully investigated. More effort has been put into more critical assemblies such as the envelope. The tail fins, for example, did not undergo a proper trade-off. The proposed design is meant as a starting point and is used to get a very rough mass estimate that is not based on statistical data.

5.11.1 Load Determination

This section presents the process used to determine the loads experienced by the envelope and suspension system. Since the envelope is composed of membrane fabrics, the thickness of the material is ignored as it is not important. The thickness of fabrics is determined by a combination of fiber layer thickness and weaving pattern as well as the environmental protection and gas retention film.

- The envelope is idealized as a cylinder, the loads in axial direction are considered equal to the ones in radial direction.

[72] J. Bouwmeester, personal communication, June 17, 2019
[73] URL: `https://www.lenovo.com/gb/en/desktops-and-all-in-ones/thinkcentre/m-series-tiny/ThinkCentre-M715q-Tiny/p/11TC1MT715Q` [Accessed on 22/06/2019]
[74] URL: `https://www.element14.com/community/community/raspberry-pi` [Accessed on 14/06/2019]

- The weight of the gondola is entirely supported by the suspension system.
- The curtains introduce negligible loads into the envelope.

Out of the stated assumptions, the one that introduces the most uncertainties is the idealization of the envelope. Its shape is optimized for aerodynamic performance, which results in a geometry that is difficult to analyze. This assumption takes the maximum stress experienced by the envelope and applies it everywhere. A way to determine the loads at each point on the envelope is presented in Chapter 8.

The loads experienced by the envelope are determined by multiplying the formula for hoop stress in a cylinder by the thickness of the material, resulting in Equation 5.74. The over-pressure P_{Op} is determined by adding together the pressure due to temperature differences, Equation 5.75, the lifting gas pressure P_{gas}, Equation 5.76, and the maximum dynamic pressure experienced by the airship, Equation 5.4. The thermal pressure was determined so that the variance in lift of the aircraft is not only minimal throughout the expansion and contraction of the envelope with changing temperature, but also so that it can maintain the altitude higher than 20 km. It is also known that due to the negative thermal expansion coefficient of the fiber, the effects of a higher volume and lower temperature complement each other resulting in a higher thermal over-pressure. To account for unforeseen changes in pressure an to conform with air worthiness agencies requirements on airships a safety factor of 4 was considered. The final loads experienced by the envelope can be seen in Table 31.

$$Load = P_{Op} \cdot Radius \tag{5.74}$$

$$P_{Thermal} = \rho \cdot R_{gas} \cdot T \tag{5.75}$$

$$P_{Lift} = (\rho_{atm} - \rho_{gas}) \cdot Grav \cdot height \tag{5.76}$$

Table 31: Envelope loads process of the envelope load.

Overpressure		
P_{Op}	0.0015	MPa
$Radius$	17278	mm
$Load_{Op}$	25.917	N/mm
Buoyant lift		
P_{gas}	$2.79 \cdot 10^{-5}$	MPa
$\rho_{atmosphere}$	0.088	kg/m^3
ρ_{gas}	0.0056	kg/m^3
$GravitationalAcceleration$	9.80665	m/s^2
$Height$	34.556	m
$Load_{gas}$	0.482	N/mm
Total load		
$TotalLoad$	26.4	N/mm
$SafetyFactor$	4	-
$StrengthRequirement$	106	N/mm

Next, the loads experienced by the suspension system are analyzed. This problem was approached the following way:

- Determine the loads introduced into the wires by the gondola.
- Determine the loads of the ballonets.
- Determine the loads carried by the curtains.

It was assumed that the gondola is supported by 8 wires. The maximum wire load was calculated by assuming that the entire weight of the gondola is carried by the suspension system. The maximum value of this load is around 4000N Compared to this, the load of the ballonets is considered insignificant. This high load makes the design of the curtain more challenging since the cross section of the curtains tapers of towards the cable attachment to better accommodate deformation. To carry this load, the thickness of the curtain must be increased by adding additional sheets of fabric or using metal plates as reinforcement. A sketch of this component and how it is integrated with the envelope can be seen in Figures 64 and 65. The material of the curtains is the same one as the envelope.

For the main wire, Dyneema is used again as it makes integration with the ballonets much simpler. A rope with a diameter of $2mm$ is more than enough to carry those loads, as the average break load is $6865N$ [75].

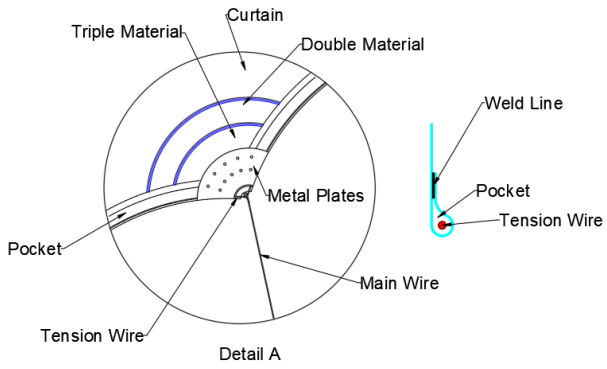

Figure 64: Curtain Reinforcement

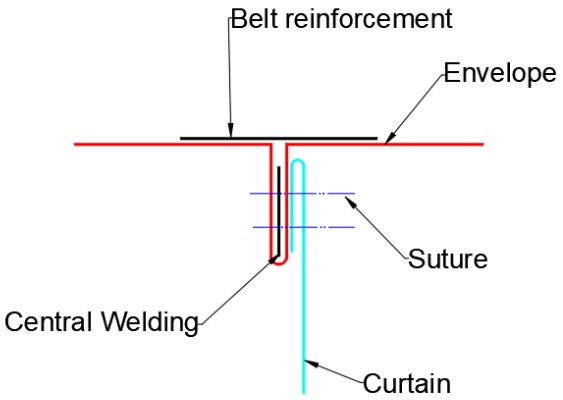

Figure 65: Curtain Attachment

5.11.2 Envelope membrane

This section presents the performance requirements of the envelope, its manufacturing process and a rough performance sizing and performance estimate.

Public data on the DARPA developed Integrated Sensor In Structure airship shows that envelope materials with aerial densities of less than 100 g/m^2 are achievable [76], [77]. This value of the areal density will be used as a reference when designing the composite fabric of the membrane.

The chosen structural material is Dyneema. Its very high tensile strength, low weight and low UV degradation make it ideal for lighter-than-air applications. The chosen type of yarn is SK99 as it provides the highest tensile strength of all of the available yarns. The material properties of this fiber can be seen in Table 32 [78].

Table 32: Dyneema Properties

Property	Tensile Strength	Tensile Modulus	Max Strain	Density	UV degradation
Value	4.1	155	3	0.97	80
Units	GPa	GPa	%	kg/m^3	%

[75] URL: http://www.vanbeelengroup.nl/products/rope/d12-sk78/item42 [Accessed on 20/06/2019]
[76] URL: https://apps.dtic.mil/dtic/tr/fulltext/u2/a510795.pdf [Accessed on 20/06/2019]
[77] URL: https://bit.ly/2Xuu90k [PDF Page 227, Accessed on 20/06/2019]
[78] URL: https://ea.newscpt.com/_fd/[nl_send_uid]/2711ad8ce5ab4999ec941356eaf00e40.html [Accessed on 20/06/2019]

The envelope is made out of a laminated membrane. The structure of the membrane consists of a load-carrying layer sandwiched between a base adhesive layer and an environmental protection and gas retention film. As stated at the beginning of this chapter, the structural layer can be either woven or not. A woven fabric suffers from crimp, which reduces the performance of the fabric, as seen in Figure 66, but it is easier to manufacture a bi-axially loaded membrane. A non-woven structural layer would have the same performance as the fiber, but it can only be loaded in one direction. This means that a second orthogonal layer is required [41].

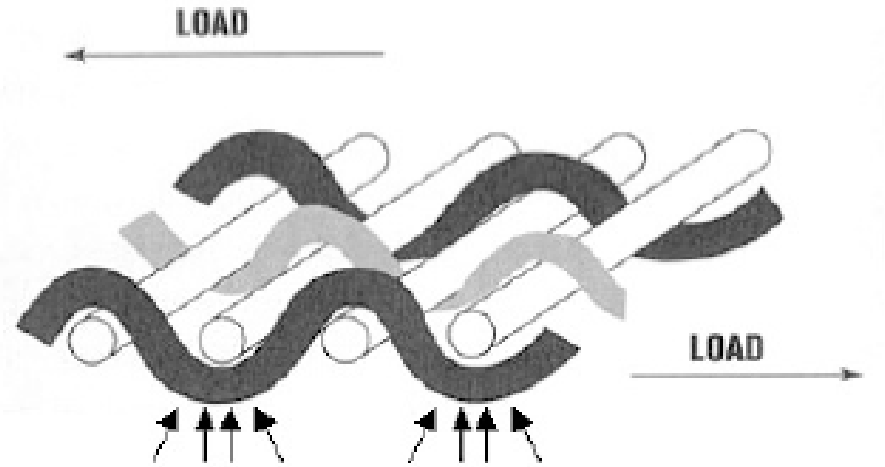

Figure 66: Crimp Diagram

Sizing of the envelope fabric has been done using the rule of mixtures. The formula used in this calculation method can be seen in Equation 5.77, where the variable E represents the tensile modulus and f is the volume fraction. This method assumes that each component carries a load proportional to its percentage of the volume. The output of this calculation is the thickness of the fabric, such that the strength and weight requirements are met as closely as possible.

$$E_{fabric} = f \cdot E_{fiber} + (1 - f) \cdot E_{film} \tag{5.77}$$

Based on the mechanical requirements presented earlier and the environmental protection film thickness requirement presented in Section 5.8 the composite membrane was sized. Table 33 presents the mechanical performance of each individual component and the mechanical performance and surface weight of the developed membrane. During the sizing process the adhesives layers were assumed to be negligible, as no information on type of adhesive that is used in such applications was found. The compliance to the requirements has been highlighted in green for compliant and red if the requirement is not met.

Table 33: Mechanical and geometrical properties of the proposed membrane

Parameter	**Value**	**Units**
Fiber Modulus	155000	MPa
Film Modulus	2068	MPa
Fiber Strength	4100	MPa
Film Strength	34	MPa
Film Thickness	0.0381	mm
Fiber Thickness	0.0519	mm
Total Thickness	0.09	mm
Strength requirement	106	N/mm
Membrane Strength	107	N/mm
Aerial Density Requirement	100	g/m^2
Achieved Aerial Density	152	g/m^2

As it can be seen, the strength requirement is met, but the membrane is overweight when compared to the reference. Further iterations of the environmental protection and envelope subsystems are required to converge the design. Possible solutions would be changing the fiber or changing the film layer. Research done by different companies and government agencies confirms that the weight of the material can be lowered, but no data regarding the film materials and volume fractions is given [41]. A similar membrane with the one presented in Table 33 was manufactured and documented in literature. This membrane used a Tedlar film with a thickness of $0.038mm$ and Vectran as the load carrying fiber. The achieved performance was a tear strength of $88N/mm$ and a fabric areal density of $106g/m^2$ [42].

The weight of the envelope is $1540kg$. This value is only for the structural layer of the composite envelope. The weight of the white Tedlar can be found in Section 5.8. The curtains have not been sized yet. The weight of the cables is $2kg$.

5.11.3 Engine pylon

This section will present an engine pylon concept and its integration with the envelope. Making a structural component that can accommodate a propeller with a diameter of about $5m$ while maintaining the weight minimum, distributing the loads over a large portion of the envelope and being stable is very challenging.

The proposed design is a truss structure. This decision was taken because it allows for a more flexible propulsion system design. Having the propulsion system attached to a single dedicated structure allows for more flexibility in the design. The only weak point of this frame is that it does not allow the propellers to rotate 180 degrees. The requirement to accommodate thrust vectoring rules out the other possibility: using the propeller duct as a structural component. This solution implies transferring loads from the propeller directly into the duct, which makes the iteration process much more difficult. Accommodating thrust vectoring would make the product much more complex. Models of the two presented concepts can be seen in Figures 67 and 68. At the time when the design was made, thrust vectoring was considered. Since this is no longer the case, the alternative design needs to be investigated further.

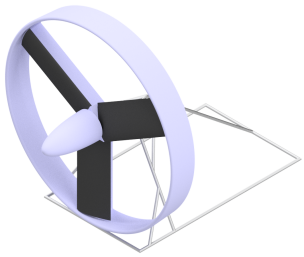

Figure 67: Proposed Design

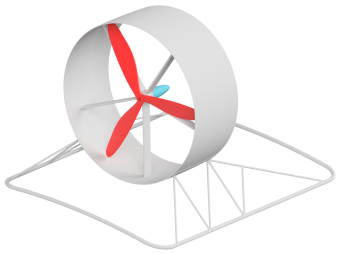

Figure 68: Alternative Design

The frame was developed using the Frame Design tools found in Autodesk Inventor. This software was chosen due to familiarity. The assembly workbench found in Inventor allows the user to easily make such a structure by defining a geometry in a reference part and add any beam found in its library of standardized frame members. Computing the loads on each member was also done using the same application.

The loads experienced by the pylon are assumed to be the generated by the weights of the propulsion assembly and the maximum thrust that can be provided. The values of those estimates were presented in Table 18. The weight acts at a 45° offset from the vertical axis. The maximum thrust acts parallel to the longitudinal axis of the airship in the direction of the tip. A safety factor of 2 was considered.

The Frame Analysis tool calculates the internal loading experienced by each member. The material used in the analysis of the frame is the Aluminum 7075 alloy. The results given by this tool were used as reference when deciding on the geometry of the beams. The loads at the interface between to members and the displacements were determined using Ansys structural analysis. Due to the lack of knowledge on how to use Ansys to its full potential and a lack of a complete geometry, the accuracy of the results is questionable and are used only as a reference. The displacemts presented by Ansys are exaggerated. A drawing depicting the geometry of the frame can be seen in Figure 69. The internal compressive loads and Ansys results can be seen in Figures 70 and 71. Since this is a metallic structure, the best way to manufacture it is welding the different beams together. The cross section of each member has a diameter of $76.1mm$ and a thickness of $2mm$. The final weight of the pylon is $44kg$. Those dimensions were taken from the $ISO10799-2$ standard and they comply with the no bucking requirement of such a structure. The Ansys simulation shows that stress concentrations occur at the welds, especially in the top part of the frame. It is therefore recommended to reinforce these locations. All of the above results are valid for the pylons mounted on the top of the airship. For the bottom mounted ones the direction of the weight must be inverted. The design of the propulsion system is not yet finalized, but the overall geometry of the frame is not expected to change drastically.

A concept of how the pylon is attached to the envelope is presented in Figure 72. This component is welded to the envelope and has not been analyzed further because its performance is strongly related to the envelope.

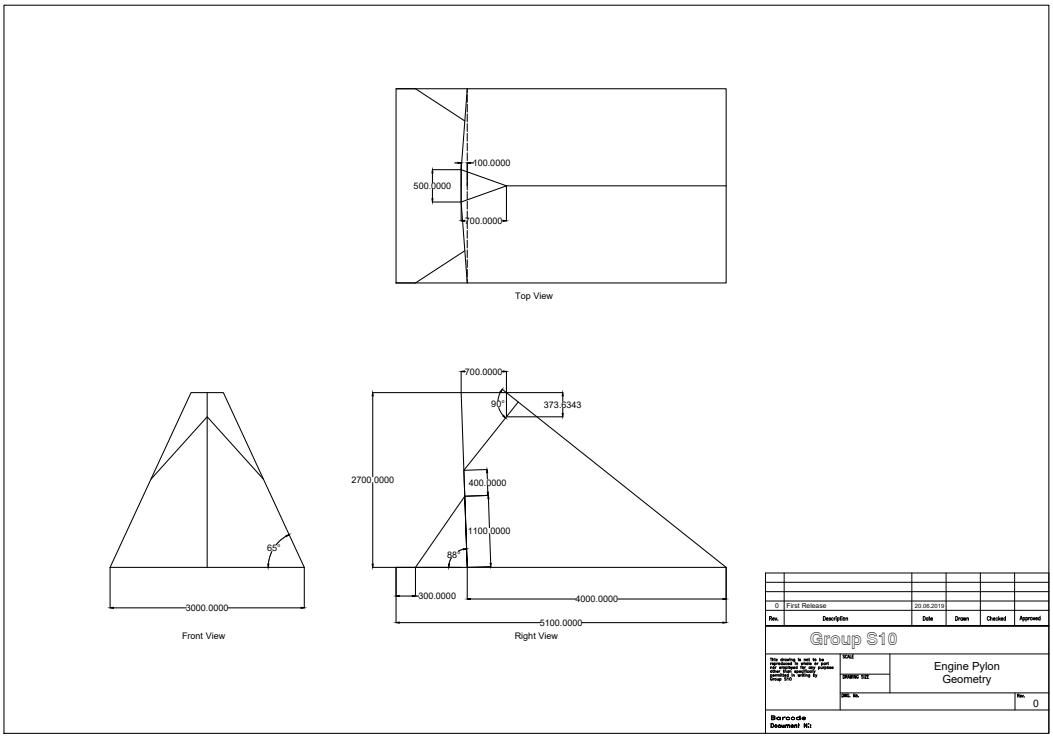

Figure 69: Engine mount drawing

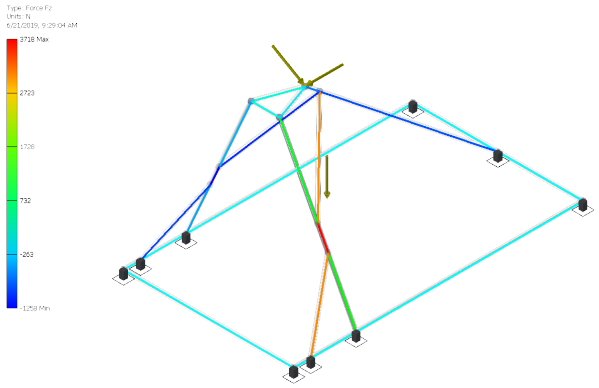

Figure 70: Engine mount axial loads

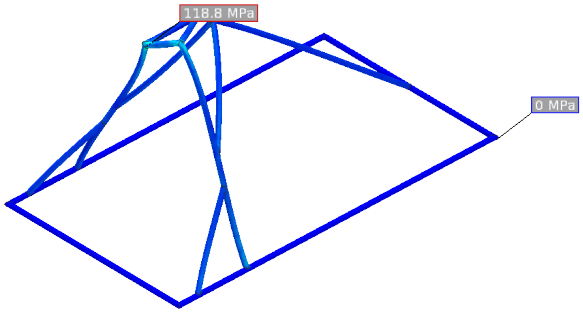

Figure 71: Ansys engine mount stress analysis

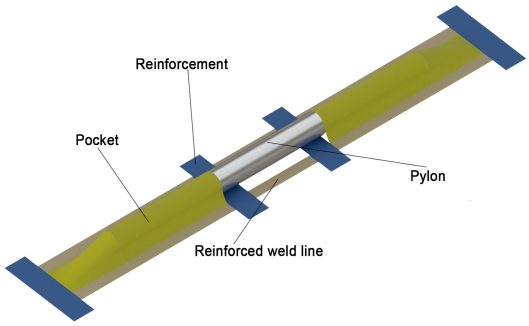

Figure 72: Engine pylon and envelope integration concept

5.11.4 Tail Surfaces

A mass estimate that is based on an actual structural solution, rather than statistical data was required to provide a starting point for investigating the possible concepts that can be used for the fins. There are two general solutions for the tails: an inflatable structure similar to that of the envelope or a rigid structure. Both solutions have been used in similar applications. The Zeppelin NT airship uses rigid tails accompanied by control surfaces while the Lockheed Martin HALE_D uses inflatable tails.

Since the tails have been designed with control surfaces in mind, the inflatable solution is automatically excluded. The loads experienced by the structure are the aerodynamic loads, taken from Section 5.6 and its own weight. The applied loads are small when compared to the size of the wings. The wing structure was designed for minimal weight while keeping the manufacturability in mind. The tip deflections and maximum stresses were evaluated as they could affect the aerodynamic performance of the components. Determining the area moment of inertia and area of the cross-sections was done using the MASSPROP function in AutoCAD. The cross-section is proportional with the airfoil that is used. The following assumptions were made:

- The wings were assumed to have no taper ratio, the chord is equal to the average chord of the initial design.
- The effect of the weight of the actuators is negligible.
- The wings were idealized as a cantilever beam loaded by a distributed load.
- The wings use a foam filled structure.
- The load taken up by the area of the moving surfaces is considered negligible.

A foam filled solution has been chosen because, as opposed to a conventional wing box, it does not require an investigation of the placement of the spars and stringers. This greatly accelerated the sizing process. The results of this estimate are to be used as a starting point for the design of the tails. Table 34 shows the mass of this type of wing. The skin is made out of a carbon fiber reinforced plastic with a density of $1155 kg/m^3$.[79] The foam is assumed to have a density of $33 kg/m^3$. Recommendations regarding a further design of this assembly are presented in Chapter 12.

Table 34: Foam filled tails mass and deflections

Parameter	Vertical Wing	Horizontal Wing	Units
Skin/Foam Thickness	1.2/15	1.2/15	mm
Skin Volume	0.238	0.093	m3
Foam Volume	2.963	1.159	m3
Skin Density	1155	1155	kg/m3
Foam density	33	33	kg/m3
Skin Mass	275	107.81	kg
Foam Mass	65.25	38.25	kg
Total Mass	340.25	146	kg
Maximum Stress	1.77	1.94	Mpa
Deflection	9.59	6.05	mm

5.11.5 Gondola

For the gondola only some rough sketches that show the placement of the equipment inside it were made. A more detailed presentetion of this component can be seen in Section 7.1. The weight of the gondola was assumed to be 15% of the weight of the components inside it [9] and a safety factor of 1.3 was applied. This resulted in a gondola weight of $571 kg$. The structure of the gondola needs to be further investigated to determine how accurate this value is.

5.11.6 Structure Costs

This section will present a material cost estimate for the envelope. The tail fins are ignored because, as stated in Section 5.11.4, a final design of these components has not been determined.

For the cost of the envelope the catalogue of extremtextil[80] was used as reference for the cost of Dyneema fabrics. Since the envelope uses an in-house developed membrane the cost was estimated using the largest cost found for lightweight fabrics. A value of 65.7 € per square meter was obtained considering a safety factor of 1.5. The total cost of the envelope is 1011.1 k€. While the white Tedlar is a component of the envelope fabric, its cost is presented in the thermal part of Section 6.1.

[79] URL:https://www.clearwatercomposites.com/resources/properties-of-carbon-fiber/ [Accessed on 20/06/2019]

[80] URL:https://www.extremtextil.de/stoffe/beschichtet/leicht.html?p=1&o=5&n=15&s=16 [Accessed on 20/06/2019]

6 System Integration

This chapter shows how the detailed designs of different subsystem, as documented in the previous chapter, combine to form the StratoCruiser. The mass, power and cost budgets are presented in Section 6.1. An overview of the software on board the StratoCruiser is given in Section 6.2. A sensitivity analysis of the system is performed in Section 6.3, and the interconnection and interfaces of the whole system are presented in a N2 chart in Figure 108 in the appendix.

6.1 Resource Allocation

In this section, the mass, power and cost budgets will be given for the entire system. Additionally, the mass and cost budgets are given for all the subsystems. The values in this section are estimations that are made to the best of the team's ability at this point in the design phase.
A safety margin of 5% is applied to the estimated mass of the StratoCruiser, as that is considered appropriate for aerospace systems in Post-Critical Design Review (CDR) phase [43]. The same margin is applied to the required power, while the safety margin for cost is set to 30%, based on average spacecraft mass growth at the CDR phase [44].

6.1.1 Mass budget

The mass breakdown in terms of the different subsystems of the StratoCruiser is listed in Table 35 and is graphically shown in the pie chart in Figure 73. Because the masses of the subsystems are still rough estimates at this point in the design phase, the total mass values from Tables 37 to 45 are rounded to two significant digits. The total sum of all subsystem is increased by a value of 3.5% to account for the mass of miscellaneous elements such as cabling, pipes, joints, etc. [9] to arrive at a final design value of 7700 kg. The majority of this mass is comprised of the structure of the airship and of the ADCS subsystem. The instrumentation subsystem, the part for which the airship is ultimately designed, only accounts for 5.1% of the mass of the entire airship. In the next section, the mass breakdown of each subsystem will be given.

Table 35: Mass budget for the StratoCruiser

Subsystem	Mass [kg]
Instrumentation	380
Thermal	1100
C&DH	3.7
TT&C	6.7
Propulsion	530
Structures	2100
Power	1400
ADCS	1100
Buoyancy control	430
Miscellaneous	230
Total	7300
Design Value	7700

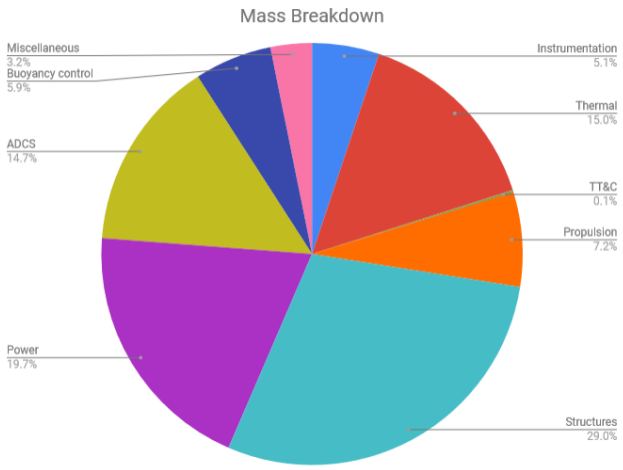

Figure 73: Mass Breakdown of the StratoCruiser

6.1.2 Cost breakdown

The total cost breakdown of the StratoCruiser is presented in Table 36 and Figure 74. Only material costs are listed here or off the shelf product costs for off the shelf products. A safety margin of 30% is applied on the total cost (excluding manufacturing costs) as explained earlier, and the final value is estimated to be about €3.6 mil. It can be seen that most of the cost is for the buoyancy control and structure subsystem, because of the significant amount of material than needs to be bought to produce the ballonets and envelope. More in-depth cost analysis, considering operational costs is performed in Section 10.1

Table 36: Cost Breakdown of the StratoCruiser

Subsystem	**Cost [k€]**
Instrumentation	222.4
Thermal	88.1
C&DH	1.1
TT&C	0.2
Propulsion	43.7
Structures	1011.1
Power	171.5
ADCS	182.0
Buoyancy control	926.3
Total	2730.2
Design Value	3549.2.0

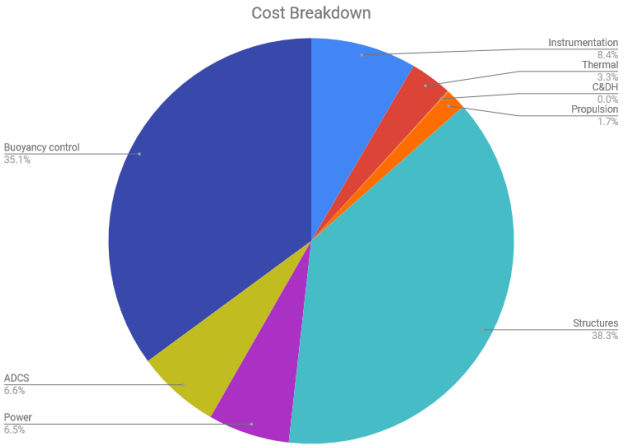

Figure 74: Cost Breakdown of the StratoCruiser

6.1.3 Subsystem Specific Mass and Cost Breakdowns

In this section, the mass and cost breakdowns of all the subsystems are given. The reasoning behind the estimated masses can be found in the section corresponding to the subsystem.

Instrumentation

Table 37: Instrumentation mass budget

Component	**Mass [kg]**	**Cost [k€]**
Mirror	20	62.0
Filter	20	100.0
Baffle	35	0.4
Sensor	0.03	20.0
Mount	300	40.0
Total	375	222.4

Thermal

Table 38: Thermal subsystem mass budget

Component	**Mass [kg]**	**Cost [k€]**
Liquid Nitrogen	24.1	-[a]
Cryosystem	270	85.3
Sensors	-	2.0
White tedlar	796	0.8
Total	1090	88.1

[a]Included in cryosystem cost.

C&DH

Table 39: C&DH subsystem mass budget

Component	**Mass [kg]**	**Cost [k€]**
Storage+CPU	1.3	0.5
PCBs	2.4	0.6
Total	3.7	1.1

TT&C

Table 40: TT&C subsystem mass budget

Component	**Mass [kg]**	**Cost [k€]**
Antennas	0.7	0.2
Mounting	6	-
Total	6.7	0.2

Propulsion

Table 41: Propulsion subsystem mass budget

Component	**Mass [kg]**	**Cost [k€]**
Blades	130.9	13.1
Motors	28	13.3
Motor Controller	23.2	10.9
Gearbox	20	0.6
Gearbox casing	58	0.1
Duct	33.6	3.3
Vectored Thrust	58.2	2.1
Pylon	176	0.3
Total	527.9	43.7

Power

Table 42: Power subsystem ass budget

Component	**Mass [kg]**	**Cost [k€]**
Solar Panels	504	114.0
Fuel Cell System	100	45.0
Hydrogen Tank	145	9.0
Oxygen Tank	27	1.7
Electrolyzer + Water Tank	140	0.5
"Fuel"	520	-
Total	1436	171.5

Structures

Table 43: Structure subsystem mass budget

Component	**Mass [kg]**	**Cost [k€]**
Gondola support	571.6	-
Envelope	1540.2	1011.1
Total	2111.8	1011.1

ADCS

Table 44: ADCS subsystem mass budget

Component	**Mass [kg]**	**Cost [k€]**
Daystar (3)	95.4	60.0
GPS receivers(2)	0.21	0.7
Gyroscope (2)	1.4	14.32
Tail surfaces	972.5	106.9
Total	1069.5	182.0

Buoyancy Control

Table 45: Buoyancy control subsystem mass budget

Component	**Mass [kg]**	**Cost [k€]**
Compressors	20	15.0
Valves	24	6.0
Ducts	57.6	14.4
Ballonets	330.9	890.8
Total	432.5	926.3

6.1.4 Power budget

The power budget of the StratoCruiser is listed in Table 46 and is graphically shown in Figure 75. The total power consumption of airship is equal to roughly 65 kW. The power subsystem is designed to deliver a little less than 68 kW as a contingency of 5% is taken into account. The majority of the power is consumed by the propulsion subsystem. The propellers require 55.6 kW of power when operating at maximum performance. This will, however, only occasionally be the required power for the propulsion subsystem as this is only required in cases of emergency when the airship must have an airspeed of 30.1 m/s. The other large contributor to the power budget is the thermal subsystem, which requires power to run the compressor that is used to by the cryocooler to cool the baffle and the mirror. The 7 kW as stated in Table 46 is, as for the propulsion system, the maximum power that is ever required to cool the instruments. This will occur during the day when the baffle receives both albedo radiation from sunlight that is reflected by the clouds and infrared radiation coming from the Earth. The incoming radiation will be substantially lower at night since there is no albedo radiation from sunlight that is reflected by the clouds.

The buoyancy control is not included in the power budget. The compressor has a peak power of 37kW. This is not included in the budget because this power is only used during descend. This is not continuous power during that the power subsystem must provide during the entire duration of the mission. The stored energy is enough for descending.

Table 46: Power budget for the StratoCruiser

Subsystem	Power [W]
Instrumentation	1500
Thermal	7000
C&DH	190
TT&C	9
Propulsion	55600
Structures	0
Power	0
ADCS	286
Buoyancy control	0
Total	64586
Design Value	67816

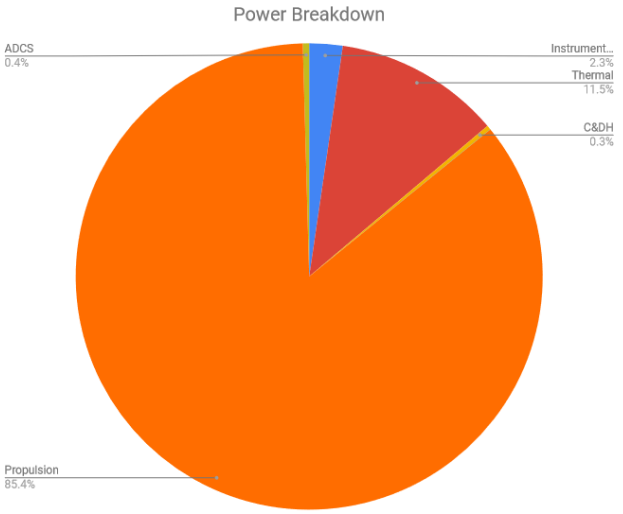

Figure 75: Power Breakdown of the StratoCruiser

6.2 Data, Communication, Software and Power Flows

As all modern systems, the StratoCruiser will receive, measure and process lots of data. Figure 77 provides an overview of exchange of information between the different system elements. The information from ATC is not part of this project. The ground station and on-board computer are. The ground station receives measured data, monitors the system and sends commands. These commands are determined by what the airship has to do at any given moment. The on-board computer performs the operations based on the on-board measurements and commands from the ground.

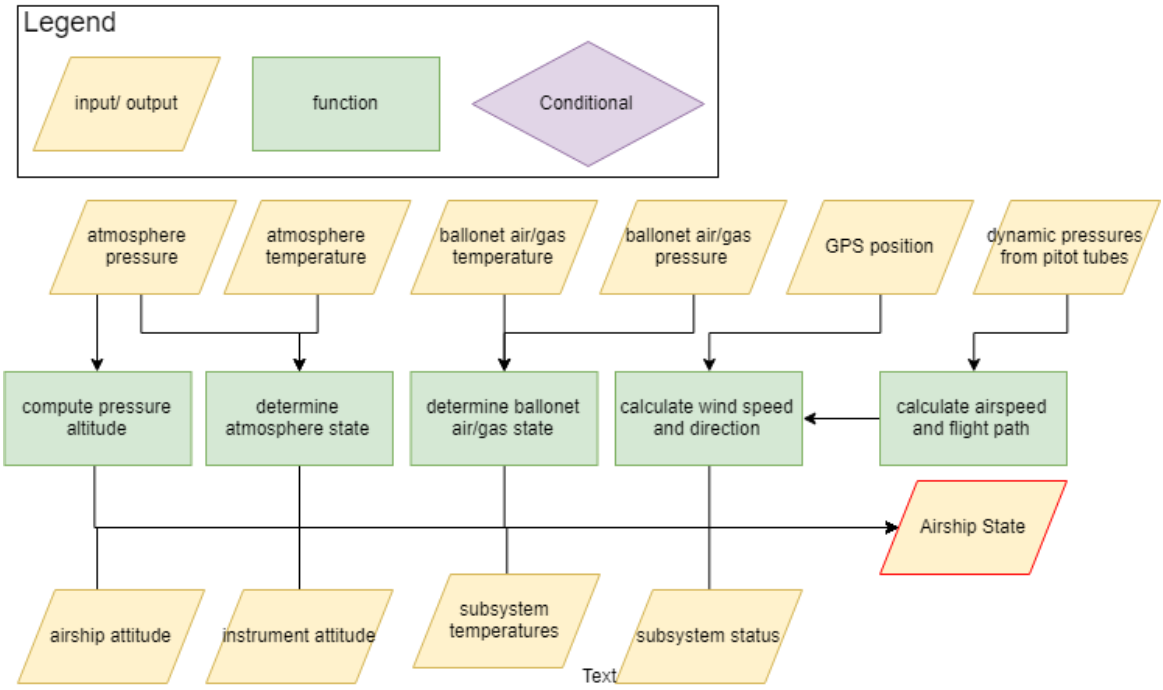

Figure 76: Information in the airship state

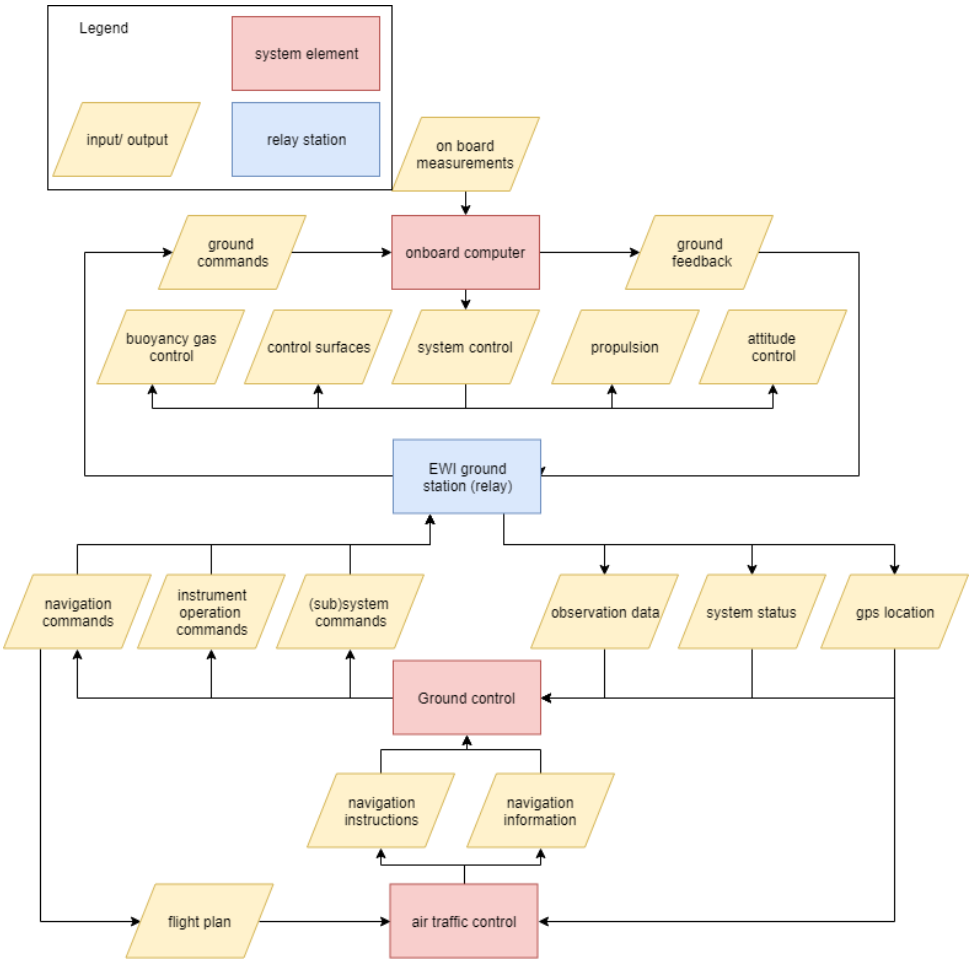

Figure 77: Communication Flow Diagram

Firstly, the airship calculates its state. The airship state is the collection of all on-board measurements processed into useful information as shown in Figure 76. The state is an input in other parts of the software and is continuously updates.

When the airship receives commands to observe a certain location, it needs to know 3 things, the target altitude, target location and the kind and number of images to take. The software is divided in three main parts. A navigation part to take to airship to the target location, the altitude control to go to the right altitude and the instrument part to perform the observations.

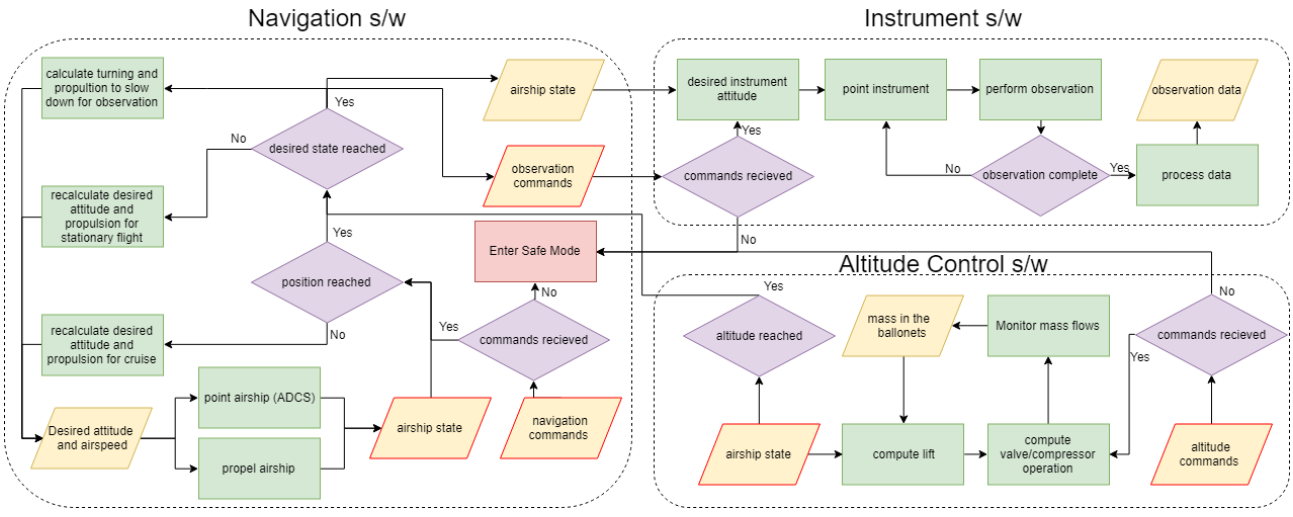

Figure 78: System Software Diagram

When the airship does not receive commands, it does not know what to do. In that case, it will enter the Safe Mode. In this mode, it automatically goes to 20.5 km which is a calm layer without air traffic or ATC. The instrument will not be active and the navigation will keep the airship in the same location while waiting for commands.

When an error occurs or something breaks down, the Safe Mode is also entered. The sequence of events then depends on what error occurred.

Other parts of software are related to monitoring and controlling the status of the airship. This includes thermal control, monitoring the power generation and consumption, etc. This is transmitted to the ground and gives a warning in case of anomalies.

The electrical flow diagram is shown in Figure 79. With this electrical architecture, a fail-safe philosophy shall be applied in the design.

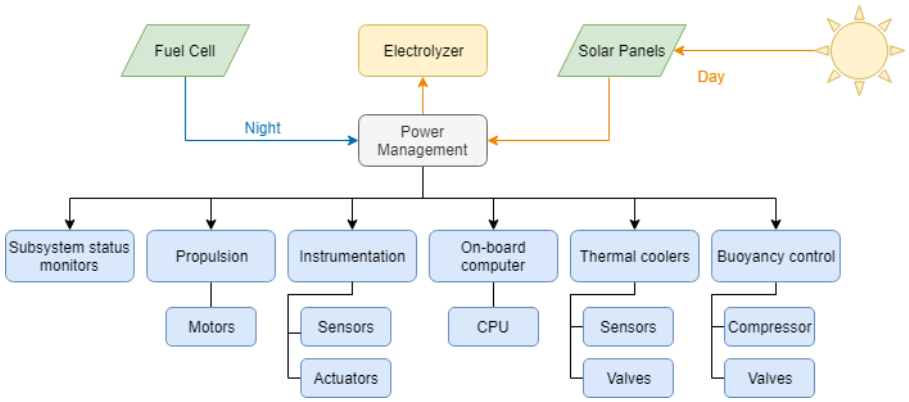

Figure 79: Electrical flow diagram

6.3 Sensitivity Analysis

In this section, the sensitivity analysis of the design is presented. The response of the system to a change of environmental parameters is presented, to show how sensitive the design is to unplanned changes. More in-depth analysis will be performed regarding the optical and stability performance of the system.

6.3.1 Optical Sensitivity

This section demonstrates the sensitivity of the SNR with respect to the following parameters: the ground temperature, the pixel temperature, the baffle temperature, the baffle length, the GSD, and the aperture. This is important to understand the process leading upto the final design of the instrumentation subsystem.

The sensitivity of the SNR to the temperature of the ground is visualized in Figure 80. It can be seen that the SNR decreases as the ground temperature increases. This is expected because as the ground temperature increases, it emits more radiation and as a result, the signal from the pixel becomes less distinguishable from the noise for the detector. It can also be seen that for the conditions specified in the figure heading, the ground temperature can be 296 K for the SNR of 100 to be met. This comes down to a temperature difference of 4 K, as the figure is valid for a pixel temperature of 300 K. This value was merely used for the sake of comparison.

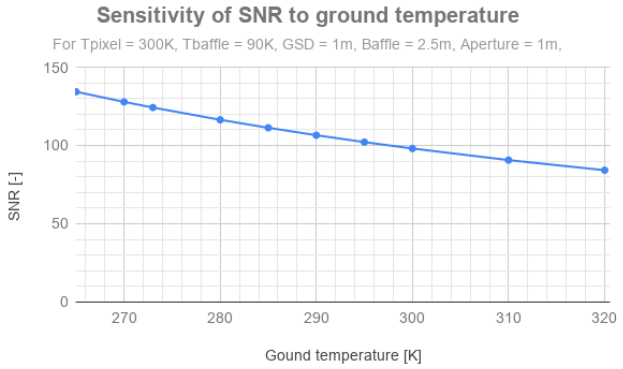

Figure 80: Ground temperature sensitivity

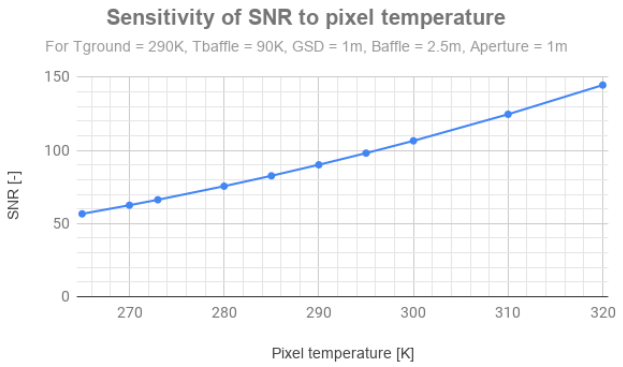

Figure 81: Pixel temperature sensitivity

The sensitivity of the SNR to the temperature of the pixel is visualized in Figure 81. As expected, the SNR increases as the pixel temperature increases, because a warmer pixel emits more radiation, which makes the difference in temperature between the signal and the noise larger. Upon comparison of Figures 80 and 81, it becomes apparent that the temperature of the pixel has a greater influence on the SNR that the temperature of the ground has. It can be seen that the magnitude of SNR varies more than in Figure 81 than in Figure 80. For the conditions specified in the figure heading, the pixel temperature can be 297 K for the SNR of 100 to be met. With the current design and the knowledge from Figures 80 and 81, it can be concluded that the instrument can take useful measurements with an SNR of 100 or higher for a combination of the ground temperature being 296 K and the pixel temperature being 300 K. As long as this 4 K difference between the two temperatures is maintained, increasing both temperatures will increase the SNR because the pixel temperature has a more dominant influence as established earlier. Therefore, this means that if an observation has to be made in an environment that is cooler than 296 K, the pixel temperature will have to be more than 4 K warmer than the environment in order to meet the SNR of 100, because the pixel temperature is more influential than the ground temperature. For a certain ground temperature, the minimum temperature that the pixel is required to be in order to have an SNR of 100 is shown in Figure 82.

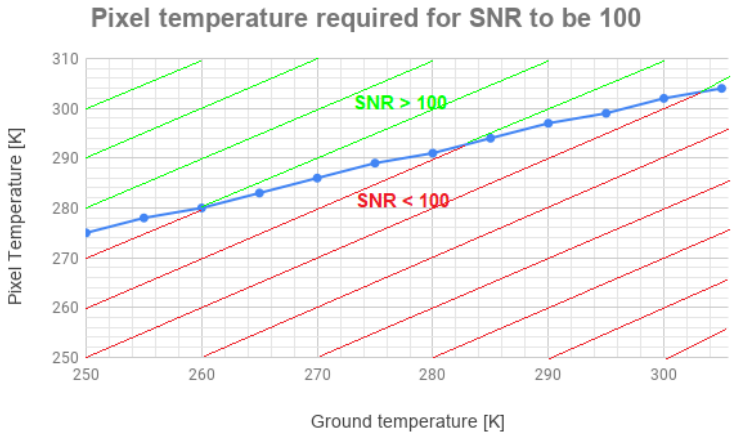

Figure 82: Required pixel temperature for certain ground temperatures

The ground temperature range covers all the temperatures that are expected in the Netherlands as it ranges from -23°C to 32°C. It can be seen that if the environment is too cold, the pixel has to be significantly warmer than the environment. As the temperature of the ground increases, the required difference between ground temperature and pixel temperature decreases. For the average temperature of the Netherlands, 283 K (10°C)[81], the pixel temperature that is required to produce clear images

[81] URL: `https://www.clo.nl/node/25690` [Accessed on 13/06/2019]

is 293 K (21°C). This means that, with the GSD of 1 m, objects like cars, trucks or ships can be observed, as their warm engines will produce radiation that is visible for the detector. This can be used to monitor traffic flows in and around cities, ports and borders.

The sensitivity of the SNR to the baffle temperature is shown in Figure 83. The SNR decreases as the baffle temperature increases. This is intuitive because the cooler the baffle, the less radiation it emits and the clearer the image will be. The non-linearity of the sensitivity stems from the fact that the baffle temperature does not influence all the noise sources. If the baffle is, for example, cooled to the absolute zero temperature, the noise from the ground is still present so there will still be some level of noise. As the temperature of the baffle is increased slightly, the noise from the ground is still the dominant source of noise and hence the SNR is not affected significantly. This reasoning holds until the noise from the baffle becomes large enough to significantly influence the SNR. In Figure 83, this point is around 90 K which is why the temperature to which the baffle will be cooled is set to this value. Cooling the baffle even further would not add to the SNR, while it would increase the power consumption of the thermal subsystem.

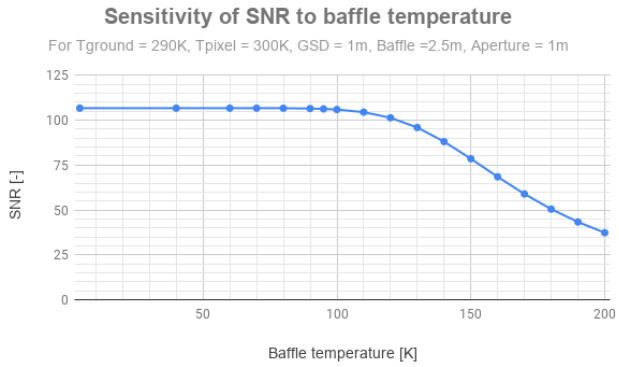

Figure 83: Baffle temperature sensitivity

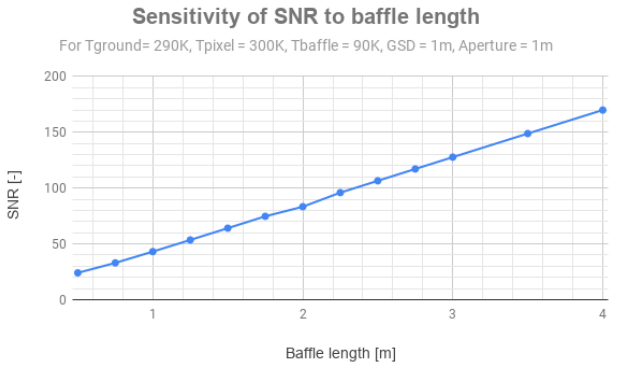

Figure 84: Baffle length sensitivity

The sensitivity of the SNR to the baffle length is shown in Figure 84. As the baffle length increases, the solid angle it covers increases which increases the SNR because the cooled baffle emits far less radiation than the warmer background. This increase is almost linear and it shows the necessity of the baffle in the instrument design. In order to meet the SNR of 100, it can be seen that a baffle length of 2.5 m is required.

The sensitivity of the SNR to the GSD is shown in Figure 85. Unsurprisingly, the SNR can be seen to be very sensitive to changes in the GSD, because an increase in the GSD means that the solid angle of the signal increases whereas the solid angle of the ground noise simultaneously decreases. This emphasizes the necessity of having to increase the GSD from 0.5 m to 1 m, as this contributes to an increase in the SNR from approximately 25 to more than 100.

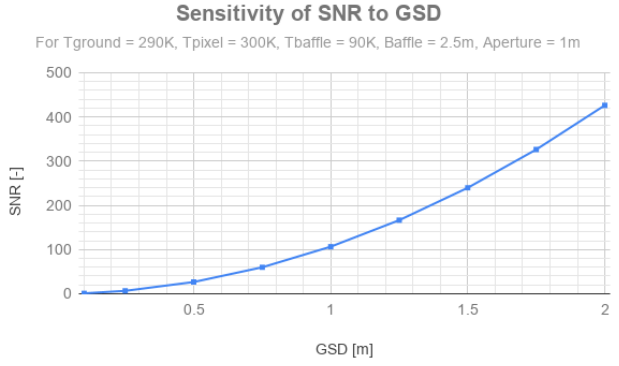

Figure 85: GSD sensitivity

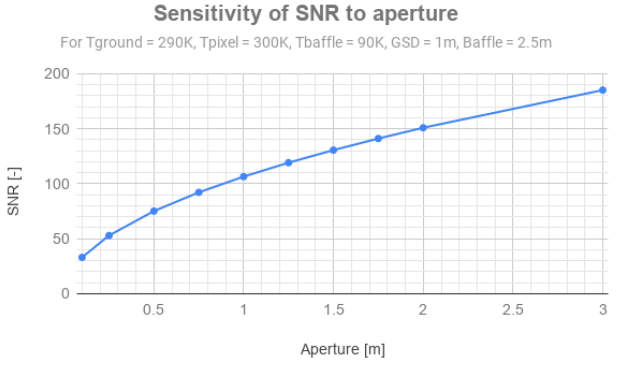

Figure 86: Aperture diameter sensitivity

The sensitivity of the SNR to the aperture diameter is shown in Figure 86. The SNR can be seen to increase with the square-root of the aperture. As the aperture increases, the signal received by the detector increases but the same relation holds for the noise. Given, however, that the noise is analyzed by the square-root of all the sources of incoming radiation, this relationship makes sense. In Figure 86 it can also be seen why the aperture of the primary mirror will be 1 m to meet the SNR of 100, whereas an aperture of only 0.3 m was required based on the diffraction limit.

6.3.2 Airship Stability Sensitivity

It is important to identify how much the stability of the airship changes when either the offset c.g. value [82] or the horizontal tail size changes. For the sensitivity analysis, The 'Wing and Plane Design' environment in XFLR5 has been used. Firstly, as Figure 87 shows, the obtained dimensions of the horizontal and vertical tails have been inputted into the program along with the chosen airfoil of NACA 0012.

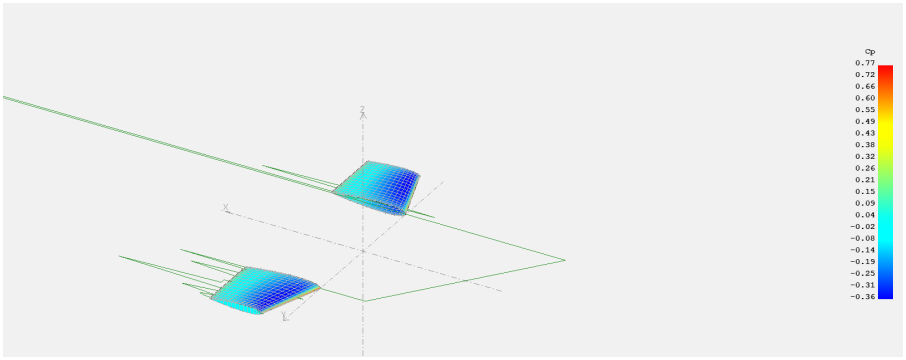

Figure 87: XFLR5 for the horizontal tail

The results of these are shown in Figure 88. The left figure of Figure 88 belongs to the vertical tail and represents the lift forces generated by a pair of the vertical tails. The right figure of Figure 88 is for the horizontal tail and represents the lift forces generated by a pair of the horizontal forces. The numbers, ranging from 0 to 30, positioned on each line, are rudder or elevator deflection angles in degrees.

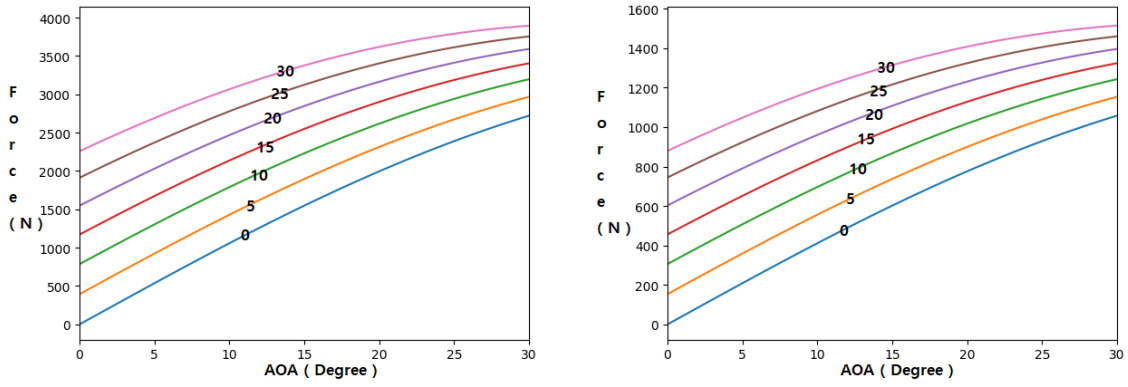

Figure 88: Results of XFLR5 analysis for the vertical and horizontal tails

[82] Offset: vertical distance between the center of buoyancy and the center of gravity

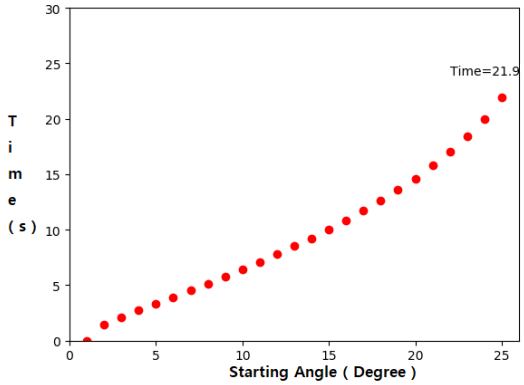

Figure 89: Recovery Yaw Rate

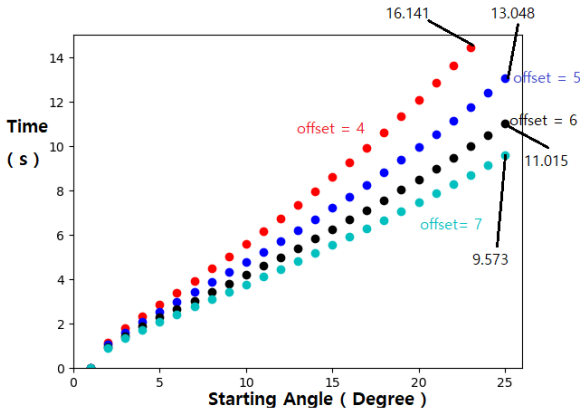

Figure 90: Time taken to return to zero sideslip angle for different offset values

By taking into account the hull aerodynamics, lift forces from the vertical tails obtained from Figure 88, added mass effect taken into account with $C_{N_{\dot{r}}}$), and propulsion, the time it takes to return to zero sideslip angle from any sideslip angle ranging from 0 to 25 degrees are shown in figure 89. For the airship to return to zero sideslip angle from 25 degree of the sideslip angle, it takes 21.9 seconds.

For the pitch angle, taking into account the hull aerodynamics, lift forces from the horizontal tails obtained from Figure 88, and added mass effect taken into account with $C_{m_{\dot{q}}}$ leads to the time it takes to return to zero pitch angle from any pitch angle ranging from 0 to 25 degrees. The results for three different offsets are shown in figure 90. For the offset value of 4 meters, it takes 16.141 seconds to return to the zero pitching angle from the starting pitching angle of 25°. For the offset of 5 meters, it takes 13.048 seconds. For the offset value of 6 meters, it takes 11.015 seconds. 9.573 second is taken for the offset value of 7 meters. This analysis shows how having different offset values significantly change the pendulum moment and therefore the longitudinal stability.

Figure 91 shows how the decision to decrease the horizontal tail in subsubsection 5.6.7 impacts the longitudinal stability with the common offset value of 6.66 meters. It can be seen that by decreasing the horizontal tail, the time it takes to return to zero pitch angle has increased by 2.83 seconds. Therefore, the longitudinal stability of the airship must be carefully designed by changing the offset or the horizontal tail size and location.

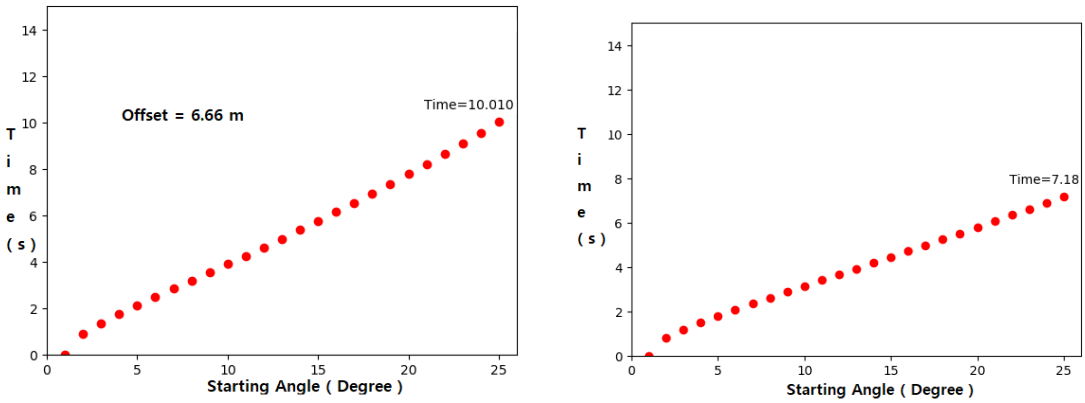

Figure 91: Comparison of performances before and after the Horizontal tail sizing change

6.3.3 Airship Temperature Sensitivity

The state of the gas and air in the airship change when their temperature changes. The buoyancy analysis in Section 5.2 assumed that the temperature of the gas and air in the airship are equal to

that of the atmosphere. In Section 5.8, it was shown that the temperature of the skin can go up to 44 K higher than the atmospheric temperature. Naturally, the temperature of the gas will approach this temperature as well. In this case, if no air is allowed to escape from the ballonets, the lift will stay to same. In that case, the temperature increase will cause the over-pressure to increase. Figure 92 shows that the over-pressure increases linearly with temperature. It can be seen that the sensitivity of pressure to a temperature change is 250 Pa/K. Section 5.11 shows that the maximum over-pressure is 1500 Pa, meaning that the temperature is allowed to increase by 60 K. Therefore, as the over-pressure increases, the structural design should also be changed to accommodate such pressure changes. Therefore, it can be said that the structural design is also sensitive to temperature increases.

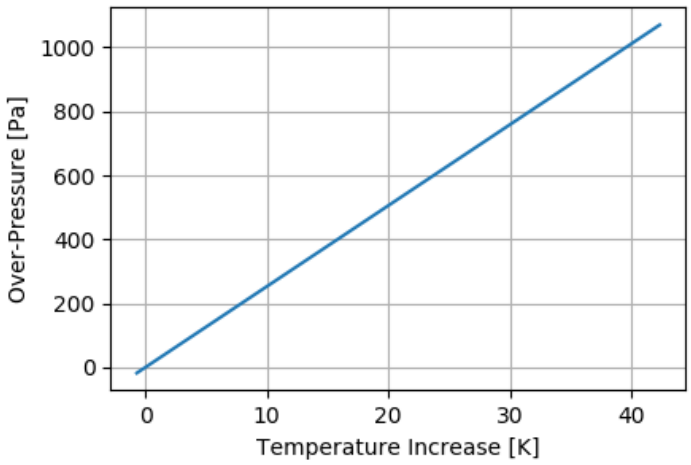

Figure 92: Over-pressure increases with increasing temperature. Lift stays constant.

7 Final Design

The system integration was explained in Chapter 6. This section presents the final design as a whole and discusses its performance and production plan.

7.1 Configuration

The configuration of the StratoCruiser will be presented in this section. The placement of the gondola, propulsion system and tail fins will be presented. The configuration of the gondola and envelope will also be discussed.

Figure 93 shows the layout of the entire airship. The tail fins and propellers are at fixed positions longitudinally. Their coordinates are 170.536 m and 104.33 m respectively from the nose of the airship. The propulsion system is placed at a 45 °angle in its respective quadrant. The gondola is placed at 44 m from the nose and is used to balance the airship, as the center of gravity of the airship must have the same longitudinal coordinate as the center of buoyancy to maintain pitch stability. The ballonets, which are part of the internal structure of the envelope, can also be seen represented with the dotted lines.

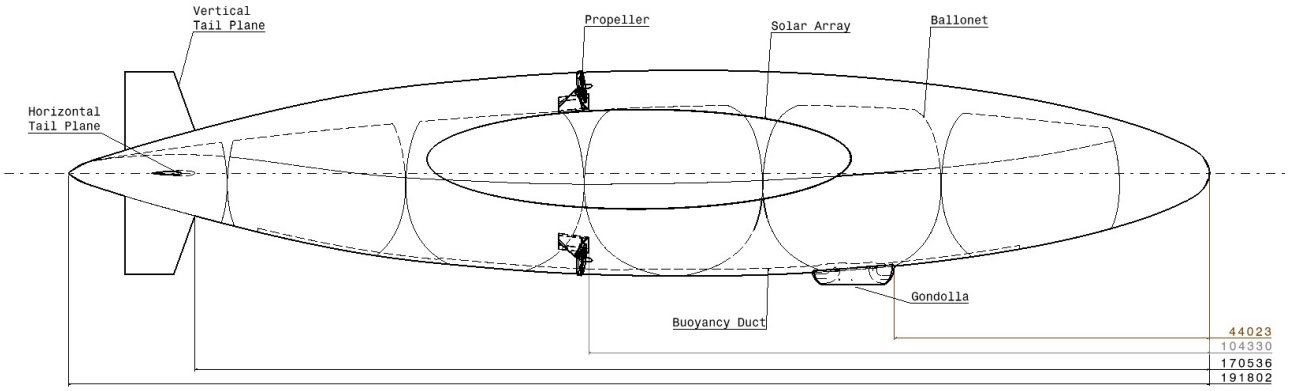

Figure 93: Airship Side View

Figures 94, 95 and 96 show the internal layout of the gondola. The components of the gondola are attached to the bottom of the envelope and as close as possible to the center line of the airship to avoid a shift in center of gravity. The layout of the structure used to provide attachment points can be seen in the top view. The longitudinal beams are fixed to the envelope and function as rails for the cross mounted ones. This allows for a highly modular configuration. The position of each component that goes into the gondola can be easily changed and, in case additional equipment needs to be added, more cross beams can be attached. Attaching the equipment vertically to each other is also an option.

The antennas are placed on the outside of the gondola and can move freely such that communication with the ground segment is possible at all times.

The side view shows that the gondola is mostly empty. This means that the geometry can be further optimized to achieve a better aerodynamic performance and lower mass.

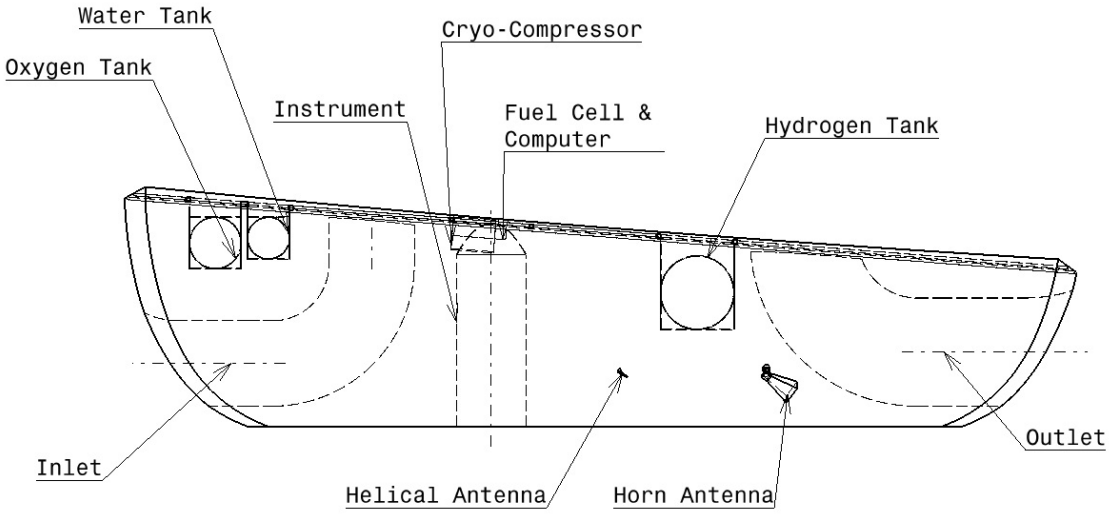

Figure 94: Gondola Side View

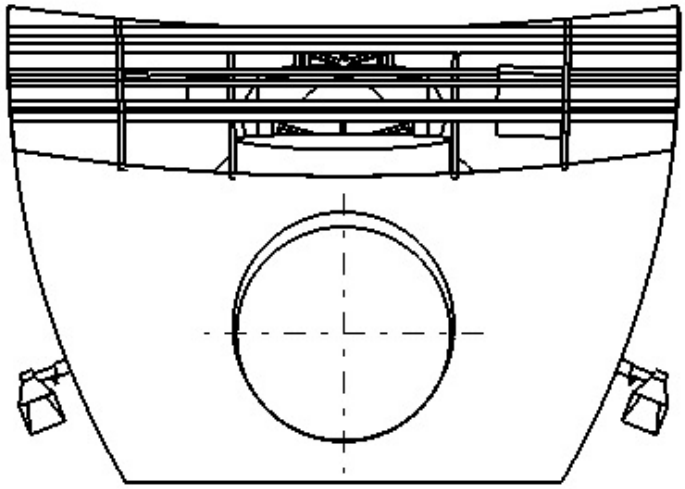

Figure 95: Gondola Back View

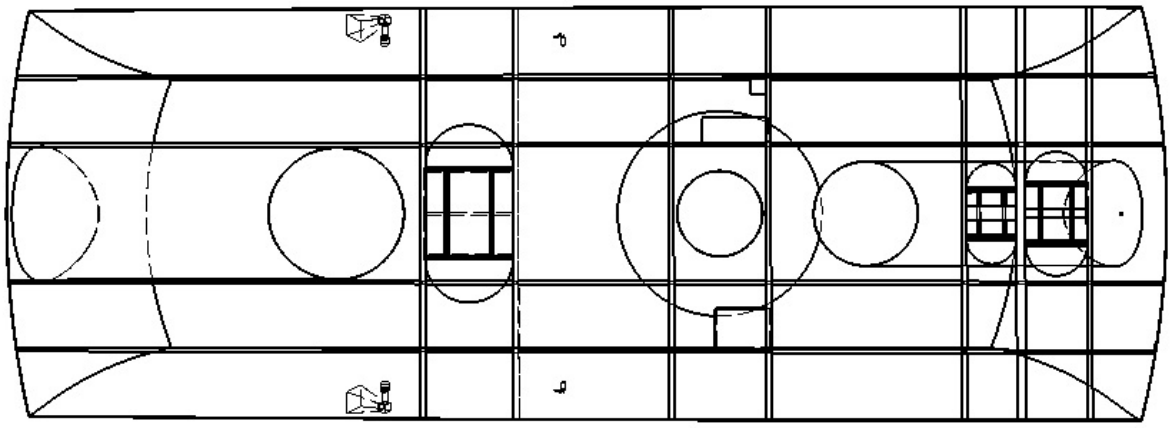

Figure 96: Gondola Top View

The section of the bottom of the gondola through which the instrument looks towards the ground should be transmitting LWIR. Infrared transmitting plastics are commercially available and are much cheaper than for example optical Ge filters. An example of such a plastic is the polycarbonate LEXAN HSP6-1125.[83]

7.2 Performance Analysis

The performance of the StratoCruiser will be discussed in this section. Ultimately, the airship is designed to perform TIR EO for as long as possible. Therefore the performance analysis will partly look at the performance of the instruments that are responsible for EO and at the aerodynamic performance of the airship. Table 47 summarizes the system characteristics. These numbers give a quick overview of the system. They include dimensions, flight performance, mass, power and observation quality.

Table 47: System Characteristics

Volume	108 170m^3
Length	192 m
Max diameter	34.6 m
Cruise speed	21 $\frac{m}{S}$
Climb/descend speed	1.5 $\frac{m}{S}$
Service ceiling	20.5 km ISA
Mass	7700 kg
Payload mass	375 kg
Hydrogen mass	612 kg
Power	68 kW
Payload power	1.5 kW
Observation band	8-12 µm
Pointing accuracy	4 $arcsec$
GSD	1 m
Observation SNR	102

The final design of the instrumentation subsystem is documented in Section 5.3. With this design, the instrument is able to take TIR images of the Earth's surface with a resolution of 1 m. The detector pixels are merged in a 4x4 configuration to form 512x512 superpixels from the original 2048x2048 pixel array. Since each of these 512x512 pixels cover an area of 1 by 1 meter on the ground, one image will cover 512 by 512 meters or 0.26 km^2. For various ground temperatures, the minimum required pixel temperature in order to take measurements is given in Figure 82. The higher the pixel temperature, the more distinctly visible the observed object will be from its environment. For all temperature ranges in the Netherlands, objects like cars, trucks and ships will be visible for the instrument. This means the airship can be used to monitor traffic flows in and around cities, ports and borders.

The instrument mounting, as documented in Section 5.4, ensures the stability of the mirror while it also allows it to rotate up until the maximum off-nadir angle. By doing so the instrument can cover more area without moving the entire airship. The mounting is designed to take 100 pictures within a minute, which means that an area of 26.1 km^2 can be imaged per minute without having to move the airship. As an example, this means that the whole of Delft can be monitored every minute with a resolution of 1 meters, if there is an event of interest. Comparing this to the performance of EO satellites such as the TUBIN and FireBIRD mission shows that the StratoCruiser lacks performance on the swath width but exceeds the performance of both satellites on the GSD and the temporal resolution [45] [46]. This emphasizes the value of the StratoCruiser, which mainly manifests itself in accurate monitoring services.

[83] URL: `https://www.gsoptics.com/transmission-curves/` [Accessed on 14/06/2019]

Besides the performance of the instrument, the aerodynamic performance of the airship is of importance for a competitive design. Requirement **SB-Sys-12** states that the endurance of the airship shall be at least 2 months [18]. This final design actually exceeds this requirement as there is almost nothing limiting the endurance of the airship. The buoyant lift does not require an airspeed that relies on fuel consumption and the solar cells are designed such that they generate enough power for all the subsystems throughout the entire year. The only factors limiting the endurance are the leakage rate of hydrogen and the degradation of the solar cells. However, the leakage rate of hydrogen is only 0.18 kg per 6 months which has a negligible effect on the lift produced by the 612 kg of hydrogen and the degradation of the solar cells is 4% per year which decreases the power generating efficiency by 1%. The safety margin in the design of the power subsystem accommodates this lower efficiency for 2 years, which would thus be the theoretical endurance limit of the airship. At that point the airship would have to be brought down and the solar cells will have to be replaced or repaired. In practice, the endurance will be lower than this, especially the first few years of operations. During the testing phase of the airship, the endurance will be at most a few days upon which the design is analyzed, evaluated and possibly iterated. Gradually the flight time will be increased until the airship will be fully operational for 6 months.

Another aerodynamic aspect of the airship's performance is the manoeuvrability. With the design of the tail as documented in Section 5.6, the airship can turn 180° in 2 minutes. The ballonet design allows the airship to ascend and descend with a vertical speed of 1.5 m/s, which makes it possible to reach the cruise altitude within 4 hours. The time it takes the cryogenic instruments to cool the baffle is 15 minutes. Therefore, the cooling of the baffle has to start just before the cruising altitude is reached. Once at cruising altitude, the nominal cruise speed of the airship is 21 m/s. When the propellers operate at maximum thrust, the airspeed can be increased to 30.1 m/s, the maximum airspeed of the StratoCruiser. When this speed is compared to the highest airspeed that is ever measured for an airship, which is 115 km/h or 32 m/s[84], it can be concluded that the manoeuvrability of the StratoCruiser meets the market standard.

Concluding, the imaging performance of the StratoCruiser exceeds that of satellites that are used for EO on resolution and revisit time. The swath width of the imaging instrument is lower than that of the satellites but that shows that the opportunity for the StratoCruiser in the market for EO lies primarily in monitoring services. The aerodynamic performance of the airship emphasizes this as the unique selling point of airships is that they can hover at a fixed spot whereas airplanes and satellites are moving at all times.

7.3 Manufacturing, Assembly and Integration

The manufacturing process and the challenges involved in the production of an airship the size of the StratoCruiser will be discussed in this section. A more detailed analysis of the production will only be made for the envelope. This decision has been taken because the envelope is the most fleshed out component, while the others are still under development. The proposed manufacturing method is a compromise between a traditional production line, where a part moves around between dedicated stations, and a shipyard, where the production line moves along the finished product. This decision was taken due to the size of the airship.

Assembly of the envelope will be done by welding together sheets of envelope fabric. Since both Dyneema and Tedlar are thermoplastic materials, Ultrasonic or RF welding can be used to produce the envelope. The joining technology is critical for the performance of the envelope. Since the loads act continuously through the entire envelope, the seams must be able to transfer those loads from one piece of the envelope to another one. It is therefore important that the mechanical properties of the finished weld must be at least equal to those of the base fabric. In lighter-than-air applications butt joints and lap joints are typically used [42]. Figure 97 [47] present those two types of joints. While the manufacturing process of the envelope is relatively simple, the final seams that finalize the production of the envelope are the most challenging ones to make due to the massive size of the skin. The same

[84]URL `https://www.guinnessworldrecords.com/world-records/fastest-speed-for-an-airship` [Accessed on 21 June 2019]

process is applied to the ballonets as well.

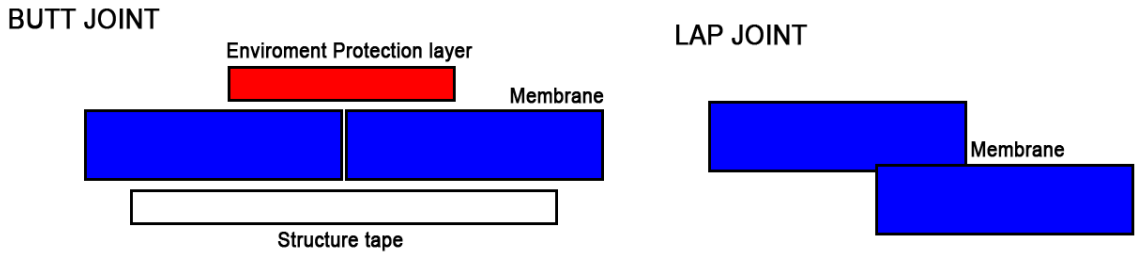

Figure 97: Butt and Lap Joints

An airship the size of the StratoCruiser with a flexible structure has never been manufactured and tested before. Specialized equipment will most likely be required to achieve this. An example of such equipment would be a rig that supports the envelope during its manufacturing process. Moving around the approximately $2000kg$ $191m$ long envelope is very challenging as it poses a severe safety hazard.

The manufacturing steps are as follows:

1. Prepare the material for assembly by cutting it and marking the weld locations and other attachment points. inTENS provides accurate cutting patterns that take into account the overlapping required by welding and optimizes the cuts such that folding does not occur.
2. Attach the sub-components to each slice of material.
3. Attach the junctions for the tail elements.
4. Weld the curtains that support the internal chords and the ballonets.
5. Weld the slices one by one.
6. Insert the ballonets.
7. Connect the ballonets to the inflating and deflating ducts.
8. Make the last seam.
9. Manufacture the gondola separately.
10. Attach the gondola.
11. Seal the connection between the balloon and the gondola.

8 Verification and Validation

This section presents the verification and validation steps taken and planned. This is important in order to make sure that the designed models and supporting calculations do, in fact, perform their designated task and are useful in practice.

8.1 Verification

Verification is required to make sure that the methods used in the design process are correctly applied. The following sections summarize verification procedures applied to subsystem design.

8.1.1 Buoyancy Contro

In the analysis and design of the buoyancy control subsystem, several Python scripts were written. Each script contains a set of functions or a class with functions. These must be verified to make sure they are correct such that they can be used with confidence. This section explains how the codes were verified.

As a first step, all scripts were visually checked for errors and formulas were derived by hand and double checked. The results of the functions are plotted and evaluated with a critical mindset. If the behaviour of the plots is not understood, this might indicate errors.

The first script is the "Atmosphere.py" file. This file contains a function that calculates the air properties at different levels in the ISA. Air properties were plotted as a function of altitude and compared with other ISA tables.

Next is the "Gas.py" file. This file contains the "Gas" class, defining an amount of gas in a given state and functions to change the state of the gas. Each function was checked using simple inputs and checking by hand. The inputs are specific gas constant R, pressure p, temperature T and mass m. A simple input was [R=1, p=1, T=1, m=1]. The volume of this is 1. The function "set_volume_p(2)" will set the volume to 2 while keeping pressure constant. After applying this function, m=2. Also corner case inputs were considered. both mass and volume are allowed to be 0 or positive. The other properties are always positive. The functions were also tested with these values at 0.

"Lift.py" is the most complex piece of code used in buoyancy control. It contains the "Combined_gasses" class and functions to change balloon properties. The inputs to this class are lifting gas mass m_g, lifting gas specific constant R_g, and total volume V_tot. The functions were also subjected to unit and corner case inputs. An example of such test is for the "calc_lift(alt)" function. This is a good example because this function uses other functions as well. Theoretical derivations showed that lift is constant with altitude until the total volume is completely occupied by the lifting gas. Then lift starts decreasing. An internal over-pressure decreases lift. This is also what was found from the simulation. For an example input, one might take the mass of hydrogen with a volume of $1m^3$ and temperature and pressure equal to ISA values at 1km altitude. The lift below 1km can be calculated by hand. At 1km lift starts decreasing. The additional mass of air with an over-pressure of $1000Pa$ can be calculated by hand. This equals to reduction of lift when this over-pressure is applied. A corner case is when the volume of the lifting gas exceeds the total volume of the airship. In this case, the code recalculates the pressure such that the volume of the lifting gas equals the total volume. Another corner case is when m_g equals zero. In that case lift=0 at all times. The other inputs are always positive.

The last file, "independent_aero_relations.py", contains some functions that calculate relations that apply to balloons in general whereas "Lift.py" applies to a balloon with given properties. These were also tested with unit and corner case inputs.

The ducts and valves were sized based on their required mass flow. A CFD analysis with the compressor represented as an actuator disk should verify whether the design mass flows is reached. This was not done due to time constraints. Using this, the ducts can be further optimized.

8.1.2 CFD Simulations

It is critical to properly verify the CFD to make sure that the boundary conditions are set correctly and the simulations are properly converged. The convergence of the simulation is dependent on the size of each mesh element. It is usually expected that for a higher number of mesh elements the solution approaches reality. Due to time and hardware limitations, the maximum number of mesh elements is limited to about 6 million, and therefore the simulations results will always vary slightly from reality. This error will be quantified in two steps: first the best simulation results are compared to analytical models to make sure that the CFD simulations were set up correctly, and then a mesh convergence study will be performed. ANSYS is a widely used commercial software, therefore it is assumed that it is properly verified and no additional model verification will be performed.

In order to make sure that the simulations are set up correctly, it is important to compare the results with an analytical model, in order to make sure that a similar value/order of magnitude is obtained. This helps to understand if the simulation is configured correctly. The envelope drag obtained from Equation 4.8 was compared to the results obtained from the CFD. The value coming from the semi-empirical model will not be very accurate but it will come close to a real value, therefore the drag coefficient calculated from the CFD simulations should be similar. The comparison is presented in Table 48. The drag coefficient are referenced to the $Vol^{2/3}$, as explained in Section 4.3. The difference is defined as the relative change between the CFD drag coefficient and the semi-empirical drag coefficient.

Table 48: Difference between CFD results and semi-empirical model.

Shape	FR	Volume $[m^3]$	Re	CFD C_{DV_0}	Semi-empirical C_{DV_0}	Difference [%]
Ellipse	6	123213	5.63E+06	0.0273	0.0261	4.38%
NPL	6	123259	5.63E+06	0.0267	0.0261	2.34%
GNVR	6	123108	5.62E+06	0.0272	0.0261	4.12%
Ellipse	5.5	123048	5.62E+06	0.0266	0.0259	2.88%

It can be seen that the volume changes slightly between shapes because of 3D modelling inaccuracies, but this does not significantly affect the results as the Re remains similar and the drag coefficient is scaled with respect to the volume. It should be noted, the volume used is the one from a previous iteration, but it was observed that results were independent from the airship size. It can be seen that the results are quite similar, therefore the conclusion is that the CFD simulations are set up correctly and are modelling the appropriate situation. Additional proof of this is be presented in Section 8.2.1.

A Mesh convergence study is always needed to quantify the discretization error, which can arise from inability of the mesh to properly represent a geometry or by inaccuracies due to insufficient refinement in region with high physical gradients [48]. This is done by simulating the same problem with different meshes, with a different degree of refinement. This analysis was performed on the full model described in Section 5.1.5. As previously stated, the finest mesh was limited by available time and computational power available. It is not expected to have obtained a fully converged simulation with negligible discretization errors, as better hardware would be required for that. The results of this mesh convergence study are presented and displayed in Table 49 and Figure 98. It was decided to analyze the convergence of the drag force as that is the most interesting result of the CFD simulations.

Table 49: Mesh Convergence Results.

Number of Mesh Elements	Drag [N]
6333218	1145
3144563	1165
2004171	1178
625445	1192
273354	1228
186542	1240

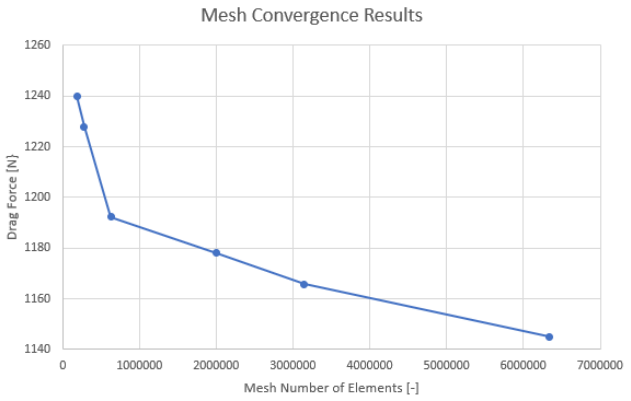

Figure 98: Drag Force against number of elements in the mesh

It can be clearly observed that the drag decreases as the number of elements increases. This means that the discretization error produces an overestimation of the drag. The drag curve closely resembles a negative exponential function, which reaches an asymptotic value as the number of elements in the mesh approaches infinity. The asymptotic value represents the correct result of the simulation, but because of hardware limitations it cannot be achieved. By looking at the graph it can be observed that the drag is starting to approach the asymptotic value, which means that the error fairly acceptable. Furthermore, the drag will be always overestimated, therefore it is okay to accept the discretization error as it will only produce a slightly over-designed design (less required power and thrust).

8.1.3 Solar Array Mesh

The surface mesh model has undergone multiple verification procedures at every single stage in its development. This was done in order to make sure that subsequent steps were built upon correct data inputs.

Various unit tests were performed within the surface simulation. As such, the solar angles were thoroughly verified and plotted. Subsequently, built upon that, the correctness of the Sun vector decomposition into unit vectors of the airship mainframe axis has been verified. Using a coarse mesh aided in the visual inspection of the model. After that, the incidence angle on each specific surface patch can be manually verified for specific cases.

At a larger scale, the plot of the power output of the solar array as a function of time of the day may be employed to check for model correctness. It has been established that, due to symmetry, power production must be symmetrical, i.e., power output in the morning should be equal to the one in the evening. Similarly to the CFD verification, a convergence analysis is done to check whether a smaller mesh size is indeed closing on onto a limit value.

Performing these checks allowed for the verification of individual building blocks of the numerical script as well as for the verification of the model as a whole. As such, the simulation is deemed to produce meaningful results, however further verification by means of comparing with similar models may be advised.

8.1.4 Instrument Integration

Although this part of the design was not reliant on complex numerical models, essential verification procedures are still conducted in an attempt to ensure correct results.

The main form of verification were unit tests; calculations regarding the kinematics and capabilities of the mount were conducted first by hand, and then both in Python and Excel. Several unit tests were conducted in Python during the construction of the sensitivity plots by running individual lines of code and checking whether the results match calculations done by hand.

Sensitivity plots were verified by visual inspection.

The design of the mounting was verified by comparison with commercially available actuators and correspondence with companies that manufacture systems of similar capabilities.

8.1.5 Propulsion

Verification of the propulsion subsystem concerns itself with the question whether the sizing of the diameter in section 5.5.2 is able to provide enough thrust for the airship. This is the central requirement for the propulsion subsystem. Potential errors may have stemmed from the fact that the design charts shown in Figure 33 are not finely represented. To verify the level of thrust, the performance chart given in Figure 34 and the method described in Section 5.5.3 are used. It can be seen from the maximum thrust level, that the thrust it provides meets the requirement.

Currently, not enough emphasis is paid to the blade design of the propellers. The design so far was based on the experimental data of a specific blade configuration. However, to investigate such things as the effect of twists, different thickness and chord combination, and different airfoils, it is crucial to develop a tool using the blade element theory. After such code is developed, the verification of this tool would entail checking whether the blades designed with the help of this tool meet the requirements set forward. This would mean verifying whether or not the blade configuration can provide enough thrust.

8.1.6 Thermal Control

Verification of the thermal control system in this report regards cryogenics and the thermal behaviour of the skin. Using computer based thermal models was found to be beyond the scope of this report and alternative methods are presented in this section.

Instrument Cryogenic Simulation

Software was unattainable for verification of the cryogenic cooling for the instrument. As a result, another means of a simple verification of the chosen system was done. Mass and power estimates obtained from [49] were used to check whether the chosen cryosystem was suitable.

Equations 8.1 and 8.2 show the estimations for a cryogenic cooler. Q_c is the cooling capacity of the coldhead, and T_c is the operating temperature of the coldhead.

$$M = \frac{1100 Q_c^{0.78}}{T_c^{1.5}} \tag{8.1}$$

$$P_{in} = \frac{0.6702^{1.8}}{M} \tag{8.2}$$

The estimated mass, M, of the cryosystem was found to be 138.3 kg and the estimated input power required, P_{in}, was found to be 9.39 kW. Comparing the mass and power input to Table 26, the aforementioned values are respectively 2.6% larger and 34.1% larger than the 'AL300' specification.

The large difference in power is expected as Equations 8.1 and 8.2 are based of statistical relationships. The similarity of the masses could be due to the fact that the proposed cryosystem was used as statistical data in [49].

In any case, further fluid flow analysis is required to investigate whether the proposed cooling system is suitable for the instrumentation.

Thermal Behaviour of Balloon Skin

For proper verification of the airship thermal behaviour, software such as thermal desktop should be used. However, for now, only unit tests can be done to verify the script used.

Firstly, it is important to verify whether the sunrise and sunset timings correspond to reality. The script does incorporate the dip angle shown in Figure 48. Meaning that the sun rises earlier and sets later than on the ground, which is evident in Figure 59.

If the dip angle were to be neglected, with sunrise and sunset occurring when the elevation angle is equal to zero, then Tables 50 and 51 can be created.

Table 50: Table showing sunset and sunrise timings from the 'MATLAB' script developed, times is in UTC.

	Sunrise (hrs:mins)	**Sunset (hrs:mins)**
Summer	03:34	20:04
Winter	8:00	15:31

Table 51: Table showing sunset and sunrise timings from 'suncalc.org', times is in UTC.

	Sunrise (hrs:mins)	**Sunset (hrs:mins)**
Summer	03:17	20:06
Winter	7:53	15:38

With the location set for 52°N and 4.5°E, the times for sunrise and sunset are quite similar. Different assumptions are used within the different models. However, the difference in timings are small, this would not affect the thermal behaviour of the StratoCruiser greatly.
Another verification procedure is to examine the size of A_{proj} throughout the day. This area should be the smallest when the solar incidence angle is equal to 0 rad or π rad. However, this is merely entering these angles into Equation 5.38.

A better verification is to plot the A_{proj} against solar incidence angle B, as shown in Figure 99. It is evident that the maximum projected area occurs at $\frac{\pi}{2}$ rad. This area decreases as B approaches 0 and π rad, which corresponds to Equation 5.57.

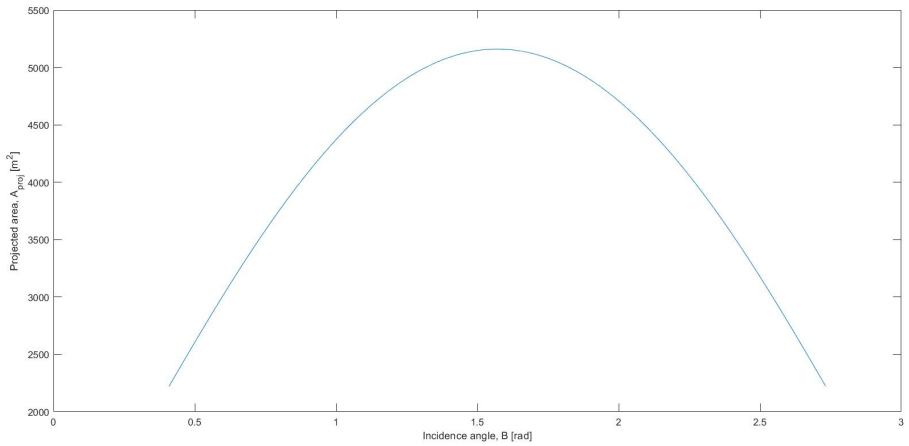

Figure 99: Plot showing how the projected area changes with solar incidence angle.

Another method of verification is by comparing the temperature results with a similar mission. In a study conducted by Zhoukou Normal University [38], an airship of similar size was tested with CFD using 'FLUENT'.

A few different parameters are used between the StratoCruiser model and the Zhoukou model, such as: altitude, location, mass, and types of heat transfer considered. In the Zhoukou model, convective heat transfers are considered during analysis.

Here the lowest temperature of the airship skin was found to be 193 K, where a temperature difference of 85 K was achieved throughout the day. This is 21.4% higher that the maximum temperature difference seen in Figure 59. This is a sensible value since convective heat transfer was neglected completely in the StratoCruiser.

8.1.7 Structure

Verification of most of the structural components is planned to be done using ANSYS. As stated in the CFD model verification section, it is assumed that ANSYS is accurate enough and has undergone a very rigorous quality assurance process.

The envelope of the airship is an exception. Due to its flexible nature, the membrane makes it such that the material folds into itself if unequal loads are experienced. While the FEM analysis produced by ANSYS is accurate for most applications, it might fail in this very specific case. A dynamic relaxation model needs to be considered to account for those errors. This type of numerical model iterates a pseudo-dynamic process, with each iteration based on the update of the geometry. Dynamic relaxation is used mainly in cable and fabric structures and in applications where a geometry that has all of the internal loads in equilibrium, i.e. in balloon envelopes. The leading software in terms of dynamic relaxation models is inTENS[85], which was developed internally by the consulting company Tensys. Since it is a product developed for internal use, it was never intended for it to be commercialized. Outsourcing this part of the envelope design is, sadly, the only solution.

8.1.8 ADCS

The methods used during the extensive design process of the tails in subsection 5.6 have been obtained from [9] the book: Fundamentals of Aircraft and Airship Design. Every code that was made during this process has been used to compute the examples given on the book and then compared to the results provided in the book.

8.1.9 TT&C

The TT&C design is verified using unit tests and comparison to other missions. Unit tests are conducted for the link budget by checking individual formulae and running calculations by hand to ensure they match the results in the link budget.

Comparison to other missions is done throughout the construction of the link budget, for example with instrument efficiencies, signal frequencies, and system noise temperatures. Additionally, the chosen antennas match the initial estimates for their requirements, indicating a verified link budget.

8.2 Validation

This section presents the validation procedures. Validation is done using real world data. Therefore, most of this section are plans for the continuation of the project.

8.2.1 CFD Simulations

It is important to make sure that the CFD simulations are modelling reality correctly, to avoid any mistakes and problems further in the design development. Aerodynamic estimations are usually validated with either wind tunnel tests or real data from flights. This is of course impossible considering the scope of the project, but wind tunnel data is available online for different types of airships. It is very complex to find and replicate data for full airship, therefore it was decided to analyze only the drag of the bare envelope. This will be easier to verify as complex tail and propeller geometry will not have to be modelled. The wind tunnel data of a GoodYear-zeppelin airship was was taken, for a bare hull model, without the parallel section, with a FR of 4.8 [50]. A 3D model of the airship was created using the data provided from the curve provided in the report [50], and the drag forces were compared at the same Re of about 5.8 millions. From wind tunnel data the real drag coefficient (referenced to $Vol^{2/3}$ for such airship (bare hull) at those conditions was found to be about 0.0255, while the CFD simulation results in a drag coefficient of 0.0250. The relative error of the CFD simulation is then just about 2%, which is considered an acceptable error considering uncertainties regarding the wind tunnel experiment conditions, the shape and the mesh convergence of the simulation. Considering the full StratoCruiser CFD simulation, the total error of the drag force would consist of only about 23 N, and that would not affect in any significant way the design of the airship. The results of the CFD simulation can therefore be considered valid and correctly modelling reality with a reasonable accuracy. For the next steps, in order to properly verify the drag results, a wind-tunnel test should be performed on the airship model. This can be done on a scaled model, by keeping the Re constant.

[85] URL: `https://www.tensys.com/intens` [Accessed on 22/06/2019]

8.2.2 Buoyancy Control

The mass flows in the ducts can be validated on a full scale model. As the material it is made from is expensive, the model can be made from other materials. The results from several runs with different compressor power settings and valve settings can be compared to the CFD results. The results can be used to correct the CFD results and extrapolate this to higher altitudes.

8.2.3 Structure

The validation of the structure will be divided into two parts: validation of the inflatable components and validation of the rigid components. This is due to the drastically different development processes the two structural solutions have.

The flexible structure validation starts with standardized material sample tests. Starting with this step is crucial because the mechanical performance of the to-be-developed fabric needs to be optimized. This process requires a very large number of experiments to properly document the behaviour of the envelope and ballonets fabrics.

The validation of the rigid components follows a similar path, but instead of starting at a very basic material level, the analysis starts with individual components and gradually increases in complexity until the entire assembly is tested.

Sadly this is outside the scope of the project, and, due to the uniqueness of the project, no data that can be used for validation is available on the Internet.

8.2.4 Instrument Integration

Validation is not possible at this stage of the design. One valuable validation method is testing, whereby the system is manufactured or bought off-the-shelf and assembled. Additionally, individual actuators and gyroscopes can be tested to compare their performance with the characteristics used in the design.

8.2.5 Propulsion

The validation of the propulsion system is mainly concerning the blade element theory tool that can be developed in the future for the propeller design. A way to do this would be to find a similar airship propeller design and checking the level of thrust calculated from the blade element theory tool. This will ensure that the blade element theory tool is producing the correct output.

8.2.6 Thermal Control

Full-scaled and scaled models should be used to validate the cryogenic system and airship temperature respectively.

Validating the cryogenic system would be first done with testing the system at sea level conditions. Once the system has been proven to work correctly at these conditions, testing can then be done at high altitude conditions. The results from the outcome of these tests would greatly benefit the validation of the cryogenic system.

The temperature of the airship can be validated with the use of a scaled-down model. A model could be placed in an environment similar to the operational environment of the StratoCruiser. Undoubtedly, the use of a scaled model would have its own idealisations as well, however, the results from this testing would be beneficial to validating the model presented in Section 5.8.2. The final validation method that can be done is in the testing phase of the full scale model [35].

8.2.7 TT&C

The TT&C is validated with one method thus far, by validating the link budget. This is done by using data from known spacecraft mission and calculating the SNR margin and comparing it to the actual value for the specified mission. Further validation procedures could be conducted by assembling the subsystem with specific off-the-shelf components and testing the performance.

8.2.8 ADCS

Validation of the ADCS system starts with the wind tunnel testing to verify obtained control and stability derivatives which are used during dynamic analysis of the airship. Next, the airship goes through the flight test in order to validate the correct operation of attitude determination sensors (eg. star sensors, gyroscopes, GNSS) and successful coordination with the TIR imaging payload.

8.3 Compliance

This section discusses the compliance of the system with the requirements. The original requirements list can be found in the Baseline Report [18]. During the design process, many requirements changed based on new insights. These changes were necessary and make the design more realistic. Some requirements turned out to be unfeasible or complicated the mission without contributing anything. If a requirement changed, the requirement number is appended with **"-mod"**. The reasoning behind the modification is documented below the table. The last column indicates the compliance of the system with the requirement. This can be Yes, No, To Be Confirmed (TBC) or Not Applicable (NA). The requirements were set very early on with little knowledge about the project. Some requirements were not quantifiable or not relevant. Proof of compliance or reasoning is documented below the table. The first set of requirements are the system requirements. These apply to the system as a whole.

Table 52: System requirements

Requirement nr.	Description	Compliance
SB-Sys-01-mod	Take-off and landing shall be allowed at wind speeds of 5 m/s at sea level (ISA).	Yes
SB-Sys-02	The unit cost of the airship shall not exceed €500,000 in FY2019 [6].	No
SB-Sys-04	The noise produced during take-off and landing shall not exceed 82 dB. [51]	TBC
SB-Sys-05	The system shall include a ground base for maintenance and storage.	Yes
SB-Sys-06	The system shall use the ground telemetry station on the EWI building for communication [6].	Yes
SB-Sys-07	The airship shall be controllable from the ground.	Yes
SB-Sys-08	The airship shall operate autonomously when not controlled by the ground segment.	Yes
SB-Sys-09	The airship shall have a safe mode.	Yes
SB-Sys-10-mod	The airship shall have a range of at least 260 km.	Yes
SB-Sys-11-a-mod	The airship shall have a cruise speed (airspeed) of at least 21 m/s at 20.5 km altitude (ISA) during daytime	Yes
SB-Sys-11-b-mod	The airship shall have a cruise speed (airspeed) of at least 20 m/s at 20.5 km altitude (ISA) during night time	Yes
SB-Sys-12-mod	The airship shall have a flight endurance of at least 6 months.	Yes
SB-Sys-13	The airship shall have a climb/descend velocity of 1.5 m/s below an altitude of 20 km (ISA) [52].	Yes
SB-Sys-14-mod	The airship shall have a service ceiling of 20.5 km (ISA).	Yes
SB-Sys-16	The airship shall have a reliability of 97% or higher over a period of 1 year.	TBC
SB-Sys-17	The airship shall have a modular integration of measuring equipment and subsystems.	Yes
SB-Sys-18-mod	The airship shall have a maintenance hosting basis of 6 months [6].	TBC
SB-Sys-19	The airship shall comply with airworthiness regulations.	TBC
SB-Sys-20	No toxic materials shall be used in the airship.	Yes
SB-Sys-21-mod	The airship mass shall not exceed 7600 kg.	Yes

SB-Sys-01-mod is met. The dynamic pressure at sea level with this airspeed equals the dynamic pressure of the cruise speed at operational altitude. The original requirement stated $10m/s$. Calm days when the wind speed is lower than $5m/s$ are not rare. The airship can take-off and land on these days.

SB-Sys-02 is not met. The estimated unit cost of the airship is € 3.6 mil. That this requirement was unfeasible was noticed and discussed on the status meeting during the Midterm Review presentation. The supervisors stated that their interest lies in the capacities of the system and agreed not to set a cost cap.
SB-Sys-04 The noise was not analyzed. Nearly all noise comes from the propulsion. The electric motors are expected to meet this requirement but this is TBC.
SB-Sys-05 The necessity of a hangar was discussed in Section 9.2.
SB-Sys-06 The use of the EWI ground station for communication was discussed in Section 5.9.
SB-Sys-07 The option of remote control was decided in the conceptual phase in Section 4.
SB-Sys-08. The software diagrams for autonomous operations are presented in Section 6.2.
SB-Sys-09 The safe mode is included in the software diagram in Section 6.2.
SB-Sys-10-mod The range of the airship is limited by the telecommunication to the EWI station. A range of 260km ensures that the entirety of the Netherlands can be observed. The original requirement stated a 500km range because this is sufficient to cross the Netherlands, also with the idea to cover the entire country.
SB-Sys-11-a/b-mod The original requirement stated 36 m/s during daytime and 21 m/s during nighttime. These were lowered after a study on stratospheric winds presented in Section 4. It was determined that 21 and 20 m/s was sufficient. The original requirement also stated an altitude range between 20 and 30km. **SB-Sys-14-mod** prescribes a service ceiling of 20.5km. The altitude in this requirement is replaced with 20.5km.
SB-Sys-12-mod The limiting factor for endurance in degradation of the solar cells. Section 5.7 shows that the system can fly for 6 months. This is confirmed in Section 7.2.
SB-Sys-13 The buoyancy control subsystem was sized to reach the mass flows of a $1.5m/s$ climb/descend. Section 5.2 shows this.
SB-Sys-14-mod The original requirement stated a service ceiling of 30km. During conceptual design in Section 4 the ceiling was changed to 20.5km because the airship size grows rapidly with altitude.
SB-Sys-16 Due to time constraints, reliability analysis have not been performed. Statistics based estimates can be used. Simulations and tests are needed to get better estimates. The team believes that 97% is achievable. Maybe some components will need to be replaced or redesigned but a large design overhaul is not expected.
SB-Sys-17 The subsystems in the gondola are installed as modules that can be replaced. Also the electric motors, propellers can be replaced. The ballonets can be individually replaced.
SB-Sys-18-mod This requirement goes hand-in-hand with the endurance requirement, **SB-Sys-12-mod**. The original requirement was 1 year. Due to the large differences in power generation and required power in winter and summer, the airship will be taken down for maintenance anyway.
SB-Sys-19 There is no evidence that the StratoCruiser does not comply with airworthiness regulations. However, this can only be confirmed after an extensive study of the regulations and extensive testing to proof compliance.
SB-Sys-20 No toxic materials are used.
SB-Sys-21-mod The original requirement stated To Be Determined (TBD). The design mass was determined after convergence of the preliminary design.

Following the system requirements was a set of budget requirements. Power, reliability, mass and cost requirements for each subsystem. In the Baseline Report [18], where the requirements were listed, the budgets were still TBD except for the reliability. The values for the mass and power budgets follow from the converged preliminary sizing. After the budget freeze, the subsystems were still allowed to change but not to exceed their budget requirements. These requirements are met. As explained for **SB-Sys-02**, no cost cap was set. Consequently, also the subsystems do not have one. The reliability requirements are TBC with extensive testing.

Next were a set of subsystem specific requirements. These are requirements that apply to a specific subsystem. Their purpose is to satisfy the system requirements. These are very detailed requirements that were set very early on. Most of these requirements were TBD and needed more analysis to quantify them. The values in this table are the values from the converged preliminary sizing. After

the budget freeze, the subsystems were still allowed to change but not to exceed their requirements were fixed.

Table 53: Subsystem requirements

Requirement nr.	Description	Compliance
SB-Subs-Aero-02-mod	The drag coefficient shall not exceed 0.045.	Yes
SB-Subs-Aero-03	The airship shall be aerodynamically directionally stable or neutrally stable.	Yes
SB-Subs-Aero-04	The maximum aerodynamic moment due to gusts shall not exceed TBD.	NA
SB-Subs-Aero-05-mod	The gas temperature inside the airship shall be controlled to within the range 217-260 K.	Yes
SB-Subs-Pow-01-mod	The end-of-life power capacity shall be 68 kW.	Yes
SB-Subs-Pow-02-mod	The end-of-life energy storage capacity shall be 1250 kWhr.	Yes
SB-Subs-Pow-03	The power subsystem temperature shall not exceed TBD K.	NA
SB-Subs-TTC-01	The link budget shall be TBD.	NA
SB-Subs-TTC-02-mod	The telemetry signal-to-noise ratio shall be at least 10.	Yes
SB-Subs-CDH-01	Commands shall be distributed to subsystem with a reliability of TBD %.	TBC
SB-Subs-CDH-02	The data measured by the instrument shall be processed to TBD format.	NA
SB-Subs-CDH-03	The data throughput shall be 48 Mb/s.	Yes
SB-Subs-ADCS-01	The attitude determination accuracy shall be 1 $arcsec$.	Yes
SB-Subs-ADCS-02	The attitude determination frequency shall be 10 Hz.	Yes
SB-Subs-ADCS-03	The attitude control accuracy shall be 5 $arcsec$.	Yes
SB-Subs-ADCS-04	The attitude control stability shall be 1 $arcsec$ [6].	TBC
SB-Subs-ADCS-05	The ADCS shall return the airship to its initial position after a disturbance in a settling time of TBD.	NA
SB-Subs-ADCS-06	The ADCS shall provide a maximum control torque of TBD.	NA
SB-Subs-Prop-01-mod	The propulsion subsystem shall provide a maximum thrust of 2.7 kN at an altitude of 20.5 km (ISA).	Yes
SB-Subs-Prop-02-mod	The propulsion subsystem shall provide a total thrust of 2.7kN at sea level (ISA).	Yes
SB-Subs-Meas-01	The instrument shall have a temporal resolution of 1 minute [6].	Yes
SB-Subs-Meas-02	The instrument shall have a spatial ground resolution of 0.5 m at an altitude of 20 km [6].	No
SB-Subs-Meas-03-mod	The instrument shall operate in the infrared band ranging from 8-12 μm [6].	Yes
SB-Subs-Meas-04	The allowable shift in focal point of the mirror shall be TBD.	TBC
SB-Subs-Meas-05-mod	The temperature of the baffle in which measurements are possible shall be below 90 K.	Yes
SB-Subs-Meas-06	A change in focal point shall be known within an uncertainty of TBD.	TBC
SB-Subs-Meas-07	The observations shall have an SNR of 100.	Yes
SB-Subs-Struc-01	Displacement of the measurement sensor not exceed TBD.	TBC
SB-Subs-Struc-02	The structures shall provide removable mounting points for all subsystems.	TBC
SB-Subs-Struc-03	The stiffness of the mirror shall be TBD.	NA

SB-Subs-Aero-02-mod The initial requirement was TBD. The value originates from the converged preliminary design. The drag coefficient meets this requirement, as shown in Section 5.1.
SB-Subs-Aero-03 The airship is aerodynamically stable thanks to the tail, as proven in Section 5.6.
SB-Subs-Aero-04 The aerodynamic moment due to gusts is not a good requirement. The instrument mounting compensates for attitude changes of the airship.
SB-Subs-Aero-05-mod The original requirement was TBD. This temperature range is the range from Section 5.8. This affects the pressure as presented in Section 5.2. Section 5.11 confirms this is within the structural limits.

SB-Subs-Pow-01-mod The converged preliminary design indicated 68 kw is required.
SB-Subs-Pow-02-mod To provide the power from **SB-Subs-Pow-01-mod** continuously, 1250 kWhr of storage is required. Section 5.7 shows this is sufficient to fly year around.
SB-Subs-Pow-03 The temperature of the power subsystem is not a relevant requirement. This might be different whether batteries or a fuel cell is used. A requirement cannot rule out solutions. The thermal control of the power subsystem depends on the specific solution.
SB-Subs-TTC-01 This is not a good requirement because it does not have a quantifiable unit. **SB-Subs-TTC-02** is a relevant requirement. The intention behind both is the same.
SB-Subs-TTC-02-mod From the analysis done in Section 5.9, it was found that an SNR of 10 is sufficient.
SB-Subs-CDH-01 This depends on the reliability of the on-board computer. This requirement is a duplicate of the reliability requirement for the computer.
SB-Subs-CDH-02 This is not a good requirement because it prescribes a solution.
SB-Subs-CDH-03-mod This value originates from an analysis on the required throughput from the imaging data as explained in Section 5.10.
SB-Subs-ADCS-01 The star sensors from Section 5.6 reach this accuracy.
SB-Subs-ADCS-02 The star sensors reach this frequency.
SB-Subs-ADCS-03 The instrument mount has a control accuracy of 4 $acrsec$ as presented in Section 5.6.
SB-Subs-ADCS-04 The airship has a large moment of inertia. Consequently, the angular rates from a disturbance are expected to be small. A dynamic model of the airship should clearify this.
SB-Subs-ADCS-05 The intention behind this requirement is that, after a disturbance, it quickly returns to the attitude in which observations can be performed. However, thanks to the moving instrument mount, it is not the magnitude of the disturbance but its stability that limits the observations. Therefore, this requirement was discarded.
SB-Subs-ADCS-06 Again, the intention is to stay in the right attitude for observations. The moving mount points the instrument so there is no requirement on the moment that the airship attitude control should provide.
SB-Subs-Prop-01-mod This is the maximum thrust the propulsion must deliver to reach the required airspeed as explained in Chapter 5.5.
SB-Subs-Prop-02-mod This is the thrust the propulsion must deliver to reach an airspeed of $5m/s$ at sea level. This speed is required to be able to land with this wind speed (**SB-Sys-01-mod**).
SB-Subs-Meas-01 The integration time is 0.06 s. This is the time to take 1 picture, far below 1 minute.
SB-Subs-Meas-02 The ground resolution is 1 m. The trade-off between GSD and SNR is explained in Section 5.3 as well as ways to meet this requirement. The violation of this requirement will be addressed in the Chapter 12.
SB-Subs-Meas-03-mod The original requirement stated a bandwidth ranging from 10 to 12 μm. Upon consultation with the stakeholder, the requirement was modified to a bandwidth ranging from 8 to 12 μm which was required to maintain an SNR of 100, as specified by **SB-Subs-Meas-07**, for an instrument with a focal ratio of 1. (Section 5.3).
SB-Subs-Meas-04 This is subject to further analysis. Because this is going very deep, the level of detail would not be in balance with the rest of the system. The team decided to postpone this to the continuation of the project and focus on other parts of the system.
SB-Subs-Meas-05-mod It was determined that this temperature is required to eliminate noise to reach the required SNR as explained in Section 5.3.
SB-Subs-Meas-06 This depends on the shape changes. These are part of the future continuation of the project.
SB-Subs-Meas-07 The SNR of the instrument presented in Section 5.3 meets this requirement.
SB-Subs-Struc-01 The team was tasked with the development of the airship and primary mirror. The sensor was treated as a black-box. As no further information was known about the sensor, the mount of this could not be designed. The stiffness of this mount can be tailored to reach the required stiffness.

SB-Subs-Struc-02 The design of all mounts was too detailed in the time frame of this project. Further detailed design must ensure that the mounts are removable such that parts can be replaced or upgraded.
SB-Subs-Struc-03 Again, the effect of deformations of the mirror was not investigated. The required stiffness depends on the effect of the deformations. The structure of the mirror can be tailored to a certain stiffness. As long as the mirror does not exceed its mass budget, this will have no effect on the rest of the airship.

9 Operations

This section discusses the operational procedures and logistics. Section 9.1 documents the functional analysis of the StratoCruiser. Section 9.2 discusses the logistics on the ground. Section 9.3 discusses the number and location of airships required to cover the Netherlands. These parameters depend on the required response time for the mission and vary throughout the year.

9.1 Functional Analysis

The functions of the airship carried out during its pre-flight procedures, launch, flight, and landing are defined in two diagrams - the functional flow diagram and the functional breakdown structure. The former organizes these functions in a chronological order, while the latter displays an extra level of detail in a non-chronological manner.

9.1.1 Functional Flow Diagram

The functional flow diagram of the StratoCruiser is visualized in Figure 109. The airship is first cleaned before it is inflated with hydrogen. This is followed by loading the propellant tanks, consisting of oxygen and hydrogen. After this, a range of pre-flight checks relating to the internal pressure, structure and subsystems must be conducted. Until these checks are satisfactorily passed, the flight shall not be instigated.

Passing the checks and establishing communication with the ground station at EWI, Delft allows the airship to be launched: it is released and autonomously controls its buoyancy to achieve its desired station-keeping altitude. At this stage, the communication should be checked again, before receiving navigation commands to determine the required observation position or landing location. With this command recorded by the OBC, a flight path is formulated for the airship to follow.

The propulsion and attitude control systems are responsible for starting and maintaining the flight trajectory, until the destination is reached and stationary flight can be established. In case of landing, the descent procedures can begin - establishing communication, decreasing and controlling buoyancy, and landing. On the other hand, if the scientific mission is continuing, the mirror should be oriented, checked, it should capture images and send them to the OBC. After completing the data measurements, the airship can return to station-keeping.

9.1.2 Functional Breakdown Structure

The functional breakdown structure, as shown in Figure 110, describes the same tasks defined in the functional flow diagram. The functions are organized by aspects of the airship rather than the order in which they are conducted. Therefore, some functions such as ‘carry loads’ are included here which do not appear in the functional flow diagram. Additionally, there is an extra level of detail to more acutely define he functions.

9.2 Logistics

Maintenance, changing payload and storage happen in a hangar, safe from weather. For short term storage, a hangar is not required. However, by nature of the mission, this airship will only return to the ground for maintenance, a replacement of the payload or long term storage, which all happen inside a hangar.

The building must be large enough to accommodate for the airship and have some margin for cranes or other large equipment.

Contrary to the concept explained in the Midterm Report [3], there will be no mooring mast nor landing gear in the gondola. The mooring mast would need to be 20m tall. A movable tower of this size would be very hard to develop and impractical in use. The gondola is located towards the front so the landing gear would not provide central support. Also, the tail is long such that the landing gear would need to be very long.

Instead, when the airship comes down for landing, mooring lines are dropped. These lines have one end connected to the airship and the other end is free and can be connected to a truck. This truck tows the airship to the hangar. In the hangar, the airship rests on a number of hammocks and is anchored to the ground with ropes. The hammocks provide a distributed support such that no reinforcement in the airship structure is required. Ropes anchor the airship to pull the airship in the hammocks such that it is not floating around. Without this support, the buoyancy control cannot be shut down for maintenance.

9.2.1 Hydrogen handling

Hydrogen is used as lifting gas. In combination with oxygen, it is highly combustible. Even a static discharge, friction from a valve, etc. can cause hydrogen to spontaneously combust.

A first measure is to avoid the hydrogen from coming in contact with oxygen. The envelope is checked for leaks by inflating the envelope with air. Inflated ballonets could seal leaks so this test must happen with empty ballonets. Only after the envelope is proven to be airtight, the ballonets are inflated to their maximum while letting air escape from the envelope. This keeps the envelope in shape to avoid wrinkling and potential formation of leaks. All air is removed from the envelope before inflating with hydrogen.

The inflation happens through a special valve. The hydrogen hose connects to this valve with an airtight connection. A vacuum is created in this connection. This avoids contact of hydrogen with oxygen in the hose and eventually in the envelope. A pure vacuum is not possible but if there is less than 5% air, the hydrogen will not combust as this is the limiting oxygen concentration [53]. When the envelope is completely filled with hydrogen, the valve is closed. On the end of the hose another valve is closed such that the hydrogen that is still in the hose cannot escape. The hose is disconnected and emptied outside, out of range of any flammable material. During disconnection, a small amount of hydrogen in between the valve on the hose and valve on the airship escapes. Fire extinguishers must be ready and no electric tools are allowed in the vicinity. Due to the small amount of hydrogen that escapes, it is unlikely to cause further issues.

If the balloon has to be deflated, this is done outside and away from anything flammable. At the valve, the hydrogen may catch fire. As long as no air can enter the envelope, neither can the flame. In this case, the valve must be closed immediately.

A conductive static discharge wire must be integrated in the mooring lines to provide a conductive path from the airship to the ground. Also the truck must have a static discharge wire to avoid a build up of charges.

No electric or mechanical systems are allowed in the envelope. The only system is a special hydrogen valve which is designed to be safe. The envelope material must be a non-flammable material and the envelope around the hydrogen valve must be either fire proof or have a fire proof shield such that in case of a flame, the envelope does not burst.

Before moving the airship in the hangar, it is checked for leaks. This is done by monitoring the pressure in the airship for some time with all valves closed and through visual inspection with drones. The inspection drones must keep a safe distance to avoid igniting hydrogen from a leak.

In the hangar, hydrogen detectors in the hangar warn the personnel in case of a leak. Air pressure operated tools are preferred over electric tools. The tools that are not used must stay out of the hangar. All personnel must be trained and well informed about the hazards of hydrogen and wear fire proof clothing. The hangar must be fire proof and must have double doors and fire extinguishers attached to the roof. Finally, it must be constructed in such a way that a fire is contained within the building.

The combination of these measures allow the use of hydrogen by handling the inherent risk it brings.

9.3 Constellation Analysis

Monitoring the totality of the Netherlands is a challenging task. Many different methods and balloon arrangements can be used. Firstly, the coverage of a single balloon was analyzed. From 20 km

altitude, the visible horizon distance is about 500 km [1], but because of off-nadir angle restrictions due to perspective and focus issues, the maximum off nadir angle of an airship was set to 25 degrees, as presented in Section 5.3.2. This means that a maximum coverage radius of about 9.32 km can be correctly monitored with the instrument. It is clear that to obtain complete near-real time coverage of the whole country, many balloons are needed. As previously presented in Section 5.3, the airship will be able to perform ground observation only in absence of clouds. During cloudy days the balloon can be used to perform analysis regarding the cloud area coverage and temperature, as thermal infrared observation is often used by meteorologist for analysis[86].

In order to maximize the coverage, an optimization script was developed to obtain the best placement of a certain amount of balloons over the Netherlands. The program was developed in Python. The airships are assumed to maintain an altitude of 20 km. Constant wind during the simulation is assumed. The inputs of the program are the number of airship, the observation region, the airship cruise speed, the maximum coverage and finally the wind speed.

Firstly, the program discretizes the observation region in a grid, secondly the balloons are distributed uniformly in the observation area as an initial guess. A function was created to calculate the time required to reach any point of the grid from a starting airship point. This is done by calculating the best flight path angle taking into consideration the starting and destination point, the cruise speed and the wind speed. For multiple balloons, the function is called for each one of them and the resulting time arrays are intersected to get the overall minimum response time. An optimization algorithm then minimizes the mean of the resulting minimum response time arrays by varying the position of the balloons. Different algorithms were tested to find the most suitable and time efficient one. In the end, it was found that the basin hopping algorithm, implemented in the scipy library[87], performed the best in terms of results and computational time. The basin hopping algorithm, or Monte Carlo minimization, is a global optimization technique that combines local minimization with a stochastic approach to locate the global minimum of a scalar function [54]. Due to its stochastic nature, final results can vary if not enough iterations are performed, but it was found that stable optimized results could be consistently obtained, by tuning the initial parameters and setting the total number of iterations to 100. It was observed that, as the number of airship increases, the computational time significantly increases because of the higher number of variables to optimize. In order to tackle this, the script was parallelized to allow simultaneous multiprocessor optimization of different runs (different number of airships or different environmental conditions). Examples of the optimized result for different airship placement are presented in Figures 100, 101, 102 and 103. The small purple dots represent the location of the airship.

[86]URL: `https://www.theweatherprediction.com/habyhints2/512/` [Accessed on 24/06/2019]

[87]URL: `https://docs.scipy.org/doc/scipy-0.19.0/reference/generated/scipy.optimize.basinhopping.html` [Accessed on 23/06/2019]

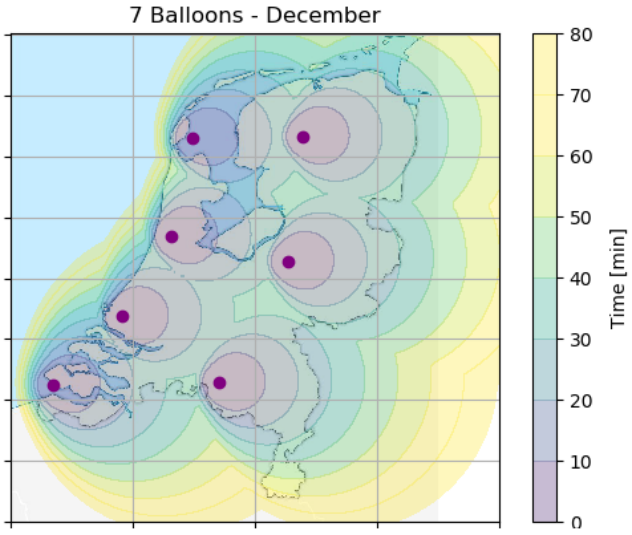

Figure 100: Airships response time coverage.

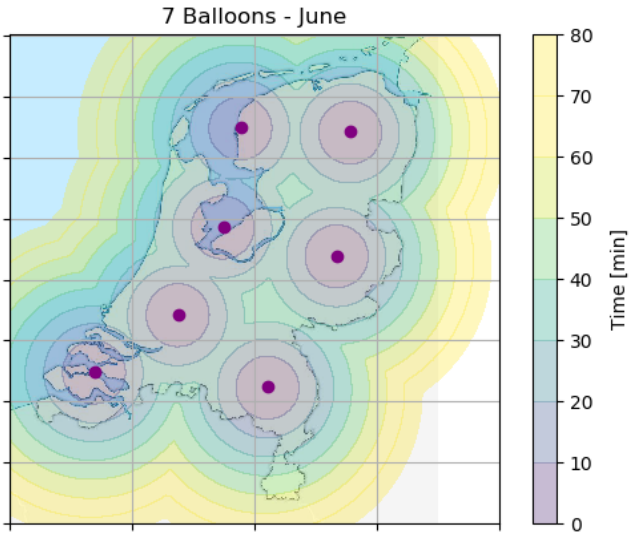

Figure 101: Airships response time coverage.

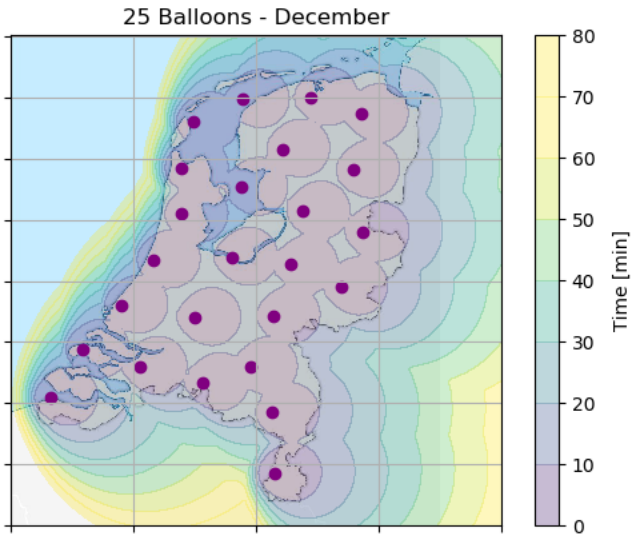

Figure 102: Airships response time coverage.

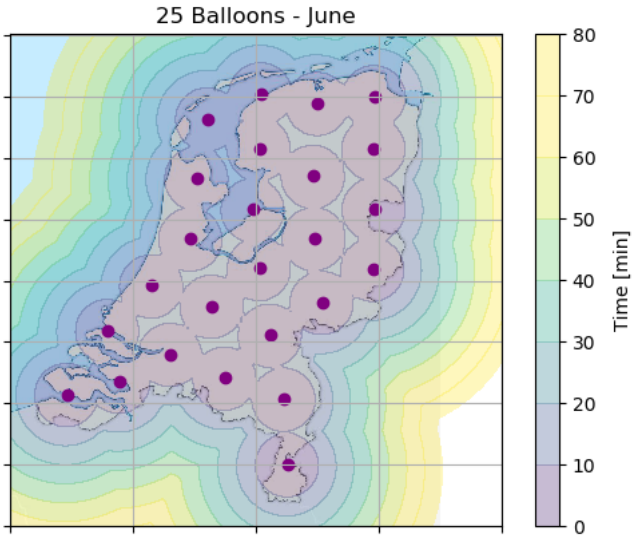

Figure 103: Airships response time coverage.

It can be noted that the airships tend to be arranged on the west side of the Netherlands during the winter case. This is due to the strong West-East winds, which make it harder for the airships to fly westwards.

The algorithm can be used for multiple purposes. Firstly, it is a great tool to obtain an idea of how many airships are needed to monitor an area given a response time. A plot visualizing this is presented in Figure 104. It can be observed that the average response time increases significantly with less airships, while it slowly decreases as the number of airships increases. It is theoretically possible to monitor the entire Netherlands with constant coverage, but this is achievable only with an unreasonably high number of airships, making this option economically unfeasible. An example of the achievable real time coverage with 25 airships is shown in Figure 105, where the purple areas represent the actual real-time coverage of each airship, and, once again, the small purple dots represent the balloon locations.

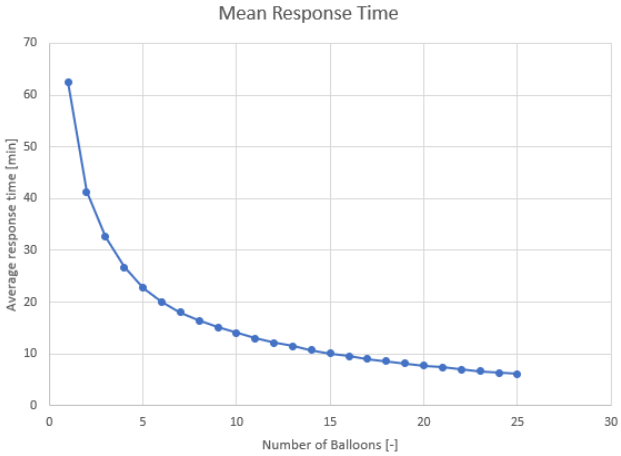

Figure 104: Airships response time coverage.

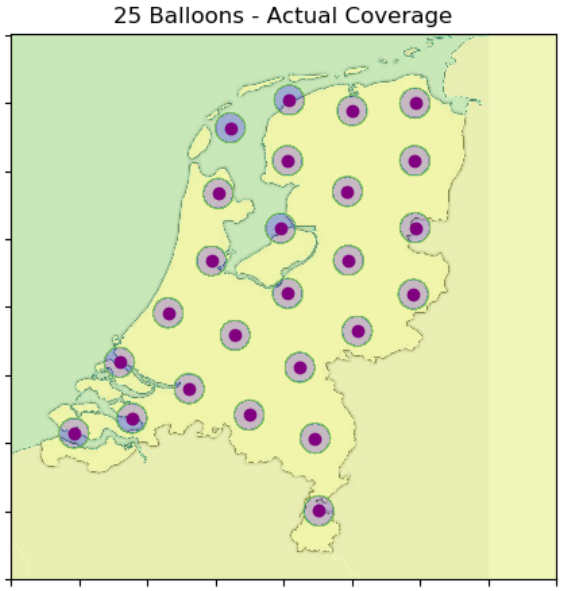

Figure 105: Real time coverage of 25 airships.

In order to quantify the worst-case scenario response time, it is chosen to analyze the 99th percentile value (2 standard deviations) of the response time. Doing this, small outliers are eliminated and a worst case scenario value can be found. These values are shown in Table 54. June and December are chosen as months to represent winter and summer as they contain the longest and shortest day of the year, respectively.

Table 54: Optimization time coverage.

	Worst - Case Response Time [min]		Mean Response time [min]	
Number of Airships	Winter	Summer	Winter	Summer
1	195.16	127.64	65.50	59.49
5	57.80	55.03	23.54	21.95
10	36.15	30.86	14.57	13.46
15	23.01	21.17	10.62	9.67
25	17.13	14.46	6.47	5.72

It can be observed that during winter the airships responses time slightly increases due to the winds. Based on this results, the total number of airships can be selected by the client, depending on the needs, the financial resources and on the type of service required. For the return of investment analysis presented in Section 10.2, a number of airships needs to be chosen for further analysis. Three airships are selected as they provide a good comprise between response time and cost. The algorithm could be modified with a weighted system to optimize the airships distribution also considering what areas are more significant for monitoring (e.g. cities, borders, ports etc.). Finally, the program could be used real-time during the mission based on the actual winds to place the airships in the most efficient distribution possible to minimize response time.

10 Non-Technical considerations

This chapter documents the non-technical parts of the project. Aspects including the cost (Section 10.1), RoI (Section 10.2), risk (Section 10.3), Reliability, Availability, Maintainability and Safety (RAMS) (Section 10.4) and sustainability (Section 10.5) are considered.

10.1 Costs

The costs of a single StratoCruiser is comprised of material, manufacturing, and operational costs. The material cost was already described in Section 6.1.2. Manufacturing cost is hard to estimate; it is mainly comprised of cost of labour and capital. For the sake of estimating operational costs, and revenues in proceeding sections, it is assumed that 3 airships are in operation around the country. The operational cost can be estimated by finding the wages of the ground crew labour and the rental price of a hangar. Assuming the wage of ground crew is comparable to that of an air traffic manager, and four full time members are employed, this results in $\$260,000/year$[88]. In addition, there should be at least one technician for maintenance of the hangar, this would cost another $\$60,000/year$[89]. Maintenance is planned to occur twice a year per airship, a week each time maintenance takes place. If 20 employees are required for maintenance, then this amounts to another 6,720 manhours of technician labour, which costs approximately $\$210,000$. Therefore, the total annual labour cost is approximately $\$530,000$.

Hangar cost is estimated by surveying rental costs of hangars[90]. The average cost is about $\$0.8/squarefoot/month$. If the hangar needs to accommodate the airship and equipment, it can be assumed to be 400 $m \times 80$ m. This results in an annual hangar rental cost of $\$2,073,000$.

The total operational cost would also include the cost of new materials, parts and maintenance equipment. An in-depth depreciation analysis cannot be done due to a lack of time, therefore by imposing a safety factor of 2 the total annual operational cost is found to be $\$5,206,000$.

10.2 Return on Investment

A 'top-down' analysis of the potential annual RoI of the StratoCruiser is performed by comparison with other missions recording similar data. RoI is defined by Equation 10.1:

$$RoI = \frac{annual\ revenue - annual\ costs}{annual\ costs} \tag{10.1}$$

Annual revenue is estimated by analysis of the types of goods and services that could be sold by the StratoCruiser. Based on the analysis performed in Section 3, and assuming that the StratoCruiser can occupy 30 % of the EO data and monitoring dutch markets, the revenue for 2017 would be approximately $14.36 million.

This estimate of the annual revenue adopts a 'top-down' approach; the market is evaluated and an estimate for the revenue of the StratoCruiser is subsequently made. A 'bottom-up' approach was also attempted: this was done by contacting a company that specializes in the sale of EO data and finding that the average price of thermal infrared data for comparable resolution sold was $\$8/km^2$ [91]. In one minute, the StratoCruiser can capture a data of a 5.1 $km \times 5.1$ km square area on the ground. The image capturing time is one minute, following the temporal resolution requirement. Assuming an average continuous ground speed of 21 m/s, the airship travels 5.1 km in 303 seconds, therefore it spends 363 seconds in total on a 5.1 $km \times 5.1$ km square area. At this rate, assuming continuous movement to new areas, the airship could capture up to 7400 km^2 in a day. With the given price estimate, this data is valued at $\$60,000$. Presumably, the airship will not cover new areas everyday and will not find clients interested in all the data. However, the StratoCruiser could focus on areas

[88] URL: `://www.prospects.ac.uk/job-profiles/air-traffic-controller` [Last accessed: 24/06/2019]

[89] URL: `//www.bls.gov/ooh/installation-maintenance-and-repair/mobile/aircraft-and-avionics-equipment-mechanics-a` `htm`[Last accessed: 24/06/2019]

[90] URL: `https://www.loopnet.com/airplane-hangars-for-lease/` [Accessed on 24/06/2019]

[91] Deimos Imaging, personal communication, June 5th, 2019

of interest such as Amsterdam or The Hague-Rotterdam area to maximize revenue. Considering this, if the StratoCruiser sells 15 % of the daily maximum measurable data, and 3 airships perform at this level, it would yield an annual revenue of about \$9.78 *mil*. This is relatively close to the estimate offered by the top-down approach. Although both are rough estimates, the fact that they are close is somewhat of a verification of both methods.

Annual operational costs were evaluated in the previous section, amounting to about \$5.21 *mil*. Equation 10.1 yields an annual RoI of 176% for the top-down approach, and 88% for the bottom-up approach to revenue calculation. It must be noted that these figures do not include a number of costs, as stated previously.

10.3 Risks

Risks accompany all facets of a design. Not being able to appropriately accommodate these risks spells the recipe for possible catastrophe. Therefore, it is crucial to identify and analyze the extent of the risks and to finally follow-up with mitigation strategies during one's design process. Similarly, in this section, the risks will be identified, then their criticality will be analyzed by looking at the chances of occurrences as well as the impact of the consequences. Finally, the mitigation strategies that the group has implemented are presented and explained, going in-depth on how this is integrated into the design as a whole.
The risks can be categorized into seven main categories. These are categories based on the various subsystems. First, the risks are presented in Figure 106, together with the corresponding numerical IDs, as shown in the legend. Then, the risks are divided into the seven categories as shown in Table 55. It should be noted that the likelihood of the risks given in the below sections are all from Lees' Loss Prevention in the Process Industries, Hazard Identification, Assessment and Control [55]. The data presented in the source is actually from the Reliability Technology by A.E. Green and J. R. Bourne in 1972. Therefore, a further slight reduction in the probability of failure occurring can be expected from the current data.

Table 55: Table showing the risks separated into different categories represented by the numbers given to each risk in the list above.

Instrument	ADCS	Balloon Control	Propulsion	Structure	Communication	Miscellaneous
1, 6	2, 3	4, 5, 7, 8, 9, 14	10, 16	11, 15	13	12

The risks are basically divided into categories that are mostly based on the subsystem it belongs to. As it can be seen, the balloon control has the highest number of potential risks that has been identified. This is because the balloon control is an intricate subsystem that naturally has multiple points of failure. With all these risks, however, it is more crucial to identify the ones which the group needs to focus on reduce the criticality and probability of occurrencess. This is done by the use of a risk map that is presented in Figure 106. The risks will be explained in more depth following the risk map.

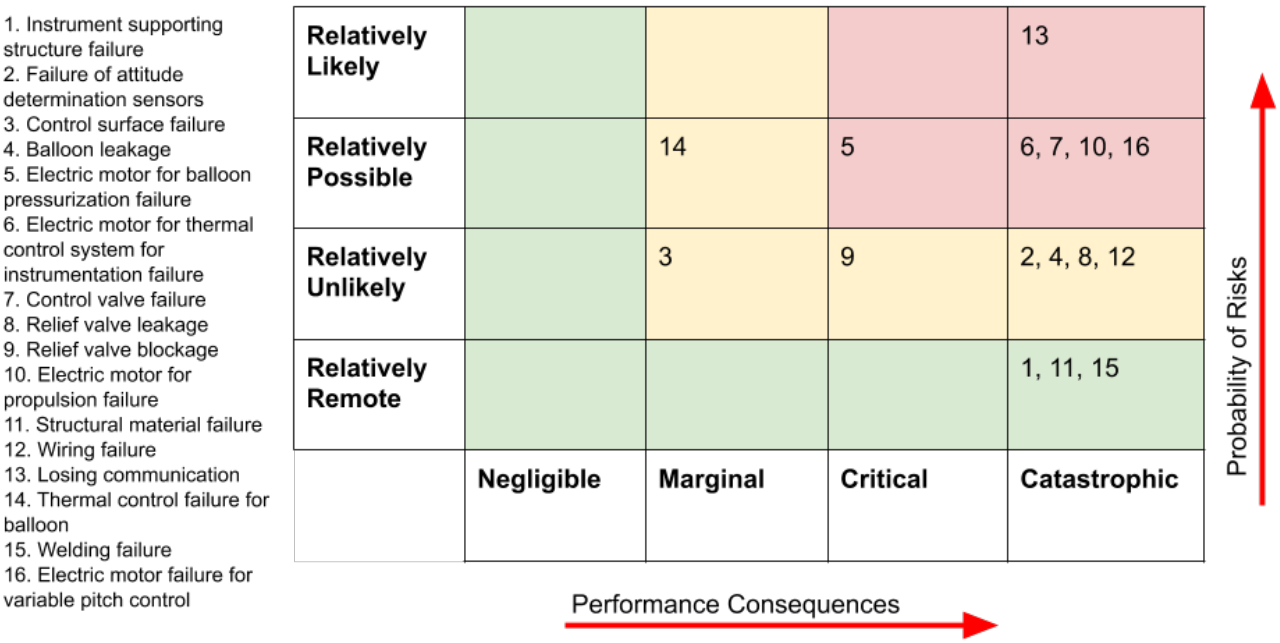

Figure 106: A priori risk map

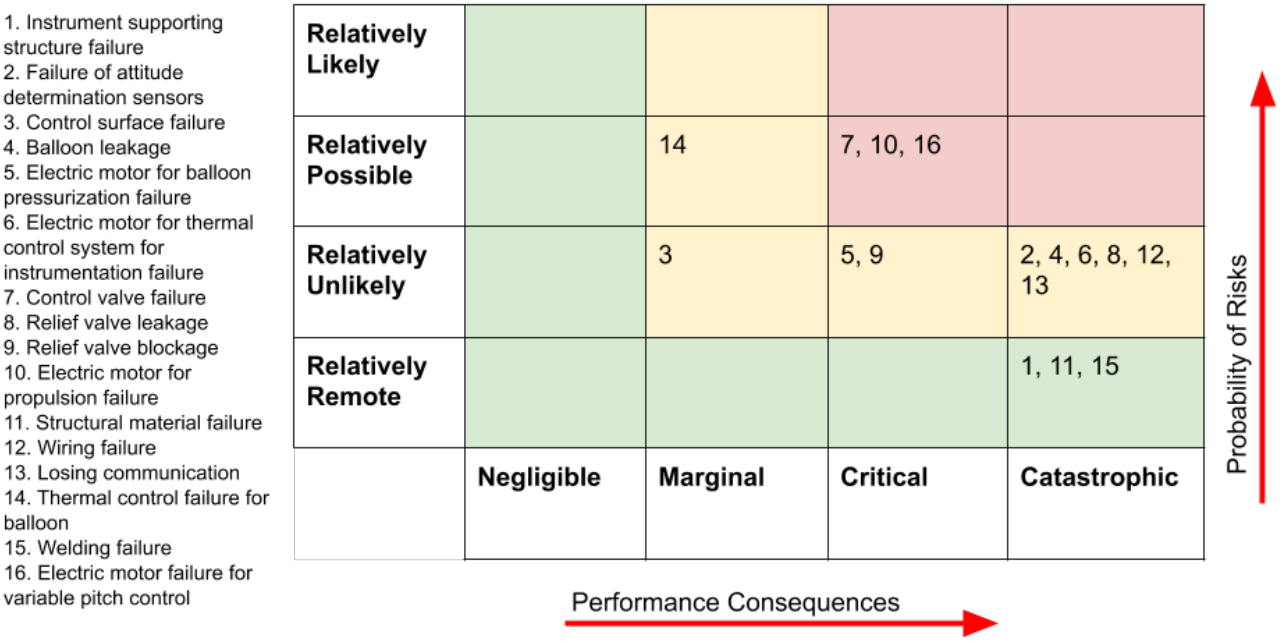

Figure 107: A posteriori risk map

For brevity, only the risks that are deemed overall 'critical', the ones in the red region, are presented in more detail and the mitigation strategies are presented. Resources are finite and not every risk can be mitigated and handled effectively. Therefore, it is crucial to choose the risks that the group will address. The positions of the respective risks, in Figure 106 and 107, can be compared once mitigation has been done. This showcases the effect of the mitigation strategies on the highlighted risks.

First, it should be noted that both the likelihood and the consequences of the risks are divided into four degrees. As for the probability of risks, scaling in the vertical direction, it is divided into 'relatively likely', 'relatively possible', 'relatively unlikely', and 'relatively remote'. It is crucial to note the use of the word, 'relatively', in this. In fact, the risks showcased here are all quite unlikely to occur with one of the likeliest risk to occur having an occurrence rate at magnitude of 10^{-4} $failure/hrs$ [55].

Therefore, although it may seem like some risks are very critical and should be dealt more radically, it should be noted that these are already highly unlikely risks. To give a general sense of how unlikely some risks are, the relative measures of likelihood are categorized by the following range:

- Relatively likely: $> 1 \times 10^{-5}$ $failure/hrs$
- Relatively possible: $\approx 1 \times 10^{-5}$ $failure/hrs$
- Relatively unlikely: $\approx 1 \times 10^{-6}$ $failure/hrs$
- Relatively remote: $< 1 \times 10^{-6}$ $failure/hrs$

The consequences are divided into four grades as well, scaled by the relative criticality of the individual items of risks to the mission success and to the craft.

When handling the risks, there are two possibilities: adding redundancies or devising a contingency plan. The former aims to reduce the likelihood of the entire system failing. For example, if one motor fails, but there is another back-up motor, it would mean that the entire system has not failed. One can simply engage the back-up motor. The latter on the other hand aims to reduce the consequence or the criticality of a particular failure. This is particularly useful if the particular risk cannot be mitigated through the use of better components and therefore cannot be avoided.

4. Balloon leakage: Although this is not a 'critical' risk as it is not in the red region of the risk map due to its low probability, this risk is perhaps the most iconic risk for an airship filled with hydrogen. Once the balloon starts to leak hydrogen, there is a real risk of loss of the airship as hydrogen combusts readily with contact with air. However, it should be noted that the risk of the hydrogen leakage from the balloon ranges at 3×10^{-6} $failure/hrs$ in general and is therefore a relatively unlikely risk [55]. Therefore, although preconception of hydrogen-filled airships may suggest otherwise, in the current day and age, hydrogen-filled airships are relatively safe from exploding. Additionally, in the design of the StratoCruiser, the electrical components are placed in the gondola away from the lifting hydrogen gas, in an effort to avoid any risk of spark in the electrical component leading to an explosion.

5. Electric motor for balloon pressurization failure: An electric motor is used to pressurize and depressurize the balloon to control the altitude. If this electric motor fails, the pressure within the ballonet cannot be controlled, so the airship loses its main method of precisely controlling the pressure of the ballonet and thus controlling the altitude of the airship. It can be seen from Figure 106 that this risk is rated at relatively possible. This is because the statistical likelihood of this risk is given at 1×10^{-5} $failure/hrs$ once the motor has already started [55]. The likelihood of the motor failing when starting is slightly higher than this, but since the motor is continuously running for the majority of the mission duration, the risk of motor failure when the motor has already been started is taken. The consequence of this is critical, because the airship cannot achieve the full range of altitude it is designed to achieve. More specifically, it severely affects the airship's capability to descend. This could in turn hinder its ability to ground itself or to use the stratospheric air currents to move to specific locations. However, this is not deemed catastrophic, because although it cannot descend, there are other ways for the airship to ground itself. This includes methods such as the controlled venting of gas from the airship. In the end, the airship can still partially carry out its mission and most importantly, the airship is not lost. A way to handle this risk is to add a back-up electric motor. Considering that the mass and power requirement for this additional electric motor is not significant, this is a plausible risk mitigation strategy. This redundancy has been implemented in the balloon pressurization mechanism as showcased in Section 5.2. Introducing this redundancy would mean that the likelihood of the system of balloon pressurization mechanism being lowered. This can be seen when comparing the a priori and a posteriori risk maps shown in Figures 106 and 107. Risk number five is seen to have been moved lower from 'relatively possible' to 'relatively unlikely'.

6. Electric motor for thermal control system for instrumentation failure: If the electric motor for the thermal control system for the instrumentation fails, this would mean that the temperature

of the instrument cannot be effectively controlled. Therefore, this would mean that the measurements taken by the instrument will not meet the requirements set through the project as there will be substantial interference. Similar to the previous risk, as it is the failure of the electric motor that the risk is concerned with, the likelihood of the risk is rated at relatively possible. Again, the absolute value for the likelihood of this risk occurring is 1×10^{-5} $failure/hrs$ [55]. However, the failure is considered catastrophic this time, because it significantly hinders the key aspect of the mission success: to carry out accurate observations. A way to handle this risk is to again introduce a redundant electric motor which is implemented in the design of the thermal control system for the instrument. This effectively reduces the likelihood of the entire system failing and is shown in Figure 107.

7. Control valve failure: The control valve controls the inflow and the outflow of the gas in and out of the ballonets. The control valves failure also hinders the ability for the airship to precisely control its altitude. Additionally, it can also impact the airship pitching control, which uses the different buoyancy forces in the ballonets placed in the airship. The control valve failure is deemed a relatively possible risk, which is substantiated by the absolute value of failure rate of 3×10^{-5} $failure/hrs$. This risk is deemed catastrophic however, because the motion of the airship is restricted to the point where the mission cannot be carried out anymore and the airship may be lost as the altitude cannot be easily controlled. It is impractical to introduce redundant control valves in the ballonets, therefore, another method to address this risk would be to introduce a contingency plan. A simple contingency plan would be to vent gas out of the ballonet through the relief valves. This would bring down the criticality of the failure since, the airship is not lost although the mission has to be aborted.

10. Electric motor for propulsion failure: The failure of the electric motor for the propulsion system would mean that the airship will have no means to move against the flow of the air in the stratosphere or when landing. This reduces one of the main advantage of the group's airship, which is the capability to maneuver in the stratosphere. The likelihood of this risk occurring is similar to all the other electric motor failure and therefore is rated relatively possible. The performance consequence of this risk is rated at catastrophic. This is because the mission has to be aborted, and in adverse weather conditions, there is no way for the airship to safely land. Since it is too costly and heavy for the group to introduce a back-up motor for the engine, it is crucial for the group to develop a contingency plan. The contingency plan for this failure is two-fold. First, if the airship is not at its target altitude, i.e. on its way up, the simple solution would be to vent out the gas and descend quickly to the ground. This is possible as the launch conditions mandate that the wind is at minimal levels. However, when the airship has already reached its target altitude in the stratosphere, it is crucial for the airship to wait until the weather in the lower parts of the atmosphere calms before descending. More importantly, it's crucial to account for the wind direction in the stratosphere when choosing a landing site.

13. Losing communication: The loss of communication would mean that the ground station will not be able to receive the location or the state of the airship as well as not being able to communicate new commands to the airship. The likelihood of this is relatively likely [92]. The consequence of this failure would spell disaster for the airship as not only the mission has to be aborted, but also, the entire airship may be lost. Therefore, it was categorized as a catastrophic risk. A mitigation strategy for this risk can be to simply introduce a back-up communications system. This is implemented in Section 5.9. The effect of this mitigation strategy is shown in Figure 107 and as it can be seen, the communications system as a whole has a lower chance of failing as a result of this.

16. Electric motor failure for variable pitch control: If the variable pitch control fails, the propulsion system essentially becomes a fixed propeller. This can mean two things. Firstly, that the airship's thrust may be limited, although it may be enough to meet the propulsion requirements. Secondly, when the airship is coming to a halt in landing, the propellers will not be able to provide reverse thrust. This would mean that the airship has to rely on its drag to reduce its speed enough

[92] URL: `http://spydergrid.com/eshop/voracitysubsystems/2016/07/20/cubesat-satellite-risk-analysis/` [Accessed on 24/06/2019]

for it to safely land. Preliminary calculations showed that without the capability to provide reverse thrust, the time to stop will be in magnitude of hours. The likelihood of this risk occurring is the same as all electric motor failures and is therefore relatively possible. The consequence of this risk would be catastrophic as there will be a high probability that the airship cannot come to a halt in time or be severely affected by gusts at the ground level, which it cannot withstand. This would mean that the airship may be lost due to an accident. A mitigation strategy for this failure can be to develop a contingency plan. The contingency plan would be, in case the variable pitch control stops working, the propeller can still be simply spun the other way to provide some level of reverse thrust. This would be significantly inefficient, and the level of thrust it can provide will be significantly less than what would have been possible if pitch of the propeller could be reversed. However, this would give more control to the airship, especially when landing. This would mean that there is less chance of the airship being entirely lost during landing and therefore the consequence of this risk is lowered to 'critical'. This change is shown in Figure 107.

10.4 Reliability, Availability, Maintainability and Safety (RAMS)

RAMS stands for **Reliability, Availability, Maintainability and Safety**. To define each aspect [56]:

1. Reliability is the probability that a system will perform in a satisfactory manner for a given period of time when used under specified operating conditions.
2. Availability is the degree, percent, or probability that a system will be ready or available when required for use.
3. Maintainability is the ease, accuracy, safety, and economy in the performance of maintenance actions.
4. Safety is the freedom from hazards to human and equipment.

Theses four aspects are closely interrelated and influence each other. Therefore, thorough analysis of each component and identification of how they interact with each other are critical for a reliable, efficient, and safe operation of the airship.

10.4.1 Reliability

Reliability in essence is very closely related with risks. In fact, it can be said that since the reliability is the probability of a certain component not failing in a certain time period, risk is a complement of reliability. Therefore, the smaller the risks, the higher the reliability. Components with high risks, and hence low reliability are identified in Figure 107 and described more in depth in Section 10.3. The communication subsystem has a redundant antenna module which increases its reliability. For the ADCS subsystem, one redundant star sensor, gyroscope and GPS receiver are added for higher reliability. There are total of 6 electric motors, 4 of which belongs to the propulsion subsystem and the rest to the buoyancy control subsystem. For the propulsion subsystem, there is no redundancy which limits the reliability. One extra electric motor is added for the buoyancy control. Regarding the six control valves, if one of the six valves fails, then the whole system fails and this makes it a critical failure mode. Fault Tree Analysis (FTA) can be utilized to analyze the system reliability. It starts with identifying top events and determine lower level events that can cause these. It is a top down approach and it helps identifying interrelation between events and calculate the reliability of the whole system.

10.4.2 Maintainability

Maintaining and repairing the airship are inherently challenging due to its big size. As it is mentioned in Section 9.2, the hangar must provide protection against strong winds and any adverse weather conditions, especially during lengthy maintenance. Also, the hangar must be large enough so that it accommodates the airship and other required equipment inside. Inspections of the external parts of the airship can be easily done with the use of cranes and lifts. However, inspecting the interior and the envelope is usually not as simple. One method for overcoming this is to install a window on top of the gondola for visual inspection of the envelope and the ballonets.

Every six months, the airship is taken down for maintenance. The high frequency of this regular maintenance implies that more reliable performance can be expected from the airship but it comes at a cost of decreased availability.

In order to fully capitalize on the potential functionality of the airship, the airship can be updated with different types of payloads (Modular Design).

10.4.3 Availability

The airship is designed to be operational for several months at a time. The only mandatory downtime is for regular check-up, maintenance and seasonal adjustments every six months. Assuming one week downtime for maintenance every six months, the availability is 96 %.

10.4.4 Safety

As the airship is to be operated semi-autonomously, there is no crew on board and therefore no chance of any casualty onboard during most of its mission phases.

However, due to the innately large size of the airship, the airship is susceptible to gusts and strong winds during taking off and landing phases. This leads to highly unpredictable movement of the airship. This is especially a problem since the airship is moving very slowly during these phases, the tail stabilizers and the control surfaces are ineffective in countering these disturbances. Therefore, the airship can inflict a huge safety concern for ground handling crews, nearby structures and the airship itself. During ascent and descent, the airship must follow every instruction from ATC to ensure safe airspace.

As the hydrogen is used as a lifting gas, the gas must be handled with very cautiously as explained in Section 9.2.1.

10.5 Sustainability

This section discuses the sustainability of the StratoCruiser and is based on Section 15.3 of the MTR [3]. Sustainability in design refers to the elimination of negative effects on the environment as a result of skillful and sensitive design [57].

One of the reasons why the StratoCruiser is designed as a platform for TIR EO in the first place is because of its sustainability. As an alternative to a satellite, an airship in general is more sustainable due to its reusability, its maintainability and its upgradeability. A satellite is usually expensive to develop and upon its end-of-life it is either maneuvered into a graveyard orbit or it is slowed down to burn up in the atmosphere. If the satellite is small enough, it will completely burn up in the atmosphere but if it is too large, it will only burn partly and the remainder will end up in the 'Spacecraft Cemetery' in the Pacific Ocean.[93] Either way, a satellite is harmful to the environment when it reaches its end-of-life and it is not reusable. On top of that, the launch vehicle releases various chemicals into the troposphere as well as the stratosphere. On the contrary, the StratoCruiser is capable of both ascending and descending without emitting chemicals into the upper parts of the atmosphere. While the airship is on the ground, maintenance is done. Moreover, the payload or other components of the airship can be upgraded to implement state-of-the-art technologies to stay competitive in the market for EO or to utilize the higher solar incidence to take less solar cells and more payloads onboard. The reusability, maintainability and upgradability of airships make them more sustainable than satellites, as one airship can be used for multiple missions and upon its end-of-life it can be either recycled or properly disposed of. So by designing the StratoCruiser, the solution to the need for EO is already a sustainable one on the mission level.

The sustainability of the design on system level mainly manifests in the way in which the StratoCruiser will descend. A simple way to do this would have been to vent the lighter-than-air gas

[93] URL `https://spaceplace.nasa.gov/spacecraft-graveyard/en/` [Accessed on 12/06/2019]

to decrease the buoyant force. The StratoCruiser will, however, descend by over-pressurizing the ballonets with air, which is a more complex but sustainable solution. By doing so, no lifting gas is lost in the atmosphere and refilling the entire envelope is not necessary when the airship has to be relaunched. The lifting gas was chosen to be hydrogen, as discussed in Section 4.7. This choice was, partly, based on the fact that hydrogen is more sustainable than helium because hydrogen is extracted from water using electricity. This makes hydrogen gas widely available. More importantly, the creation of hydrogen does not produce any harmful byproducts for the environment. Other than the gas used for buoyancy, the chosen propulsion method is a sustainable one compared to its alternatives. The electric motors, that are fed by the power generation from the solar cells, produce no emissions and allow for a long mission time since it is not limited by the amount of fuel that is taken on-board as for, for example, fuel based propulsion. This makes the electric motors more sustainable compared to fuel based propulsion.

On the subsystem level, sustainability was ensured by including it as a criteria in trade-offs where applicable. Not all trade-offs lend themselves to including sustainability as a criteria because all the options may be equally sustainable. Criteria for which all options are equally scored, do not add any useful information and were therefore discarded within the trade-offs. For some trade-offs, however, sustainability was included, like for the trade-off of the material selection for the primary mirror substrate, as performed in the MTR. One of the reasons for which Beryllium was not selected was because of its toxicity, which violates **SB-Sys-20**. For the production of the selected SiC for the mirror substrate, studies are being done to find sustainable ways of producing it, like making it from macadamia nut shells [58]. Moreover, the trade-off that selects the surface finish of the balloon takes sustainability into account through using degradability as a criterion. By selecting a finish that degrades slowly, the surface finish will not have to be re-applied regularly, which is beneficial for the sustainability of the balloon. Furthermore, the power that is required for operations will be generated by non-toxic thin film solar cells which is a more sustainable way of generating power than for example using RTGs to do so.

Recognizing that labelling a design as sustainable is a buzz-word used to describe the slightest efforts to make a design less harmful to the environment, the sustainability of the StratoCruiser has to be quantified. The emissions of the airship are indicative of its sustainability. The design has been affected by the sustainability strategy in such a way that ascending, descending and generating power will produce zero harmful emissions. As no other component produces emissions during the operations of the StratoCruiser, stating that the design of the airship is a sustainable one is justified.

11 Conclusion

The purpose of this report was to present the reader an extensive summary of the design processes for a thermal infrared Earth observation (EO) system. This system aimed to be cheaper, more maintainable, and sustainable than current Earth observation satellite systems such as current satellites. This report covered the conceptual design & detailed design processes for each subsystem, as well as the system integration for the final design. Also, the operations, logistics, and non-technical considerations were described.

First, the market analysis was performed to analyze the current state of Earth observation and identify potential clients. Potential markets include EO data, monitoring, telecommunications, and scientific experiments. The first two of these are analyzed quantitatively and found to be worth $11 million and $36 million, respectively. The StratoCruiser's strengths in these markets are rooted in its comparative flexibility, durability and sustainability with regards to competitors.

The conceptual design chapter described the various concepts envisioned on a system level and the brief analyses done to support trade-offs between the concepts. The chosen concept was a solar powered, autonomous, conventional hydrogen airship with a moving instrument.

The detailed design described the design of subsystems within the chosen concept. This meant, for instance, conducting computational fluid dynamics simulations to optimize the envelope shape, modelling the solar incidence on the surface of the airship through the year to choose the placement of solar cells, and designing the arrangement of linear actuators around the mirror to ensure it achieves its required pointing stability. The rationales and results of the design of each subsystem were brought together in the system integration chapter. Here, the mass, power, and cost budgets were presented, along with diagrams illustrating the flow of electricity, data, and commands through the system. A sensitivity analysis was conducted on the navigation, attitude control, and observation in order to analyze the effects on the performance of the airship. The final design consists of a conventional airship operating at maximum altitude of 20.5 km, providing a sub-arcsec pointing accuracy, a ground sampling distance of 1 m and a payload data signal-to-noise ratio of 102.

Following the final design, the verification and validation methods at both the system and subsystem level were presented, as well as suggested procedures for further model improvement. The verification of the requirements was also presented.

To investigate whether the StratoCruiser is commercially viable, a cost analysis was performed with an analysis of the return on investment. Using the market analysis, it was found that using 3 StratoCruisers across the country would yield a revenue between €9 million and €13 million, both of which result in a positive return on investment. Following this, the risks were identified and the mitigation strategies for the critical risks were implemented in the design. These involved either introducing redundancies or coming up with contingency plans. A RAMS analysis was also performed; since maintenance is estimated to be required for a week every six months, the availability is rated at 96 %. Safety of the ground crew and ground supporting structures was considered especially when taking off, landing, and handling hydrogen. The sustainability of the StratoCruiser was described here, which justified clearly how the StratoCruiser is far superior in this aspect compared to competing platforms.

The proposed StratoCruiser design has a lot of potential for commercial success and if the project were to continue with ample time and resources, it would serve a niche area in the current market.

12 Recommendations

This section answers the sections of if and how the project should be continued.

The team believes this project is technically feasible and has commercial potential. This project is a technical study and design. What is missing is an understanding of the business aspects. The first recommendation is to do a very extensive market analysis and make a solid business plan. This market analysis should also look beyond the Netherlands as it has potential in many regions. As the team members are lacking knowledge and skills in finance, business and law, a more diverse team would benefit the project. The team should be expanded by one or two people familiar with business and contacts in the start-up world.

An important part of the business plan is logistics. This report includes a section about logistics. This section does not specify potential locations, costs of the logistics, number of employees needed, etc. These have to be understood to asses the commercial potential.

If the project can get an interesting business plan, the product must be further developed. As the team is missing electrical engineers, the team should be expanded with electrical engineers to develop the motors, communication, on-board computers, etc.

In this continuation, the subsystems also have to be further developed. The following subsections discuss the recommendations for the subsystems.

Aerodynamics

Further work can be invested into optimizing the gondola shape in order to avoid separation and thus minimize the drag of the StratoCruiser. Similar work can also be done on the envelope shape to further minimize the drag. More detailed CFD simulations shall be done, firstly with a higher computational power to obtain a properly converged simulation, and secondly including wall heating effects, propeller rotation and cabling. Furthermore, additional analysis shall be performed in non-steady conditions and with rotations to obtain coefficient for a full dynamic stability analysis. Finally, the aerodynamics estimation cannot be considered valid until a wind-tunnel test is performed.

Instrumentation

The design of the instrumentation subsystem that is presented in Section 5.3, although presented in the detailed design chapter, is preliminary in the sense that if it were to be used on an actual airship, a lot of steps have to be taken before it can be fully operational.

First and foremost, the secondary and possibly tertiary optical elements will have to be designed in detail. Initially these were neglected and treated as a black box but Dr.ir. J.M. Kuiper and his PhD-candidate made a preliminary design for these optical elements in the course of the detailed design. However, before the instrument can be fully operational, the design of the secondary and tertiary optical elements will have to be more detailed. These elements will be used to change the path of the rays, coming from the primary mirror, to the detector in order to reduce the required volume of the instrument. This will significantly affect the geometry of the instrument as for example a hole in the primary mirror might be required if the detector is located behind the primary mirror like for example for a Cassegrain telescope. Depending on how much the geometry of the imaging instrument changes, the baffle design might have to be revisited. In any case, the baffle will have to be designed in more detail, including for example vanes to reflect the incoming stray light outwards.

Secondly, a detailed structure will have to be designed to host the instrument. At this point, only the mirror mount has been designed as this is required to analyze the coverage area of the airship. A supporting structure is, however, required to keep the instrument in place and prevent deformations of both the mirror and the baffle. As the only loads that act on the instrument include its own weight and the forces that are introduced by the actuators of the mount, the structure will likely not have to be too complex. With a well defined structure hosting the instrument, a thorough structural analysis should be done. Deformations of the mirror will have to be analyzed and related to the distortion of the image. To study the thermo-mechanical behaviour of the instrument the effect of temperature

differences of the mirror has be included in this analysis. The results of these analyses can then be used to optimize the design of the instrument for mass.

Thirdly, recognizing that requirement **SB-Subs-Meas-02** is still not met although the resolution has been improved since the preliminary design from 1.5 m to 1 m, a recommendation is made to evaluate the possibility of using super-resolution image construction. According to ESA, this makes it possible to improve the resolution of obtained images with the use of post-processing algorithms.[94] If this proves to be viable, the resolution of the captured images can be enhanced without having to change the design.

Finally, the design of the optical surfaces has to be verified by using ray trace software. With a program such as OSLO, the optics of the entire system can be analyzed in detail. The spot size can be plot and quantitative metrics like the Strehl ratio can be determined to prove whether or not the system is diffraction limited [20]. The ray trace software should also be used to analyze which rays hit the detector and which rays miss it. This will influence the noise calculations and lead to a more detailed SNR. Likely, this will increase the SNR because at this point all the rays coming from the ground are assumed to reach the detector which results in a lot of noise reaching the detector.

Instrumentation Integration

There are several aspects about the design of the instrument integration that need to be considered before finalizing the design of the instrument integration:

- Choose or design specific components: each component of the mounting system must be designed or purchased before the requirement on stability can be conclusively satisfied. This would also result in a more detailed accuracy budget.
- Detailed deformation analysis: with a design of the components and assembly of the mounting, the deformation of each can be analyzed, for example, using a finite element model. This would provide a more accurate picture of the stability of the instrument.
- Detailed vibrational analysis: the vibrational analysis described in this chapter is reliant on assumptions that make it too unrealistic to retain for a final design, for example, the baffle is modelled as a mass on the end of a beam rather than a distributed weight. More importantly, the vibration of the mirror itself was not modelled due to its complexity. This is out of the scope of this project but it must be performed before the design is ready.
- Research into additional mechanical components: with a rigorous vibrational analysis of the mirror and the mount, it may be useful to include dampers in the assembly. These can be in the form of vibration pads at the bases of the actuators, for example[95].
- Research into stabilization algorithms: as previously noted, the requirement on stability is a very stringent one that is difficult to meet through mechanical systems exclusively due to their inherent limits on accuracy. To improve the performance of the StratoCruiser in terms of image stability, the instrument could instead capture several tens or hundreds of images of the same view which do not satisfy the stability requirement, but can be combined using artificial intelligence software. This may result in a cheaper and more accurate image capturing system.

Power

At this stage of the power subsystem design, a number of assumptions and idealizations were considered to simplify the design process. A further immediate refinement of it lies in the following:

[94] URL `https://www.esa.int/gsp/ACT/projects/proba-v.html` [Accessed on 21/06/2019]
[95] URL: `http://scientificcomponents.com/prod37.htm` [Accessed on 24/06/2019]

- As mentioned in [3], having a power subsystem which is able to fulfil its requirements for the entirety of the year would produce an overdesigned system. Mainly because of daylight duration increase, the storage unit becomes redundantly large. On the other hand, this excess energy may come in handy in the operational scenario in which the airship has to travel in a direction different to West-East. Similarly, according to the optimization algorithm, the favourable position of solar array changes every day. The pros and cons of having multiple configurations in light of the mission requirements shall be identified once a better operational cost and overall economical/societal/political value should be assessed.
- In view of the necessity to relocate the airship across large distances at all times, backup fuel may be accounted for in the design of the energy storage unit. This is particularly important for the months of January and March when nominally operating solar cells provide the least excess energy.
- The effect of atmospheric sun irradiance attenuation as a function of solar elevation can be implemented. At high solar elevation angles, atmospheric attenuation is smaller than at low angles, meaning that surface patches closer to the top of the airship have a higher power output. Unfortunately, no credible model quantifying this effect has been found up to this point.
- Temperature degradation of solar cells has not been taken into account. It is estimated that the array temperature may have fluctuations in the order of tens of degrees. Array efficiency drops with increasing temperature.
- A more accurate model of reactant gases being pumped into their designated storage tanks can be developed. During tank filling up, depending on how full the tank is, different hydrolysis may be required to pressurize the reactants.
- Solar flux density as a function of time of the year can be implemented to increase the accuracy of the model.
- The basic electrical circuit can be designed. A decision should be made on whether the array is interconnected in a parallel or a series circuit.

Structures

This section will present a list of recommendations to further the design of the structural system. The suggestions will be mainly targeted at the presented components. A new iteration for the size of the airship is required as some of the sub-systems can be greatly optimized in terms of mass and their effect on the structure. Having a smaller envelope snowballs into a much lighter fabric as the loads are directly proportional with the radius of the envelope.

As of this moment the assumptions made in the sizing process of the envelope material introduce too many inaccuracies. A finite element analysis is required to obtain a more accurate stress distribution. Since the diameter of the envelope is variable, the hoop stresses will vary. This difference in stresses might allow for sections of the airship to have different aerial thicknesses. Having a value for the axial stresses will also help in optimizing the laminated membrane composite. Currently it is assumed that the stresses in axial direction are equal to those in hoop direction. The effects of the loads introduced by the suspension system also need to be determined. A finite element analysis of the membrane itself is also required to get a better estimate of the performance of the envelope membrane. The effects of gusts must also be determined.

The propulsion system assembly needs to be finalized. The duct, propeller, nose cone and nacelle need to be sized and analyzed. The interface between the pylon and the rest of the assembly also has to be created. Finally a new FEM analysis needs to be made as a verification.

A proper investigation regarding the tail fin structure needs to be done. The design presented in this section has only been used to have a mass estimate that is based on a known solution, rather than statistical data. As presented in the tail surface section there is a multitude of plausible concepts.

Collaboration with the control department is required to identify which one of those concepts is the best for the performance of the airship. Investigating the feasibility of inflatable fins is recommended because the weight of those components can be drastically decreased. The main challenge of this type of tails is integrating them with the buoyancy control system.

The gondola has not been investigated at all. Ideally the gondola allows for modular configuration of the systems inside it. This means that the position of each of the components can be easily moved and changing components can be done with minimum effort. Regarding the skin of the gondola it is not necessary for it to have attachment points for the payloads. The skin should be an aerodynamic surface, not a structural component. The current CAD model of the gondola is used to get a first look at the geometry of this component and how all of the different sub-systems that go inside it can be placed.

Propulsion

The main point of recommendation for the propulsion subsystem is to develop a code for the blade element theory to theoretically obtain the level of thrust needed. This way, the airfoil section, as well as the effect of twist could be analyzed and optimized more effectively. At this point, the effect of twist has not been looked into as much as the group would like to. It is believed that utilizing the effect of twist will optimize the performance of the blade, i.e., reduce drag but deliver enough thrust. Additionally, the choice of the airfoil section could be optimized for optimal use alongside the variable pitch capabilities.

Another point of recommendation would be to analyze the cabling through the propulsion subsystem. Currently, there is not much detail into the cabling and how they would all be interconnected to power, controllers, motors, etc. However, these would need to be finalized and optimized to be able to manufacture the airship. It is expected that the cabling would introduce some complications in the design as well, although it is not so clear what.

Buoyancy

The mass flow capacity of the ducts should be simulated and tested. The results are likely to slightly change the design. However, the mass is not likely to change drastically. The structural design of the ducts must be analyzed to check that they do not collapse due to the over-pressure.

Further detailed design is required. A motor has to be selected for the compressor and the blades must be designed. Also the valves require more detailed design.

The recommendation is to communicate clearly about the integration of the ducts in the gondola, simulate the mass flows and perform the detailed design. However, as the overall design is not very sensitive for changes in this subsystem, this should not be the focus. Other tasks are more urgent.

ADCS: Control and Stability

In order to accurately analyze the control and stability of the airship, a dynamic analysis must be carried out. Dynamic analysis utilize the state space system. This consists of linearized equations of the pitch, roll and yaw motions. The linearized equations are further transformed into non-dimensional forms using the dimensionless coefficients and derivatives. Due to limited time given for DSE, finding all the necessary derivatives was not possible. Airship Technology [11] Chapter 4: Stability and Control, covers the steps to obtain the state space system of equations of motion. As soon as the derivatives can be estimated, the further dynamic analysis can be performed with which the vertical and horizontal tail sizing can be further refined.

Bibliography

[1] A. Colozza. Initial Feasibility Assessment of a High Altitude Long Endurance Airship. Technical report, NASA, 2003.

[2] R. Tafazolli and A.K. Widiawan. High Altitude Platform Station (HAPS): A Review of New Infrastructure Development for Future Wireless Communications. *Wireless Personal Communications*, Aug 2007.

[3] B. Debeuckelaere, S.J. Kim, M. Maricic, G. Monechi, P.C. Nae, Y.H. Ryu, S. Seremet, R. Vohra, S. Willems. *Midterm Report.* TU Delft, May 2019.

[4] S. Fishman. Earth observation: State of play and future prospects. 2018.

[5] Copernicus: Market report. 2016.

[6] J.M. Kuiper. *Project Guide Design Synthesis Exercise.* TU Delft, Delft University of Technology, Delft, 2019.

[7] D.P. Drob et al. An Empirical Model of the Earth's Horizontal Wind Fields: Hwm07. *Journal of Geophysical Research*, 2008.

[8] D.P. Drob et al. An Update to the Horizontal Wind model (HWM): The Quiet Time Thermosphere. *Earth and Space Science*, 2015.

[9] L.M. Nicolai G.E. Carichner. *Fundamentals of Aircraft and Airship Design Volume 2.* AIAA Education Series, 1801 Alexander Bell Drive, Reston, VA 20191-4344, 2013.

[10] J.D. Anderson. *Fundamentals of Aerodynamics.* McGraw-Hill Education, 2010.

[11] G.A. Khoury. *Airship Technology.* Airship Technology. Cambridge University Press, 2012.

[12] H. Liang S. Yin, M. Zhu. Multi-Disciplinary Design Optimization with Variable Complexity Modeling for a Stratosphere Airship. *Chinese Journal of Aeronautics*, 32(5):1244 – 1255, 2019.

[13] T. Li, G.C. Lin, X.Y. Sun, Y. Wu. A Study on the Aerodynamic Characteristics of a Stratospheric Airship in its Entire Flight Envelope. *Proceedings of the Institution of Mechanical Engineers, Part G: Journal of Aerospace Engineering*, 232(5):902–921, 2018.

[14] C.M. Benphil K. Nidhul, A.S. Sunil. Effect of domain size and grid spacing on flow past a circular cylinder at low reynolds number. *International Journal of Engineering Research & Technology*, 3, aug 2014.

[15] M.E Youssef G. Hassan, A. Hassan. Numerical investigation of medium range re number aerodynamics characteristics for naca0018 airfoil. *CFD Letters*, 6, 01 2015.

[16] Fluent User Services Center. Modeling turbulent flows introductory-fluent training. Lecture Slides, 2006.

[17] R.K. Calay V. Voloshin, Y.K.Chen. A comparison of turbulence models in airship steady-state CFD simulations, Oct 2012.

[18] B. Debeuckelaere, S.J. Kim, M. Maricic, G. Monechi, P.C. Nae, Y.H. Ryu, S. Seremet, R. Vohra, S. Willems. *Baseline Report.* TU Delft, May 2019.

[19] A. Kamp. *AE4880 - Space Instrumentation Engineering.* TU Delft Reader, 2018.

[20] D. Dolkens. Msc thesis: *A Deployable Telescope for Sub-Meter Resolutions from MicroSatellite Platforms*, 2015.

[21] B. deBlonk I.A. Palusinski L.E. Matson, M.Y. Cheng. *Silicon Carbide Technologies for Lightweighted Aerospace Mirrors*, 2008.

[22] B. Hässler. *Atmospheric Transmission Models for Infrared Wavelengths*, 2008.

[23] J. Farmer N. Thomas, J. Wolfe. *Protected Silver Coating for Astronomical Mirrors*, 1998.

[24] D. Ostrower. Optical thermal imaging – replacing microbolometer technology and achieving universal deployment. Technical report, 2006.

[25] K.J. Dinkel, J.H. Diller, Z.J.B. Dischner , N.A. Truesdale, E.F. Young. Daystar: Modeling and test results of a balloon-borne daytime star tracker. In *2013 IEEE Aerospace Conference*, March 2013.

[26] W.C. Nelson. *Airplane Propeller Principles.* John Wiley & Sons, 1944.

[27] D. Biermann and E.P. Hartman. *Report No. 640: The Aerodynamic Characteristics of Full-Scale Propellers Having 2, 3, and 4 Blades of Clark Y and R.A.F. 6 Airfoil Sections.* National Advisory Committee for Aeronautics, U.S. Department of Commerce, Springfield, VA, 22161, USA, 1938.

[28] P. Lolis. Development of a preliminary weight estimation method for advanced turbofan engines. Technical report, 2014.

[29] X. Fei and Y. Zhengyin. Drag reduction for an airship with proper arrangement of propellers. Technical report, 2009.

[30] K. Gopinath and M.M. Mayuram. Module 2, gearbox, lecture 17: Design of gearbox.

[31] R.E.S. Dunbar and P.K. Pal. Optimum design for propellers using series data, 1983.

[32] Y. Li, J. Jiao, B. Song, Y. Zhang. Optimal design and experiment of propellers for high altitude airship. Technical report, 2018.

[33] W.J. Larson and J.R. Wertz. *Space Mission Analysis and Design.* Microcosm Press, K1uwer Academic Publishers, Segundo, USA, 2005.

[34] A. Doi et al. A Balloon-Borne Very Long Baseline Interferometry Experiment in the Stratosphere: Systems Design and Developments. Technical Report 1, Jan 2019.

[35] P. Fortescue, J. Stark and G. Swinderd. *Spacecraft Systems Engineering.* John Wiley & Sons, 2011.

[36] M.A. Green. Cryogenic refrigeration requirements for superconducting insertion devices in a light source.

[37] M.A. Green. The cost of coolers for cooling superconducting devices at temperatures at 4.2 k, 20 k, 40 k and 77 k. *AIAA*, 2015.

[38] Y. Liu and Y. Wang. Numerical simulation about thermal environment of solar energy airship in stratosphere. Technical report, 2012.

[39] R. Humphries, Dr. J.M. Stuckey, L.M. Thompson , D. Wilkes. *Development of an Improved Protective Cover/Light Block for Multilayer Insulation.* NASA, 1983.

[40] B.T.C Zandbergen. *Aerospace Design & Systems Engineering Elements I Part: Spacecraft (bus) design and sizing.* Delft University of Technology, Delft, 2017.

[41] Cubic Tech Corp. High strength-to-weight ratio non-woven technical fabrics for aerospace applications. *AIAA*, AIAA Balloon Systems Conference, may 2009.

[42] W. Kang. *Mechanical property characterization of film-fabric laminate for stratospheric airship envelope*, volume 75. sep 2006.

[43] Mass properties control for space systems, 2015.

[44] R. Bitten et all. Historical mass, power, schedule & cost growth for nasa instruments & spacecraft. NASA Cost Symposium, aug 2016.

[45] M.F. Barschke, J. Bartholomäus, M. Lehmann. *The TUBIN mission within the context of present and future satellite-based fire detection systems*, 2018.

[46] W. Halle et al. *Infrared Remote-Sensing and Results of the DLR FireBIRD Mission*, 2018.

[47] A. Euler. Material challenges for lighter-than-air systems in high altitude applications. *AIAA*, jun 2005.

[48] S.J. Hulshoff. *AE2220-II Computational Modelling.* TU Delft, version 1 edition, 2017.

[49] D.R. Ladner. Performance and mass vs. operating temperature for pulse tube and stirling cryocoolers. Technical report, 2011.

[50] I.H. Abbott. Airship model tests in the variable density wind tunnel. Technical report, National Advisory Committee For Aeronautics, 1931.

[51] Electronic Code of Federal Regulations. *Noise Standards: Aircraft Type and Airworthiness Certification*, 2017.

[52] Rijksluchtvaartdienst and Luftfahrt-Bundesamt. *Transport Airship Requirements*, 2000.

[53] G.M. Green and I.A. Zlochower. The limiting oxygen concentration and flammability limits of gases and gas mixtures. *Journal of Loss Prevention in the Process Industries*, pages 499–505, 2009.

[54] J. Doye and D. Wales. Global Optimization by Basin-Hopping and the Lowest Energy Structures of Lennard-Jones Clusters Containing up to 110 Atoms. Mar 1998.

[55] F. Lees. Loss Prevention in the Process Industries: Hazard Identification, Assessment and Control, 2012.

[56] Prof. Dr. R. Curran and Dr. W. Verhagen. *AE3221-I Systems Engineering and Aerospace Design Lecture 8 - Risk Management & Reliability Engineering*. TU Delft Powerpoint Slides, 2019.

[57] J.F. McLennan. *The Philosophy of Sustainable Design*. Ecotone Publishing Company LLC, Kansas City, MO, USA, 2004.

[58] R. Rajarao and V. Sahajwalla. A cleaner, sustainable approach for synthesising high purity silicon carbide and silicon nitride nanopowders using macadamia shell waste. 2016.

Control Surfaces	-Balloon Attitude	-Balloon Attitude											
	Mirror Gimbal					-Mirror operating attitude							
		Attitude Sensors		-Current Attitude			-Current Attitude						
			Propulsion		-Balloon Position								
-Control surfaces deflection	-Required mirror attitude		-Required engines thrust	**Main Computer**		-Observation Commands	-Processed observation data		-Required components temperatures			-Total Required power	-Required Ballonets volume -Required Overpressure
				-Current Position	**Navigation Sensor**		-Balloon position -Balloon altitude						
				-Observation raw data		**Optical System**	-Observation raw data						
				-Navigation Commands -Observation Commands -Weather forecast data			**Communication system**	-Observation data -Balloon state data -Atmospheric state data					
							-Commands -Weather forecast	**Ground Station**					
				-Main computer cooling		-Optical system temperature			**Thermal Control System**			-Power storage temperature	-Balloon temperature
							-Balloon temperature -Balloon pressure		-Balloon temperature	**Balloon State Sensors**			
				-Atmospheric temperature -Atmospheric pressure -Wind information			-Atmospheric temperature -Atmospheric pressure -Wind information		-Atmospheric temperature		**External Sensors**		
-Actuator power	-Actuator power	-Sensors power	-Engine Power	-Required supply power	-Sensors power	-Sensor power	-Required power		-Required power	-Sensors power	-Sensors power	**Power Subsystem**	-Compressors Power
		-Balloon Pitch attitude			-Balloon Altitude								**Buoyancy Control**

Figure 108: N2 Chart of the StratoCruiser

Figure 109: Functional Flow Diagram of the StratoCruiser

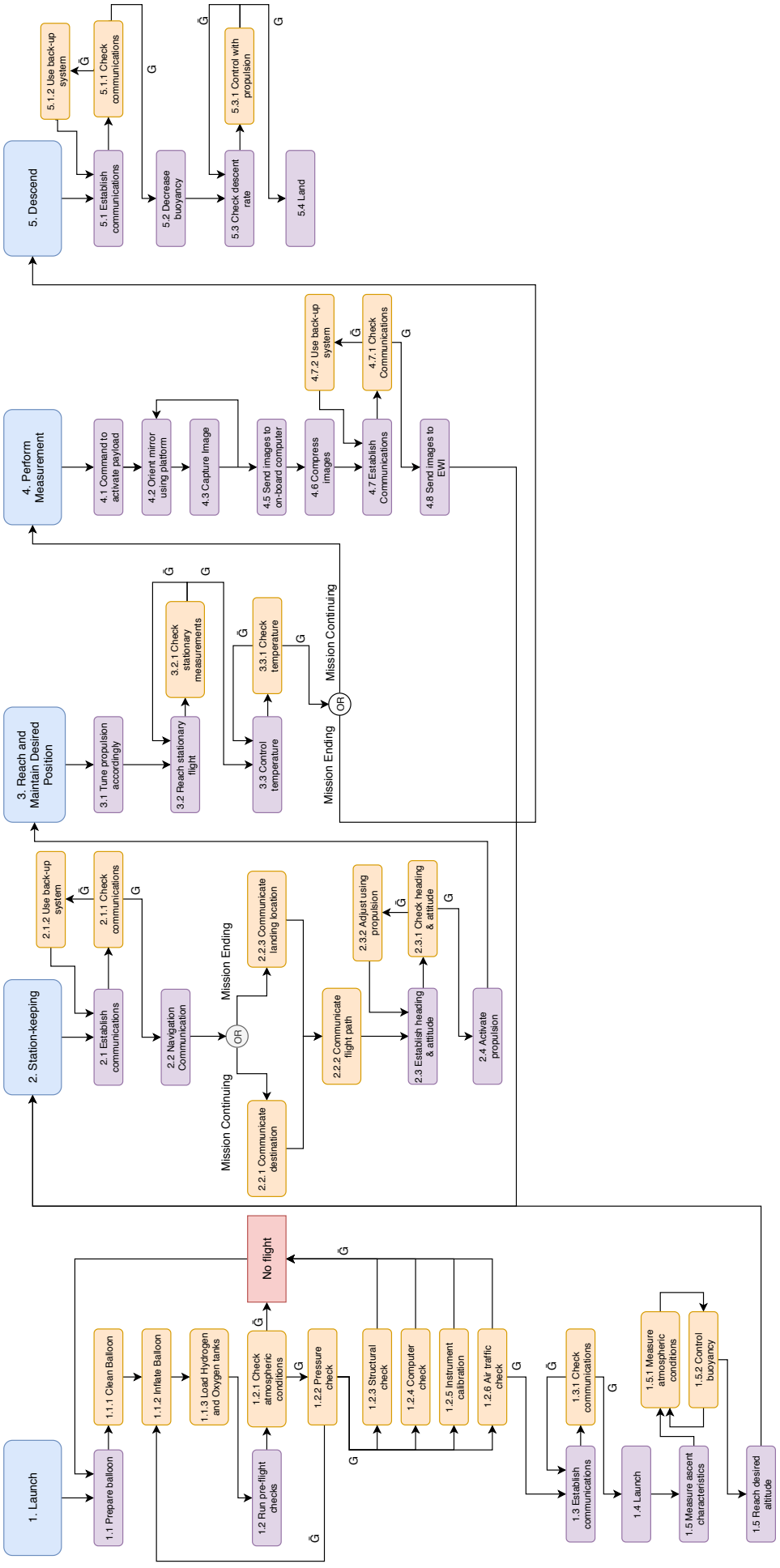

Figure 110: Functional Breakdown Structure of the StratoCruiser

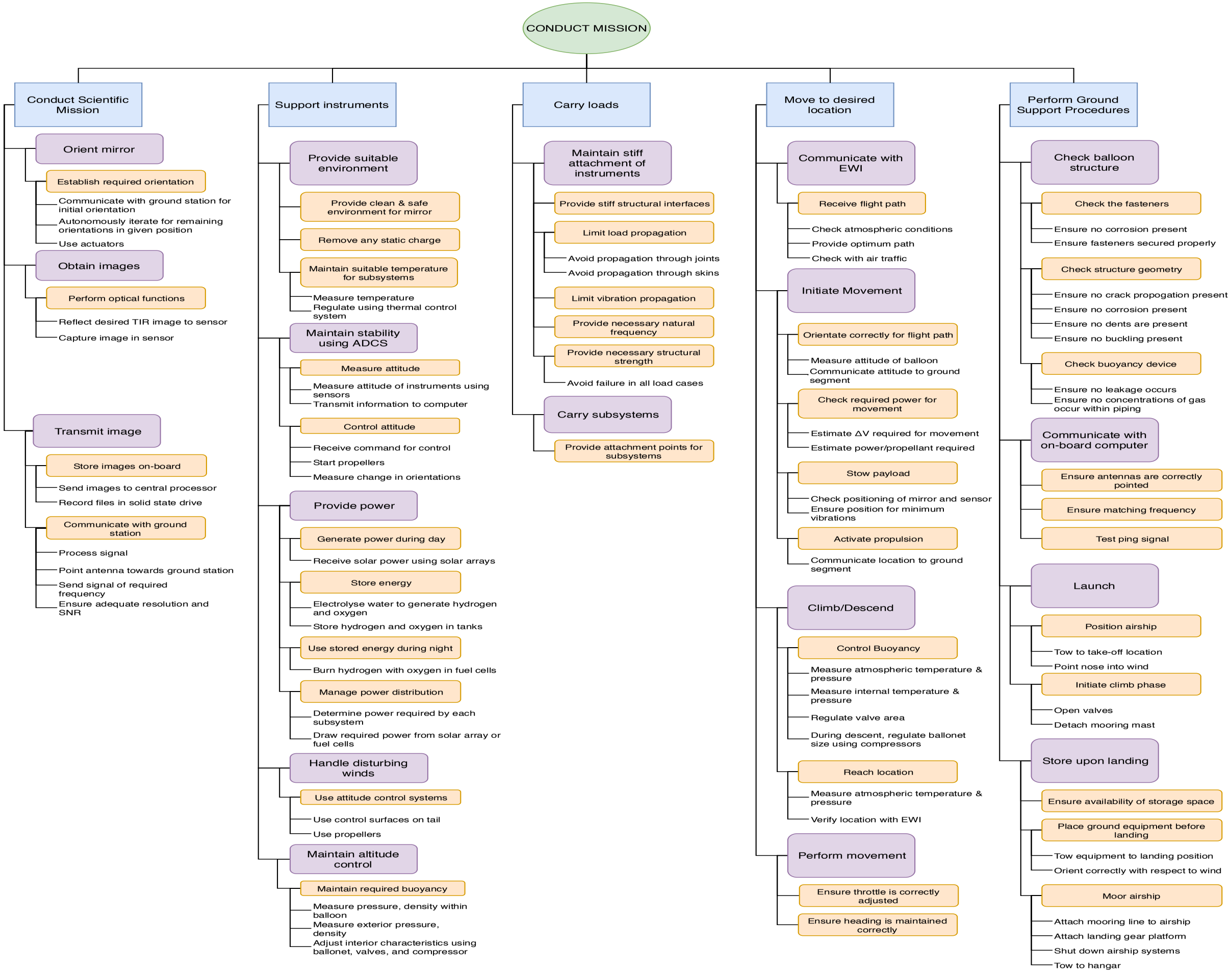

Figure 111: Project design & development logic for hypothetical progression

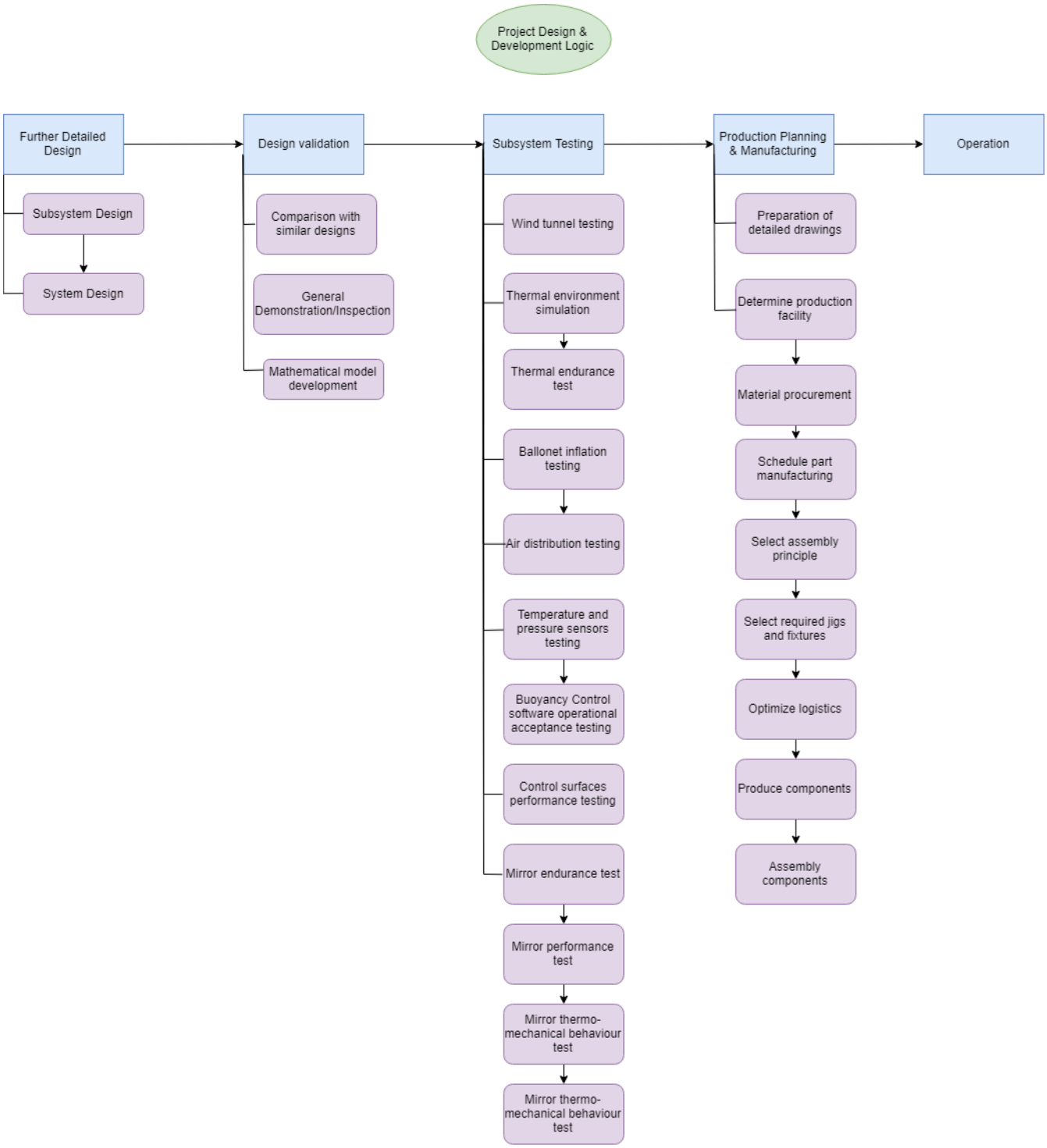

Figure 112: Gantt chart for hypothetical progression of project

ID	Task Mode	WBS	Task Name	Duration	Predecessors	% Complete
1		**1**	**Project Management**	**467 hrs**		**73%**
75		**2**	**Deriving Requirements**	**14 hrs**	**11,12,38SS**	**100%**
87		**3**	**Conceptual Design**	**13 hrs**	**75**	**100%**
100		**4**	**Preliminary Design**	**111 hrs**	**87**	**100%**
263		**5**	**Detailed Design**	**117 hrs**	**51**	**100%**
667		**6**	**Further Detailed Design**	**116 hrs**	**263**	**0%**
668		**6.1**	**Subsystem Design**	**104 hrs**		**0%**
817		**6.2**	**System Design**	**32 hrs**	**668FS-20 hrs**	**0%**
843		**7**	**Design validation**	**1120 hrs**	**667**	**0%**
844		7.1	Comparison with similar design	16 hrs		0%
845		7.2	Demonstration/Inspection	10 hrs	879	0%
846		7.3	Develop mathematical validation model	20 hrs		0%
847		**7.4**	**Subsystem Testing**	**115 hrs**	**845,846**	**0%**
848		7.4.1	Wind tunnel testing	30 hrs		0%
849		7.4.2	Thermal environment simulation	25 hrs		0%
850		7.4.3	Thermal endurance test	25 hrs		0%
851		7.4.4	Ballonet inflation testing	10 hrs		0%
852		7.4.5	Air distribution testing	15 hrs		0%
853		7.4.6	Temperature and pressure sensors testing	60 hrs		0%
854		7.4.7	Buoyancy Control software operational acceptance testing	16 hrs		0%
855		7.4.8	Control surfaces performance testing	35 hrs		0%
856		7.4.9	Mirror endurance test	25 hrs		0%
857		7.4.10	Mirror performance test	40 hrs	856	0%
858		7.4.11	Mirror thermo-mechanical behaviour test	50 hrs	857	0%
859		7.4.12	Rotor blade structural analysis	75 hrs		0%
860		7.4.13	Propeller pylon structural testing	35 hrs		0%
861		7.4.14	TT&C and C&DH combined testing	25 hrs		0%
862		7.4.15	Subsystem Testing	50 hrs	878	0%
863		7.5	Full-scale Structural Testing	50 hrs	847	0%
864		7.6	Full-scale Compatibility Test	75 hrs	847	0%
865		7.7	Software Validation	50 hrs	847	0%
866		7.8	Mission Scenario Tests	30 hrs	864	0%
867		7.9	Operations Readiness Tests	15 hrs	866	0%
868		7.10	Design Certification	60 hrs	867	0%
869		7.11	Stress-Testing and Simulation	30 hrs	879,846	0%
870		**8**	**Production planning & Manufacturing**	**815 hrs**	**667**	**0%**
871		8.1	Preparation of detailed drawings	80 hrs		0%
872		8.2	Determine production facility	3 hrs		0%
873		8.3	Material procurement	25 hrs	871	0%
874		8.4	Schedule part manufacturing	3 hrs	871	0%
875		8.5	Select assembly principle	2 hrs		0%
876		8.6	Select required jigs and fixtures	20 hrs	871	0%
877		8.7	Optimize logistics	15 hrs	876	0%
878		8.8	Produce components	400 hrs	877	0%
879		8.9	Assembly components	300 hrs	878	0%
880		9	Operational Phase	100 hrs?	870,843	0%

Project: Stratospheric Balloon
Date: Mon 24/06/19

Task, Split, Milestone, Summary, Project Summary, Inactive Task, Inactive Milestone, Inactive Summary, Manual Task, Duration-only, Manual Summary Rollup, Manual Summary, Start-only, Finish-only, External Tasks, External Milestone, Deadline, Critical, Critical Split, Progress, Manual Progress

Page 1

Equations for parametric tail sizing [9]

$$
\begin{array}{ll}
(C_{L_\alpha})_{tail} = \frac{2\pi AR_T}{2+\sqrt{4+AR_T^2(1+tan^2(\Delta)}} & AR_T = \frac{b_T^2}{S_{T_{Total}}} \\
(C_{n_\beta})_T = N\frac{(C_{L\alpha})_{tail}S_{T_{total}}l_T\eta_M}{Vol^{\frac{2}{3}}\times l_B}\sin^2(\Gamma) & (C_{Y_\beta})_T = -N\frac{(C_{L\alpha})_{tail}S_{T_{total}}\eta_F}{Vol^{\frac{2}{3}}}\sin^2(\Gamma) \\
(C_{n_{\hat{r}}})_T = -N\frac{(C_{L_\alpha})_{tail}S_{T_{total}}l_T^2}{Vol\times l_B}sin^2(\Gamma) & (C_{Y_{\hat{r}}})_T = N\frac{(C_{L_\alpha})_{tail}S_{T_{total}}l_T}{Vol}sin^2(\Gamma) \\
(C_{n_{\delta r}})_T = N\frac{(C_{L_\alpha})_{tail}\tau S_{T_{total}}l_{T_\delta}\eta_{M_\delta}}{Vol^{\frac{2}{3}}\times l_B}sin(\Gamma) & (C_{Y_{\delta r}})_T = -N\frac{(C_{L_\alpha})_{tail}\tau S_T\eta_{F_\delta}}{Vol^{\frac{2}{3}}}sin(\Gamma) \\
(C_{m_\alpha})_T = -N\frac{(C_{L_\alpha})_{tail}S_{T_{total}}l_T\eta_M}{Vol^{\frac{2}{3}}\times l_B}\cos^2(\Gamma) & (C_{L_\alpha})_T = N\frac{(C_{L_\alpha})_{tail}S_{T_{total}}\eta_F}{Vol^{\frac{2}{3}}}\cos^2(\Gamma) \\
(C_{m_{\hat{q}}})_T = -N\frac{(C_{L_\alpha})_{tail}S_{T_{total}}l_T^2}{Vol\times l_B}cos^2(\Gamma) & (C_{L_{\hat{q}}})_T = N\frac{(C_{L_\alpha})_{tail}S_{T_{total}}l_T}{Vol}cos^2(\Gamma) \\
(C_{m_{\delta e}})_T = N\frac{(C_{L_\alpha})_{tail}\tau S_T l_{T_\delta}\eta_{M_\delta}}{Vol^{\frac{2}{3}}\times l_B}cos(\Gamma) & (C_{L_{\delta e}})_T = -N\frac{(C_{L_\alpha})_{tail}\tau S_T\eta_{F_\delta}}{Vol^{\frac{2}{3}}}cos(\Gamma)
\end{array}
\tag{12.1}
$$